Internal field 59Co Nuclear Magnetic Resonance, application to catalysts and related structures

Andrey Andreev

Université Pierre et Marie Curie

Boreskov Institute of Catalysis SB RAS

Physique et Chimie des Matériaux (ED 397)

SIMM, ESPCI ParisTech / SSNMR BIC SB RAS

Résonance Magnétique Nucléaire du ^{59}Co en champ interne, application aux catalyseurs et à des structures similaires

Par Andrey ANDREEV

Thèse de doctorat de Physique

Dirigée par Jean-Baptiste d'ESPINOSE de LACAILLERIE et Olga LAPINA

Présentée et soutenue publiquement le 2 Octobre 2015

Devant un jury composé de :

M. Christian MÉNY	DR CNRS, DMONS, Strasbourg	Rapporteur
Mme. Sharon ASHBROOK	Professeur, NMR group, St Andrews	Rapporteur
M. Christian BONHOMME	Professeur, SMILES, Paris	Examinateur
M. Fabrice DIEHL	Ingénieur R&D, IFP, Solaize	Examinateur
M. Jean-Baptiste D'ESPINOSE DE LACAILLERIE	Maître de Conférences, SIMM, Paris	Directeur
Mme. Olga LAPINA	Professeur, SSNMR group, Novosibirsk	Directrice

Dédicace

Remerciements

Sommaire

Sommaire 3
List of acronyms and abbreviations 4
Academic context 7
Introduction 8
1. Principles of internal field NMR 12
1.1. Hamiltonian operator in magnetic materials 12
1.2. Bloch model of internal field NMR. 16
1.3. Conclusions to Chapter 1: 28
2. Practical aspects of internal field NMR spectroscopy application 30
2.1. Co metal 30
2.2. Cobalt alloys 42
2.3. Conclusions to Chapter 2: 46
3. Experimental 50
3.1. Internal field ^{59}Co NMR. 50
3.2. Complementary methods 54
4. Results and publications 56
4.1. Short review on FTS 56
4.1.1. Historical perspective 56
4.1.2. FTS catalysts 57
4.1.3. Structure of FTS catalysts 58
4.2. Basics on internal field ^{59}Co NMR 60
4.2.1. Co metal powder 60
4.2.2. Physics of Co nanoparticles 70
4.3. Catalytic and related materials 82
4.3.1. Supported FTS catalysts 82
4.3.2. High temperature strong CoAlO/Co-Al cermets 92
4.3.3. Low-temperature Al_2O_3/CoAlO/CoAl cermet 109
4.4. Co/MWCNT hybrids 119
5. Conclusion 150
5.1. Summary of results 150
5.2. Future work 153
Résumé en français 156
Bibliographie 165
List of publications 181

List of acronyms and abbreviations

EXAFS - Extended X-Ray Absorption Fine Structure

HRTEM – High Resolution Transmission Electron Microscopy

hcp – hexagonal close packed

fcc – face centered cubic

HTT – hydrothermal treatment

sfs – stacking faults

BIC – Boreskov Institute of Catalysis (Siberian Branch of the Russian Academy of Sciences)

IRS (FT-IRS) – infra-red spectroscopy (Fourier transform infra-red spectroscopy)

rf – radiofrequency

hf – hyperfine (interaction)

FTS – Fischer-Tropsch synthesis

NMR – Nuclear Magnetic Resonance

B_0 – external magnetic field

B_1 – magnetic component of radiofrequency pulse

B_c – magnetic field due to Fermi contact interaction

B_a – magnetic anisotropy field

B_{hf} – magnetic field due to hyperfine interaction

B_{loc} – local magnetic field at the nucleus

N_d – demagnetizing factor

M – electron magnetization

m – nuclear magnetization

e – electron charge, $4.8 \cdot 10^{-10}$ $cm^{3/2} \cdot g^{1/2} \cdot s^{-1}$

$\hbar$ - Planck constant, $1{,}054 \cdot 10^{-27}$ erg·s

$\hat{H}$ - Hamiltonian operator

$\hat{L}$ - angular momentum ($\hat{r} \times \hat{p}$).

β – Bohr magneton ($\frac{e\hbar}{2m_e c}$), $927{,}4 \cdot 10^{-23}$ erg/G

β_N – nuclear magneton ($\frac{e\hbar}{2m_N c}$)

g – electronic g-factor

g_N – nuclear g-factor

$\psi(r)$ – wave function

$\overline{S}$ – average spin number per atom

T_1 – spin-lattice longitudinal relaxation time

T_2 – spin-spin transverse relaxation time

η – enhancement factor

STEM-HAADF - Scanning Transmission mode with High Angle Annular Dark Field

MAS – magic angle spinning

FWHM - full width at a half maximum

d.w. – domain wall

FID – free induction decay

NN – nearest neighbor

bcc - base-centered cubic lattice

syngas – synthesis gas

CNT - carbon nanotube

SWCNT - single-walled carbon nanotube

MWCNT - multi-walled carbon nanotube

Academic context

This work is a joint-PhD project (*co-tutelle*) between Novosibirsk State University in Akademgorodok (Russia) and the *Université Pierre et Marie Curie – Paris VI* in Paris (France).

According to the joint PhD agreement, the manuscript had to be written in Russian and defended at the Boreskov Institute of Catalysis in Akademgorodok (Novosibirsk, Russia). The Russian manuscript was presented and successfully defended on April 8, 2015. The Russian version of the manuscript is available online at:

http://www.kinetics.nsc.ru/seminar/Andreev1.pdf.

Nevertheless, to allow a fair evaluation of the work by non-Russian speakers, a PhD defense in Paris and in English has been planned. This manuscript was written in support of this defense.

The author of the manuscript and his advisors not being native English speakers, the author would like to apologize in advance to his readers for possible imperfections in the English language used.

Introduction

Since the 1940-s Co based catalysts are widely used in industry. There are many catalytic and related processes based on Co metal, for example, acetic acid production from acetaldehyde, methanol homologation reaction, the processes of hydrocarbon oxidation *etc.* However, one of the most important and large scale catalytic processes based on Cobalt is the Fischer-Tropsch synthesis (FTS), *i.e.* the hydrocarbons production from synthesis gas (syngas) ($CO + H_2$). The feedstock can be coal (even lignite, or brown coal, the lowest rank of coal), natural gas or biomass. The active phase in FTS catalysts is often Co metal particles and there is thus a strong interest for developing efficient ways to characterize cobalt metal particles. The primary aim of this PhD work is thus to assess the potential of ^{59}Co internal field nuclear magnetic resonance (NMR) to characterize cobalt based catalysts. As it turns out, the structure of cobalt metallic particles is also of interest in other fields of material sciences such as materials for energy storage or electro-magnetic devices. The knowledge and know-how developed during this PhD were thus also applied to materials other than catalysts but also involving cobalt metal particles.

Various physico-chemical techniques have been used in the literature to study Co metal based chemical objects such as scanning and transmission electron microscopy (SEM and TEM), X-ray diffraction (XRD), Fourier transform infrared spectroscopy (FTIR), Raman spectroscopy, and Extended X-ray absorption fine structure (EXAFS). These methods offer complementary molecular and structural information; however all of them have their limitations when dealing with faulted or nanosized disperse systems. For example, XRD is suitable for perfect Co metal phases but the occurrence of stacking faults (sfs) or of very small nanoparticles drastically broaden the XRD peaks sometimes beyond detection. This is particularly regrettable as small nanoparticles and faulted structures are very often the most active phases.

Unlike other technique, internal field ^{59}Co NMR can distinguish not only pure Co phases (fcc and hcp), sfs, but also different magnetic parts of the specimens such as magnetic domains, domain walls, and single-domain particles. Because all ferromagnetic domains contribute to the signal, internal field ^{59}Co NMR provides in principle a quantitative analysis of the sample (at least the part in a ferromagnetic state). Moreover, the method is very sensitive to the Co metal first coordination sphere, and it can follow quantitatively the effect of foreign nuclei in the nearest Co shell (for example in Co alloys).

Despite the long history of internal (or local) field NMR, a lot of questions remain left without attention in the case of Co metal. The generally accepted internal field ^{59}Co NMR spectra description is based on comparisons with what is observed in "pure" fcc and hcp Co metal phases including a set of stacking faults sf_1-sf_5. However, this approach does not account for the main feature of internal field NMR, *i.e.* its magnetic origin. Since the resonance occurs in the internal field, the numerous contributions to this internal field should be considered as well. Also the different magnetically ordered parts of the specimen (domains and domain walls) require a special attention since the NMR signal induction mechanism is different. All this can affect the NMR signal intensity, as well the line position (for example, the effect of the demagnetizing field). Therefore, the contribution all these magnetic effects to the internal field must be considered when interpreting a ^{59}Co internal field NMR spectrum. An important preliminary part of this PhD work was thus devoted to carefully collect and sum up the literature on the subject, both concerning theoretical and experimental aspects.

Structure of the manuscript

C*hapter One* presents a review of internal field NMR principles. Although the theory presented there is not original, internal field NMR is a somewhat confidential technique. It is thus necessary to summarize its theory to allow the reading of the manuscript by non-specialists. The nature of the magnetic interactions responsible for NMR in magnetically ordered compounds at zero applied external magnetic field is discussed. In this chapter, we provide the Bloch model, which give a good insight to the internal field NMR mechanism. The internal field NMR distinctive features, which are not observed in NMR in diamagnetic materials at high external magnetic fields, are also enumerated.

Chapter Two covers the historical stages of the internal field ^{59}Co NMR development. The main stages, controversies and progresses are emphasized. Further, a short description of the possible range of materials that can be studied by internal field NMR is provided.

Chapter Three is a description of the main experimental methods that have been used in this work (mainly internal field ^{59}Co NMR since the experimental details concerning other supporting techniques are already described within our published or submitted articles reproduced thereafter).

Chapter Four consists of several subchapters. *Chapter 4.1* gives a particular emphasis on Co the Fischer-Tropsch synthesis (FTS) catalysts, as it is today the main domain of application of the technique; a brief history of FTS, and short review on the synthesis and structure of Co based FTS catalysts is also presented. *Chapter 4.2* is the study of a model sample used to assess our understanding of ^{59}Co internal field NMR spectra. The model consists of a commercial Co metal powder of micron size. A model of spectral interpretation is proposed in this chapter. This model is based on separating the structural (fcc, hcp, and sfs) and magnetic (domains, domain walls, and single-domain particles) contributions. The model was verified by comparing the hcp/fcc ratio obtained by NMR with the one obtained by XRD on the same specimen. A quantitative agreement is reached, to our knowledge for the first time. This work was published in *Applied Magnetic Resonance* (doi: 10.1007/s00723-014-0580-0) [1]. Further this chapter uncovers the thermal stability of small Co nanoparticles probed by *in situ* by internal field NMR. The Co metal supported on *β*-SiC is studied within the 300-850 K temperature range. A full analysis of line position, width and NMR signal intensity is given in this chapter. The line position and width is mainly determined by magnetic properties (*i.e.* the behavior of electron magnetization), whereas the absolute and relative NMR intensities give crucial information regarding Co particle stability and the allotropic phase transition from hcp to fcc, which is found to occur within a temperature range of 600-650 K. This work was published in *PCCP* (doi: 10.1039/C4CP05327C) [2].

Chapter 4.3 is devoted to the study by internal field $_{59}$Co NMR of catalysis and related structures. The *first part* is a study of a Fischer-Tropsch catalyst synthesized by a non-conventional co-precipitation route on different modification of aluminum oxides. This work was published in *Journal of Structural Chemistry* (doi: 10.1134/S0022476613070093)[3]. The *second part* describes the application of internal field NMR to a CoAlO/CoAl ceramic material, which is examined by a set of techniques including NMR that provide unique information on the metallic cermet part structure. This work is published in *Journal of Materials Science and Engineering A* (doi: 10.17265/2161-6213/2012.02.001) [4]. Finally, the last and *third part*, discloses the structure of modified Al_2O_3/CoAlO/CoAl cermet with enhanced surface area, a material which is an ideal candidate as a catalytist support in non-conventional reactors heated by microwave irradiation. This work is published in *Advance Materials Research* (doi: 10.4028/www.scientific.net/AMR.702.79) [5]

Chapter 4.4 discloses the structure and stabilization of different size Co metal nanoparticles on a multi-walled carbon nanotubes (MWCNTs). Promising hybrid structures including stable ferromagnetic nanoparticles were formed. The hybrid structures were examined by internal field ^{59}Co NMR, HRTEM, and *in situ* synchrotron XRD, which provide crucial information on Co particles reduction, stability and structures. The physical principles of stabilization of certain Co metal particles are also discussed. Except for the relaxation studies, this work was submitted to *Journal of Materials Chemistry A*.

In Chapter 5, a general conclusion of the manuscript is done with future perspective for the internal field ^{59}Co NMR method.

CHAPTER 1
PRINCIPLES OF INTERNAL FIELD NMR

1. Principles of internal field NMR

1.1. Hamiltonian operator in magnetic materials

To facilitate the understanding of the manuscript by non-specialist readers, it is essential to start from the description of the Hamiltonian operator relevant to magnetic substances.

At first, let us recall the well-known relationship between the magnetic moment and the angular momentum operator used in quantum mechanics:

$$\hat{\mu} = \frac{\mu}{s}\hat{s},$$

where the proportionality coefficient between the magnetic moment μ and the intrinsic angular momentum s of a particle of non-zero spin is given by $\frac{\mu}{s} = -\frac{|e|\hbar}{mc} = -2\beta$, thus defining the Bohr magneton β. c is the speed of light, $\hbar$ the Plank constant, and e and m the charge and mass of the particle respectively. For nuclear spins, the proportionality between the magnetic moment and the intrinsic angular momentum is usually expressed in terms of the nuclear magneton $\mu_N = \frac{e\hbar}{2m_p c}$, where m_p is the proton mass (for example, $\mu_{neutron}$ is equal to 1.91 μ_N).

The Hamiltonian of a charged particle in an electromagnetic field is determined by

$$\hat{H} = \frac{1}{2m}(\hat{p} - \frac{e}{c}\vec{A})^2 + e\phi. \qquad (1.1.1)$$

where $\hat{p} = -i\hbar\nabla$ is the generalized momentum operator of the particle, $\vec{A}$ is the vector potential of the magnetic field, ϕ the scalar potential of the electrical field, c the light speed velocity constant, and m the mass of the particle.

However, this expression is correct only for a particle without spin. Otherwise, the additional interaction of the intrinsic magnetic moment of the particle with the magnetic field B must

also be taken into consideration. [6] Under the usual conditions of magnetic resonance experiments, the electrical field vanishes and the Hamiltonian takes the form:

$$\hat{H} = \frac{1}{2m}(\hat{p} - \frac{e}{c}A)^2 - \hat{\mu}B. \qquad (1.1.2)$$

According to classical electrodynamics, a magnetic dipole μ creates, at a distance r, a magnetic field B, which is determined by the following set of equations:

$$A = \frac{\mu \times r}{r^3} = rot\left(\frac{\mu}{r}\right), \qquad (1.1.3)$$

$$divA = 0 \text{ and } rotA = B.$$

Considering (1.1.3), the Hamiltonian of (1.1.2) can be re-written with the form

$$\hat{H} = \frac{|e|}{2mc}(\hat{p}A + A\hat{p}) + 2\beta \cdot s \cdot rotA. \qquad (1.1.4)$$

where only the terms linear in A are conserved since A is considered to be small enough for other terms to be neglected to first order. The term $\hat{p}^2/2m$ is also omitted since it is responsible for free particle motion and is out of interest when the effect of magnetic field is considered.

Taking into account the commutativity of $\hat{p}$ and A ($\hat{p}A - A\hat{p} = -i\hbar \cdot divA = 0$), (1.1.4) can be rewritten using (1.1.2) as:

$$\hat{H} = 2 \cdot \frac{|e|}{2mc}(\frac{[\mu \times \hat{r}]}{r^3} \cdot \hat{p}) + 2\beta \cdot s \cdot rotrot(\frac{\mu}{r}),$$

or

$$\hat{H} = 2\beta \frac{\hat{L} \cdot \mu}{r^3} + 2\beta \cdot s \cdot rotrot(\frac{\mu}{r}) \qquad (1.1.5)$$

where $\hat{L} = \hat{r} \times \hat{p}$ is the angular momentum operator. Further, the spin-dependent part, can expressed by re-writing $rotrot(\frac{\mu}{r})$ as a vector product using $[a \times [b \times c]] = b(ac) - c(ab)$:

$$\hat{H}_1^s = 2\beta \cdot s \cdot [\nabla \times [\nabla \times (\frac{\mu}{r})]] = 2\beta \left[(s \cdot \nabla)(\mu \cdot \nabla) - (s \cdot \mu)\nabla^2 \right] (\frac{1}{r}) \qquad (1.1.6)$$

The expression (1.1.6) can be re-organized in a more convenient form to emphasize the dipole-dipole coupling

$$\hat{H}_1^s = 2\beta \left[(s \cdot \nabla)(\mu \cdot \nabla) - \frac{1}{3}(s \cdot \mu)\nabla^2 \right] (\frac{1}{r}) - \frac{4\beta}{3}(s \cdot \mu)\nabla^2 (\frac{1}{r}) \qquad (1.1.7)$$

The magnetic interaction of the nuclear moment with the electron spin is given by the matrix element $W_m^s = \left\langle \psi_e \mid \hat{H}_1^s \mid \psi_e \right\rangle = \int \psi_e^* \hat{H}_1^s \psi_e r^2 dr d\Omega$ where ψ_e is the wave function of the electron spin and (r, Ω) the electron coordinates. If $r \neq 0$, $\hat{H}_1^s$ (according to (1.1.7)) is a function of r, whose first term equals to $2\beta \left[\frac{3(s \cdot r)(\mu \cdot r)}{r^5} - \frac{(s \cdot \mu)}{r^3} \right]$ - the dipole-dipole interaction - and whose second term vanishes according to the Laplace equation. When $r \to 0$, the matrix element of the first term $\left\langle \psi^{(l)} \mid \hat{H}_1^{s'} \mid \psi^{(l')} \right\rangle$ in (1.1.7) is a second order spherical harmonic. Hence, if ψ_e is expanded in a series of spherical harmonics $\psi_e = \sum_l a_l \psi^{(l)}$, by symmetry, only the $\left\langle \psi^{(l)} \mid \hat{H}_1^{s'} \mid \psi^{(l')} \right\rangle$ terms of the expansion with $|l - l'| \leq 2 \leq l + l'$ have a non-zero contribution to $\left\langle \psi_e \mid \hat{H}_1^s \mid \psi_e \right\rangle$. The wave function $\psi^{(l)}$ behaves as r^l near the coordinate origin, therefore, an integrand in the matrix element

$$\left\langle \psi^{(l)} \mid \hat{H}_1^{s'} \mid \psi^{(l')} \right\rangle = \int \psi^{(l)*} \hat{H}_1^{s'} \psi^{(l')} r^2 dr d\Omega$$

behaves as $r^{l+l'+2-3}$ near the nucleus, and thus is always finite since $|l-l'| \le 2 \le l+l'$. In accordance with the theory of Coulomb potential, the second term in (1.1.7) is equal to $\frac{16\pi}{3}\beta(s\cdot\mu)\delta(r)$, and its integration leads to

$$\frac{16\pi}{3}\beta(s\cdot\mu)\,|\psi_e(0)|^2$$

for s-electrons and zero for other. Finally, the Hamiltonian of the magnetic interaction of electron and nucleus can re-written under the form:

$$\hat{H}_1 = 2\beta\gamma\hbar\,\hat{L}\cdot\left[\frac{l}{r^3}-\frac{s}{r^3}+3\frac{r(s\cdot r)}{r^3}+\frac{8}{3}\pi s\delta(r)\right]. \qquad (1.1.8)$$

If a nucleus is surrounded by several electrons, the Hamiltonian of the interaction represents a sum of the Hamiltonians of individual electrons.

The vectorial quantity

$$H_e = -2\beta\left[\frac{l}{r^3}-\frac{s}{r^3}+3\frac{r(s\cdot r)}{r^3}+\frac{8}{3}\pi s\delta(r)\right] \qquad (1.1.9)$$

can be considered as the effective magnetic field caused by the electrons at the nucleus. If the electron in the atom under consideration possesses an orbital angular momentum *l* and a total angular momentum $j = l \pm ½$, the Hamiltonian (1.1.8) can be re-written as

$$\hat{H}_1 = -\gamma_n\hbar(H_e\cdot L) \simeq a_j\, j\cdot L$$

by defining

$$a_j = \frac{\langle(-\gamma\hbar H_e\cdot j)\rangle}{\langle(j\cdot j)\rangle}.$$

The value of a_j is obtained by writing that the expectation values of $\langle a_j j \cdot j \rangle$ and $\langle -\gamma(H_e \cdot j) \rangle$ are equal. Using (1.1.9), $j = l + s$, $r \cdot l = (1/\hbar) r \cdot [r \times p] = 0$, and the relations of $s = ½$ ($s_x^2 = ¼$, $s_x s_y = - s_y s_x$, $s_x s_y = ½ i s_z$) the following expressions are derived:

$$a_j = \frac{16\pi}{3} \beta\gamma\hbar \, |\psi_e(0)|^2 \text{ for s-electron}$$

$$a_j = 2\beta\gamma\hbar \left\langle \frac{1}{r^3} \right\rangle \frac{l(l+1)}{j(j+1)}, \text{ if } l \neq 0. \text{ [7]}$$

1.2. Bloch model of internal field NMR.

In contrast to classical NMR[1], the external magnetic field in internal field NMR is negligibly small compared to the internal field. Indeed, the average Earth magnetic field is 0.5 G (up to 2 G in anomalies) whereas the local field in Co metal is 210 kG. Therefore, the main role is played by the hyperfine (hf) interaction as explained in the previous section.

At the same time, a complex situation arises due to the fact that the local field is not constant since it interacts with the magnetic field of the rf pulse, something that is out of consideration in classical NMR. Thus, internal field NMR in general results from a nonlinear interacting system. A satisfactory explanation of occurring phenomena can be obtained using Bloch magnetization formalism.

Let us first list the salient features of internal field NMR.

1. Local field (hyperfine hf field[2]). The behavior of nuclear spins in magnetically ordered substances is under the control of static local magnetic fields which are in a first approximation proportional to the spontaneous magnetization of the sublattice to which they belong. These local fields originate from the hyperfine interactions, and the observation of nuclear magnetic resonance without external magnetic field application becomes possible.

---

1 Hereinafter, the term "classical NMR" denotes NMR with application of strong constant external magnetic field when the strength of Zeeman interaction is much higher than hf interaction.

2 Further the terms internal (local) and hf fields will be used on a par since the the local field of Co metal is mainly determined by the hf interaction, while the dipolar field contribution is less than 5% of the hf field. In general though, the local field is determined by the hf field and the dipolar contributions from nearest nuclei.

2. Enhancement factor of rf fields. It is the time dependent component of the local field that tilts the nuclear magnetization. Its effects many times exceeds the one of the oscillating $B_1(t)$ rf field pulse applied to the sample. This effect arises in different ways for nuclei in magnetic domains and magnetic domain walls. Inside the domains, the $B_1(t)$ rf field tilts the electronic magnetization M from its equilibrium state (along the anisotropy field of a crystal structure) thus creating a transverse component of the local field $B_{loc}^{\perp}$, which is 10-100 times larger than the $B_1(t)$ rf field (see fig. 1.2.1). A definition of the enhancement factor in domains is given in the formula (1.2.1), where $B_{loc}^{\perp}$ is the transverse component of the local field. The electron magnetization adiabatically follows the applied $B_1(t)$. The modulation frequency of the rf pulse is such that one is far from the electron magnetization resonance conditions, and the deviation angle from equilibrium of the electron magnetization remains very small but non-zero.

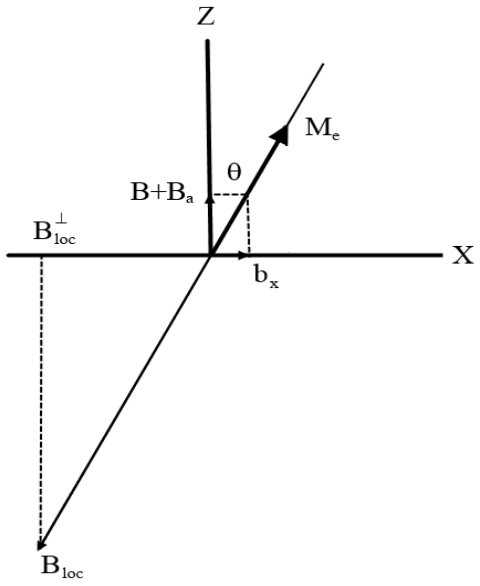

Figure 1.2.1. A schematic illustration of the internal field NMR mechanism in a magnetic domain. B – external magnetic field, B_a – anisotropy field, M_e – electron magnetization, b_x – magnetic component of rf pulse ($B_1(t)$), B_{loc} – local field. The figure is adapted from ref. [8].

$$\eta = \frac{B_{loc}^{\perp}}{B_1} \qquad (1.2.1)$$

In domain walls, the mechanism slightly differs since it is caused by the vibration of the domain walls under the $B_1(t)$ rf pulse. A domain walls can be pictured as the part of the sample where the local fields change their direction from one domain to another (usually 180°). During the rf pulse, the domain walls behaves like acoustic membranes. They move back and forth due to the change of direction of the local fields by rotation around the rf pulse (and not adiabatically as in domain walls). This "pumping" during the rf pulse produces large resonant signals. The enhancement factor η can reach values in the order of 10^3-10^5 (see fig. 1.2.2).

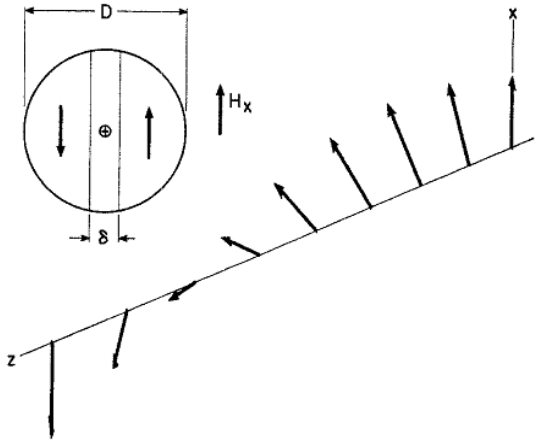

Fig. 1.2.2. Schematic diagram of a particle possessing a domain wall. here, H_x ($B_1(t)$ rf pulse), by tilting the local field inside the wall, shifts its boundaries to the left. Local fields in the domain wall are slightly rotated counterclockwise inside domain wall exciting the transitions of nuclear spins. The figure is adapted from ref. [9]. D – particle size, δ – domain wall size.

3. *Resonance line width.* A resonance line full width at a half maximum (FWHM) of magnetically ordered materials is usually an order of magnitude more than for solid state NMR in diamagnetic materials. This is caused by a distribution of the local magnetic fields (and demagnetization fields) which are observed in magnetic materials that results in inhomogeneous broadening. The quadrupolar electric effects also may contribute to the FWHM.

4. *Spin waves.* In contrast to non-magnetic materials, which display a precession of nuclear moment in phase (homogeneous coherent regime), magnetic materials exhibit spatially inhomogeneous collective spin oscillations, *i.e.* spin waves [10].

To describe NMR in magnetic materials, in contrast to classical NMR, it is absolutely necessary to consider simultaneously the coupled electronic and nuclear magnetizations. If **m** and **M**[3] stand for the electron and nuclear magnetizations, respectively, the Bloch equations in the laboratory frame take the form:

$$\begin{aligned} \frac{d\vec{m}}{dt} &= \gamma_n \vec{m} \times \vec{b} + \vec{r} \\ \frac{d\vec{M}}{dt} &= \gamma_e \vec{M} \times \vec{B} + \vec{R} \end{aligned} \tag{1.2.2}$$

where **r** and **R** are the relaxation terms of nuclear and electron system, b and B the magnetic fields acting on a corresponding subsystem (nuclear and electronic), and γ_n and γ_e the corresponding gyromagnetic ratios.

The time-evolution of the transverse components of the magnetization, or the magnetic susceptibility when continuous wave spectrometers are used, is obtained by solving this system of coupled differential equations system [8; 11].

Taking the form for the magnetizations in a stationary conditions as $\boldsymbol{m}(t) = \boldsymbol{m_0} e^{i\omega t}$ and $\boldsymbol{M}(t) = \boldsymbol{M_0} e^{i\omega t}$, the magnetic field acting on both nuclei and electrons in molecular field approximation is given by:

$$\begin{aligned} \vec{b} &= \vec{B}_1 e^{i\omega t} + \lambda_m \vec{M} = \vec{B}_1 e^{i\omega t} + \vec{B}_{hf} \\ \vec{B} &= \vec{B}_0 + \vec{B}_a + \vec{B}_1 e^{i\omega t} + \lambda_m \vec{m} \end{aligned} \tag{1.2.3}$$

where $\boldsymbol{B_a}$ is the magnetic anisotropy field acting on the electrons. This field is aligned with the external magnetic field, and in the absence of the external magnetic field it defines the *z* axis. $\boldsymbol{B_0}$ is the external constant magnetic field (it defines z axis when present), and B_1 is the magnetic part of the circular polarized rf field. The molecular field parameter λ_m constitutes a link between local field (hf field) and electron magnetization $\boldsymbol{B}_{hf} = \lambda_m \boldsymbol{M}$. [12] The expression (1.2.3) also does not consider the contribution of the demagnetizing fields.

Because the NMR signal is proportional to the component of the magnetization in a plane perpendicular to the *z* axis, the following complex representations more convenient:

[3] Hereinafter, in the text, vector designation is given by **bold** text symbols, however equations display arrows

$$\vec{M}_{\pm} = \vec{M}_x \pm i\vec{M}_y$$
$$\vec{m}_{\pm} = \vec{m}_x \pm i\vec{m}_y \qquad (1.2.4)$$

The magnetic field components take the form

$$\vec{B}_{\pm} = \vec{B}_{1\pm} + \lambda_m \vec{m}_{\pm}$$
$$\vec{b}_{\pm} = \vec{B}_{1\pm} + \lambda_m \vec{M}_{\pm}$$
$$B_z = B_0 + B_a + \lambda_m m$$
$$b_z = B_0 + \lambda_m M$$

where the longitudinal z axis components of nuclear and electronic magnetization are assumed to be equal to the equilibrium magnetizations, *i.e.* $m_z \approx m$, a $M_z \approx M$. Although, these magnetizations are far from saturation, this simplification is justified in ref. [13]. In a stationary regime (the pulsed regime can be considered as a set of stationary regimes of fixed and limited duration), we expect

$$\vec{M}_{\pm} = \vec{M}_{\pm}(0)e^{i\omega t}$$
$$\vec{m}_{\pm} = \vec{m}_{\pm}(0)e^{i\omega t} \qquad (1.2.5)$$

The substitution of expressions (1.2.3) - (1.2.5) into the initial system of Bloch equations (1.2.2) gives a system of linear equations regarding $\boldsymbol{M}_{\pm}$ and $\boldsymbol{m}_{\pm}$

$$-\gamma_n \lambda_m m M_{\pm} + [\pm\omega + \gamma_n B_{hf}]m_{\pm} - \gamma_n m B_{1\pm} = 0$$
$$[\pm\omega + \gamma_e (B_a + \lambda_m m)]M_{\pm} - \gamma_e B_{hf} m_{\pm} - \gamma_e m B_{1\pm} = 0 \qquad (1.2.6)$$

The relaxation terms were here neglected.

Considering that $\boldsymbol{B}_{1\pm} << \boldsymbol{B}_a$, one gets

$$-\gamma_n \lambda_m m M_{\pm} + [\pm\omega + \gamma_n (B_0 + B_{hf})]m_{\pm} = 0$$
$$[\pm\omega + \gamma_e (B_0 + B_a + \lambda_m m)]M_{\pm} - \gamma_e B_{hf} m_{\pm} = 0 \qquad (1.2.7)$$

The initial coupled Bloch equations (1.2.2) split into sets of equations for the longitudinal components of electronic and nuclear magnetizations (which is not interesting) and for the

transverse ones. To solve (1.2.7), the determinant of the system should be equated to zero. The eigenvalues provide normal oscillation modes of the coupled system.

$$\begin{aligned} &\pm\omega^2 \pm \omega[\gamma_n(B_0 + B_{hf}) + \gamma_e(B_0 + B_a + \lambda_m m)] \\ &+\gamma_n\gamma_e(B_0 + B_a + \lambda_m m)(B_0 + B_{hf}) - \gamma_n\gamma_e\lambda_m m B_{hf} = 0 \end{aligned} \tag{1.2.8}$$

The quadratic equation has two roots, and if the external magnetic field is negligible compared to the local field (as is the case of the resonance in the local, or internal, field when the external field is the Earth magnetic field), *i.e.* one can put $B_0 = 0$. Thus, the equation (1.2.8) assumes the form of

$$\pm\omega^2 \pm \omega[\gamma_n B_{hf} + \gamma_e(B_a + \lambda_m m)] + \gamma_n\gamma_e B_a B_{hf} = 0$$

It must be noted that $\gamma_n << \gamma_e$, $m << M$, and as a consequence $\omega_e = \gamma_e B_a >> \omega_n = \gamma_n B_{hf}$. Therefore, the first solution of (1.2.8) gives the NMR frequency:

$$\Omega_n = |\omega_1| = \left|-\gamma_n B_{hf}(1 - \eta\frac{m}{M})\right| \approx \left|-\gamma_n B_{hf}\right| = \left|-\gamma_n \lambda_m M\right| \tag{1.2.9}$$

where η is so-called enhancement factor, which has already been mentioned. In the case of a non-zero external magnetic field, it is equal to

$$\eta = \frac{B_{hf}}{B_0 + B_a} \tag{1.2.10}$$

Thus, the application external magnetic field application is not beneficial in ferromagnetic materials as it decreases the observed signal amplitude. A small frequency detuning given by

$$\delta\omega = \Omega_n \eta \frac{m}{M},$$

called “dynamic frequency shift” [13–15], can complicate the issue. However, this phenomenon is observed only for high enough values of the nuclear magnetization m. In practice it is of concern only for nuclei with 100% abundance of magnetic isotopes and at extremely low temperatures (close to the temperature of liquid helium) since the nuclear magnetization is inversely proportional to the temperature (m ~ 1/T). Furthermore, since m

depends also on the rf pulse power (amplitude of magnetic component of the pulse), the dynamic frequency shift must have a dependence on the applied power. As an example, Mn2+ ions display large dynamic frequency shifts, which have the temperature dependence of the order:

$$\delta\omega/\Omega_n \cong 10^{-3}/T$$

The second solution of equation (1.2.8) gives the electronic resonance frequency (so called ferromagnetic resonance)

$$\Omega_e = |\omega_2| = \left|-\gamma_e B_a(1+\eta\frac{m}{M})\right| \approx \left|-\gamma_e B_a\right| \tag{1.2.11}$$

This formula also exhibits a small shift from a simple precession frequency around the anisotropy field, shift which is proportional to *m/M*. The term containing $\boldsymbol{B_{1\pm}}$ should be included in the initial equation (1.2.7) to get eigenvectors

$$-\gamma_n\lambda_m mM_\pm + [\pm\omega + \gamma_n B_{hf}]m_\pm - \gamma_n mB_{1\pm} = 0$$
$$[\pm\omega + \gamma_e(B_a + \lambda_m m)]M_\pm - \gamma_e B_{hf} m_\pm - \gamma_e mB_{1\pm} = 0$$

From the bottom equation, one gets $M_\pm$

$$M_\pm = \frac{\gamma_e(B_{hf}m_\pm + B_{1\pm}M)}{\pm\omega + \gamma_e(B_a + \lambda_m m)} \approx \frac{B_{hf}m_\pm + B_{1\pm}M}{B_a}, \tag{1.2.12}$$

where the term $\lambda_m m$ is neglected compared to B_a. ω is taken as close to the nuclear resonant frequency and thus small compared to the electron resonance frequency $\omega_e = \gamma_e B_a$ since the case of nuclear resonance is our only concern in this manuscript. Substituting the expression of $M_\pm$ into the first equation in (1.2.6) and simplifying it, the expression of $m_\pm$ is given by

$$m_\pm = -(1+\eta)\frac{\gamma_n B_{1\pm} m}{\omega - \Omega_n} \tag{1.2.13}$$

To get the resonance phenomenon, the solution of negative sign should be retained, and the transverse nuclear susceptibility takes the form

$$\chi_m^{\pm} = \mu_0 \frac{m_{\pm}}{B_{1\pm}} = -\mu_0(1+\eta)\frac{\gamma_n m}{(\omega - \Omega_n)} \tag{1.2.14}$$

where μ_0 is the magnetic susceptibility of the vacuum. Hence, an expression of the static nuclear susceptibility should be used, which is determined by

$$\chi_n = \mu_0 \frac{m}{B_0}, \tag{1.2.15}$$

Eventually, the expression of the transverse nuclear susceptibility is obtained using $\omega_0 = \gamma_n B_0$

$$\chi_m^{\pm} = -(1+\eta)\frac{\omega_0}{(\omega - \Omega_n)}\chi_n \tag{1.2.16}$$

Despite the fact that expression (1.2.16) is definitely proportional to $\omega_0 = \gamma_n B_0$, there is no dependency on the external magnetic field since $\omega_0 \chi_n = \gamma_n B_0 \cdot \mu_0 \frac{m}{B_0} = \gamma_n \mu_0 m$ contains only the nuclear magnetization as a variable.

It is clearly seen from equation (1.2.16) that the transverse nuclear susceptibility is enhanced by a factor $(1+\eta)$ compared to nuclei in non-magnetic matrixes. The resonant character of the expression is also well underlined with a maximum at $\omega = \Omega_n$.

Substituting the obtained expression of $m_{\pm}$ from (1.2.13) into (1.2.12), the following expression of $M_{\pm}$ can be obtained

$$M_{\pm} = \frac{\gamma_e M B_{1\pm}}{\pm\omega + \gamma_e(B_a + \lambda_m m)} + \frac{\gamma_n m B_{hf}(B_a + B_{hf})}{[\pm\omega + \gamma_e(B_a + \lambda_m m)]B_a}$$

Similarly to the nuclear susceptibility, the static electron susceptibility can be obtained

$$\chi_e = \mu_0 \frac{M}{B_a} \tag{1.2.17}$$

Dividing by $B_{1\pm}$ and applying the described above simplifications, the following expression is obtained for the transverse electron magnetization

$$\chi_M^{\pm} = \chi_e - \eta(1+\eta)\frac{\omega_0}{(\omega - \Omega_n)}\chi_n \qquad (1.2.18)$$

The total transverse susceptibility of electronic and nuclear subsystems, which is responsible for the NMR signal, is given by the following expression resulting from the summation of (1.2.16) and (1.2.18)

$$\chi(\omega) = \chi_e - (1+\eta)^2\frac{\omega_0}{(\omega - \Omega_n)}\chi_n \qquad (1.2.19)$$

From this equation, the transverse magnetization, besides a constant frequency independent term, which does not contribute to the transient NMR signal, contains another term multiplied by a factor of $(1+\eta)^2$. Considering that $\eta >> 1$, comparing (1.2.19) and (1.2.16) it thus turns out that the total transverse magnetization is roughly η times higher than the nuclear magnetization contribution (apart for the constant term). Physically, this means that even at nuclear resonance conditions (when the carrier frequency is close to Ω_n) the main contribution to the NMR signal arises from electrons.

To calculate the absorbed power by NMR in magnetic materials, it is essential to consider the relaxation terms into Bloch equations that we have neglected so far. The absorbed power is obtained from the imaginary component of the total transverse susceptibility [12].

To get the solution of the modified Bloch equations, the following method can be used. The expression (1.2.2) should be modified, and $\boldsymbol{m}(t) = \boldsymbol{m}_0 e^{i\omega t}$ and $\boldsymbol{M}(t) = \boldsymbol{M}_0 e^{i\omega t}$ should be substituted for $\boldsymbol{m}$ and $\boldsymbol{M}$. This effectively leads to an exponential decay, or exponential magnetization relaxation. A new term should appear in the expression of the nuclear frequency, *i.e.*

$$\Omega_n \rightarrow \Omega_n + i\Gamma_n$$

where Γ_n is the nuclear relaxation term which in contributes to the signal as a line width. Substituting this expression in (1.2.19), the real and imaginary parts of the transverse susceptibility are obtained

$$\chi'(\omega) = \chi_e + (1+\eta)^2 \chi'_n(\omega)$$
$$\chi''(\omega) = (1+\eta)^2 \chi''_n(\omega) \tag{1.2.20}$$

where

$$\chi'_n(\omega) = -\frac{\omega_0(\omega - \Omega_n)}{(\omega - \Omega_n)^2 + \Gamma_n^2}\chi_n$$
$$\chi''(\omega) = \frac{\omega_0 \Gamma_n}{(\omega - \Omega_n)^2 + \Gamma_n^2}\chi_n \tag{1.2.21}$$

The absorbed power of the spin system as a function of imaginary susceptibility is given by the equation [10]

$$P = \omega\chi''(\omega)B_1^2$$
$$P = \omega\chi''_n(\omega)(1+\eta)^2 B_1^2 \cong \omega\chi''_n(\omega)(\eta B_1)^2 \tag{1.2.22}$$

It turns out that the absorbed power is enhanced by a factor η^2compared to nuclei in nonmagnetic matrix. To obtain the last equations, only the nuclear relaxation is considered. The effect of including the of electron relaxation is discussed in ref. [16].

Nowadays, continuous wave spectrometers are rarely used because they require long spectra accumulation times. In general, the spin-echo pulse sequence is used to generate NMR signal. The sequence results in spin system excitation by means of several pulse of equal or different duration [17; 18]. Immediately after a set of pulses the spin system is considered as freely precessing and is recorded (in the continuous wave approach, the precession is forced during signal acquisition). Also the initial conditions in both types of excitation are different. The magnetic structure of the crystal under study should also be taken into account since magnetic domains and magnetic domain walls have different mechanisms of NMR signal excitation [19].

The equations discussed above are only relevant for magnetic domains. As it is said earlier, domain walls display an enhancement factors, which one or two orders larger than in domains. This phenomenon is connected with the mechanism of wall shifting shown in fig. 1.2.2. Application of a rf B_1 field shifts the domain wall, and this motion of the wall induces electron magnetization rotation inside the wall thus leading to the occurrence of an additional

component of the local field along the applied rf field. Therefore, the rf field B_1 is effectively multiplied by a factor of 10^3-10^5, and maximal enhancement is achieved in the center of the domain wall since magnetization in the center is tilted on the largest angle. The enhancement at the wall edge is much smaller compared to the center but it is still rather large compared to the enhancement factor inside domains. The simultaneous observation of signals from the center and the edge of the same wall has been proposed by Kurkin, Turov, and Tankeev [20; 21]. This rational has successively explained the spectra of hexagonal close packed (hcp) crystals of Co metal [22–26]. Unfortunately, the exact expression of the enhancement factor depends on the type of domain wall, but for the simplest case of a particle with a single domain wall as shown in fig. 1.2.2, it is given by the equation [9]

$$\eta_w = \frac{\pi D B_{hf}}{\mu_0 N_d \delta M_s}, \tag{1.2.23}$$

Where D is the particle diameter, δ is the domain wall width, N_d the demagnetizing factor, and M_s the saturation magnetization. Numerically, the enhancement factor calculated for face-centered cubic (fcc) metallic Co phase, which resonance has been acquired by Gossard and Portis in 1959 [27], equals to 2000.

The nuclear magnetization in Bloch formalism in pulse NMR experiment is tilted from the equilibrium position along z axis to the xy plane after application of the rf pulse B_1. The tilting angle of the nuclear magnetization after a rf pulse of B_1 amplitude and t_a duration is given by the formula [28]

$$\theta = \gamma t_a (\eta B_1) \tag{1.2.24}$$

where γ is the gyromagnetic ratio of the nuclei. As it is mentioned earlier, the nuclei in magnetic materials “feel” an effective rf field B_2, which is equal to rf pulse B_1 augmented by the enhancement factor η, *i.e.* $B_2 = \eta B_1$.

The amplitude of free induction decays (FID) in classical NMR after a single pulse or a set of pulses (for simplicity, we consider pulses of the same duration) depends on the θ angle.

The situation is cardinally differed in the case of strong magnetism (for example, ferromagnetism) since several factors (instead of one, the strength of rf pulse, in diamagnetic

materials) affect the signal intensity in magnetically ordered materials. The simplest model of NMR in magnetic materials assumes (i) a constant enhancement factor; (ii) usage of a spin echo sequence consisting of two equivalent pulses of t_a duration; (iii) rf B_1 field perpendicular to the external static magnetic field B_0 (*or* perpendicular to all individual anisotropy fields in the sample – they are collinear at *zero* external magnetic field). Within those assumptions, the spin echo amplitude takes the form [29]

$$E(\mathrm{t_a}, \mathrm{B_1}) = \mathrm{C}\sin(\gamma\eta\,\mathrm{B_1 t_a})\sin^2(\frac{\gamma\eta\,\mathrm{B_1 t_a}}{2}) \tag{1.2.25}$$

The expression coincides with the equation of nuclei in nonmagnetic matrix where the rf field B_1 amplitude is enhanced by the factor of η.

The analysis of the spin-echo formation problems in magnetic materials has been extended to the case not only of domains, but also of domain walls (d.w.) [30]. The model include a set of parameters: (1) θ angles distribution between rf B_1 fields and the magnetizations in different domains of the sample (that is essential for microcrystalline sample without any external magnetic field); (2) spatial alternation of the enhancement factor η inside Bloch domain wall; (3) oscillatory motion of the domain walls; (4) a distribution of the areas of domain walls. The model has been slightly modified and proposed in the ref. [31] where the authors simultaneously calculated the contribution from domains and domain walls. The formula of domain walls spin-echo NMR signal is then given by

$$\begin{aligned}
&E_T^w(\omega_0, B_1) = m_0\eta_{0w}\int_0^\infty\int_0^1 \sin^2(\frac{\alpha_0 z\sec h(x)}{2}) \\
&\times\sin[\alpha_0 z\sec h(x)]z\sec h(x)\,p(z)dz\,dx \\
&z = (1-r^2)h_m\cos\theta,\ p(z) = \frac{1}{2}\ln^2(1/z) \\
&for \quad Ap(A) = const. \\
&\alpha_0 = \gamma_n\eta_{0w}B_1\tau
\end{aligned} \tag{1.2.26}$$

where A is the area of the domain walls; $p(A)$ is the probability of finding domain walls with the specified value of the area A; h_m is the displacement of the center of domain walls normalized on the displacement maximum; m_0 is nuclear magnetization; α_0 is maximal tilting angle of nuclear magnetization m_0 after rf pulses. The enhancement factor evolution as a

function of nucleus position inside the domain walls is described by a function with a maximum in the center of the domain walls ($x = 0$)

$$\eta(x) = \eta_0 \sec h(x)(1 - r^2)h_m \tag{1.2.27}$$

The equation for the intensity in spin-echo experiments for domains has a more simple form; it can be expressed in terms of usual trigonometric functions

$$E_T^d = \frac{\eta_d m_0}{\alpha^2}\left[\sin\alpha - \frac{1}{8}\sin 2\alpha - \alpha\cos\alpha + \frac{1}{4}\alpha\cos 2\alpha\right] \tag{1.2.28}$$
$$\alpha = \gamma_n \eta_d B_1 \tau$$

A last factor should be emphasized that affects the NMR intensity in magnetic materials. This is the so-called skin effect, which is responsible for the exponential decay of signal intensity with the penetration depth inside the conductor. Typical values of the penetration depths for Co metal at the resonant frequencies are several microns, *i.e.* the study of aggregates larger than 10-100 microns reflects mainly the contribution of the outer shell since internal nuclei are affected by very weak rf pulse, which cannot excite efficiently the nuclei.

1.3. Conclusions to Chapter 1:

Internal field NMR is a non-linear resonance process, which in first approximation can be regarded as classical NMR of non-magnetic matrixes, but with rf pulsed multiplied by the *enhancement factor*. The enhancement factor drops with the application of constant external magnetic field.

Zeeman interaction is negligibly small compared with hyperfine interaction. Therefore, *the NMR frequency is determined by the local magnetic field*.

The principles of internal field NMR should be separately considered for different magnetic parts of the sample as *domains* and *domain walls*, since they have different enhancement factors, the induction of NMR signal occurs in them using different mechanisms.

The dependence of NMR signal versus applied power and temperature takes a more complicated form than in classical NMR especially for the nuclei inside domain walls.

Continuous wave NMR spectrometers are more sensitive to resonances in domain walls compared to transient spin echo NMR Fourier spectrometers. This follows from the fact that energy absorption in continuous wave spectrometer is proportional to $(\eta B_1)^2$, and the spin echo signal in pulse regime is proportional to (ηB_1) while $\eta >> 1$. Therefore, continuous wave spectrometers mainly observe the signal from domain walls (domain wall have much stronger enhancement factor than domains).

CHAPTER 2

PRACTICAL ASPECTS OF INTERNAL FIELD NMR SPECTROSCOPY APPLICATION

2. Practical aspects of internal field NMR spectroscopy application

2.1. Co metal

Co metal is ferromagnetic. In 1958, Marshall [32] has performed one of the first theoretical estimations of the internal field of ferromagnets, Co metal magnetic field, and in particular Co metal has been investigated. The total internal magnetic field is a sum of three components:

$$B = B_l + B_c + B_{hf}\,, \tag{2.1.1}$$

where B_l is the local magnetic field at the position of nucleus; B_c is the effective magnetic field which acts through the contact interaction with *4s* electrons; B_a is the effective field due to interactions of the nucleus with the electrons on the same atom. In turn, the local field B_l is given by

$$B_l = B_0 - DM_e + \frac{4}{3}\pi M_e\,, \tag{2.1.2}$$

where B_0 is the external magnetic field, $-DM_e$ is demagnetizing magnetic field depending only on the shape of the specimen, $\frac{4}{3}\pi M_e$ is the usual Lorentz field. The magnetization depends on the external magnetic field $M_e(B_0)$, and the saturation in ferromagnets is reached at very low magnetic fields (hundreds of G). Therefore, a good estimation of M_e is the saturation magnetization (even at room temperatures) which is equal to 1446 G. Therefore, the $\frac{4}{3}\pi M_e$ term contributes ~6 kG to the internal field.

The effective field B_c consists of two parts. The first is proportional to the conduction electron polarization, and the seconds is due to the mixing of *4s* electron wave functions into the *3d* band.

$$B_c = -\frac{8\pi}{3}\beta\left|\psi(0)\right|^2 n(p + \frac{2\overline{S}a^2}{n})\,, \tag{2.1.3}$$

where β is the Bohr magneton, $|\psi(0)|^2$ is the average probability density of a conduction electron evaluated at a lattice point, p is the electron polarization, $\overline{S}$ is the mean spin per atom, a^2 is the average of the amount of 4s wave function mixed into a mainly *3d* wave function, n is the number of conduction electrons per atom. A rough estimation of the polarization contribution gives approximately 40 kG of internal magnetic field, and the wave function intermixing contributes an additional 137 kG to the internal magnetic field of Co metal.

The effective hyperfine field B_{hf} can be estimated using Van Vleck model [33; 34]. In this model, the correlation effects are considered to play a main role so that on any particular atom there will always be an integer number of *3d* electrons coupled together according to Hund's rules. Thus, for example, Co is supposed to have 70% of atoms in $(3d)^8\ ^3F$ configuration and 30% in $(3d)^9\ ^2D$. This gives a mean moment of 1.7 β_N per atom. Of course two configurations do not persist in the same atom but are continually exchanging positions. The listed configurations emerge when *4s* electron decoupling occurs, and one of the electrons migrate in the *3d* level ($(3d)^8$). The case of two electrons migration leads to ($(3d)^9$) configuration. The main contribution into the internal field is given by the hyperfine constant:

$$B_{hf} = -\frac{A\overline{S}}{g_N\beta_N}, \tag{2.1.4}$$

which contains three main contributions:

$$A = -P(k + 3Jl_{zz} + 2\lambda\Lambda_{zz}),$$

$$B_{hf} = \frac{P\overline{S}}{g_N\beta_N}(k + 3Jl_{zz} + 2\lambda\Lambda_{zz}) = B_{hf1} + B_{hf2} + B_{hf3} \tag{2.1.5}$$

where $P = 2g_N\beta_N\beta(\frac{1}{r^3})$, $J = \frac{5-4S}{21(2L-1)S}$, $l_{\alpha\beta} = \frac{1}{2}\left\langle 0\left|L_\alpha L_\beta + L_\beta L_\alpha\right|0\right\rangle - \frac{1}{3}L(L+1)\delta_{\alpha\beta}$

$$\Lambda_{\alpha\beta} = \sum_{n=0}\frac{\left\langle 0\left|L_\alpha\right|n\right\rangle\left\langle n\left|L_\beta\right|0\right\rangle}{E_n - E_0}.$$

The first term B_{hf1} in (2.1.5) arises trough the contact interaction of the nucleus with the inner *3s* and *2s* electrons [35]. The second term B_{hf2} represents the dipole-dipole magnetic

interaction between the nuclear and electron spins averaged over the zero-order wave function. Finally, the third term B_{hf3} is the magnetic interaction between the nucleus and the unquenched part of the orbital moment [36].

The first component estimation gives $B_{hf1} = -128\ kG$, and it is equal for all Co metal sublattices. The cubic symmetry averages to zero the second term B_{hf2}. The third summand can be estimated for fcc Co as $(B_{hf3})_{fcc} = 54 \pm 18\ kG$. The estimation of two last contributions in hcp Co gives $(B_{hf2})_{hcp} = 81\ kG$, $(B_{hf3})_{hcp} = 83\ kG$. Summing all terms in the initial equation (2.1.1), Marshall showed the Co metal internal field to be equal to $B = 219\ kG$ in cubic Co stacking.

Marshall was a pioneer who estimated the different contributions to the internal field of ferromagnetic materials, however later Watson and Freeman [37] have shown that the main contribution to the effective internal field arises from the exchange polarization of s electrons with unpaired d and f electrons. Aside from the core polarization, these terms should be also considered:

1. The field from the contact interaction with the *4s* electrons polarized by the *3d's*.
2. The field from the contact interaction with *4s* electrons partly admixed into *3d* band.
3. A contribution from the dipolar field of the 3d electrons (zero for cubic symmetry).
4. An orbital contribution from any unquenched angular momentum of the *3d* electrons.

One of the first experimental confirmations of Marshall's internal magnetic fields estimations in Co metal, which marks the birth of internal field NMR, was a work done by Gossard and Portis from the University of California (Berkley, USA). They were the first who acquired the NMR signal on ^{59}Co nuclei in the internal field (*i.e.* without application of any external magnetic field) in 1959 [27], and they registered the signal from fcc Co metal at 213.1 MHz (see fig. 2.1.1).

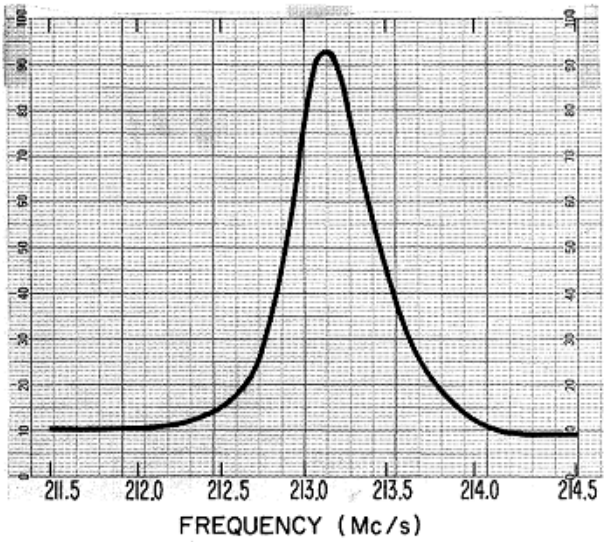

Fig. 2.1.1. Reproduction of the first ever registered internal field ^{59}Co NMR spectrum of fcc Co metal [27].

The sample studied by Gossard and Portis had been synthesized by the reduction of Co_3O_4 oxide in pure hydrogen H_2. The obtained Co metal had predominantly hcp Co phase according X-ray diffraction (XRD) experiments; it had a spherical shape and the particle size varied from 5 to 10 μm. The attempt to find a resonance from hcp Co metal failed; therefore only the fcc part of the sample had been investigated. Co metal is known to have the allotropic phase transition from hcp to fcc Co metal at ~ 693 K [38], therefore the reduced Co metal had been calcined at 703 K temperature. The subsequent XRD data showed 70% rate of Co transformation from hcp to fcc [9]. In calculation of the internal field, Gossard and Portis used Watson and Freeman argumentation that the main contribution to the internal magnetic field of Co metal is given by partly hybridized electrons.

In another paper [9], Gossard and Portis also examined a temperature dependence of fcc Co metal resonance frequency (only three temperatures used in the experiments 77.4 K, 194.7 K and 296.5 K due experimental setup limitations). Assuming that the frequency should be proportional to saturation magnetization, and using [39], they obtained the formula:

$$\upsilon(T) = \upsilon(0)\sqrt{1-(T/\Theta)^2},$$

where $\upsilon(0)$ is equal to 217.2 MHz (as a result of extrapolation to 0 K), and Θ = 1400 K is the Curie temperature of Co metal. The authors also tried to obtain the relaxation times of Co metal. The spin-spin relaxation time T_2 = 25 μs is found to be independent on the temperature within the studied range. As for T_1 spin-lattice relaxation time, it changed with the temperature from 280 μs at room temperature to 600 μs at liquid nitrogen temperature.

Gossard and Portis were the first who indicated that internal field NMR signal is not straightforwardly dependent on the applied rf pulse amplitude. They proposed that the NMR signal is connected with the rf pulse according to the formula

$$\left(B_{hf}\right)_{\perp} = \eta B_1,$$

where η is an enhancement factor, which comes from the fact that the resonance transitions are induced by the transverse part of the internal field but not directly by the applied rf pulse as usual in classical NMR. In turn, the transverse component of the internal field is created by the applied rf pulse. Gossard and Portis made an estimation of the enhancement factor for the atoms in domain wall. The following values have been used in the formula (1.2.23): domain size D = 1 μm, domain wall thickness δ = 0.1 μm, the internal field (hyperfine field) B_{hf} = *220 kF*, and saturation magnetization M_s = *1440 G.* The authors estimated the enhancement factor to be ≈ 1200.

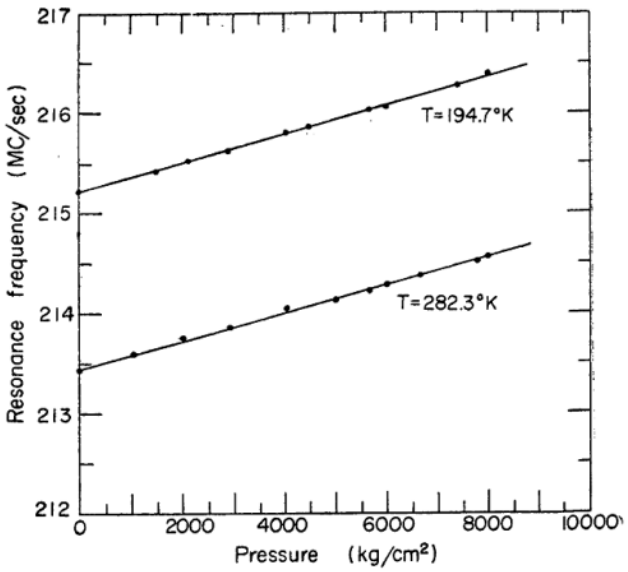

Fig. 2.1.2. The dependence of internal field ^{59}Co NMR frequency of fcc Co metal on the pressure [40].

Further study of Co metal has been carried out on fcc Co under applied external pressure[40]. The authors assumed that the pressure dependence was caused by the modification of the hyperfine constant with pressure, whereas the electron magnetization is weakly dependent on the applied pressure within the 0 – 800 MPa region according to [41]. The linear dependence has been obtained of fcc Co metal resonance frequency versus applied pressure at two temperatures (194.7 K and 282.3 K) as demonstrated in fig. 2.1.2.

The resonance form hcp Co metal has been measured by Koi et. al. [42] at 228 MHz frequency (the value is extrapolated to zero K). In addition, Koi has studied the temperature dependence of fcc and hcp Co metal stackings within 4 and 650 K (see fig. 2.1.3). The dependence of the hcp resonance line at higher temperatures (approximately up to ~650 K) has been also reported by Pogorelov and Kotov in 1971 [43] (reference in Russian).

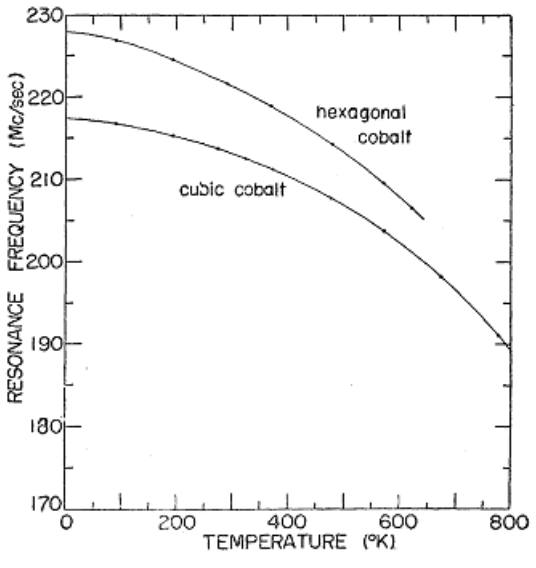

Fig. 2.1.3. The temperature dependence of internal field ^{59}Co NMR resonance line of hcp and fcc Co metal reported by Koi et.al. in 1960 [42].

The work by Koi et.al. [42] has been carried out on superregenerative spectrometer, the sample was 0.5 mg of a well annealed powder. A superregenerative spectrometer was used for the detection of weak signals due to its high sensitivity. The estimated line width was 0.4 MHz. The authors claimed that the intensity of hexagonal Co metal is much lower than the

intensity of the fcc line, and that the hcp Co line reaches maximal intensity at T = 500 K, with an intensity approximately 10 times larger than the one obtained at room temperature. This result does not seem odd since hcp Co metal is known to have a rather larger field anisotropy (due to crystallographic anisotropy in hcp lattice). The work done by Takahashi and Suzuki reveals that hcp Co metal changes its magnetic structure starting from ~ 510 K, and a new type of magnetic domains emerges in hcp Co metal. This additional type of magnetic domains reduces the magnetic anisotropy in hcp Co, which in turn decreases the FWHM of hcp Co metal resonances, and the line narrowing pushes up the signal intensity at the maximum. Also a part of the hcp signal could be invisible in continuous wave NMR spectrometer (which was used in first work) thus line narrowing causes previously unseen Co metal resonances to appear.

After the first observation of internal field NMR in Co metal by Gossard and Portis [9; 27], several papers on spin-spin and spin-lattice relaxation time measurements and spin diffusion were published [44; 45].

Internal field NMR was very popular in 1960-s after the work by Gossard and Portis [27]. It was applied to study different Co metal containing materials, and the number of works was increasing from year to year. However, some authors did not realize that the technique reflects not only the structural aspects of studied specimen as different structural Co metal lattices but as well the magnetic structure, *i.e.* magnetic domains and domain walls. Thereupon, other authors stepped on a way of searching the resonances from magnetic domains and domain walls in different Co metal stacking.

In particular, the authors in ref. [46] studied multi-domain and single-domain Co metal particles stabilized in various matrixes. At first, the authors demonstrated that the fcc domain signal is shifted compared to fcc domain wall signals. In the manuscript, the signal has been detected at 216.3 MHz resonance frequency whereas the signal arising from fcc domain wall Co metal is measured at 213.1 MHz. The explanation of this phenomenon lies in demagnetizing fields (which have been omitted from the consideration in section 1.2). Actually, fcc Co metal stacking is highly symmetric, therefore the contribution from neighboring domains are compensated inside the wall (see fig. 2.1.4) since the magnetic moments (or overall magnetizations) of domain are antiparallel, *i.e.* this causes zero shift of the line.

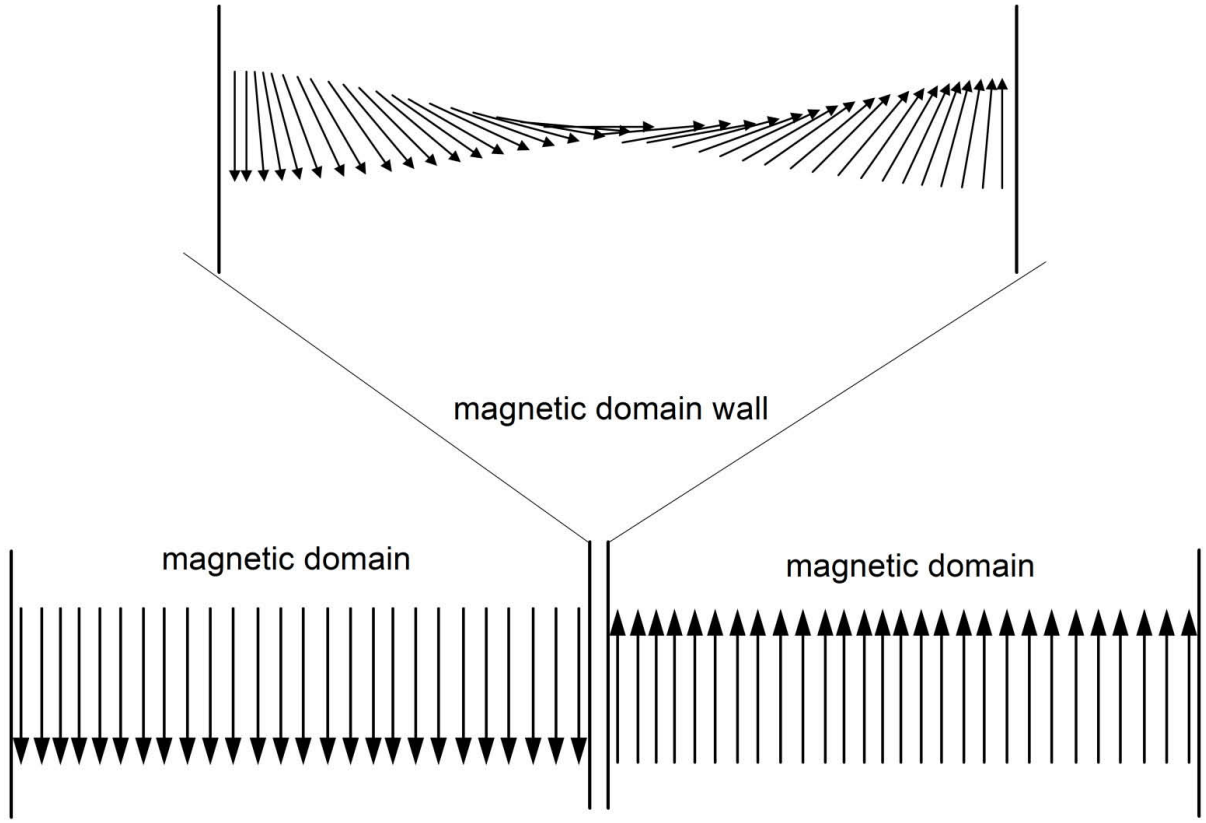

Fig. 2.1.4. Schematic illustration of a domain wall. A Neel 180° domain wall is considered in this case where the magnetic moments rotation occurs in the plane perpendicular to the total magnetic moments in domains.

In a single domain particle or when the number of domain walls is too small, compensation by symmetry does not occur, and the observable shift of the line reflects the value of the demagnetizing field, which is essentially averaged to zero for bulk Co metal. A simple calculation of demagnetizing field of isolated single-domain magnetic nanoparticle is given by the formula

$$B_{demag} = 4\pi DM \qquad (2.1.6)$$

where D is a form factor. For spherical shape particles D is 1/3, for thin film in perpendicular axis is 1, and this factor is 1/2 for the axis, which is perpendicular to a cylinder axis. The simple calculation for a spherical Co metal particle gives the magnetic field of 6 kG, for Co metal cylinder is 9 MHz, and for Co metal thin film is 18 MHz. The maximal registered value of the shift (recalculated into magnetic field using cobalt gamma ratio) for a spherical Co

metal particle is 3.5 kG. This shows that usually Co metal nanoparticles are not isolated; a dipole-dipole magnetic interaction decreases the value of demagnetizing field. The authors in ref. [47] have made an attempt to estimate Co metal particles sizes from the position of domain (or single-domain) fcc Co metal line. A second paper tried to tackle this issue, authors in ref. [48] used a continuous wave spectrometer that gave an uncertain line position due to the superposition of absorption and emission signals. From the listed above, the position of single-domain line has no fixed value, and it can be interpreted in term of magnetic field lines as it is shown in 2.1.5. If these lines go far away from the particle (as for sing-domain particle in 2.1.5), the demagnetizing field is strong, *i.e.* the line shift is substantial. If magnetic field lines start from one part of a particle and then go to another, the demagnetizing field is weak, and line shift is small or even not observable experimentally. The illustration of the demagnetization mechanism by field lines also facilitates the understanding why interacting assembly of nanoparticles show smaller shift than non-interacting system. The neighbor particles act as negative and positive poles of the magnet thus diminishing demagnetizing field.

Also the important part of domain theory is that the single-domain particle size is restricted to certain values. The magnetization in a single-domain particle is homogeneous through the particle (by definition). However, a particle size increase also affects the magnetic anisotropy field, and at a certain particle size a lower energy state is obtained by a creation of a domain wall. This phenomenon can be apprehended in the following way. The magnetic field lines must form a loop (in contrast to electrical field lines), therefore a single-domain particle (which is in fact a magnetic dipole) closes its magnetic field far away from the specimen (see fig. 2.1.5), and the emergence of a domain wall makes the field lines more compact, which results in a reduction of the total energy.

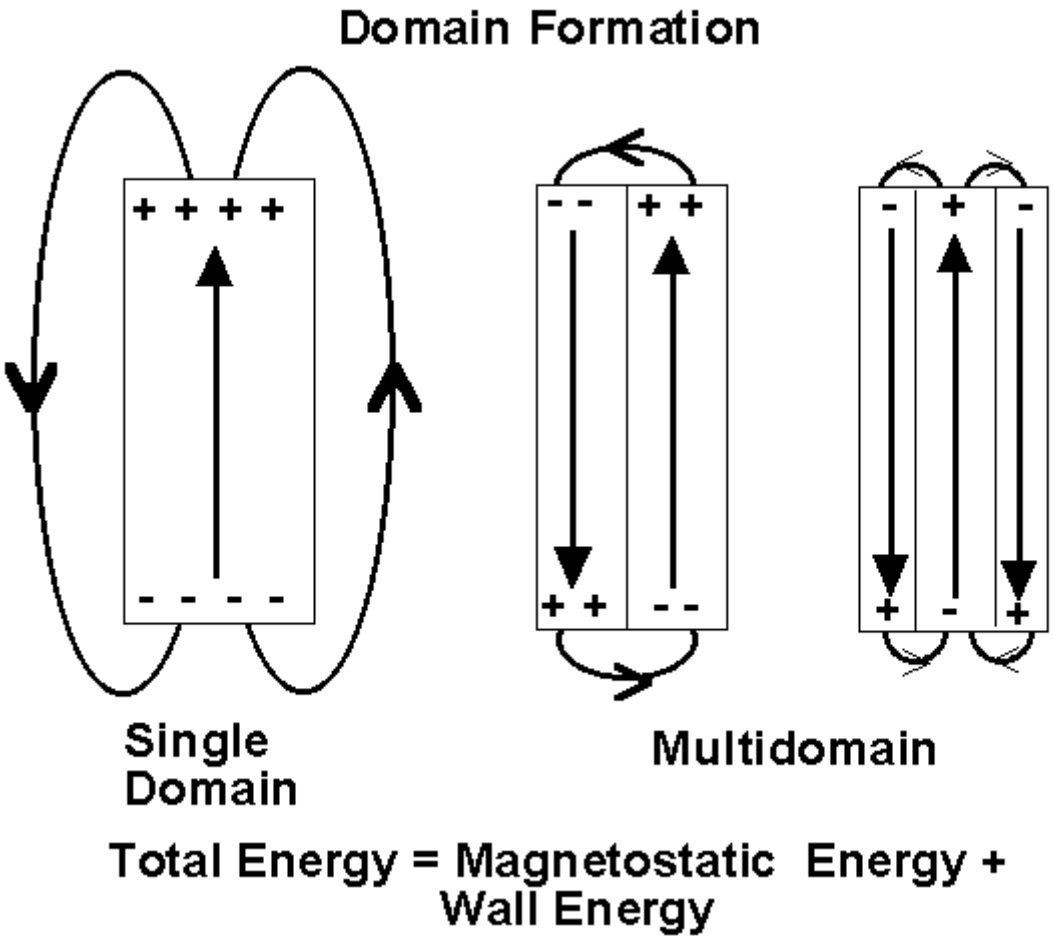

Fig. 2.1.5. Schematic representation of magnetic field lines in a single domain particle and in multidomain ones.

Simple calculations can provide an estimate of the critical size (upper margin size) of the single-domain Co metal particle for a spherical particle with no shape anisotropy: 70 nm [49–51]. In a real system of Co nanoparticles, the critical size is considered to be less since Co-support (matrix) interactions contribute to the magnetic and shape anisotropy. In any case, magnetic particles above the critical size possess, at least, one magnetic domain wall. The literature data state the usual critical size to be within 50-70 nm [52–54]. Therefore, internal field NMR is sensitive to particle sizes.

Concerning the interpretation of the spectra, important discrepancies arose in the literature after Gossard and Portis pioneer work in 1959 [27]. The spectra acquisitions and physical properties examinations from ^{59}Co internal field NMR spectra firstly had been carried out on pure fcc or hcp Co phases.

The interpretation problems have started from the moment when the researchers turned to bulk Co metal powders study, *i.e.* to the samples without a special treatment to get pure phases. Hardy in ref. [55] was the first who observed additional lines in internal field ^{59}Co NMR spectra at 215.5, 218 and 223.5 MHz (in addition to the "usual" 213 and 221 MHz Co metal lines from d.w. fcc and d.w. hcp Co metal, respectively). These additional lines have been attributed to Co metal stacking faults (sfs). Unfortunately, Hardy made several mistakes since the spectra description has been made considering only structural aspects but not both structural and magnetic effects. Such approach became very popular, but it had difficulties to correlate hcp/fcc ratio with other techniques [56–58]. The majority of modern papers cite three early works [59–62], where the positions of resonance line have been calculated using fixed positions of "perfect" fcc and hcp Co metal at 213.1 and 211 MHz, respectively. The authors did not mention that internal field ^{59}Co NMR strongly depends on the magnetic properties of the sample (*i.e.* magnetic structure as domains and domain walls). All calculations in ref. [59–62] have been carried out using an assumption that the position of the resonance line depends only on the *a/c* ratio of crystallographic parameters, *i.e.* on the density of the stacking (which is obviously is not true). Despite this obvious shortcoming and the contradictions with later works [46; 48], this approach has found many supporters. The number of papers using only crystallographic description of internal field NMR spectra is relatively high [56–58; 63–75], however, in a majority of them this attribution does not affect the conclusions. Nevertheless, more accurate spectra description is thus essential since it can provide unique additional information, which cannot be obtained by other methods. An attempt to give the historical insight to internal field ^{59}Co NMR spectra description problem can be found in ref. [3].

Similarly as for fcc Co metal, the focalization on Co metal sfs caused many disputes regarding internal field ^{59}Co NMR spectra of pure hcp Co metal since the first work by Koi et.al. [42] who observed only one single hcp resonance line at 221 MHz. Kawakami et.al. in 1972 [22] criticized the paper by Jackson et.al. [76] since Jackson ascribed a second line in internal field ^{59}Co NMR spectrum to pure hcp single crystal arising from hcp sfs. Kawakami et.al. [22] proposed instead the following explanation for this additional signal. The anisotropy of hcp crystal has been considered, and as a result hcp domain magnetic moments are aligned with the crystallographic *c* axis of hcp Co, but the total magnetization of hcp domain walls should lie in a perpendicular axis. With respect to this, the line at 214 MHz (see fig. 2.1.6.) has been attributed to come from hcp Co domains instead.

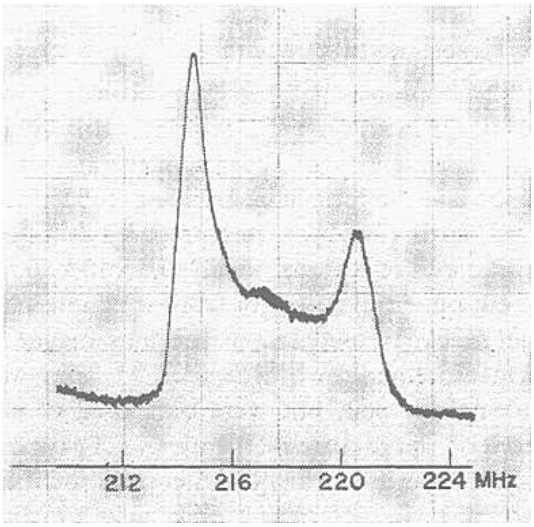

Fig. 2.1.6. Internal field ^{59}Co NMR spectrum obtained by Kawakami et.al. at T=290 K [22].

Such attribution is, in principle, correct, but in bulk crystals it requires more attention. As it shown in formula (1.2.27), the enhancement factor is not homogeneously distributed across the domain wall; it weakens to the edge of the domain wall. However, at the edge of domain wall it is still larger than in domain, therefore in large particles the signal from the edge of domain wall should prevail over the domain signal. However, some authors do not differentiate domain wall edge and domain signal in hcp Co using only domains. A theory stating two different resonances for one domain wall has been suggested by Turov, Kurkin, and Tankeev [20; 21], and its experimental verification in pure hcp Co metal has been performed in papers [23–26; 77]. Also hcp Co domain wall edge (d.w.e.) line can exhibit a quadrupolar splitting [22–24; 63].

In conclusion, despite the fact that internal field ^{59}Co NMR spectroscopy has been established many years ago, providing a detailed spectral line attribution is still a challenge. The existence of several description models restrains the widespread application of the technique in chemistry and material science. A consensual classification of resonance lines of internal field ^{59}Co NMR spectra combined with several application examples in different spheres of chemistry and material science might spread the technique into a wider scientific community, possibly making in the future it as common as XRD to study Co metal.

2.2. Cobalt alloys

Gossard and Portis work [27] undoubtedly gave rise to study of Co metal and other pure ferromagnets as Fe [78–89], Ni [90–95], and Mn [96–100]. The main Co advantage is the 100% natural abundance of the magnetic isotope (^{59}Co), whereas the one of ^{57}Fe is 2.2%, and the one of ^{61}Ni 1.14%. Also the two latter nuclei have low gamma ratios thus resulting in a low sensitivity. At first sight, Mn is a good candidate; however the diversity of reduction extents leads to the formation of antiferromagnetic compounds with low Néel temperatures (within 4-77 K), thus requiring special low-temperature equipment. Moreover, internal field NMR spectra of ^{55}Mn display very large widths up to several hundreds of MHz. A large range of possible positions of the resonance complicates the search of internal field NMR lines. On the other hand, Co possesses strong ferromagnetism, and its study is relevant to various important field of applications such as catalysis, memory storage devices, lithium-cobalt battery materials, and magnetic composites. Interest for Mn is more fundamental due to a variety of different magnetic effects in Mn compounds.

Hereinafter, only Co-based alloys, thin films and magnetic salts are considered. In the early years after Gossard and Portis work [27], the extent study of different Co-X alloys aimed a precise internal field measurements for magnetism theory verifications. Several binary systems such as Co-Fe [68; 101–115] and Co-Cu [68; 108; 116–124] were extensively studied in relation with the search for new memory storage devices. Specifically for Co-Fe system, the emphasis is placed on Co rich films and alloys Co_xFe_{1-x}, where $x > 0.5$ since these alloys possess strong ferromagnetism and are more suitable for memory devices. As well, some papers deal with diluted Co alloys, *i.e.* when x is close to 0 with the principal concern of studying the internal field distribution and defect structure in Co-Fe alloys.

Other Co-based metal systems such as films Co^0 [125], Co-Ni [108; 109; 126–129], Co-Mn [108; 109; 130–133], Co-P [124; 134], Co-V [109; 135–137], Heusler alloys [138; 139], Gd, Tb, Dy-containing magnetic compounds [31], and various binary alloys and films Co-Cr [68; 108–110; 136], Co-Ru [68; 140], Co-Pt [68], Co-Al [108], Co-Si [141–143], Co-Ti [109], Co-Ag [129; 144; 145], Co-Au [146], Co-Mg [147–150], Co-Ge [151] have been examined systematically but not so comprehensively as Co-Fe and Co-Cu. Also a contribution of Russian authors to the structure of Co films and alloys can be found in ref. [152–155].

Since the number of papers on different Co alloys is extremely high, we draw here only the main conclusions of more than 50 years of studies.

Co metal dilution by foreign element of lower magnetic moment than Co leads to the formation of a long tail to lower frequencies relatively to the 213 MHz Co fcc d.w. line. Depending on the degree of ordering, the alloy can have different features. A typical example of Co alloys is shown in fig. 2.2.1 where the Co-Si multilayers are displayed.

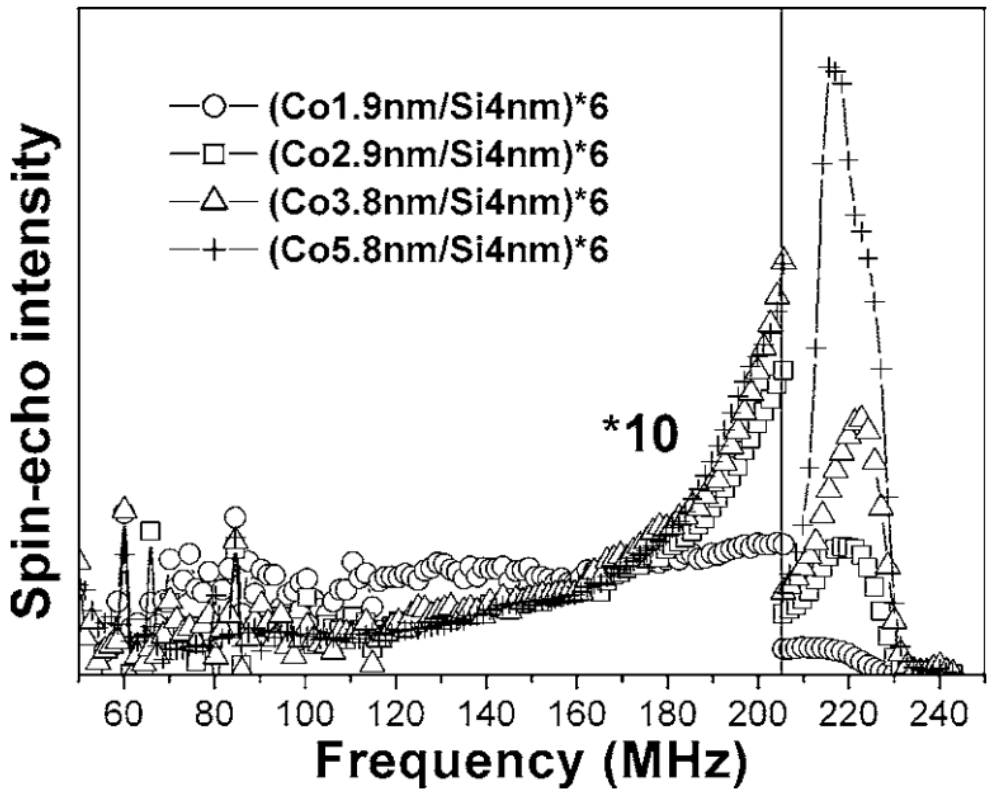

Fig. 2.2.1. Internal field ^{59}Co NMR spectra of Co-Si multilayers (T = 1.5 K) of different number of component layers. The enlarged part of spectrum shows the usual tail in internal field ^{59}Co NMR spectra of Co alloys with nuclei of lower magnetic moment. Figure is adapted from [156].

The general tendencies of different Co alloys can be seen in one of the early works by Koi et.al. in 1960 [157]. Figure 2.2.2 displays the internal field ^{59}Co NMR spectra of different Co-*X*, where *X* stands for Fe, Ni, Cu, Al, Mn, and Cr.

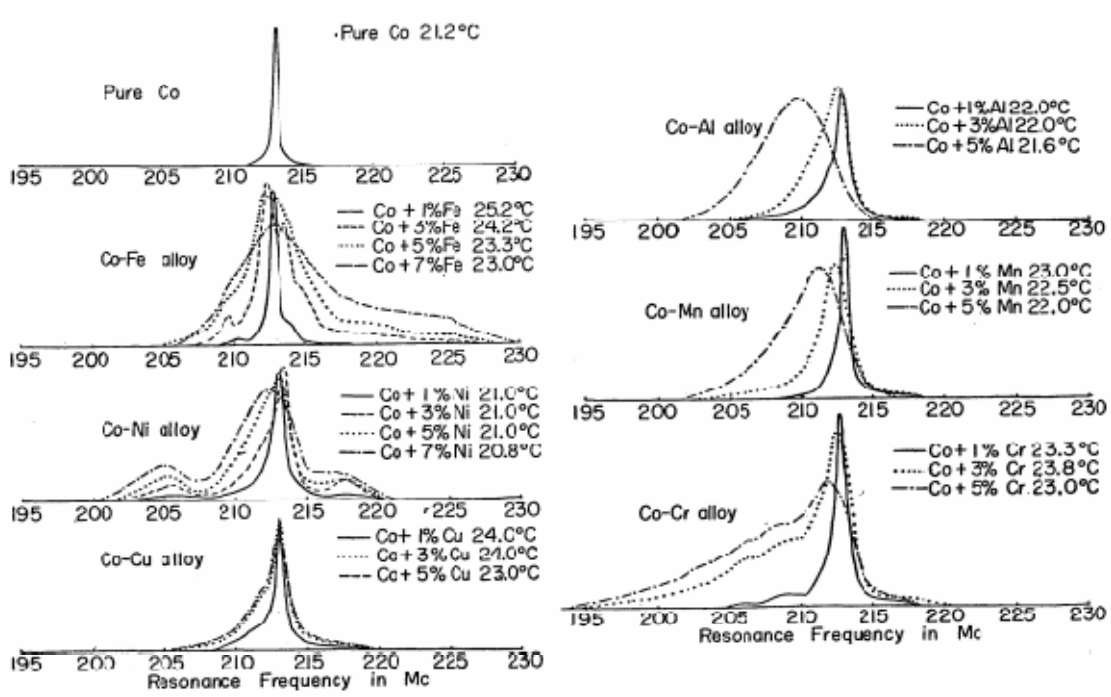

Fig. 2.2.2. Internal field ^{59}Co NMR spectra of different Co-*X* alloys, where *X* is Fe, Ni, Cu, Al, Mn, and Cr [157]. All measurements have been performed at ambient temperature.

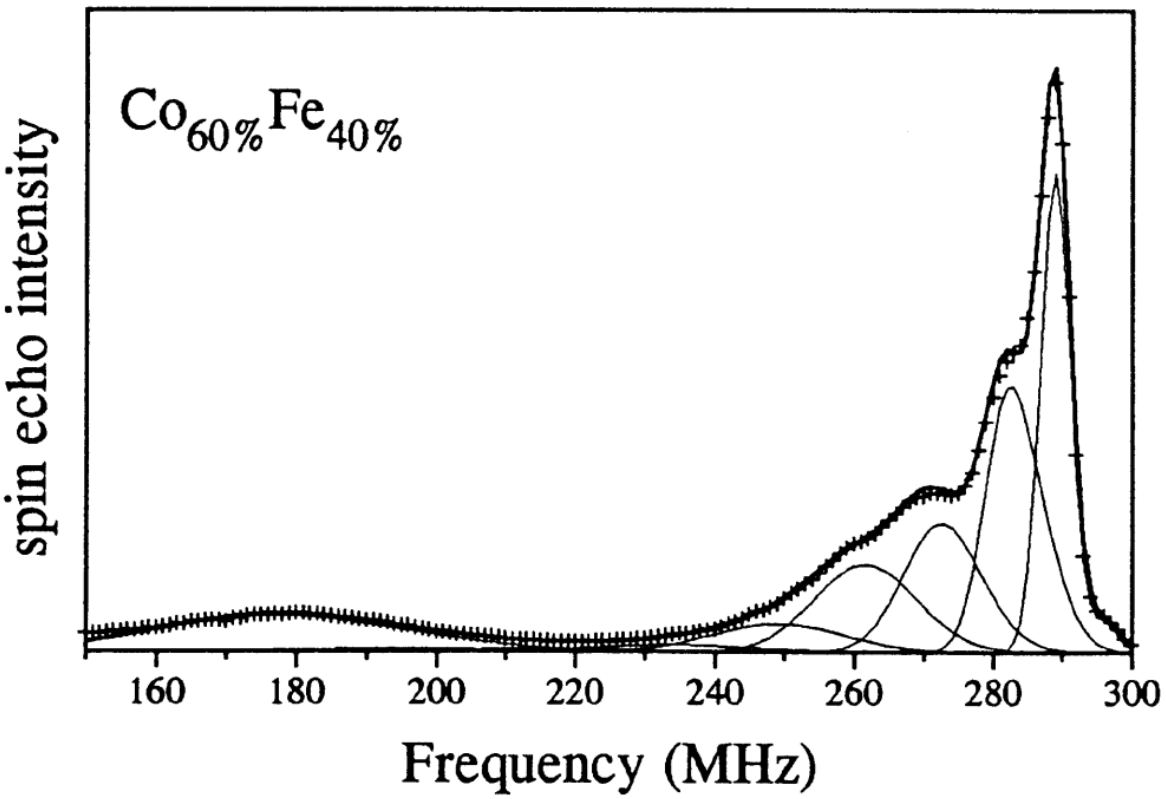

Fig. 2.2.3. Internal field ^{59}Co NMR spectrum of $Co_{60}Fe_{40}$ alloy acquired at 4.2 K taken from the work by Jay et.al. [114].

Co-Fe alloys show different behavior compared to the ones listed above. Iron nuclei have large magnetic moment shifting the lines in internal filed ^{59}Co NMR spectra up to 300 MHz at room temperature. A typical spectrum of Co-Fe alloy is shown in figure 2.2.3, which is taken from the work by Jay et.al. [114]. It has been empirically found that Co_xFe_{1-x} alloys with $x > 0.5$ show 10-11 MHz shift of the internal field ^{59}Co NMR spectrum resonance line per each additional Fe in the Co nearest neighbor (NN) shell (first coordination sphere) [74; 107; 114] compared to the higher frequency of relatively pure Co metal resonances. These Co_xFe_{1-x} alloys ($x > 0.5$) also can form base-centered cubic lattice (bcc) (the resonance lines at ~200 MHz and lower), however in general Co has close-packed lattice (fcc or hcp). Also these alloys exhibit a B2 ordered phase (see phase diagram in ref. [158]) at temperatures below 1000 K; thus spectra can exhibit only one narrow line (corresponding to the ordered B2 Co-Fe phase) instead of a broad binomial distribution. B2 stands for a NaCl lattice, in which each Co atom is surrounded by 8 Fe atoms in NN, and, vice versa, each Fe atom is surrounded by 8 Co atoms in NN [102; 104].

And finally, a special role is played by magnetically ordered compounds, which can be represented by different Heusler alloys (X_2YZ gross formula) [138; 139].

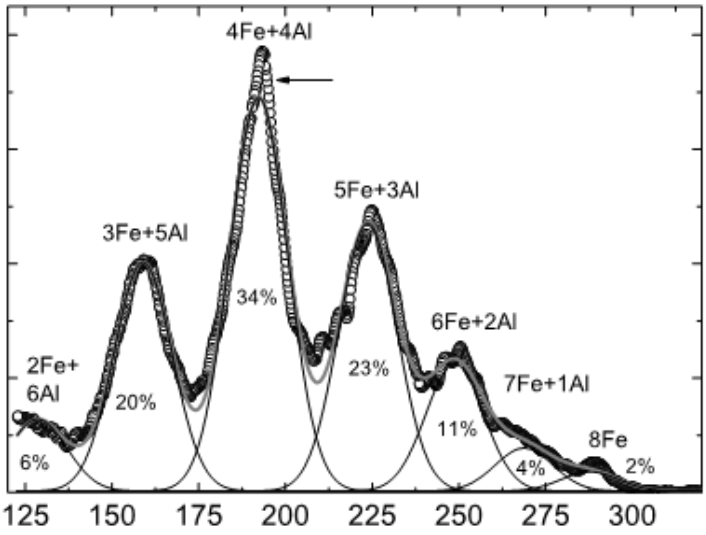

Fig. 2.2.4. Internal field ^{59}Co NMR spectrum of Co_2FeAl Heusler alloy corrected for the enhancement factor. The dots show the experimental points. The horizontal axis is resonance frequency (MHz). The percent's indicate the relative content of each type Co[(n)Fe (8-n)Al] site. reproduced from [139]. The spectra have been acquired at 4.2 K.

Heusler alloys have ordered $L2_1$ structure, which makes all possible configurations of Co[(n)Fe (8-n)Al] environment resolvable in internal field ^{59}Co NMR spectra (see figure 2.2.4). The structure exhibits a competitive replacement of Co positions by Fe and Al in first coordination sphere that drastically changes the internal field on Co nuclei since iron and aluminum nuclei possess much differed magnetic moment. Herewith, in a first approximation, the distribution of the satellite line intensities follows a binomial law. It should be noted that the spectrum has very large width (up to 200 MHz). This width complicates the spectra acquisition due to instrumental limitations. The typical tuning and matching capacitor in the rf circuit of the NMR probe covers 50-70 MHz of spectral width. Wider spectra require coil changing that therefore alters the circuit characteristics, and spectra overlapping (5-10 points) in two coils must be acquired to ensure line intensity correctness within the spectrum. Also spectra must be recorded at several rf power intensities and this extremely increase the experimental time.

Several report have been published for binary Co metal alloys [15; 73; 74; 159]. The main drawback in them is inconsistent information regarding pure Co metal, but not for alloy study. Indeed, early works were carried out using continuous wave spectrometers, which suffered from low sensitivity. Also, phase detection was a challenge in old spectrometers.

2.3.Conclusions to Chapter 2:

Internal field ^{59}Co NMR is known form the end of 1950-s. High attention has been paid for studying bulk Co metal, and especially Co alloys. This technique allows identification of both structural (fcc, hcp and sfs) and magnetic (domains, domain walls, and single-domain particles) features. In the best case, a quantitative estimation of the phase content can be performed. On the other hand, there are only a few studies of dispersed Co metal particle by internal field NMR for catalytic and other applications.

The long history of the method also conceals several internal contradictions on the attribution of resonance lines in internal field ^{59}Co NMR spectra. There are two models for the spectra description. The first one considers only the crystallographic parameters to assign the internal field NMR lines while the second one considers with both structural and magnetic features. Based on statements described in this chapter, the latter model, in the author's opinion, is more adequate describes the internal field ^{59}Co NMR spectra.

The main resonance lines of pure Co metal, which can be included in this model, are summarized in Table 2.3.1. First of all, the stacking faults of Co metal resonate at the edge of the spectrum at 210 and 224 MHz. The attribution of these resonances to a certain phase is not totally unambiguous, but both can be attributed to hcp Co with a good level of confidence [1; 56]. The fcc Co metal resonance lines are well defined: fcc domain walls are attributed to 213 MHz line [27], and fcc single-domain Co can be found within the 215-216.5 MHz region [2; 46; 48] depending on the strength of inter-particle interactions [47]. The hcp resonances of Co blk metal are sharp, however a broad line at 219 MHz is observed in Co metal nanoparticles [2; 160]. The lines at 214 MHz and 221 MHz are commonly observed in hcp monocrystals or very large particles (several microns in size). The lower frequency 214 MHz line is attributed to hcp domain wall edge (or domain signal) [22–24; 63], and 221 MHz line to Co nuclei in hcp domain wall center [23–26; 77].

Table 2.3.1. Summary of the line positions reported in the literature and retained in this thesis, which account for both magnetic and crystallographic features of Co metal. In alloys, the effect of nearest neighbor should be considered separately since the spectra exhibit different satellite lines depending on the magnetic moment of the foreign nuclei.

Line assignment	sfs	fcc d.w.	hcp domains*	hcp	hcp d. w.**
Line position (MHz)	210 ~224	213	214	219	221

* Sometimes the term "domain wall edge" is used instead.

** Sometimes the term "domain wall center" is used instead.

The position of single domain fcc particles is not shown here since it strongly depends on the particle shape and can be found 2-6 MHz higher then fcc d.w. line (213 MHz) for spherical particles, 9 MHz higher for cylinder particle, and 18 MHz higher for thin films.

Better structural understanding obtained by internal field NMR provides a link between different phases and performance of the material. Strong Co interaction (going all the way to alloy formation) with support can also be potentially revealed by this technique. Furthermore, its instrumental simplicity is a key to achieve *in situ* study of active species formation during the reactions and processes at stakes.

CHAPTER 3
EXPERIMENTAL

3. Experimental

3.1. Internal field ^{59}Co NMR.

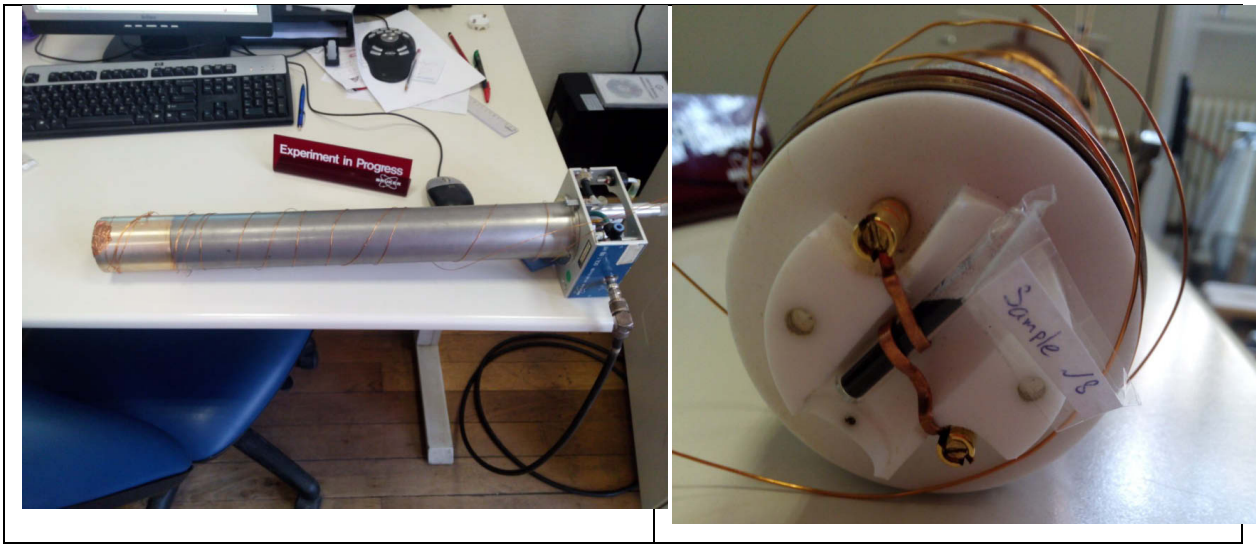

Fig. 3.1.1. A photo of the broadband NMR probe, which is used for the internal field ^{59}Co NMR spectra acquisition (outside of the NMR magnet).

Internal field ^{59}Co NMR spectra measurements was carried out on three spectrometers: Bruker Avance 400 MHz (magnetic field 9.4 T) in Novosibirsk (Russia), Bruker Avance II 500 MHz (magnetic field 11.7 T) in Paris (France), and Bruker Avance III 500 MHz (magnetic field 11.7 T) in Ekaterinburg (Russia). All experiments have been performed without application of external magnetic field, *i.e.* outside of the magnet. To cover the desired frequency range (~ 195-300 MHz), a set of rf coils has been made. Also, this wide range requires using the additional inserts as tuning capacitors from 1.5 to 64 pF capacitance. Large spectral width (20 MHz and more) requires point by point spectra acquisition with a step of 0.5 MHz. A frequency-stepper technique has been used in some cases. Since the optimal excitation of domains and domain walls occurs at different power levels, the spectra have been recorded at several power levels (from 7 to 10) covering 14-20 dB (the power changed from 25 to 100 times that is equal to a 5 to 10 times change in B_1 rf field amplitude) range with 2 dB step. A typical 2D dependence of signal intensity on applied power pulse and resonance frequency is shown in figure 3.1.2.

A special program collected spectrum from many files. The program can extract raw data from TopSpin files, makes Fourier transform, left/write shifts in time domain data as well as the integration of time and frequency domain data that fully covers all needs of spectra plotting and relaxation time curve processing.

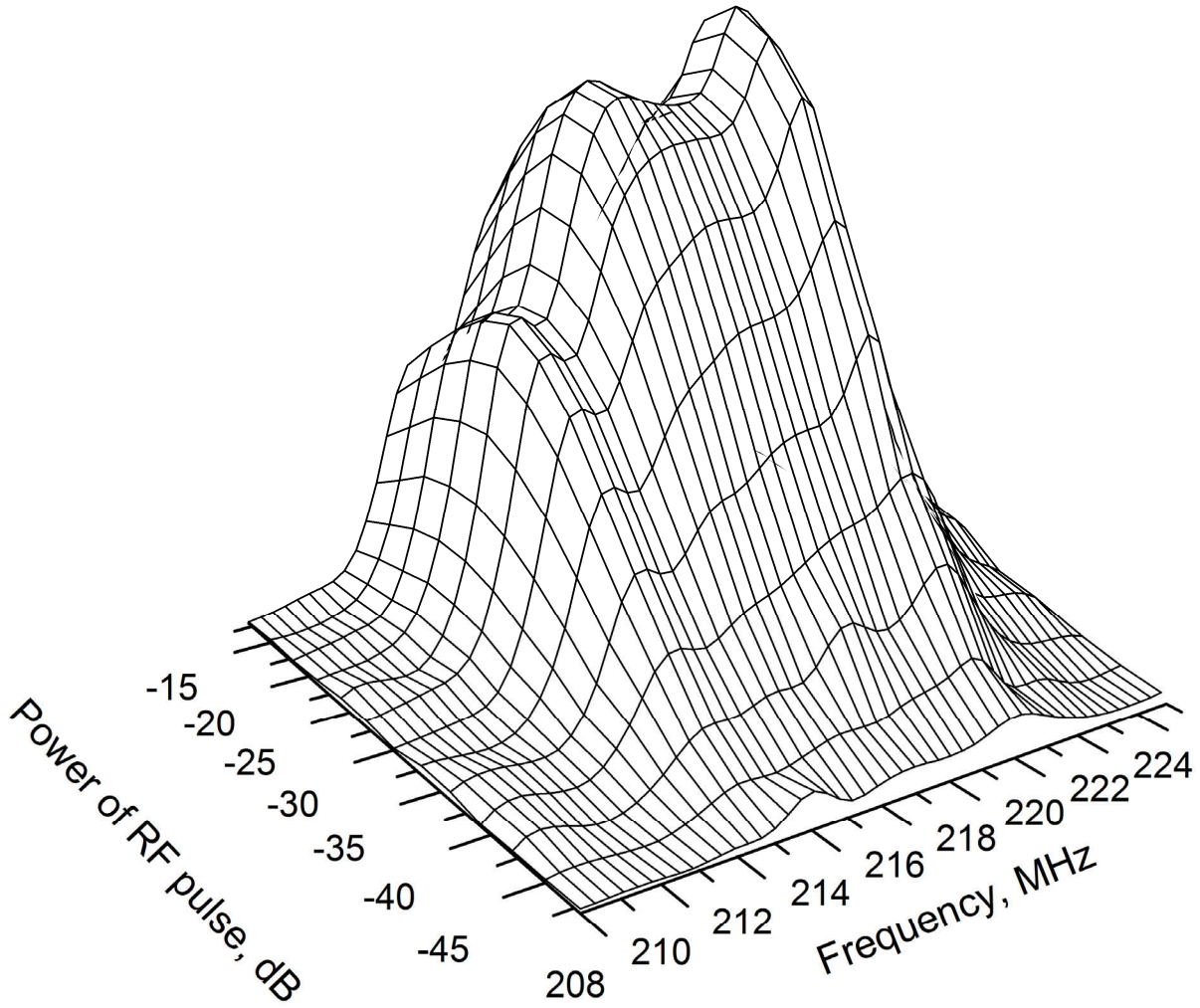

Fig. 3.1.2. An example of obtained 2D dependencies of signal intensity on applied power pulse and resonance frequency.

The pulse lengths varied within 0.3-4 μs (depending on T_2 relaxation time and rf contour quality factor of the specimen). The number of transients in each point of power and frequency was from 512 to 16,000. It is also important that skin effect in all presented experiments is negligible since the skin effect characteristic depth at the frequencies used in

the experiments is 8 μm. The maximal particle size of Co metal in experiment was limited to 1 μm.

To get real intensities ratio within each spectra, a correction for the enhancement factor η should be applied, which is proportional to rf B_1 magnetic field (in accordance with (1.2.1)). Unfortunately, knowledge of the real B_1 value is close to impossible to obtain with the required accuracy. As it turns out, absolute values of the enhancement factor are not an absolute necessity for the correction of the spectrum acquired using the same rf coil. Commercial Bruker spectrometers (Avance and Avance II) can vary applied rf powers (only in dB) P_1, which is proportional to the amperage in the coil:

$$P_1 \propto I^2$$

Attenuation of the power is given by the formula:

$$Value\ in\ dB = 10 \cdot \lg \frac{P_1}{P_0},$$

where P_0 is a reference power (which is, in principal, unknown), or the maximal power at a given frequency. All experiments have been carried out with rf contour tuning and matching, therefore P_0 is assumed to be constant (or to vary insignificantly)

The magnetic field is proportional to the current as:

$$B_1 \propto I$$

Correction for the enhancement factor η necessitate relative B_1 values. Therefore, what is important is that the values taken in dB can be easily recalculated as somewhat proportional to B_1:

$$B_1 \propto 10^{-0.05 \cdot (Value\ in\ dB)}$$

Different structures in internal field NMR spectra can have different enhancement factors and thus different dependence of their signal on the applied rf field intensity delivered at the nucleus which in turns cannot be known *a priori*. Consequently, the internal field NMR spectra acquired at one power level are irreproducible when different spectrometer and probes

are used. Nevertheless, full reproducibility can be attained using the optimal spectra representation. This approach requires knowing the rf field dependency of the resonance at each frequency as shown by Mény, Panissod and co-workers [74; 116]. These authors provided a formula of the internal field NMR signal dependence on frequency and applied power (which is true for nuclei in domains, but its relevance in domain walls requires additional justifications) [161; 162]

$$S(B_1,\omega) = \eta I_0(\omega)\exp\left[-\log^2\left(B_1/B_{1opt}\right)/2\sigma^2\right] \qquad (3.1.1)$$

where $S(B_1,\omega)$ is the observed intensity in the spectrum, $I_0(\omega)$ its « true » intensity, B_1 the rf field inducing the signal, B_{1opt} the applied rf field when the signal is maximal (i.e. optimal), σ the width of the Gaussian distribution in the units of $ln(B_1)$, and η is the enhancement factor.

Generally, a majority of studies uses a simplified expression of equation (3.1.1) working at conditions where $B_1 = B_{1opt}$. Since the applied rf field B_{1opt} causes maximal intensity in the spectra, the spectrum plotted using B_{1opt} at each frequency is called optimal. The main advantage of this approach consists in its universality, *i.e.* the optimal spectrum is not dependent on instrumental specifications (whereas attempting to correct for the enhancement factor is tainted by measurement errors of the rf field amplitude B_1). Practically, the optimal spectrum is obtained as follows. The NMR signal is acquired in two dimensions, that is intensity *versus* frequency and rf power as described elsewhere [74; 116]. The optimal spectrum is simply a projection along the rf power dimension and does not require exact knowledge of the power values (hence its reproducibility).

Unfortunately, this representation is not quantitative because each point has its own enhancement factor η (i.e. different optimal excitation field B_{1opt}, at which the signal is maximal). To get quantitative results, a correction is required. It consists in a multiplication of the optimal spectrum by a calibration curve showing the B_{1opt} rf field frequency dependence [73]. The resulting spectral representation is called a spectrum corrected for the enhancement factor [1].

NMR lines simulation was performed using PeakFit program. All Gaussian peak positions were determined from the ”optimal” spectrum and were matched with literature meanings. Only line width and line intensities were varied, the peak positions were fixed during simulation. Manual deviation from obtained line positions within 0.2 MHz were implemented

to get the best fit. Due to line superposition, the fit is not unique, *i.e.* all line relative content can be changed within 2-3 at.%.

3.2. Complementary methods

It is obvious that no one technique can provide comprehensive information regarding the studied samples. Since the number of additional physico-chemical methods that were used in this thesis is high and varies from sample to sample, their detailed description is kept within the articles in Chapter 4 to facilitate the access to this information when relevant.

CHAPTER 4
RESULTS AND PUBLICATIONS

4. Results and publications

4.1. Short review on FTS

4.1.1. Historical perspective

The first experiments on catalytic hydration of carbon monoxide CO were performed by Sabatier and Senderens in 1902 by methane synthesis from a CO and CO_2 mixture with hydrogen. In 1922, Hans Fischer and Franz Tropsch proposed the Synthol process [163] using iron chips as catalyst. Significant progress in FTS has been made in 1923. Longer hydrocarbon (HC) chains [164] were obtained while decreasing the overall pressure to 0.7 MPa. In 1926, the first report on HC synthesis has been published [165].

In 1934, FTS has been certified by Ruhrchemie and was industrially applied within two years. In 1936, the first large-scale reactor has been launched in Braunkohle-Benzin. In 1938, Germany reached ~13,000 barrels per day production of raw product. After the Second World War, Arbeitsgemeinschaft Ruhrchemie und Lurgi (ARGE) established large-scale plants based on fixed bed reactors. Simultaneously, Kellog proposed the concept of circulating catalyst bed. Both the Kellog and ARGE processes have been used by Sasol in the RSA. Sasol 1 plant has been constructed in 1955 in Sasolburg, Sasol 2 and Sasol 3 in Secunda in 1980 and 1982, respectively [166]. The main progress brought by Sasol is summarized in a monograph (monograph chapters [167–175]).

In 1980-s, the interest for FTS has risen again due to the perspective of concomitant gas utilization. The synthetic fuel contains less sulfur and aromatics; therefore it is safer for the environment.

The modern interest for FTS consists in biomass conversion as well as natural gas conversion to olefins. In 1993, Shell Bintulu launched a plant producing 12,500 barrels per day. In 2006, Sasol Oryx established a plant with 34,000 barrels per day. Sasol Chevron is currently building its Escarvos “gas-to-liquids” (GTL) plant in Nigeria. Shell and Exxon signed an agreement for building 140,000 and 150,000 barrels per day GTL-FT plants in Qatar. The history of FTS catalyst design has been reviewed by Bartholomew [176].

4.1.2. FTS catalysts

All metals of VIII group have noticeable catalytic activity in monoxide CO hydrogenation towards hydrocarbons (HC)

$$nCO + 2nH_2 \rightarrow C_nH_{2n} + nH_2O$$

$$nCO + (2n+1)H_2 \rightarrow C_nH_{2n+2} + nH_2O$$

Iron, nickel, cobalt and ruthenium are the most active metals in FTS process. The average molecular weight decreases in the following sequence: *Ru* > *Fe* > *Co* > *Rh* > *Ni* > *Ir* > *Pt* > *Pd* [177]. The most desirable products are C5-C8, especially alpha-olefins that can be easily polymerized to get more plastic materials compared to ones based on paraffin. Thus, only *Ru, Fe, Co,* and *Ni* have catalytic performance that can be used in large scale industry. However, Ni in normal FTS conditions produces only methane. Ru is very expensive for large scale usage, and its reserves are not sufficient to be used in FTS. Consequently, it is usually iron and cobalt that are utilized in FTS plants [178].

Co based catalysts are more expensive than Fe ones; however they are more resistant to deactivation. The activity at low conversion rates is comparable, but productivity at higher conversion rates is more significant on Co FTS catalysts. Water created in FTS reaction slows more the reaction rate on Fe catalysts than on Co ones. At relatively low temperatures (473 – 523 K), the probability of chain growth on Co catalysts is 0.94, and on Fe catalysts it is 0.95 [179–181]. The water-gas shift reaction is more significant on Fe than on Co based catalysts.

$$CO + H_2O \rightarrow CO_2 + H_2$$

Iron catalysts usually give more olefins. Both metals are sensitive to sulfur content, which easily deactivates them. The upper critical sulfur content in the feed is limited to 0.2 ppm for Fe, and to 0.1 ppm to Co [180–182]. The Co supported on oxides catalysts are in general more resistant to attrition than bulk Fe ones. Fe FTS catalysts produce HC and their oxygenates at different pressures, H_2/CO ratios, and different temperatures up to 609 K. Co FTS catalysts work in a very narrow range of temperatures and pressures, and temperature increase leads to selectivity shift mainly to methane. Fe based catalysts in general are more suited for biomass conversion since they can work at lower H_2/CO ratio.

There two main temperature ranges in FTS: low and high temperature processes [182–184]. In high temperature FTS [185], syngas reacts in a fluidized bed reactor in the presence of iron-based catalyst to yield hydrocarbons in the C1-C15 hydrocarbon range. This process is primarily used to produce liquid fuels, although a number of valuable chemicals, e.g., R-olefins, can be extracted from the crude synthetic oil. Oxygenates in the aqueous stream are separated and purified to produce alcohols, acetic acid, and ketones including acetone, methyl ethyl ketone, and methyl isobutyl ketone [178].

Both iron and cobalt (Fe and Co) catalysts can be used in the low temperature FTS process [179; 181] for synthesis of linear long-chain hydrocarbon waxes and paraffins. High-quality sulfur-free diesel fuels are produced in this process. Most of the FT technologies developed in last two decades are based on the LTFT process. These new low temperature FTS processes have involved syngas with a high H_2/CO ratio, which is generated by vapor forming, auto-thermal reforming, or partial oxidation using natural gas as a feedstock. Because of their stability, higher per pass conversion [179], and high hydrocarbon productivity, cobalt catalysts represent the optimal choice for synthesis of long-chain hydrocarbons in the low temperature FTS process [178].

4.1.3. Structure of FTS catalysts

The structural study of FTS catalysts is essential for improving their performance (activity and selectivity). Also the knowledge of the catalyst structure is needed to increase the cost efficiency of the catalyst preparation process. The question of the active species in FTS catalysts is also still under consideration.

There are many preparation techniques of Co FTS catalysts such as coprecipitation in solution, mechanochemical activation under inert atmosphere of Co and support and *etc.* However the most common one is by incipient wetness impregnation (ICP). The impregnated supports are usually γ-Al_2O_3 [186], but also TiO_2 [187], ZrO_2, SiO_2 [188] or *ZSM-5* [70]. The Cobalt source is a water solution of Co^{2+}, mainly as Co nitrate $Co(NO_3)_2 \cdot 6H_2O$, chloride $CoCl_2 \cdot 6H_2O$ or acetate $Co(CH_3COOH)_2 \cdot 4H_2O$. To increase metal content, multistage impregnation is used. Then the catalysts are dried in the air at 353-431 K for up to 16 h, and calcined at 573-673 K for 4-6 h to decompose Co salts into Co_3O_4 oxide.

Generally, all Co FTS catalysts are promoted by different species, mainly by Noble metal (*Ru, Pt, Re*) and cations (*B, Na, Zr, La*). Addition of promoters to catalysts improves properties as activity, selectivity, reduction temperature, *etc.* The promoter is introduced after impregnation, but before drying and calcination. Standard promoter precursors are ruthenium nitrosyl nitrate $Ru(NO)(NO_3)_3$, platinum nitrate tetraammin (II) $[Pt(NH_3)_4](NO_3)_2$, rhenium oxides , boracic acid H_3BO_3, sodium carbonate Na_2CO_3, zirconium nitrate $Zr(NO_3)_4$, and lanthanum nitrate $La(NO_3)_3$ [187; 189].

The Co FTS catalysts on γ-Al_2O_3 exhibit a two-stage reduction process. The first low temperature stage is $Co_3O_4 \rightarrow CoO$ reduction, and the second high temperature one is $CoO \rightarrow Co^0$ reduction. Catalyst promotion by *Pt* or *Ru* shifts the first reduction stage to lower temperatures. Re also decreases the second stage temperature. The addition of 1% Re to the catalyst decreases the average Co particle size, but Re does not change the Co^0 reduction rate. Re stabilizes the Co particles and as a result smaller Co particles can be obtained [186].

Many authors (for example, [186; 190]) point to residual CoO content on the surface of Co metal particles after reduction from Co_3O_4 to Co^0. According to these authors, this CoO is also responsible for carbon chain growth in FTS . The interaction of Co metal and alumina results in a $CoAl_2O_4$ spinel film, which prevents full Co reduction. However, other supports (SiO_2, ZrO_2, TiO_2) do not display as strong metal-support interaction as gamma alumina γ-Al_2O_3 [191]. Finally, it is not fully understood if it is the Co metal or the Co/CoO interface that plays the crucial role in FTS.

It should be noted that to get FTS products different from diesel, mainly Co based catalysts are used. The nature of this phenomenon likely consists in Co-support interaction that stabilizes appropriate Co size and Co phase, which is active and selective in FTS towards olefins alcohols and other desirable products.

4.2. Basics on internal field ^{59}Co NMR

4.2.1. Co metal powder

It is essential to start experimental internal field ^{59}Co NMR investigations by looking at bulk Co metal powder since literature data are sometimes contradictory. In this chapter, the internal field NMR is essentially coupled with XRD since these techniques are the only ones that can provide quantitative data on hcp/fcc ratio in Co metal. A method to plot internal field NMR data in universal way is also shown here as well as a classification of resonance lines. The content of this chapter is published in *Applied Magnetic Resonance* [1].

Despite the fact that a full description of field ^{59}Co NMR lines was done in this paper several important notices can be mentioned. First of all, the particle size of studied particles was 2-5 μm, and the presence of small (< 70 nm) single-domain particles is not expected. At the same time, this sample can be described as bulk material with high number of domains and domain walls. Therefore the demagnetizing field should be averaged to zero. However, we claimed 216.5 MHz line to arise from fcc magnetic domains, which is not the case of Co metal particles of micron size. The residual demagnetizing field (if exists) of magnetic domains in multidomain sample is negligible compared to observed shifts in single-domain particles (several MHz). Therefore, 216.5 line should be attributed to fcc stacking faults.

Appl Magn Reson (2014) 45:1009–1017
DOI 10.1007/s00723-014-0580-0

Applied
Magnetic Resonance

A New Insight into Cobalt Metal Powder Internal Field ^{59}Co NMR Spectra

A. S. Andreev · O. B. Lapina · S. V. Cherepanova

Received: 1 July 2014 / Revised: 11 August 2014 / Published online: 28 August 2014

Abstract The authors present a new approach of internal field ^{59}Co NMR spectra assignment leaving apart from "usual" decomposition on "pure" hcp and fcc stackings, and a set of stacking faults (sfs) sf_1–sf_5 with a certain lines position. The authors propose including into consideration not only cobalt structural features as well as its magnetic nature due to the strong ferromagnetism in Co metal. The last fact supposes an existence of different magnetic species such as magnetic domains, domain walls, and single-domain particles, thereby helping to spectral lines assignment according to both structural and magnetic origin. The examined sample contains fcc and hcp resonance peaks in both domains and domain walls giving the hcp to fcc ratio equal to 1.9, as well a significant amount of Co sfs, or Co in loose coordination, up to 10 %. The research exhibits a good agreement of all implemented techniques.

1 Introduction

A combination of X-ray diffraction (XRD) and nuclear magnetic resonance (NMR) to study metallic Co particles has been implemented many times [1–6] since the first observation of internal field (IF) ^{59}Co NMR by Gossard and Portis in 1959 [7]. The main reason of all investigations is to correlate the structural data extracted from XRD and magnetic information given by IF ^{59}Co NMR. Co metal is known to have two allotropic modifications as fcc and hcp, also it tends to faulting [8–10]. Many authors have been confused by the last fact straightly correlating observed lines in

A. S. Andreev · O. B. Lapina (✉) · S. V. Cherepanova
Novosibirsk State University (NSU), Pirogova str., 2, 630090 Novosibirsk, Russia
e-mail: olga@catalysis.ru

A. S. Andreev · O. B. Lapina · S. V. Cherepanova
Boreskov Institute of Catalysis SB RAS (BIC SB RAS), pr. Lavrentieva, 5, 630090 Novosibirsk, Russia

IF ^{59}Co NMR spectra and structural features. The question requires more comprehensive understanding starting from local field NMR principles [11–13]. Shortly, since the applied magnetic field is zero, all nuclear spin transitions occur in a local field created by hyperfine interactions of nuclei and electrons. The local field therefore includes dipolar contributions from neighboring nuclei, i.e. depending on stacking. Concurrently, an excitation by modulated RF pulse (h_1) is also indirect, and there are two possibilities depending on magnetic species of the sample (magnetic domains or domain walls). In domains, RF pulse first tilts on a small angle the electronic magnetization since a modulation frequency is far from the electronic resonance. However, such a small angle is enough to create rather strong transverse component of local magnetic field B_1, i.e. a real field interacting with nuclear spins is B_1, thus the signal is enhanced by a factor $\eta = B_1/h_1$. In domain walls (d.w.), RF pulse directly shifts the wall, therefore nuclei in the center of domain wall rotates on a large angle producing higher B_1, thus the enhancement factor η in domain wall is more than in domains. This illustrates that not only structural features affect IF ^{59}Co NMR spectra. Structurally, fcc Co is highly symmetrical and should give only one line taking into account only structural features. Adding magnetic system, a new possibility is emerged; fcc Co can be a part of domain or domain wall. In the center of domain walls, contributions from demagnetization fields are compensated since the domains are antiparallel (resonance frequency of fcc d.w. Co is 213 MHz) [14]. However, both domains and single-domain particles cannot fully compensate the demagnetization field, therefore, fcc Co line is shifted (resonance frequency of fcc Co in domains or single-domain particles is within 215–216.5 MHz) [15]. On the other hand, hcp Co is less symmetric, and it should have a local field anisotropy in parallel and perpendicular to hcp *c* axis [16]. Co atoms in hcp domains are aligned to hcp *c* axis and Co atoms inside domain walls are perpendicular. The local field anisotropy reaches 0.8 T providing an observation possibility of hcp resonance in the center of d.w. (221 MHz) and in d.w. edge (d.w.e.) or domains (depending on enhancement factor η in d.w.; for high η in d.w. domain contribution is negligible) at 214.2 MHz [17–21]. Unfortunately, the particles size decrease leads to anisotropy averaging, and only a broad line of hcp Co at ~219 MHz in nanoscale both in domains and d.w. [6, 22–24] can be resolved. Summarizing all above, one can state at least 5 lines in IF ^{59}Co NMR spectra, such as fcc d.w. at 213 MHz, hcp domain or d.w.e. at 214.2 MHz, fcc domain or single-domain fcc at 215–216.5 MHz, nanoscale hcp in domains and d.w. at ~219 MHz, and hcp in d.w. center at 221 MHz. Also one can add line at ~210 MHz for Co in loose coordination or grain boundaries [4, 25] and rarely observed stacking faults line at ~223.5 MHz [4, 26].

The work proposes a new model for Co metal powders IF ^{59}Co NMR spectra assignment described above. The authors do not try to prove the assignment listed above since it has been performed for each certain line separately in the references; however, the full model containing all small puzzles is introduced for the first time. The model contradicts the previous one based on the observation of two pure phases fcc and hcp at 213 and 221 MHz, respectively; and a set of stacking faults (sfs) sf_1–sf_5 at frequencies of 214, 215.5, 217, 219, and 223.5 MHz accordingly. The former model based on two early papers [1–3] relies only on the structural cobalt features

missing magnetic structure as it is described in [22]. Thus, the research aims to give a new insight on Co metal powders structure providing an appropriate correlation between magnetic resonance and structural techniques.

2 Experimental

Commercial grade cobalt PK-1Y (GOST 9721-79) powder of 99.35 % purity was used as a material to study. The powder particles size was not measured directly; however, estimation from microscopic data gives 2–5 μm average size. The sample was sealed in a glass ampoule for internal field (IF) ^{59}Co NMR experiments for more convenience. A 10-mm outer diameter glass tube was used for these experiments.

All IF ^{59}Co NMR experiments were carried out on Bruker Avance 400 MHz (magnetic field 9.34 T) without any external magnetic field application, i.e. outside of the magnet, and at the ambient temperature. A standard broadband static low Q NMR probehead was utilized during experiments, and it had frequency tuning and quality factor matching capacitors. The spectra were acquired using the spin-echo Fourier transform point by point technique, described elsewhere [27]. The train of two pulses was used to generate spin echo with two equivalent pulses of 4 μs, interpulse delay of 20 μs, 8,000 numbers of transients in each point, and 20 Hz repetition rate due to very short T_1 relaxation time in ferromagnetic cobalt. An extremely low for solid-state NMR pulse power was implemented (20–30 dB attenuation from 300 W RF low power supplier within frequency range 206–223 MHz) due to high enhancement factor in the pure metallic Co [14].

NMR peaks simulation was performed using PeakFit program. All Gaussian peak positions were determined from the "optimal" spectrum and were matched with literature meanings. Only line width and line intensities were varied, the peak positions were fixed during simulation. Small manual deviation from obtained line positions within 0.2 MHz were implemented to get the best fit. Due to line superposition, the fit is not unique, i.e. fcc d.w. line at 213 MHz and hcp domain line at 214.4 MHz allow deviation within 5–7 % of integral intensity, and fcc domain line at 216.5 MHz and hcp NPs line at 219 MHz within 3–5 %.

The X-ray diffraction (XRD) patterns were registered using a X'TRA (Thermo ARL) diffractometer (Bragg–Brentano geometry, CuK_α radiation, energy dispersed detector, step scan mode). Data registration was made in the 2θ angle range from 15° to 120° with step of 0.05° and accumulation time of 40 s in each point. Quantitative phase analysis was carried out by Rietveld refinement with the use of PCW software [28]. Simulation of XRD patterns for disordered metallic cobalt particles was carried out using the program described elsewhere [29]. The calculations were performed using the model of a crystal disordered in one dimension (1D). The model is built as a statistical sequence of a finite number of 2D periodic layers. The Markov chain is used as a generation rule for the statistical stacking sequence. Stacking sequences were simulated as consisting of identical hexagonally close-packed (hcp, or AB type) layers. In this AB–AB–AB–AB… structure, there is no shift between AB layers (the first type of superposition). In the

cubic close-packed (fcc) structure, AB layers are shifted on the (1/3, 2/3) vector (the second type of superposition) to provide AB–CA–BC–AB–… sequence.

Deformation stacking faults mean statistical appearance of the extrinsic type of superposition which creates fcc fragments (AB–CA) in hcp structure and hcp fragments (AB–AB) in fcc structure. Such kind of disorder can be described by using one parameter which defines the probability of appearance of extrinsic type of superposition.

Microdomain structure consisting of slabs having fcc and hcp structures can be defined by using two probabilistic coefficients. The first one is the probability W_1 of appearance of the first type of superposition between AB layers (W_2 is calculated as $1-W_1$). The second coefficient is conditional probability P_{11} of following the first type of superposition by the first type of superposition. P_{11} determines the average thickness of fcc slabs $\langle L_{\mathrm{fcc}} \rangle$. The ratio W_2/W_1 gives relation between the average thicknesses of hcp and fcc slabs. So the average thickness of hcp slabs $\langle L_{\mathrm{hcp}} \rangle$ can also be calculated. The average crystallite sizes within and normal to densely packed layers $\langle D_{\mathrm{xy}} \rangle$ and $\langle D_{\mathrm{z}} \rangle$ are also variable parameters of the model.

3 Results and Discussions

As it is mentioned above, Co metal requires a special approach during spectra acquisition since it possesses of different magnetic species. Thus, the approach consists in 3D spectra (intensity; frequency; power) acquisition as it is described in [30, 31]. The most appropriate spectra representation is a projection of maximal intensity points of 3D spectrum to (intensity; frequency) plane, i.e. so-called an "optimal" spectrum since it reflects "effective 90° pulse" in each point using NMR terms. Unfortunately, the representation is not quantitative because each point has its own enhancement factor η (i.e. different optimal excitation field $h_{1\mathrm{opt}}$, at which the signal is maximal); however, it gives more precise information concerning observed peaks number and their positions. To get quantitative results a correction is required, which consists in optimal spectrum multiplication by calibration curve showing $h_{1\mathrm{opt}}$ RF field frequency dependence [32]. A resulting curve presents the corrected for the enhancement factor spectrum. Figure 1a and b illustrate all said above. Indeed, the optimal spectrum in Fig. 1a shows five peaks with certain positions, however, Fig. 1b clearly exhibits only three of them and positions of fcc d.w. and hcp NPs d.w. are smoothed. The resonances obtained from Fig. 1a can be assigned as follows 211 MHz—grain boundaries or Co with loose coordination; 213 MHz—fcc Co resonance in d.w.; 214.4 MHz—hcp domain or single-domain resonance; 216.5 MHz—fcc domain or single-domain resonance; and 219 MHz—hcp Co resonance usually observed in nanoparticles [6, 22–24] can be both resonance in domains or d.w., an assignment of the line to d.w. is proven further. All peaks correspond to the majority of observable peaks in Co metal, and an observation of all the peaks in one sample is unlikely since the Co metal structure is determined by the sample origin.

Therefore, to receive a quantitative peak ratio (as it is shown in Fig. 1a) the following procedure is implemented. Optimal spectrum first is decomposed into

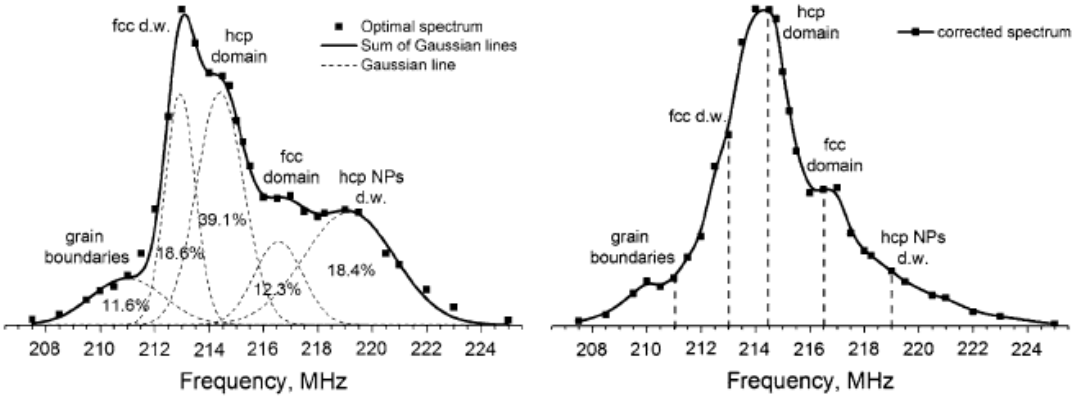

Fig. 1 a The optimal IF ^{59}Co NMR spectrum of pure metallic cobalt powder. *Squares* represent the optimal spectrum reflecting 2D distribution. A *thick solid line* corresponds to the sum of Gaussian lines, and *dash lines* to Gaussian peaks. Numbers indicate corrected relative ratio of a given peak. A representation of optimal spectrum is chosen since it does not contain correction errors reflecting observed signals effective 90° pulses intensities at each frequency. b The corrected for the enhancement factor IF ^{59}Co NMR spectrum of pure metallic cobalt powder. *Squares* represent corrected experimental points, a *thick solid line* corresponds to cubic spline of experimental points, and *dash lines* to the position of Gaussian peaks in (a)

Gaussian lines; after all Gaussian lines are multiplied by the correction line (relative distribution of h_1 optimal fields in Fig. 2) and then the ratio is calculated. The procedure is similar to the usual where optimal spectrum is multiplied by the correction curve and then it is decomposed, however, in our case the decomposition substitutes for correction.

The distribution of h_1 optimal fields also gives valuable information. As it is said above, Co metal exhibits several magnetic species and they can be determined by the response on RF pulse [30, 31]. Also the enhancement factor is inversely proportional to h_1 field, i.e. low h_1 corresponds to high enhancement factor and etc. With a help of the relative distribution of h_1 optimal fields (Fig. 2), a magnetic nature of lines in spectra can be determined. Minima corresponds to d.w. resonances and maxima to domain ones (or to single-domain particles). As well Fig. 2 points to five spectral lines stating higher optimal spectrum importance compared to the corrected one (Fig. 1a, b). The distribution in Fig. 2 helps to assign the line at 214.4 MHz to domain hcp Co line but not to d.w.e. line since the $h_{1\mathrm{opt}}$ filed is high, i.e. the enhancement factor η is low and however, low η corresponds to domain resonance scheme [14].

A quantitative analysis allows receiving hcp/fcc ratio that can be examined by XRD to make a correlation between two techniques. The hcp/fcc ratio can be extracted from NMR data by summation of fcc d.w. and fcc domain lines to get full fcc content, and hcp domain and hcp NPs lines to get full hcp content. According to IF ^{59}Co NMR data the hcp/fcc ratio is 1.9 that is smaller than XRD pattern simulation shown in Figs. 3 and 4 gives. The line of Co sfs is out of consideration during ratio calculations. However, hcp Co metal tends to faulting, and attributing sfs line as hcp Co the hcp/fcc ratio becomes 2.2 compared to 1.9. The fit inaccuracy leads to ratio dispersion, i.e. it can be within 1.6–2.2 depending on fit parameters.

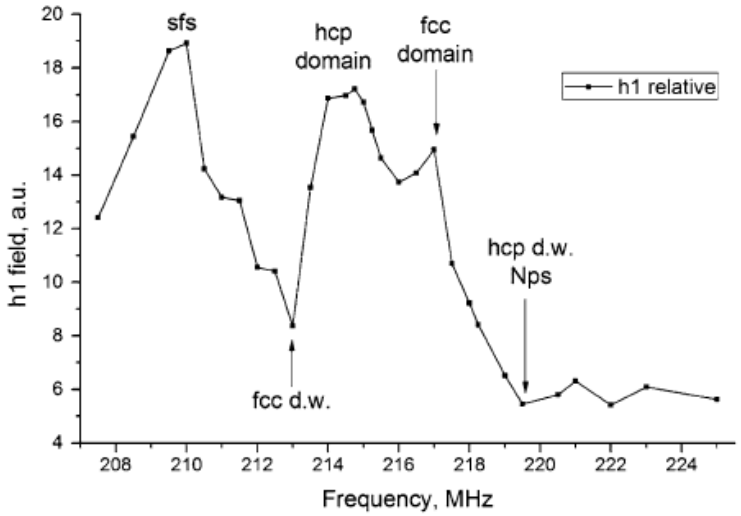

Fig. 2 Relative distribution of h_1 optimal fields. *Square* stands for experimental points and *solid line* is a connection line

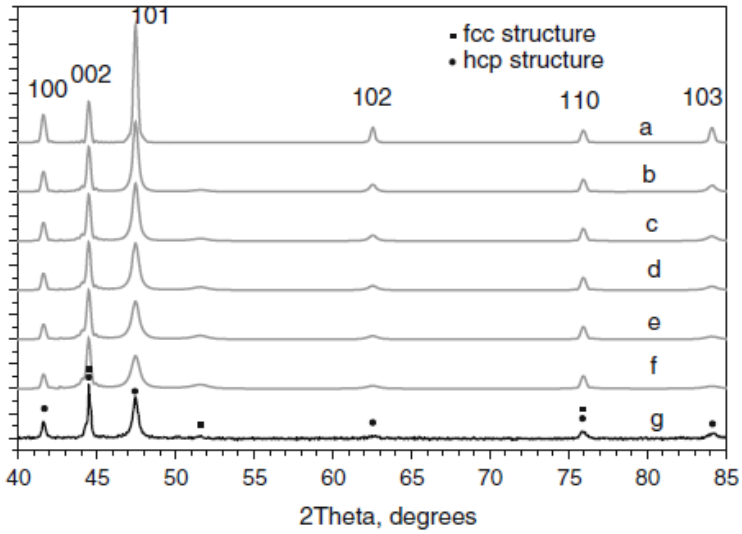

Fig. 3 XRD patterns simulated for perfect hcp structure (**a**) and lamellar domain structures with average thickness of fcc and hcp domains equal to 2 and 10 nm (**b**), 8 nm (**c**), 6 nm (**d**), 5 nm (**e**), 4 nm (**f**) respectively. Experimental XRD pattern is present in (**g**)

Thus, 1.9 is chosen as an average from NMR peaks analysis (excluding out of sfs Co line).

XRD patterns contain peaks of two cobalt modifications simultaneously (Fig. 3g). Peaks for each modification are anisotropically broadened. Similar XRD patterns have been analyzed earlier [33, 34]. They can be interpreted by two ways as a lamellar domain model and a two phase model.

The first lamellar model introduces lamellar domains having fcc structure with average thickness $\langle L_{fcc} \rangle$ equal to 2 nm into hcp matrix. The average crystallite size $\langle D \rangle$ is simulated to be equal to 30 nm. Figure 3 shows how XRD pattern changes

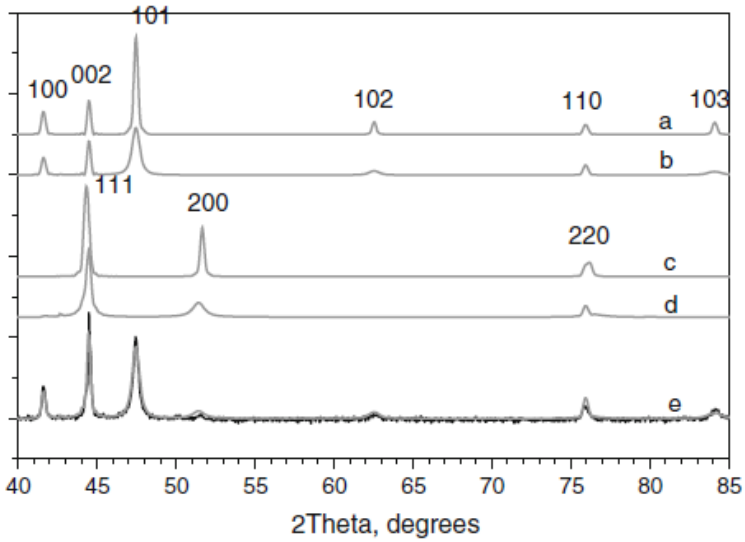

Fig. 4 XRD patterns simulated for perfect hcp structure (**a**), hcp structure containing stacking faults with probability of 0.05 (**b**), perfect fcc structure (**c**), fcc structure containing stacking faults with probability of 0.10 (**d**), two phase system combining particles with (**b**) and (**d**) structure with weight coefficients 1.45 and 0.55, respectively (e, *gray line*). Experimental XRD pattern is shown in (e, *black line*)

with average thickness decrease of hcp domains $\langle L_{hcp} \rangle$ from 30 nm (all particles have perfect hcp structure) to 4 nm. Several diffraction effects are observed such as (1) hcp 101 peak broadens; (2) 100 peak slightly falls down; (3) 002 peak slightly grows; and (4) very broad peak of diffuse scattering emerges in the range of 50–53 degrees.

It should be noticed that the lamellar domain structure where ratio $\langle L_{hcp} \rangle$ to $\langle L_{fcc} \rangle$ is equal to $\sim$2–2.5 (Fig. 1e, f) can be recognized as the most suitable model in the relation of intensities and widths of peaks on the experimental XRD pattern.

In the second two phase model, the XRD patterns simulates for particles with average size of 30 nm having perfect hcp and fcc structure represented in the Fig. 4a and c, respectively. Obviously, a perfect structure does not fit enough experimental data due to anisotropic peak broadening for both modifications in the experimental XRD pattern. For example, hcp 101, 102, 103 peaks are significantly broader than 100 and 002 peaks, and fcc 200 peak is broader than 111 one. Therefore, XRD patterns are simulated for hcp and fcc structures containing stacking faults (Fig. 4b, d). The probabilities of stacking faults are chosen to fit anisotropic broadening. The most suitable probabilities are $\sim$0.05 and 0.10 for hcp and fcc phases accordingly. To fit experimental XRD pattern, the sum of the simulated XRD patterns with suitable weight coefficients of 1.45 for hcp phase and 0.55 for fcc one is performed. The coefficients give hcp-to-fcc phase ratio equal to $\sim$2.6.

It should be noticed that sfs in hcp structure ABAB… mean an appearance of three layer fragments ABC of fcc structure. And controversially sfs in fcc structure ABCABC… mean the appearance of three layer fragments ABA of hcp structure. Taking this into account, stacking faults reduce hcp-to-fcc ratio to 2.5.

Despite of all two models give an appropriate hcp/fcc ratio similar to that of given by IF ^{59}Co NMR, the second model is more suitable in the current study. HRTEM results show that mainly hcp phase with sfs is present in the sample, thus no Co metal particles with alternating hcp-fcc lamellar are found. Unfortunately, HRTEM is not quantitative technique and it cannot provide hcp/fcc ratio.

4 Conclusion

Despite of NMR and XRD provide different types of information (NMR probes short-range environment and XRD does long-ranges order) a good agreement between two techniques is reached on quantification of Co metal powder phases due to a relatively new approach of IF ^{59}Co NMR spectra assignment. The approach consists not only in taking into account Co metal structural changes (hcp, fcc, sfs) but also the magnetic structure (domains and d.w.). The assignment is following: 211 MHz—grain boundaries or Co with loose coordination; 213 MHz—fcc Co resonance in d.w.; 214.4 MHz—hcp domain or single-domain resonance; 216.5 MHz—fcc domain or single-domain resonance; and 219 MHz—hcp Co resonance usually observed in nanoparticles can be both resonance in domains or d.w. All this leads to hcp/fcc ratio 1.9 by IF ^{59}Co NMR. The value does not include Co sfs line in 211 MHz, however, its attribution to hcp phase since HRTEM data indicate only to hcp Co metal particles with sfs changes the hcp/fcc ratio to 2.2 that is very close to 2.5 by XRD. HRTEM data also helps choosing two phase model XRD pattern simulation model due to absence of alternating hcp-fcc lamellar in Co metal particles. Finally, h_1 optimal field distribution also gives valuable information facilitating spectral line assignment in IF ^{59}Co NMR spectra, since it helps attributing the species to magnetic domain or d.w. The techniques show a good agreement within experimental errors.

Acknowledgments The authors thank Prof. V.I. Zaikovskii for provided HRTEM study. Also the authors thank for partial financial support grant RFBR # 14-03-31684 mol_a, # 13-03-00482 a, and # 15-53-15035, President Program of PhD students scholarships SP-389.2012.1, and the Ministry of Education and Science of the Russian Federation. Also A.S. Andreev thanks French Embassy (a scholarship within the joint postgraduate study).

References

1. L.E. Toth, S.F. Ravitz, J. Phys. Chem. Solids **24**, 1203 (1963)
2. L.E. Toth, G.F. Day, R.C. La Force, S.F. Ravitz, Acta Metall. **12**, 311 (1964)
3. L.E. Toth, T.R. Cass, S.F. Ravitz, J. Washburn, Philos. Mag. **9**, 607 (1964)
4. J. Sort, S. Surinach, J.S. Munoz, M.D. Baro, M. Wójcik, E. Jędrica, S. Nadolski, N. Sheludko, J. Nogues, Phys. Rev. B **68**, 14421 (2003)
5. D.C. Creagh, S.G. Bailey, G.V.H. Wilson, Philos. Mag. **32**, 405 (1975)
6. V.V. Matveev, D.A. Baranov, G.Y. Yurkov, N.G. Akatiev, I.P. Dotsenko, S.P. Gubin, Chem. Phys. Lett. **422**, 402 (2006)
7. A.C. Gossard, A.M. Portis, Phys. Rev. Lett. **3**, 164 (1959)
8. C.R. Houska, B.L. Averbach, M. Cohen, Acta Metall. **8**, 81 (1960)
9. T.R. Anantharaman, J.W. Christian, Acta Crystallogr. **9**, 479 (1956)

10. G.B. Mitra, N.C. Hadler, Acta Crystallogr. **17**, 817 (1964)
11. E.A. Turov, Am. J. Phys. **41**, 935 (1973)
12. A.M. Portis, R.H. Lindquist, in *Magnetium*, ed. by G.T. Rado, H. Suhl. Nuclear Resonance in Ferromagnetic Materials, Chap. 6, vol IIA (Academic Press Inc., New York, 1965)
13. A.P. Guimarães, *Magnetism and Magnetic Resonance in Solids* (Wiley, Chichester, 1998), p. 298
14. A.M. Portis, A.C. Gossard, J. Appl. Phys. **31**, S205 (1960)
15. A.C. Gossard, A.M. Portis, M. Rubinstein, R.H. Lindquist, Phys. Rev. **138**, A1415 (1965)
16. M. Kawakami, T. Hihara, Y. Koi, J. Phys. Soc. Jpn. **33**, 1591 (1972)
17. S.G. Bailey, D.C. Creagh, G.V.H. Wilson, Phys. Lett. A **44**, 229 (1973)
18. H. Enokiya, J. Phys. Soc. Jpn. **42**, 796 (1977)
19. D. Fekete, H. Boasson, A. Grayevski, V. Zevin, N. Kaplan, Phys. Rev. B **17**, 347 (1978)
20. C. Searle, H. Kunkel, S. Kupca, I. Maartense, Phys. Rev. B **15**, 3305 (1977)
21. H.P. Kunkel, C.W. Searle, Phys. Rev. B **23**, 65 (1981)
22. A.S. Andreev, O.B. Lapina, J.-B. d'Espinose de Lacaillerie, A.A. Khassin, J. Struct. Chem. **54**, S102 (2013)
23. E. Jędryka, M. Wójcik, S. Nadolski, H. Pattyn, J. Verheyden, J. Dekoster, A. Vantomme, J. Appl. Phys. **95**, 2770 (2004)
24. W. Hines, J. Budnick, D. Perry, S. Majetich, R. Booth, M. Sachan, Phys. Status Solidi **B248**, 741 (2011)
25. A.A. Sidorenko, C. Pernechele, P. Lupo, M. Ghidini, M. Solzi, R. De Renzi, I. Bergenti, P. Graziosi, V. Dediu, L. Hueso, A.T. Hindmarch, Appl. Phys. Lett. **97**, 162503 (2010)
26. W.A. Hardy, J. Appl. Phys. **32**, S122 (1961)
27. A.S. Andreev, S.F. Tikhov, A.N. Salanov, S.V. Cherepanova, O.B. Lapina, V.A. Bolotov, Y.Y. Tanashev, J.-B. d'Espinose de Lacaillerie, and V.A. Sadykov. Adv. Mater. Res. **702**, 79 (2013)
28. W. Kraus, G. Nolze, J. Appl. Crystallogr. **29**, 301 (1996)
29. S. Cherepanova, S. Tsybulya, Eur. Powder Diffr. Epdic **8**(443–4), 87 (2004)
30. M. Malinowska, M. Wójcik, S. Nadolski, E. Jędryka, C. Mény, P. Panissod, M. Knobel, A.D.C. Viegas, J.E. Schmidt, J. Magn. Magn. Mater. **198–199**, 599 (1999)
31. P. Panissod, J.P. Jay, C. Mény, M. Wójcik, E. Jędryka, Hyperfine Interact. **97–98**, 75 (1996)
32. P. Panissod, C. Mény, Appl. Magn. Reson. **19**, 447 (2000)
33. S.V. Cherepanova, S.V. Tsybulya, Mater. Sci. Forum **443–444**, 87 (2004)
34. S.V. Cherepanova, J. Struct. Chem. **53**, 109 (2013)

4.2.2. Physics of Co nanoparticles

In this chapter, the physical properties and temperature stability of fine Co metal nanoparticles is given. The content of these chapter is published in *Physical Chemistry Chemical Physics* [2].

PCCP

PAPER

View Article Online
View Journal | View Issue

CrossMark click for updates

Cite this: *Phys. Chem. Chem. Phys.*, 2015, 17, 14598

Thermal stability and hcp–fcc allotropic transformation in supported Co metal catalysts probed near operando by ferromagnetic NMR†

Andrey S. Andreev,[abc] Jean-Baptiste d'Espinose de Lacaillerie,*[c] Olga B. Lapina[ab] and Alexander Gerashenko[d]

Despite the fact that cobalt based catalysts are used at the industrial scale for Fischer–Tropsch synthesis, it is not yet clear which cobalt metallic phase is actually at work under operando conditions and what is its state of dispersion. As it turns out, the different phases of metallic cobalt, fcc and hcp, give rise to distinct ferromagnetic nuclear magnetic resonance. Furthermore, within one Co metal particle, the occurrence of several ferromagnetic domains of limited sizes can be evidenced by the specific resonance of Co in multi-domain particles. Consequently, by ferromagnetic NMR, one can follow quantitatively the sintering and phase transitions of dispersed Co metal particles in supported catalysts under near operando conditions. The minimal size probed by ferromagnetic Co NMR is not precisely known but is considered to be in the order of 10 nm for supported Co particles at room temperature and increases to about 35 nm at 850 K. Here, in Co metal Fischer–Tropsch synthesis catalysts supported on β-SiC, the resonances of the fcc multi-domain, fcc single-domain and hcp Co were clearly distinguished. A careful rationalization of their frequency and width dependence on temperature allowed a quantitative analysis of the spectra in the temperature range of interest, thus reflecting the state of the catalysts under near operando conditions that is without the uncertainty associated with prior quenching. The allotropic transition temperature was found to start at 600–650 K, which is about 50 K below the bulk transition temperature. The phase transition was fully reversible and a significant part of the hcp phase was found to be stable up to 850 K. This anomalous behavior that was observed without quenching might prove to be crucial to understand and model active species not only in catalysts but also in battery materials.

Received 16th November 2014,
Accepted 30th April 2015

DOI: 10.1039/c4cp05327c

www.rsc.org/pccp

Introduction

Today, Fischer–Tropsch synthesis (FTS) on cobalt is used in many countries as a key process for gas-to-liquids (GTL) technology.[1–3] The most recent developments focus on biomass conversion to produce lower olefins (C_2–C_6).[4–6] The current state of knowledge has been reviewed[7,8] and it is still not totally clear what Co phases are at play in the catalyst. The metallic phase is usually supported on oxides but composites and SiC are promising alternatives due to their higher thermal conductivity.[9–12] Unfortunately, the structural characterization of the Co FTS catalysts is usually performed at ambient or low temperature, mostly by XRD and TEM, and it is not certain that this provides an accurate description of the state of the catalyst under actual reaction temperature conditions. Recently, Co FTS catalysts have been characterized by ^{59}Co nuclear magnetic resonance (NMR)[13–15] but this technique was performed at temperatures differing from the operating ones.

In a broader context than catalysis, the phase diagram of bulk Co metal is well known. In particular, the transition from hcp to fcc stacking has been studied in detail through various techniques[16–19] including ^{59}Co NMR in the absence of an applied external magnetic field.[20,21] This method takes advantage of the fact that Co metal is ferromagnetic in a wide range of temperatures and particle sizes thus allowing the recording of the NMR signal of the sample in its internal field.[22] The magnetic behaviour related to the hcp to fcc phase transition has been investigated by NMR in the bulk,[20] as well as in micron size powders after heating and quenching.[21] However, nanosize Co metal particles have never been studied above room temperature by NMR. At first sight, this might be surprising since in principle NMR is much more

[a] *Novosibirsk State University (NSU), Pirogova str. 2, Novosibirsk, 630090, Russia*
[b] *Solid-State NMR group, Boreskov Institute of Catalysis SB RAS (BIC SB RAS), Pr. Lavrentieva 5, Novosibirsk, 630090, Russia*
[c] *Soft Matter Sciences and Engineering (SIMM), UMR CNRS 7615, PSL Research University, ESPCI ParisTech, 10 Rue Vauquelin, Paris, 75005, France. E-mail: jean-baptiste.despinose@espci.fr*
[d] *Kinetic Phenomena Laboratory, Institute of Metals Physics UB RAS, S. Kovalevskoy str. 18, Ekaterinburg, 620041, Russia*
† Electronic supplementary information (ESI) available. See DOI: 10.1039/c4cp05327c

efficient for phase determination than XRD for small crystal sizes, but actually the complex temperature dependence of the ferromagnetic NMR signal renders quantitative phase analysis intricate. In the bulk, below ~693 K, the stable phase for Co metal is hcp but for nanosize Co metal particles both fcc and hcp Co metal stacking are observed even at ambient and low temperatures.[23–27] Kitakami *et al.*[28] have considered this anomaly by studying various Co polyhedra synthesized by sputtering and comparing the results to free energy minimization predictions. They observed a close relationship between the particle size and the crystal phase at room temperature. Pure fcc is found to be the dominant phase for particles less than 20 nm in diameter, for ~30 nm particles a mixture of both hcp and fcc phases are present, while particles over 40 nm crystallize as hcp with inclusion of a very small amount of fcc. The *in situ* phase identification of dispersed nanosize Co systems has some importance as the crystal phase of the particles is expected to affect important properties such as catalytic activity[2,4] or battery charge cycles.[29,30] Concerning supported catalysts, only several early attempts have been made by ^{59}Co NMR in such catalysts,[13–15] although renewed interest has occurred recently.[9,11,31,32] In fact, the majority of the ^{59}Co NMR studies to date have been performed at low temperatures (4.2 K), and only few results are reported at room temperatures. The choice of operating at a low temperature is logical as it gives a high enhancement of the NMR signal and opens in particular the possibility to studying superparamagnetic cobalt particles[33] when applying a weak external magnetic field. Nevertheless, cobalt nanoparticles are used most of the time at, or well above, room temperature. For example, the Fischer–Tropsch synthesis takes place at 473–513 K for the so-called low temperature processes and 573–623 K for the high temperature ones,[1] and there is a need to bridge the experimental gap between measurements performed at high, ambient and low temperatures. Consequently, the present study is an *in situ* examination by ferromagnetic ^{59}Co NMR of the temperature stability and the hcp–fcc allotropic transition in supported Co metal nanoparticles.

Experimental

A sample of Co metal supported on β-SiC (15 wt% of Co) was prepared by a conventional Co nitrate impregnation technique followed by calcination under air at 623 K for 4 hours. Subsequently, the sample was reduced under an H_2 flow in a U-shape glass reactor. 0.5 g of the sample was sealed on-line to prevent Co metal oxidation in 5 mm outer diameter tubes. A residual Ar pressure of 70 Torr was maintained in the ampoule to maintain heat conductance. The sealed tube was then cooled down and transferred into the solenoid of a commercial special design Bruker broadband static high-temperature 5 mm probe. The temperature was raised "*in situ*" to the one of interest for the NMR measurement by means of a heater, which surrounded the acquisition coil. A ceramic protection covered the heating part and the coil. The term "*in situ*" indicated that the heating was performed inside the NMR probe and that all spectra were acquired at high temperature, and not at room temperature after quenching in liquid nitrogen as was previously done by Speight *et al.*[21] In that sense, the NMR signal was acquired *in situ* with respect to the hcp–fcc phase transition and near operando with respect to the catalyst activation procedure. All ferromagnetic NMR experiments were carried out using a Bruker Avance III 500 MHz console but the experiments were performed outside of the magnet, thus without application of any external magnetic field. Note that all measurements took place on a single sample and using the same detection coil at a fixed amplifier output power, thus insuring that the intensity of the radiofrequency (rf) field was constant. In this manner, the intensities of all the spectra could be compared meaningfully. The spectra were obtained by summing Fourier transformed spin echoes acquired with 500 kHz carrier frequency steps as described elsewhere.[34] Such large steps can be used because the quality factor of the rf circuit is considerably degraded by the presence of the magnetic sample thus making the circuit less frequency selective and providing a bandwidth of ~2 MHz. Two equal RF pulses (~40 W at the output of the amplifier) of 0.3 μs duration with an interpulse delay of 7 μs were implemented to generate each spin-echo. The sequence repetition rate was 300 Hz, and the number of transients was varied from 1000 to 30 000 depending on the signal intensity. Frequency tuning was insured by means of a home-made autotune device developed by one of us in Ekaterinburg. It is based on two step motors and a controller using the wobble curve exported from the Bruker Topspin software as an input. The peak positions, intensities and width were obtained by decomposition into Gaussian lineshapes. No corrections for the enhancement factors were performed due to experimental limitations. Accurate measurements of correction factors would have required additional power variations (at least 5 values), thus increasing the total measurement time to about 60 hours in the present case. Unfortunately the probe could not sustain such a long continuous high temperature heating without damage. Not using correction factors was not an issue though as only relative variations from one temperature to the next was considered in the present study. Nevertheless, the enhancement factor was measured at room-temperature. Accordingly, it was estimated that the intensities reported here without corrections overestimated the fcc multi-domain resonances by a factor of 2. The basics of ferromagnetic NMR theory are summarized in the ESI.† Likewise, the supporting characterization of the sample by powder XRD and HRTEM can be found in the ESI.†

It must be understood that since the experiments were carried out at high temperatures, not all Co metal particles were NMR visible. The blocking temperature of the ferromagnetic domains depends on the size of the particles and, below a critical size, at a given temperature, the particles are superparamagnetic and thus invisible by NMR. The actual value of the critical size is not fully known and depends on the particle shape. The critical size at room temperature for Co particles has been reported to be above 23 nm.[32] However, in a recent PhD thesis[35] it was shown experimentally that 10 nm size particles were visible by internal field ^{59}Co NMR at room temperature. Furthermore, using the calculations of Liu *et al.*,[32] a critical size of ~34 nm at 850 K can be estimated. It can thus be concluded that in the temperature range of the present study, the critical size below which the particles

become NMR invisible varies from about 10 to 35 nm going from room temperature to 850 K. These values can be considered as conservative.

Results and discussion

Identification of the resonances of the hcp and fcc phases

The temperature study by ferromagnetic NMR of nanosize Co metal clusters supported on β-SiC is presented in Fig. 1. First of all, as expected, the spectra shifted globally to lower frequency with the temperature increase due to the reduction of the electronic magnetization M (see discussion on the ferromagnetic signal and its temperature dependence in the ESI†). Nevertheless, the spectra contained all the same features, namely three resonances attributed to fcc multi-domain particles, fcc single-domain particles and hcp Co, in agreement with the literature data.[36–41] The lower frequency resonance is ascribed to the signal from fcc multi-domains (m.d.) and the middle one to fcc single-domain (s.d.) particles.

The frequency shift between the multi-domain and the single-domain fcc arises from the contribution of the demagnetization field to the local field in single-domain particles. As the depolarization tensor depends on the shape of the single-domain particles, which is distributed, the resonance of the single-domain particles is expected to be broader than the one from the multi-domains. This was indeed the case.

The large high frequency line at highest frequency was attributed to the hcp phase. In contrast to what was observed here, in large (~10 μm) hcp monocrystals the spectrum is dominated by two well-resolved resonance lines that correspond to nuclei at the edge (214 MHz) and at the center of domain walls (221 MHz). Both types of environments correspond to a magnetic field perpendicular to the c crystallographic axis at room temperature and the corresponding nuclei exhibit a significant rf enhancement factor of the domain walls η_w.[20,42–46] As a result, the resonance of the hcp domains is not visible as it is dominated by the contributions from the domain walls. However here, where the crystals were of nanometer sizes, the reduction of the crystal sizes and magnetic domains resulted in a considerable reduction of the enhancement factor of the domain walls η_w as explained by Portis and Gossard in their seminal work on nuclear resonances in ferromagnetic cobalt.[36] Consequently, in the part of the spectra arising from the hcp nanocrystals, the values of η_w and η_d (enhancement factor of the domains) became comparable and the contribution to the signal from the magnetic domain E_T^d became significant compared to the one of the domain walls E_T^w (eqn (S4) and (S5), ESI†). This contribution from the hcp domains was very broad due to the well-known large local field anisotropy in hcp crystals equal to 7 kOe.[20] Another reason for the breadth of this line was that, as for the fcc single-domains, variations of hcp particle shapes result in an additional distribution of resonance frequencies. This point was supported by the fact that T_2 was measured to be within the range 10–20 μs, values that could not account for a FWHM of more than 1 MHz. The broadening was thus inhomogeneous, that is resulting from the local field dispersion.

Temperature dependence of the spectral characteristics: frequency, intensity and width

The resonances of the fcc cobalt in multi-domains, of the fcc cobalt single-domains, and of the hcp cobalt being identified, it was possible to study their respective temperature dependence. Indeed, in order to analyse the phase transformation in a quantitative manner, it is first necessary to take into account the temperature dependence of ferromagnetic NMR experimental parameters such as the resonance frequency, the echo intensities and their widths. As discussed in the ESI,† these experimental parameters depended on the nuclear equilibrium magnetization, on the hyperfine field (proportional to the equilibrium electronic magnetization), either directly or through the enhancement factors η_w and η_d, and on the relaxation rates. Fig. 2 shows the temperature dependence of the resonance frequency of all species presented in the spectra of Fig. 1.

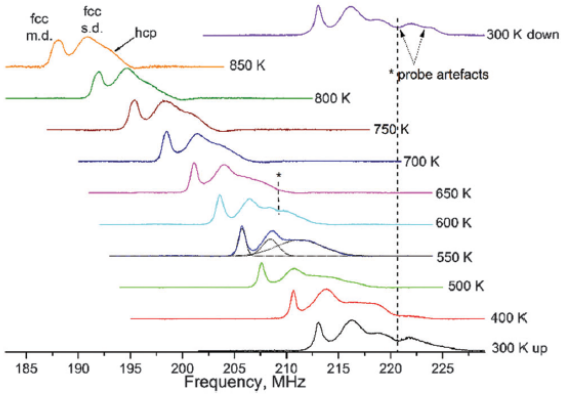

Fig. 1 Ferromagnetic ^{59}Co NMR spectra at variable temperatures in supported metal cobalt nanoparticles. Intensities are normalized to their maxima.

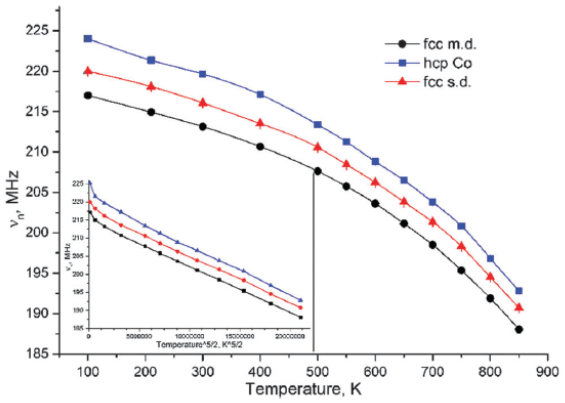

Fig. 2 Temperature dependence of the ferromagnetic NMR frequencies of the different Co species obtained by decomposition of Fig. 1. Blue squares correspond to hcp Co, red triangles – to fcc single-domain (s.d.) Co, and black circles to fcc multi-domain (m.d.) Co.

In the expression of the ferromagnetic NMR frequency in eqn (S3) (ESI†), the only term expected to depend on temperature is the equilibrium electronic magnetization M.

$$\Omega_n = 2\pi\nu_n(T) \propto M(T)$$

Since all measurements were performed well below the Curie temperature of cobalt ($\sim$1400 K), the temperature evolution of this magnetization can be predicted safely by spin-waves theory. Keeping the first two terms of the expansion, one can write

$$\frac{\nu_n(0) - \nu_n(T)}{\nu_n(0)} = \frac{M(0) - M(T)}{M(0)} = \alpha T^{3/2} + \beta T^{5/2} \qquad (1)$$

As seen from the inset in Fig. 2, the deviation from the Bloch 3/2 law is small but led to measurable values of the β parameter that can be associated with the need for a more accurate energy expression in spin-waves theory or with spin waves interaction,[22] *i.e.* in our case the interparticle interaction. The values obtained for the fitting parameters α and β are reported in Table 1. The α and β parameters for the resonances from the fcc multi-domains and fcc single domains coincided within experimental errors. This was predictable as single and multi domain particles differ only by the dipolar demagnetization field.

The difference between the single domain and multi-domain resonances corresponds to the demagnetization field. Here, the 2.8 MHz for the fcc particles led to an estimate of 2.8 kOe for the dipolar field. For a spherical particle, the dipolar field is related to the saturation magnetization M_s at 0 K through

$$H_{di} = -4\pi/3M_s$$

Leading to a saturation magnetization of 1.2 kG, a value very close to what is observed in bulk fcc Co.[47]

The frequency temperature dependence observed in the present work is compared with results of the literature in Fig. 3 and 4. From Fig. 3, it can be seen that concerning fcc single domains, the present results differed significantly from the only previous report we could find which corresponded to an α value of $(4.87 \pm 0.2) \times 10^{-6}$ K$^{-3/2}$ and an extrapolation to 0 K at 222.2 MHz instead of 220 MHz.[39] It is plausible though that the results obtained in the present study were of better quality due to experimental progress, the earlier work being performed with a continuous wave spectrometer. Under such conditions, the broad line of fcc domain Co contains a mixture of absorption and dispersion signals preventing a precise determination of the line position.

On the other hand, the temperature evolution of the fcc multi-domain resonance was in agreement with all previously published studies[20,39,43] up to 400 K (see Fig. 4). It was noticeable though that the high-temperature part (up from 400 K) of the temperature frequency dependence differed significantly from the ones previously observed on larger particles. At these temperatures, the evolution is dominated by the β parameter. It thus appeared that this parameter is more affected than α by the modification of the electronic structure due to particle size reduction. Finally, concerning the hcp resonance, the present work is to our knowledge the first one in nano-sized samples. Despite the fact that in bulk hcp Co several ferromagnetic NMR temperature studies were done,[20,43,44] in nanosize hcp Co the ferromagnetic NMR spectrum has been already reported several times[23,26,33,40] but never its temperature dependence which is crucial for catalytic studies.

The spectra of Fig. 1 are represented with normalized intensities and thus the intensity drop with temperature was not pictured.

Table 1 Parameter extracted from the fit of dependencies shown in Fig. 2 for each observed line

Parameter	fcc multi domain	fcc single domain	hcp
ν_0, MHz	217.2 (fixed)	220.0 ± 0.3	223 ± 0.3
α, K$^{-3/2}$	$(1.9 \pm 0.2) \times 10^{-6}$	$(1.8 \pm 0.2) \times 10^{-6}$	$(1.4 \pm 0.3) \times 10^{-6}$
β, K$^{-5/2}$	$(4.0 \pm 0.2) \times 10^{-9}$	$(4.1 \pm 0.2) \times 10^{-9}$	$(4.7 \pm 0.3) \times 10^{-9}$

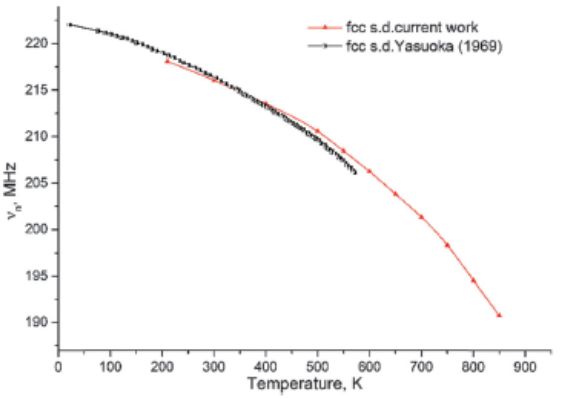

Fig. 3 Comparison with previous studies on the magnetization temperature dependencies for fcc single domains (s.d.). Red triangles correspond to the fcc s.d. line in the present work and semi-filled squares to data from Yasuoka *et al.*[39]

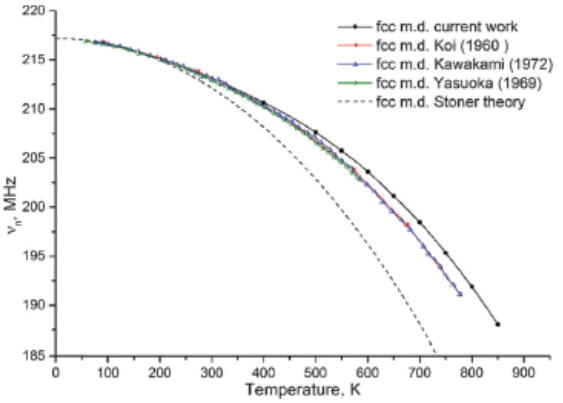

Fig. 4 Comparison with previous studies on magnetization temperature dependencies for fcc multi-domain (d.w.) reported in different studies. Black circles correspond to the fcc m.d. line in the current work, semi-filled red squares to the work of Koi *et al.*,[43] semi-filled blue triangles to Kawakami *et al.*,[20] semi-filled stars to Yasuoka *et al.*[39] and the dash lined to Stoner's theory.[48]

The evolution of the absolute integrated intensities of each contribution to the spectra is plotted with respect to temperature in Fig. 5. A drop of the overall intensity with temperature was observed.

The intensities of the Co resonances expressed in eqn (S4) and (S5) (ESI†) are impacted in different ways by the temperature: transverse relaxation (T_2^*), nuclear equilibrium magnetization (m) and enhancement factor (η_d), all vary with temperature in different ways but all such as to contribute to a decrease of the signal. The rate of relaxation can show complex variations with temperature reflecting the dependency of the various relaxation paths involved in the strongly coupled spin systems present in magnetically ordered materials,[49] but, in any case, the rate of relaxation is expected to increase with temperatures and as a consequence, at fixed echo time Δ, this contributed to the decrease of the echo intensity. Also, at high temperature, namely above 600 K, the echo intensity can be further reduced by superparamagnetic relaxation due to increased reorientation of the magnetization.[24] As far as the nuclear equilibrium magnetization m is concerned, it is expected to decrease as $1/T$. Finally, since the enhancement factors of both the domain and the domain wall scaled with the hyperfine field, itself approximated by $B_{hf} = \lambda_m m$ (where λ_m is the molecular field approximation parameter) a further intensity decrease was expected for all lines (see ESI†).

Not only the resonance frequencies and echo intensities evolved with temperature but also their width, expressed as their full width at half maximum (FWHM) as shown in Fig. 6. The most drastic changes occurred for the hcp Co resonance. Within a temperature region of 400–750 K the FWHM was progressively cut in half. Therefore, this meant that the distribution of magnetic fields mainly responsible for FWHM in hcp Co (as discussed above) decreased drastically within this temperature range. Remarkably, hcp Co is known to have a magnetic transformation starting from ~513 K, at which another type of hcp domains appears, and a gradual change of the easy axis direction of hcp Co occurs.[50] A further decrease could be attributed to the start of hcp–fcc Co metal allotropic phase transition as will be discussed below.

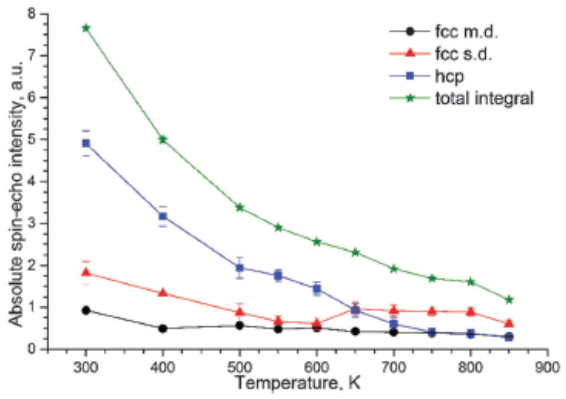

Fig. 5 Absolute integrated intensities temperature dependence. The blue squares correspond to hcp Co stacking, the red triangles to fcc single domain species, the black circles to fcc multi-domain (m.d.) resonance and the green stars to the sum of individual intensities.

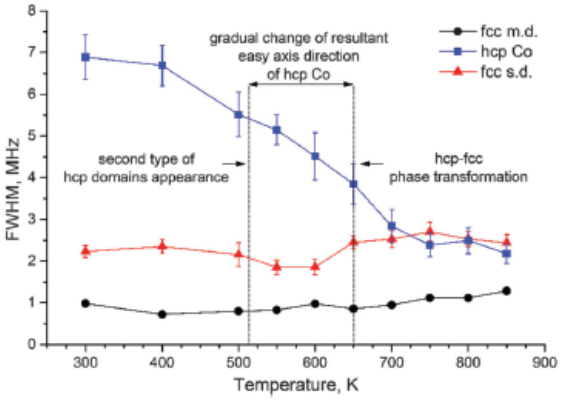

Fig. 6 FWHM dependence on temperature. Blue squares correspond to hcp Co stacking, red triangles to fcc single domain species and black circles to fcc m.d. resonance.

Allotropic hcp to fcc phase transformation in nanoparticles

The ultimate goal of this study was to evaluate the potential of ferromagnetic ^{59}Co NMR to study the hcp/fcc transformation in nanoparticles. If the nuclear (m) and electronic (M) equilibrium magnetization variations with temperature are expected to affect similarly the spin echo intensities of different phases, domains and walls, the same cannot be said *a priori* concerning the enhancement factors (η) and the transverse decay rates (T_2^*). Consequently, a quantitative analysis of the phase evolution with temperature cannot be performed directly without precaution from the relative line intensities represented in Fig. 5. In particular, it must be understood that the contribution of the smallest particles disappears progressively from the signal as they become superparamagnetic when the temperature rises. However, the relative contributions of all resonances varied little up to about 600 K (Fig. 7). This was a strong indication that no structural changes occurred below 600 K. Going back to Fig. 5, the temperature evolution of the intensity of the fcc s.d. resonance changed between 600 and 650 K: the smooth decrease was interrupted, and a small increase could be observed. As explained above, for a given amount of spins in particles of constant sizes, the echo intensity can only decrease with temperature. An increase can thus in all confidence only be attributed to a phase transition. Since the temperature changes in the spectra were fully reversible (Fig. 1) and since no sintering was observed by high resolution TEM (not shown), it was thus concluded that the amount of nuclei in fcc s.d. increased, that is that a phase transition from hcp to fcc started to occur at this temperature. This is further illustrated in Fig. 7 where the fcc to hcp ratio of the corresponding ferromagnetic ^{59}Co NMR resonances is plotted. Again, as no corrections for relaxation and enhancement factors were performed, this ratio is not quantitative. However, the occurrence of the gradual phase transformation starting at 600–650 K

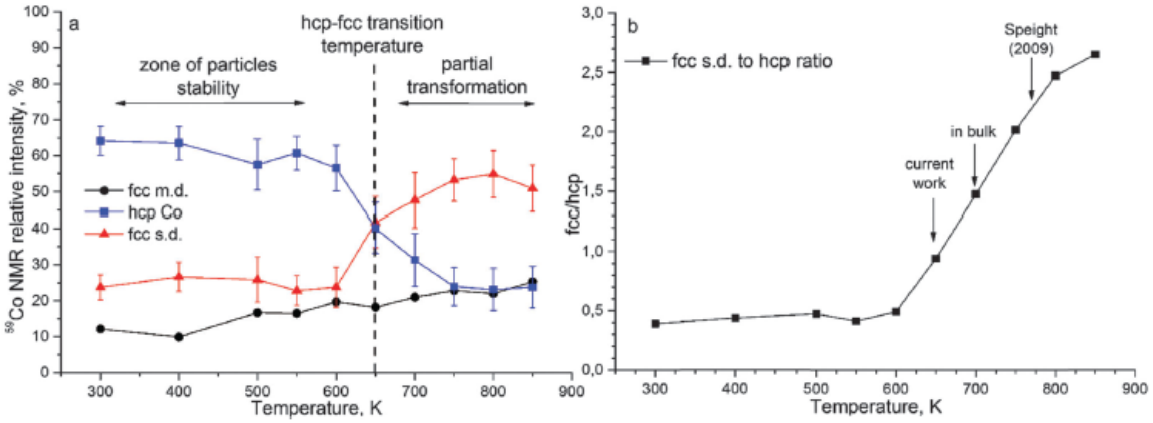

Fig. 7 (a) Plot *versus* temperature of the relative integrated intensities obtained by decomposition of the lines of Fig. 1. Blue squares correspond to the relative contribution of hcp Co, red triangles to fcc single-domain Co and black circles to fcc d.w. Co. The error could not be estimated for the fcc d.w. because the shape of the corresponding line is not Gaussian especially for temperatures below 650 K. (b) Fcc/hcp ratio plotted *versus* temperature. The ratio was calculated by dividing the fcc domain line by the hcp Co line since only these two lines participate in the transformation (the fcc m.d. relative contribution remained roughly constant).

was clearly evidenced. A phase transition temperature of 773 ± 25 K has been reported by ferromagnetic NMR in micron size Co particles but it relied on a different assignment of the resonance lines.[21] Furthermore, Co is well known to have a phase transition from hcp to fcc at ~693 K in bulk Co. The main result of the present study is thus that supported nanosize Co metal particles have a lower phase transition temperature (600–650 K) than bulk or micron size cobalt metal (700–750 K). Complementarily, according to Fig. 7, at 850 K, about 20% of the NMR intensity was still due to nuclei in hcp. Thus, despite the fact that the phase transformation had started at 600 K, there was still no full hcp to fcc Co conversion at 850 K. According to previous studies,[20] the hcp phase fully disappears at ~700 K in bulk cobalt. However, Kitakami *et al.* established theoretically that small fcc crystals can remain stable at room temperature.[28] Reversing the arguments, the stability of small hcp crystals at high temperatures can be expected.

Interestingly, the fcc multi-domain resonance intensity was basically unaffected by temperature. This might mean that particles larger than the critical size of Co metal single-domain particles, namely ~50–70 nm,[24,51] were more stable with respect to the allotropic hcp–fcc phase transition with temperature. This interpretation remains debatable though as the intensity of larger particles might simply be related to a higher superparamagnetic transition temperature.

Conclusions

The present study shows by ferromagnetic ^{59}Co NMR the temperature behaviour of Co metal nanoparticles supported on β-SiC. The resonances of the fcc m.d. particles, fcc single-domain particles and hcp Co particles were clearly distinguishable. The allotropic transition was found to start in the 600–650 K temperature range, that is 50 K less than in the bulk and approximately 100 K lower than in Co metal powders according to Speight *et al.*[21] A significant part of the sample remained in the hcp phase at the highest temperature considered (850 K). The hcp–fcc transformation appeared fully reversible in the 300–850 K temperature range.

Beyond these qualitative observations, a quantitative analysis requires a full description of the resonance behaviour with temperature. While the temperature–frequency dependence of all species could be well fitted by the two first terms of spin-waves theory, prediction of the dependence of the intensity on temperature was not possible at this stage, as the enhancement factor dependence on temperature is not known from a theoretical perspective. Quantitative analysis would have required a systematic empirical examination of the dependence of the spectrum intensity with the applied rf power, and this at all temperatures. This added complication resulted from the fact that the present study dealt with the ferromagnetic NMR spectra of cobalt nanoparticles *in situ*, contrarily to the study of Speight *et al.*[21] where the samples were quenched to room temperature before measurements. Indeed, our observation of particle stability up to 600 K is relevant to many experimental situations, including but not restricted to the FTS catalytic processes.[9,11,27,32] Our description of the Co particles stability in temperatures near operando, up to 600 K, might prove useful to understand and model active species in other catalytic or battery materials where the active species are above the superparamagnetic critical size.

Finally, the anomalous stability of some hcp domains up to 850 K (the maximal temperature implemented in the present study) had never been reported before.

Acknowledgements

The authors thank Prof. V. I. Zaikovskii and PhD S. V. Cherepanova for providing HRTEM and XRD results. Anonymous reviewers must also be thanked for constructive comments. The sample

preparation and treatment is supported by RAS project V.44.1.17. The NMR study is made possible by grant RFBR # 14-03-31684. Also A. S. Andreev acknowledges a doctoral grant from the French Embassy in Moscow and Zamaraev fund for a travel grant.

Notes and references

1 A. Y. Khodakov, W. Chu and P. Fongarland, *Chem. Rev.*, 2007, **107**, 1692–1744.
2 M. Tijmensen, *Biomass Bioenergy*, 2002, 23, 129–152.
3 M. M. Wright, R. C. Brown and A. A. Boateng, *Biofuels, Bioprod. Biorefin.*, 2008, 2, 229–238.
4 H. M. Torres Galvis and K. P. de Jong, *ACS Catal.*, 2013, 3, 2130–2149.
5 B. Buragohain, P. Mahanta and V. S. Moholkar, *Energy*, 2010, 35, 2557–2579.
6 T. V. Malleswara Rao, X. Dupain and M. Makkee, *Microporous Mesoporous Mater.*, 2012, **164**, 148–163.
7 N. E. Tsakoumis, M. Rønning, Ø. Borg, E. Rytter and A. Holmen, *Catal. Today*, 2010, **154**, 162–182.
8 A. Jean-Marie, A. Griboval-Constant, A. Y. Khodakov and F. Diehl, *C. R. Chim.*, 2009, **12**, 660–667.
9 B. de Tymowski, Y. Liu, C. Mény, C. Lefèvre, D. Begin, P. Nguyen, C. Pham, D. Edouard, F. Luck and C. Pham-Huu, *Appl. Catal., A*, 2012, **419–420**, 31–40.
10 B. Lee, H. M. Koo, M.-J. Park, B. Lim, D. J. Moon, K. J. Yoon and J. W. Bae, *Catal. Lett.*, 2012, **143**, 18–22.
11 Y. Liu, B. de Tymowski, F. Vigneron, I. Florea, O. Ersen, C. Mény, P. Nguyen, C. Pham, F. Luck and C. Pham-Huu, *ACS Catal.*, 2013, 3, 393–404.
12 A. R. de la Osa, A. de Lucas, L. Sánchez-Silva, J. Díaz-Maroto, J. L. Valverde and P. Sánchez, *Fuel*, 2012, **95**, 587–598.
13 A. N. Murty, A. A. Williams, R. T. Obermyer and V. U. S. Rao, *J. Appl. Phys.*, 1987, **61**, 4361–4363.
14 A. N. Murty, M. Seamster, A. N. Thorpe, R. T. Obermyer and V. U. S. Rao, *J. Appl. Phys.*, 1990, **67**, 5847–5849.
15 M. J. Ledoux, O. Michaux, G. Agostini and P. Panissod, *J. Catal.*, 1985, **96**, 189–201.
16 P. Tolédano, G. Krexner, M. Prem, H.-P. Weber and V. Dmitriev, *Phys. Rev. B: Condens. Matter Mater. Phys.*, 2001, **64**, 144104.
17 C. R. Houska, B. L. Averbach and M. Cohen, *Acta Metall.*, 1960, 8, 81–87.
18 H. L. Gaigher and N. G. van der Berg, *Electrochim. Acta*, 1976, 21, 45–49.
19 J.-E. Bidaux, R. Schaller and W. Benoit, *Acta Metall.*, 1989, 37, 803–811.
20 M. Kawakami, T. Hihara and Y. Koi, *J. Phys. Soc. Jpn.*, 1972, 33, 1591–1598.
21 R. Speight, A. Wong, P. Ellis, P. T. Bishop, T. I. Hyde, T. J. Bastow and M. E. Smith, *Phys. Rev. B: Condens. Matter Mater. Phys.*, 2009, 79, 054102.
22 E. A. Turov and M. P. Petrov, *Nuclear Magnetic Resonance in Ferro- and Antiferromagnets*, Jerusalem: Israel Program for Scientific Tr. (Halsted Pr. N.Y.), 1972.
23 E. Jdryka, M. Wójcik, S. Nadolski, H. Pattyn, J. Verheyden, J. Dekoster and A. Vantomme, *J. Appl. Phys.*, 2004, 95, 2770–2775.
24 Y. D. Zhang, J. I. Budnick, W. A. Hines, S. A. Majetich and E. M. Kirkpatrick, *Appl. Phys. Lett.*, 2000, 76, 94–96.
25 T. Thomson, P. C. Riedi, S. Sankar and A. E. Berkowitz, *J. Appl. Phys.*, 1997, **81**, 5549–5551.
26 A. A. Sidorenko, C. Pernechele, P. Lupo, M. Ghidini, M. Solzi, R. De Renzi, I. Bergenti, P. Graziosi, V. Dediu, L. Hueso and A. T. Hindmarch, *Appl. Phys. Lett.*, 2010, 97, 162503.
27 A. S. Andreev, O. B. Lapina, J.-B. d'Espinose de Lacaillerie and A. A. Khassin, *J. Struct. Chem.*, 2013, **54**, S102–S110.
28 O. Kitakami, H. Sato, Y. Shimada, F. Sato and M. Tanaka, *Phys. Rev. B: Condens. Matter Mater. Phys.*, 1997, **56**, 13849–13854.
29 C. Rosant, B. Avalle, D. Larcher, L. Dupont, A. Friboulet and J.-M. Tarascon, *Energy Environ. Sci.*, 2012, 5, 9936.
30 J. Cabana, L. Monconduit, D. Larcher and M. R. Palacín, *Adv. Mater.*, 2010, 22, E170–E192.
31 A. S. Andreev, S. F. Tikhov, A. N. Salanov, S. V. Cherepanova, O. B. Lapina, V. A. Bolotov, Y. Y. Tanashev, J.-B. d'Espinose de Lacaillerie and V. A. Sadykov, *Adv. Mater. Res.*, 2013, **702**, 79–87.
32 Y. Liu, J. Luo, M. Girleanu, O. Ersen, C. Pham-Huu and C. Meny, *J. Catal.*, 2014, **318**, 179–192.
33 W. Hines, J. Budnick, D. Perry, S. Majetich, R. Booth and M. Sachan, *Phys. Status Solidi B*, 2011, **248**, 741–747.
34 Y. Y. Tong, *J. Magn. Reson.*, 1996, **119**, 22–28.
35 A. S. Andreev, PhD thesis, Novosibirsk State University, Boreskov Institute of Catalysis, 2015, p. 147 (in Russian).
36 A. M. Portis and A. C. Gossard, *J. Appl. Phys.*, 1960, **31**, S205–S213.
37 A. C. Gossard and A. M. Portis, *Phys. Rev. Lett.*, 1959, 3, 164–166.
38 A. C. Gossard, A. M. Portis, M. Rubinstein and R. H. Lindquist, *Phys. Rev.*, 1965, **138**, A1415–A1421.
39 H. Yasuoka and R. T. Lewis, *Phys. Rev.*, 1969, **183**, 559–562.
40 V. V. Matveev, D. A. Baranov, G. Y. Yurkov, N. G. Akatiev, I. P. Dotsenko and S. P. Gubin, *Chem. Phys. Lett.*, 2006, **422**, 402–405.
41 A. S. Andreev, O. B. Lapina and S. V. Cherepanova, *Appl. Magn. Reson.*, 2014, **45**, 1009–1017.
42 S. G. Bailey, D. C. Creagh and G. V. H. Wilson, *Phys. Lett. A*, 1973, **44**, 229–230.
43 Y. Koi, A. Tsujimura and Y. Yukimoto, *J. Phys. Soc. Jpn.*, 1960, **15**, 1342.
44 M. Kawakami and H. Enokiya, *J. Phys. Soc. Jpn.*, 1986, 55, 4038–4043.
45 C. Searle, H. Kunkel, S. Kupca and I. Maartense, *Phys. Rev. B: Solid State*, 1977, **15**, 3305–3308.
46 H. P. Kunkel and C. W. Searle, *Phys. Rev. B: Condens. Matter Mater. Phys.*, 1981, 23, 65–68.
47 W. Marshall, *Phys. Rev.*, 1958, **110**, 1280–1285.
48 E. C. Stoner, *Proc. R. Soc. London, Ser. A*, 1938, **165**, 372–414.
49 M. Weger, E. L. Hahn and A. M. Portis, *J. Appl. Phys.*, 1961, 32, S124–S125.
50 M. Takahashi and T. Suzuki, *Jpn. J. Appl. Phys.*, 1979, **18**, 1071–1078.
51 D. L. Leslie-Pelecky and R. D. Rieke, *Chem. Mater.*, 1996, 8, 1770–1783.

Supplementary materials

Thermal stability and hcp-fcc allotropic transformation in supported Co metal catalysts probed *near operando* by ferromagnetic NMR

Andrey S. Andreev[a,b,c], Jean-Baptiste d'Espinose de Lacaillerie*[,c], Olga B. Lapina[a,b], Alexander Gerashenko[d]

[a] Pirogova str. 2, Novosibirsk State University (NSU), Novosibirsk, 630090, Russia

[b] Pr. Lavrentieva 5, Solid-State NMR group, Boreskov Institute of Catalysis SB RAS (BIC SB RAS), Novosibirsk, 630090, Russia

[c] 10 Rue Vauquelin, Soft Matter Sciences and Engineering (SIMM), UMR CNRS 7615, PSL Research University, ESPCI ParisTech, Paris, 75005, France

[d] S. Kovalevskoy str. 18, Kinetic Phenomena laboratory, Institute of Metals Physics UB RAS, Ekaterinburg, 620041, Russia

The ferromagnetic NMR signal

The theory of magnetic resonance in magnetic materials, albeit complex, is well understood and has been described elsewhere with great clarity in books and reviews.[1] Only relevant aspects are recalled here.

The total magnetization of the sample, M_T, results from the sum of two magnetizations, electronic (M) and nuclear (m):

$$\vec{M}_T = \vec{M} + \vec{m}.$$

Those two magnetizations are coupled through two Bloch equations

$$\begin{aligned} \frac{d\vec{m}}{dt} &= \gamma_n \vec{m} \times \vec{b} + \vec{r} \\ \frac{d\vec{M}}{dt} &= \gamma_e \vec{M} \times \vec{B} + \vec{R} \end{aligned} \qquad (1S)$$

Where b (B), r (R), and γ_n (γ_e) are the magnetic field felt by the nucleus (electron), the relaxation of the nuclear (electronic) magnetization and gyromagnetic ratio of the nucleus (electron). In the absence of a permanent external field, within the molecular field approximation and identifying the magnetic hyperfine field felt by the nuclei with the molecular field, the local fields can be written as

$$\vec{b} = \vec{B}_1 e^{i\omega t} + \lambda_m \vec{M} = \vec{B}_1 e^{i\omega t} + \vec{B}_{hf}$$

$$\vec{B} = \vec{B}_a + \vec{B}_1 e^{i\omega t} + \lambda_m \vec{m}$$

where λ_m is the molecular field parameter.
Looking for the stationary solutions of equations (1S) leads to the determination of the ferromagnetic nuclear magnetic resonance (FNR) and the ferromagnetic electronic resonance frequency (FMR)

$$FNR: \Omega_n = \left| -\gamma_n \left[B_{hf} \left(1 - \eta_d \frac{m}{M} \right) \right] \right|$$
$$FMR: \Omega_e = \left| -\gamma_e \left[B_a \left(1 + \eta_d \frac{m}{M} \right) \right] \right| \qquad (2S)$$

where $\eta_d = B_{hf}/B_a$, m and M are the amplitudes of the nuclear and electronic magnetization respectively. The frequency pulling associated with the second term of each resonance frequency has been discussed by de Gennes,[2] but in metallic cobalt in the range of temperatures studied here, $m/M << 1$ and the frequencies can be approximated with a good level of confidence as simply

$$\Omega_n \approx \left| -\gamma_n B_{hf} \right| = \left| -\gamma_n \lambda_m M \right|$$
$$\Omega_e \approx \left| -\gamma_e B_a \right| \qquad (3S)$$

As far as the ferromagnetic NMR frequency is concerned, in the bulk, it is thus simply the Larmor frequency in the hyperfine field proportional to the electronic magnetization. In small particles with a limited number of domains (mainly single-domain particles), the demagnetization field must be added (note that the hyperfine field is negative in Co metal). Because we operated near the nuclear resonance frequency and since the experimental setup was a conventional NMR one (detection by Faraday induction in a solenoid), the signal was directly proportional to the total nuclear transverse magnetization.[3] In a sample containing several crystallites and magnetic domains, integration must be performed over all the relative orientations of the RF field with respect to of the hyperfine field. Building on,[4] the transverse magnetization echo intensity after two-pulse at resonance with the nuclei and of equal duration τ has been derived[5] leading to the following expression for the signal from the ferromagnetic domains

$$E_T^d \propto \frac{V_d}{V_d + V_w} \frac{\eta_d m}{\alpha^2} \left[\sin\alpha - \frac{1}{8}\sin 2\alpha - \alpha\cos\alpha + \frac{1}{4}\alpha\cos 2\alpha \right] G\left(\Delta / T_2^* \right) \qquad (4S)$$
$$\alpha = \gamma_n \eta_d B_1 \tau$$

where V_d and V_w are the volumes of domains and walls respectively. The function $G(\Delta/T_2^*)$ accounts for the decay Δ during the interpulse with a characteristic time T_2^* (Fourier transform of the lineshape).
For the domain walls, the situation is more complex. The spatial variation of the hyperfine and anisotropy fields within the walls, and the motion of the walls under the influence of the rf field must be taken into account. Furthermore, assumptions on the particle size (D), wall structures, and distributions must be made.[4] In any case, the following behaviour can be expected for the part of the echo arising from the nuclei within the domain walls

$$E_T^w \propto \frac{V_w}{V_d + V_w} \eta_{0w}\, m\, F\left(\alpha_0, \eta_{0w}, D, \ldots \right) G\left(\Delta / T_2^* \right)$$
$$\eta_{0w} = a\eta_d \qquad (5S)$$
$$\alpha_0 = \gamma_n \eta_{0w} B_1 \tau$$

Where the proportionality factor $a > 1$ between the domain enhancement factor and the maximum enhancement factor accounts for the angle between the magnetic moments of adjacent atoms.[4,6] The function F will depend on the way the walls are modelled. Concerning the temperature behaviour of the ferromagnetic signal, from the above equations, the following conclusion can be drawn. The resonance frequency Ω_n is expected to vary simply as the hyperfine field. In turn, the electronic magnetization M and hyperfine constant λ_m can have a more complex temperature dependence.[7] The temperature dependence of the echo intensity from the domains and domain walls is thus not expected to be straightforward according to (4S) and (5S). The nuclear equilibrium magnetization m is expected to vary as $1/T$ while the one of M is dictated by spin-waves theory.[8]

TEM and XRD characterization

Experimental

The samples used for characterization were not exposed to air. They were manipulated in a glove box under argon atmosphere and conserved in hexane for HRTEM study. Prior to TEM measurements a drop of the sample suspension in hexane with sample was put onto a copper grid and immediately transferred into the microscope chamber. By capillarity, hexane remains inside the pores and the bulk of the sample is thus protected from air. TEM working by transmission, surface oxygen oxidation does not contribute significantly to the signal. For XRD measurements, the samples were evacuated under argon atmosphere and transferred into hermetically locking XRD probe.

HRTEM micrographs were obtained with a JEM-2010 microscope (JEOL Co) with a lattice resolution of 0.14 nm and an accelerating voltage of 200 kV. The high-resolution images of periodic structures were analyzed by the Fast Fourier transformation (FFT) method. Local energy-dispersive X-ray (EDX) analysis was carried out on an EDAX spectrometer (EDAX Co) fitted with a Si (Li) detector with a resolution of 130 eV. Samples to be examined by HRTEM were prepared on a holey carbon film mounted on a copper grid.

The X-ray diffraction (XRD) patterns were acquired using a X'TRA (Thermo ARL) diffractometer (Bragg–Brentano geometry, CuKa radiation, energy dispersed detector, step scan mode). Data acquisition was performed with a 2θ angle range from 30° to 80°, a step of 0.05° and an accumulation time of 9 s per point.

TEM

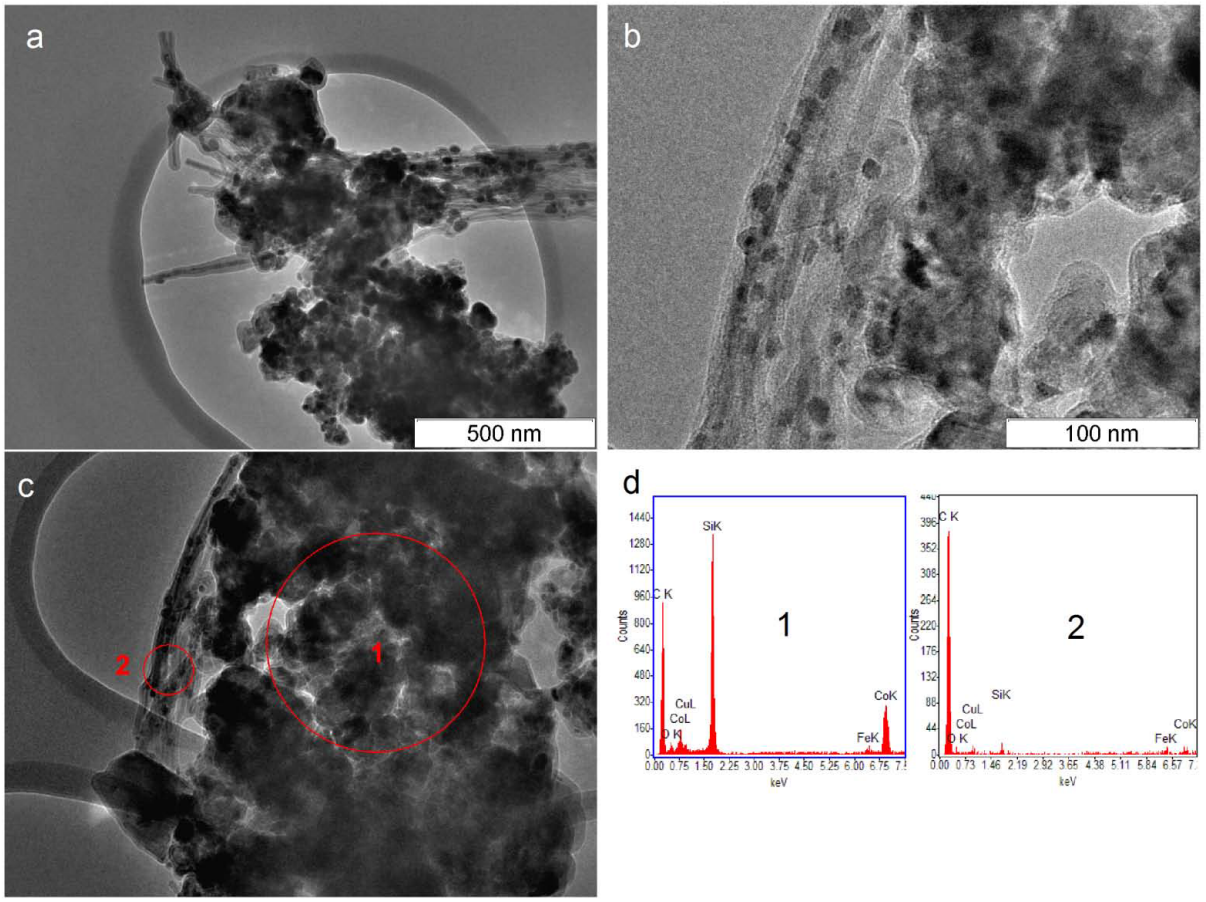

Fig. S1. HRTEM images of initial sample showing morphology and particle sizes (a) - (b); (c) – (d) HRTEM image of Co-Fig S1. HRTEM images of low resolution showing morphology of the sample and Co particle sizes (a)-(b); (c)-(d) HRTEM image of cobalt containng (1) and cobalt free (2) part of the initial sample. Hightened carbon content is a result of residual hexane content in

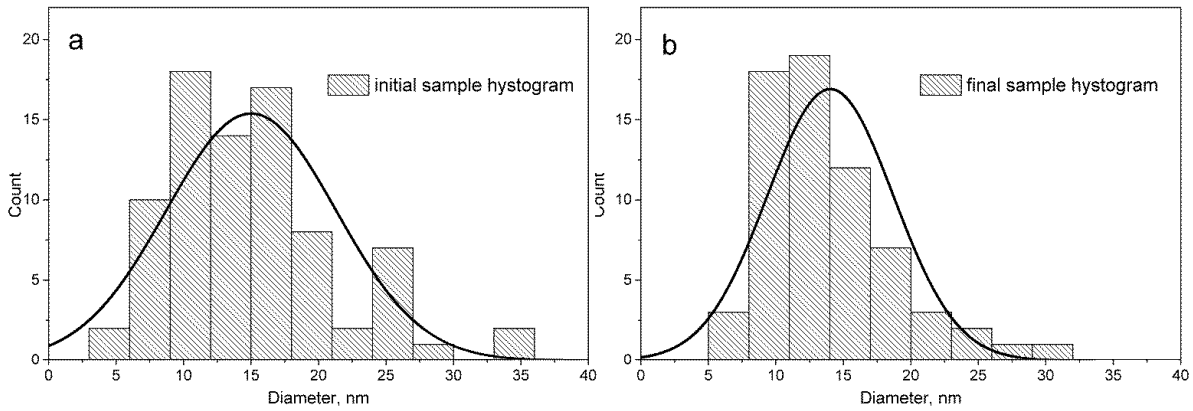

Fig. S2. A histogram obtained from HRTEM analysis of the sample before (a) and after heating in the NMR spectrometer (b).

HRTEM images n Fig. S1 display the morphology and structure of Co/SiC catalysts. EDX images in Fig S1d show Co free and Co-containing parts of the sample. The histograms shown in Figure S2 state the conservation of average Co particle size after temperature experiment.

XRD

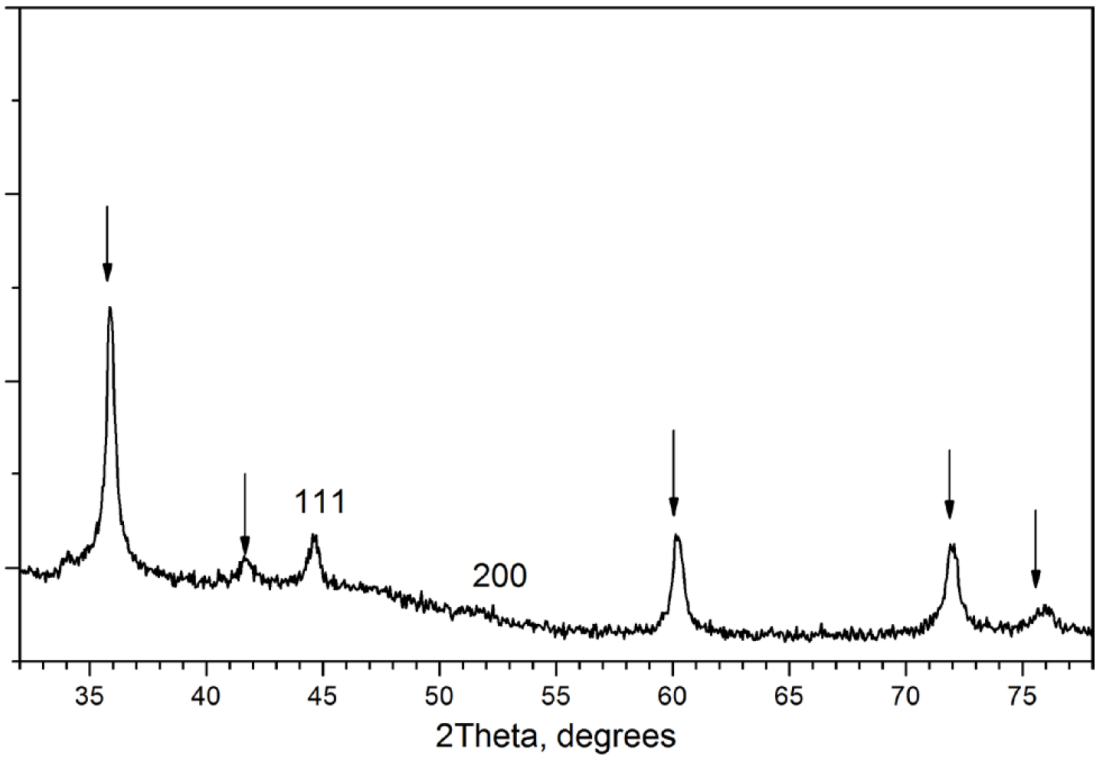

Fig. S3. XRD pattern of the initial reduced sample of Co/SiC. Arrows indicate SiC diffraction peaks (3C polytype, space group F4(-)3m). Numbers show fcc Co diffraction peaks.

The XRD pattern of the initial sample displays *111* fcc Co peaks in addition to the ones of SiC (shown by arrows). The *200* C metal peak is highly broadened indicating a faulted structure for the fcc Co metal. It should be noticed that stacking faults (sfs) i hcp structure ABAB correspond to the ABC fcc structure. And conversely, sfs in fcc structure ABCABC correspond to layers hcp structure. Therefore, the XRD observation of a highly faulted fcc structure is in a good agreement with ferromagnetic ^{59}C NMR data, which evidenced the occurrence of both fcc and hcp stackings of Co metal.

References

1. A. P. Guimarães, *Magnetism and Magnetic Resonance in Solids*, John Wiley & Sons, Chichester, 1998.

2. P. G. de Gennes, P. A. Pincus, F. Hartmann-Boutron and J. M. Winter, *Phys. Rev.*, 1963, **129**, 1105–1115.

3. D. I. Hoult and N. S. Ginsberg, *J. Magn. Reson.*, 2001, **148**, 182–99.

4. M. Stearns, *Phys. Rev.*, 1967, **162**, 496–509.

5. I. S. Oliveira and A. P. Guimarães, *J. Magn. Magn. Mater.*, 1997, **170**, 277–284.

6. A. M. Portis and A. C. Gossard, *J. Appl. Phys.*, 1960, **31**, S205–S213.

7. D. M. Edwards, *J. Phys. F Met. Phys.*, 1976, **6**, L185–L189.

8. E. A. Turov and M. P. Petrov, *Nuclear Magnetic Resonance in Ferro- and Antiferromagnets*, Jerusalem : Israel Program for Scientific Tr. (Halsted Pr. N.Y.), 1972.

4.3. Catalytic and related materials

4.3.1. Supported FTS catalysts

In this chapter, the application of the internal field ^{59}Co NMR to Fischer-Tropsch synthesis is shown. The emphasis is on the influence of different supports obtained by specific preparation technique such as co-precipitation. The content of this chapter is published in *Journal of Structural Chemistry* [3], which is a translated version of an original publication in Russian (*Zhurnal Structurnoi Khimii*, vol 54, 2013, S103-S111; http://jsc.niic.nsc.ru/JSC/jsc_rus/2013-t54/n7/n7_1/09.htm).

In this paper, the attribution of the lines is not in accordance with the introduction of the manuscript since we re-considered several things. However, this article provides historical review, which is not influenced by NMR line assignment.

Journal of Structural Chemistry, Vol. 54, Supplement 1, pp. S102-S110, 2013

EFFECT OF ALUMINA MODIFICATION ON THE STRUCTURE OF COBALT-CONTAINING FISCHER–TROPSCH SYNTHESIS CATALYSTS ACCORDING TO INTERNAL-FIELD ^{59}Co NMR DATA

© **A. S. Andreev,[1,2,3,4] O. B. Lapina,[1,2] J.-B. d'Espinose de Lacaillerie,[3,4] and A. A. Khassin[1,2]**

UDC 539.143.43:541.128

An internal-field ^{59}Co NMR study of cobalt-containing Fischer–Tropsch synthesis catalysts supported on different alumina modifications was reported. The Co/δ-Al_2O_3 sample was shown to contain single-domain fcc packing and stacking faults, whereas Co/γ-Al_2O_3 gave signals from the fcc domain walls, hcp and stacking faults, thus indicating differences in the particle size of the studied samples. T_2 relaxation times were measured; their distribution in a spectrum is non-uniform, which allows signals to be distinguished by their relaxation times. Quantitative measurements of the relative atoms content in different packings revealed that the catalysts have mostly a defect structure. A brief historical background was presented to characterize the internal-field ^{59}Co NMR technique, the related problems, and different approaches to acquired data interpretation.

DOI: 10.1134/S0022476613070093

Keywords: internal-field ^{59}Co NMR, cobalt-containing catalysts, cobalt.

INTRODUCTION

The internal-field ^{59}Co NMR technique was employed quite widely to investigate various class objects containing metallic cobalt. First of all, bulk alloys [1-6] that were of interest due to different magnetoresistance effects. Then, the reduced dimension systems, i.e. thin films [7-15], were studied; they were essential in terms of data recording and long-term storage. Great attention was paid also to nanosized objects (other than films) [16-21] that were of basic importance as they show increased magnetic moments and anomalous behavior (in comparison with bulk large-sized cobalt) in the applied external magnetic field and at a decreased temperature. Thus, the technique had been employed only to solve physical problems; however, metallic cobalt materials were widely used in chemistry and particularly in catalysis. The list of large-scale industrial catalytic processes based on metallic cobalt began with the Fischer–Tropsch synthesis (FTS); this was a set of reactions that produced liquid hydrocarbons from syngas [22-24], which was obtained from natural gas, coal or biomass. In the literature, there were some attempts to use the internal-field ^{59}Co NMR for investigation of catalysts [25, 26], but no spectra were presented in these works. The authors of [27, 28] demonstrated informativeness of the technique with respect to ceramometallic samples considered as promising supports for the catalysts.

[1]G. K. Boreskov Institute of Catalysis, Siberian Division, Russian Academy of Sciences, Novosibirsk, Russia; aandreev@catalysis.ru. [2]Novosibirsk State University, Novosibirsk, Russia; olga@catalysis.ru. [3]University of Paris VI: Pierre et Marie Curie, Paris, France. [4]Soft Matter Sciences and Engineering, UMR CNRS 7615, ESPCI ParisTech, France.
Translated from *Zhurnal Strukturnoi Khimii*, Vol. 54, Supplement 1, pp. S104-S112, 2013. Original article submitted March 13, 2013.

As in many other catalytic processes, in FTS catalysts cobalt was used in the supported rather than bulk state. SiO_2 [29], Al_2O_3 [30], TiO_2 [31], MgO [32], ZSM-5 [26] and other more rare substances can serve as the supports. Al_2O_3 supported catalysts were widely employed in industry because alumina provides the optimal interaction of active component and substrate; this prevents cobalt agglomeration in the course of reaction and its leaching from the support surface, but did not lead to irreversible cobalt oxidation with the formation of mixed oxides.

The present paper was devoted to attribution and interpretation of signals in the internal-field ^{59}Co NMR spectra. A literature review of the problem was presented, and the potential of the technique for investigation of supported cobalt-containing FTS catalysts was demonstrated.

CATALYST SYNTHESIS

The catalysts were prepared by deposition-precipitation of cobalt ions from a solution on various aluminas (γ and δ) during urea hydrolysis. Details of the preparation procedure are reported elsewhere [33]. The catalysts were then calcined under an argon atmosphere at a temperature of 270°C for 2 h and reduced in a hydrogen flow; the ultimate reduction temperature was 600°C; heating rate, 1°C/min; and time of holding at the ultimate temperature, 2 h. The reduced samples were poured into ampoules in a inert gas flow and then sealed in glass ampoules in the absence of oxygen and water. According to chemical analysis, the samples contained 18.1 wt.% and 22.9 wt.% Co for the catalysts on δ-Al_2O_3 and γ-Al_2O_3, respectively. As revealed by thermogravimetric analysis of the temperature-programmed oxidation, the content of metallic cobalt in the reduced catalysts was 11.9 wt.% and 13.8 wt.%, respectively.

EXPERIMENTAL PROCEDURE

All the measurements were carried out on a Bruker Avance II spectrometer (400 MHz, magnetic field of 9.4 T) with no applied field, i.e. outside the magnet. The spectra were taken using an upgraded standard high-power broadband detector with a 10 mm copper coil for a frequency range of ~195-230 MHz. Since metallic cobalt has a very large spectrum width (≈15 MHz), the spectra were recorded using point-by-point technique with a frequency step of 0.5 MHz and power step of 2 dB, and then the spectrum was processed by means of a specially developed software program. RF pulse length was equal to 4 μs, a repetition pulse rate was ~35 Hz. The number of accumulations in a single point with respect to frequency and power was 8000 for supported catalysts with low cobalt content. Skin effect could be neglected since the thickness of skin layer for cobalt at frequencies used in the experiment was 8 μm.

The main feature of nuclear magnetic resonance in magnetically ordered substances (in our case, ferromagnetic Co) was that it can be observed without application of the external permanent magnetic field to the sample, because large and quite uniform magnetic fields existed on Co nuclei in magnetically ordered substances [34]. It should be noted that the observed signal intensity in the NMR spectrum of ferromagnetic Co did not reflect the number of atoms at a given point [8]. The reason was that an alternating radiofrequency (RF) field affected the nuclear spins not directly but rather via electronic magnetization, which is responsible for the formation of a large local magnetic field in the atomic nucleus point (~21 T). Under the action of RF pulse, electronic magnetization deviated from its equilibrium position (along the easiest magnetization axis coinciding with crystallographic axis), this produced a transverse (with respect to equilibrium position) component of the local field (or magnetization) inducing nuclear transitions. Since RF pulse excited transitions indirectly, the enhancement factor (inversely proportional to the applied RF field) was introduced [35] to correct the intensities; a two-dimensional spectrum should be acquired by varying not only the pulse frequency but also the power. To obtain a typical spectrum, it was necessary to record a series of spectra or a 2D spectrum [36-38].

BRIEF HISTORICAL BACKGROUND

At present, there are several approaches to interpretation of the peaks from metallic cobalt observed in the internal-field ^{59}Co NMR spectra. Same peaks can be interpreted differently in the literature; to elucidate causes of such disagreement, it would be reasonable to consider the history of discovering magnetic resonance in magnetic substances.

The founders of internal-field NMR for magnetic substances were Gossard and Portis [39], who observed in 1959 the resonance from face-centered cubic (fcc) cobalt powder at a frequency of 213.1 MHz at room temperature. Interpretation and theoretical description of the obtained signal were made in their next work [35] clearly demonstrating the observed signal to correspond to the fcc cobalt atoms in domain walls (dw). The mechanism of signal enhancement was related to the motion of the walls under the action of RF field. For the first time the resonance of hexagonal close-packed (hcp) cobalt was observed in [40] at a frequency of 221 MHz at room temperature and at 228 MHz when the temperature dependence was extrapolated to 0 K. The observed signal was attributed to the nuclei in dw (or, more exactly, to the dw center, as will be shown below). Fig. 1 schematically illustrates the simplest 180° (Bloch) dw to reveal the origin of resonance signals in magnetic substances. In dw, magnetic moments were continuously shifting by 180°; thus, when the wall moved during a RF pulse, the moments deviated by a larger angle as compared to that in domains. This was illustrated by the fact that the signal enhancement factor for dw was 10-1000 times greater than that for domains.

Problems with signal interpretation appeared in the work by Hardy [41], who observed additional resonances at frequencies 215.5 MHz, 218.5 MHz, and 223.5 MHz and assigned them to cobalt stacking faults (sfs). This work gave rise to numerous ^{59}Co NMR papers where all additional lines in the spectrum were assigned to sfs. Such approach was based mainly on the early works [42] and [43] where positions of the stacking fault resonance lines were calculated from the resonance frequency of "pure" fcc and hcp phases at frequencies 213.1 MHz and 221 MHz, respectively. The authors of these works did not even mention that the resonance originated from the atoms in dw that were much less in number as compared to the atoms in domains. The resonance was supposed to depend only on a ratio of crystallographic parameters c/a, i.e. only on the packing density. This approach was not quite correct because it did not consider the effect of magnetic structure on the cobalt resonance. Irrespective of its drawbacks, the approach had many adherents. There were many works based on the indicated interpretation of ^{59}Co NMR data [3, 8, 9, 12, 13, 20, 36-38, 44-58].

Another approach in the internal-field ^{59}Co NMR of metallic cobalt was to search for resonances not only from the nuclei in dw, but also from the nuclei located directly in magnetic domains. Such way was proposed by the founders of internal-field resonance, Gossard and Portis [59]. They studied cobalt particles of different size supported on γ-Al_2O_3 for stabilization and observed a new resonance at a frequency of 216.85 MHz for the particles of size 100-150 Å at room

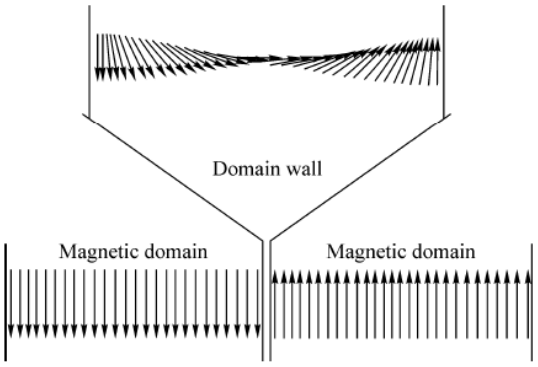

Fig. 1. A schematic representation of the simplest 180° (Bloch) domain wall.

temperature. Gossard and Portis suggested the following explanation for different resonance frequencies in the domains of fcc cobalt and on their walls: particles in the domain are subjected to the action of anisotropy field, or degaussing field, which was averaged for the domain wall, because contributions from different domains compensated each other. Smaller particles, with a size less than 100 Å, were also examined, but no signal was detected in this case. Gossard and Portis attributed this phenomenon to a transition of such small particles to superparamagnetic state at room temperature. A later work [60] also confirmed the presence of a signal from domains; its temperature dependence was investigated. Unfortunately, the authors did not present a Table with the obtained values of resonance versus temperature, instead they displayed a plot which gave a value of 216.3 MHz.

A comprehensive investigation of resonances in hcp cobalt was made later, in 1972 [61]. Criticizing the approach suggested by Jackson and co-authors [62], who assigned second line in the spectrum of pure hcp cobalt to sfs, the authors of [61] attributed this peak to the resonance of atoms located at the hcp cobalt dw edge, and the line at 221 MHz — to the dw center. Kawakami and co-authors [61] observed resonance from atoms on the dw edge at a frequency of 214 MHz at 290 K. In hcp cobalt, magnetic moments of the domains were parallel to hexagonal axis *c* and magnetic domains were connected with a 180° domain wall, in the center of which magnetic domains were perpendicular to axis *c*. Resonances from the domains and domain walls could have different frequencies only in the case of large anisotropy of hyperfine, or local field. Anisotropy of the local field found by the authors was equal to 8 kE, which gives a 8 MHz frequency shift for cobalt assuming the gyromagnetic ratio to be 1.0054 kHz/G [63]. However, according to the theory proposed by Turov, Kurkin and Tankeev in [64, 65], the local dw line width was not a constant value; due to anisotropy of the local field, signals from dw edge and from its center should be observed. A signal from atoms residing in the domain depth did not give a substantial contribution to the overall signal (although for hcp cobalt the resonance frequency at the dw edge should coincide with the frequency in domains) because atoms in the domains had at least an order of magnitude lower enhancement factor. A signal from dw edge was also affected by quadrupole splitting, a distance between its transitions being ~167 kHz [66]; in this paper the authors presented a detailed Table of frequency resonances at the dw edge in dependence on temperature ($\nu = 219.78$ at 4.2 K). The dw center and edge resonance investigation for hcp cobalt was reported also in other works [67-70] verifying the presence of two lines in the spectrum. Taking into account two hcp cobalt dw resonances, it was necessary to turn again to incorrectness of the works where sfs were calculated [42, 43], since these papers dealt with changes of the local field along crystallographic axis *c* of hcp cobalt (i.e., the field in domains and in the dw edge), whereas the calculations used the value for dw center, i.e. perpendicular to the *c* axis.

Turning back to the NMR studies of sfs in cobalt, in particular to the first publication [41] initiating a large number of works, it was essential to remember the resonance frequency observed by Hardy. In [41], he observed additional resonances at the frequencies of 215.5 MHz, 218.5 MHz, and 223.5 MHz. It should be noted that these resonances did not coincide with the resonance frequencies from domains and dw of "pure" phases described above. Hardy gave a "metallurgical interpretation" of the observed resonances. The first type (1) included the fcc structures that have density of neighbors similar to that in hcp structures and were associated with simple growth faults. The second type (2) was the fcc symmetry of the first and second coordination spheres, density of neighbors being between fcc and hcp; such structures were associated with deformation and complex growth faults. An finally, the third type (3) implied hcp symmetry with the same density of neighbors, which was associated with all sfs of the second type (2) and had phase boundaries between fcc and hcp. Respectively, the attribution was made as follows: (3) — 215.5 MHz, (2) — 218.5 MHz, and (1) — 223.5 MHz. The ^{59}Co NMR spectra of metallic cobalt, which were published in refs. [3, 37, 38, 42, 43, 49, 71-73] devoted to sfs in metallic cobalt, were analyzed with due regard to technological opportunities of the earlier works and irrelevance of some peaks that were observed only in single studies and could be caused by instrumental features. This analysis allows a conclusion that along with the signals from dw edge and domains (214 MHz and ~217 MHz), only three additional lines were observed in cobalt: 215.5 MHz, ~218.5 MHz, and 223.5 MHz.

APPLICATION OF INTERNAL-FIELD ^{59}Co NMR TO INVESTIGATION OF FTS CATALYSTS

In the present work, cobalt-containing Fischer–Tropsch synthesis catalysts supported on two modifications of alumina (γ-Al_2O_3 and δ-Al_2O_3) were examined. Details of the synthesis procedure were reported earlier. Although the preparation and reduction conditions were similar for these catalysts, they had different contents of metallic cobalt (11.9 wt.% in Co/δ-Al_2O_3 and 13.8 wt.% in Co/γ-Al_2O_3) due to differences in the structure of initial aluminum oxides and in the degree of their hydration.

Distinct additional peaks assigned to sfs were observed in the bulk samples; nevertheless, such peaks were absent in the case of nanosized systems fixed in a matrix. A typical spectrum for such nanosized systems is a broad poorly resolved line with a minimum number of characteristic points (Fig. 2). In this connection, positions of the peaks corresponding to sfs in bulk cobalt can be used to deconvolve spectra of small ultradispersed particles, but this required additional bases.

Fig. 2 depicted the internal-field ^{59}Co NMR spectra of the catalysts supported on γ-Al_2O_3 (■) and δ-Al_2O_3 (▲). It was difficult to interpret the signals shown in Fig. 2 because, in distinction to bulk large-sized cobalt, the supported systems often gave broad poorly resolved resonance peaks. However, a radical difference between the spectra is clearly seen in Fig. 2.

Co/δ-Al_2O_3 catalyst spectrum deconvolution into Gaussian components with attribution of the signals was illustrated in Fig. 3*a*. According to the literature data presented above, a distinct peak at ~216.3 MHz corresponded to magnetic single-domain fcc cobalt. Besides, there was no signal at a frequency of 213.1 MHz, which indicated a complete absence of multidomain fcc cobalt; this allowed estimating the particle size. As shown in [74, 75], critical size of a single domain for metallic cobalt was 70 nm. This suggests that each metallic cobalt particle in the catalyst had a size less than 70 nm.

The ultimate reduction temperature was 600°C and the spectrum had no lines corresponding to pure hcp phases; thus, the broad line can be attributed to fcc cobalt sfs.

A different pattern was observed for cobalt supported on γ-Al_2O_3 (Fig. 3*b*). A peak at 213.6 MHz corresponding neither to pure multidomain fcc (213.1 MHz) nor to the atoms at the edge of dw of hcp cobalt (214 MHz) suggested the contribution just from two lines. In addition, full width at half maximum of this peak was virtually equal to 3 MHz, strongly exceeding the values typical of fcc and hcp signals. In this connection, the spectrum was deconvolved into three lines, one of them being a broad shoulder in a strong field.

The broad line center was shifted toward a weak field in comparison with Co/δ-Al_2O_3, testifying a different nature of the broad signal on Co/γ-Al_2O_3. This suggests that in this case there was also a contribution from hcp sfs. To verify the hypothesis on the presence of two lines, T_2 relaxation times were measured in several points of the spectrum. As seen from Table 1, T_2 relaxation times were different for the lines at 213.1 MHz and 214 MHz. In addition, T_2 relaxation time remained

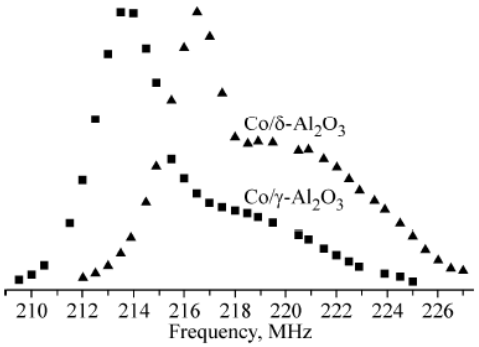

Fig. 2. The optimal internal-field ^{59}Co NMR spectra of cobalt catalysts with different alumina modifications (Co/γ-Al_2O_3 — ■, Co/δ-Al_2O_3 — ▲).

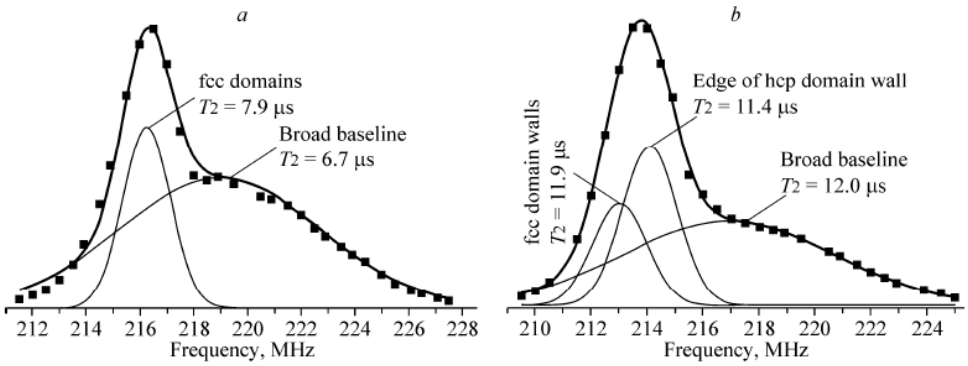

Fig. 3. The optimal internal-field ^{59}Co NMR spectrum of cobalt-containing catalyst supported on δ-Al_2O_3 (*a*) and γ-Al_2O_3 (*b*). Squares indicate the experimental points, bold curve corresponds to the sum of Gaussian peaks, and thin curves — to the Gaussian lines themselves.

TABLE 1. T_2 Relaxation Times in the Samples

Parameter	Co/γ-Al_2O_3						Co/δ-Al_2O_3	
Frequency, MHz	213	214.1	215.1	216.5	219.5	222.9	216.5	219.6
T_2, μs	11.85	11.36	11.44	11.88	12.02	12.14	7.85	6.68
Standard deviation, μs	*0.19*	*0.17*	*0.19*	*0.20*	*0.26*	*0.27*	*0.21*	*0.20*

virtually constant over the broad line. Noteworthy was the fact that these relaxation times strongly differed between samples, thus testifying to the structural differences of the catalysts. And finally, signals from multidomain particles indicated the presence of Co^0 particles with a size greater than 70 nm.

In NMR spectra, the area under a signal usually corresponded to the content of a certain type nuclei in the sample. This held true also for NMR in magnetic systems, but with some stipulations. First, as it was shown in the study, T_2 relaxation time did not remain constant over the entire spectrum. So, when considering the contributions from different lines, they should be taken with appropriate weights using the dependence of spin echo signal on T_2 (~exp(-2τ/T_2), where τ is the time between pulses in a sequence). Second, the spectrum should be corrected, since the amplitude of spin echo signal was inversely proportional to the frequency at which the measurement was carried out [7, 76]; as the spectrum was very broad, the contribution can be substantial. And finally, correction for the enhancement factor mentioned in many works [7, 8, 36] was necessary, but accurate determination of the amplitude of magnetic field was a difficult task for standard NMR instruments. However, absolute values of the enhancement factor were not needed for such correction; this slightly simplified the problem. In the present work, relative contents of different packings in a sample were estimated

	Co/γ-Al_2O_3			Co/δ-Al_2O_3	
Frequency, MHz	213	214.1	216.9	216.3	219
Relative content, at.%	15	25	60	25	75

Fig. 4 displayed the signal intensity dependences on attenuation of the RF pulse power, which were used to construct the optimal spectra and correct for the enhancement factor.

CONCLUSIONS

The internal-field ^{59}Co NMR technique provided unique data on the composition and magnetic structure of a sample, distinguished the contributions from magnetic dw and magnetic domains, and differentiated between regular fcc and hcp packings as well as contributions from various sfs.

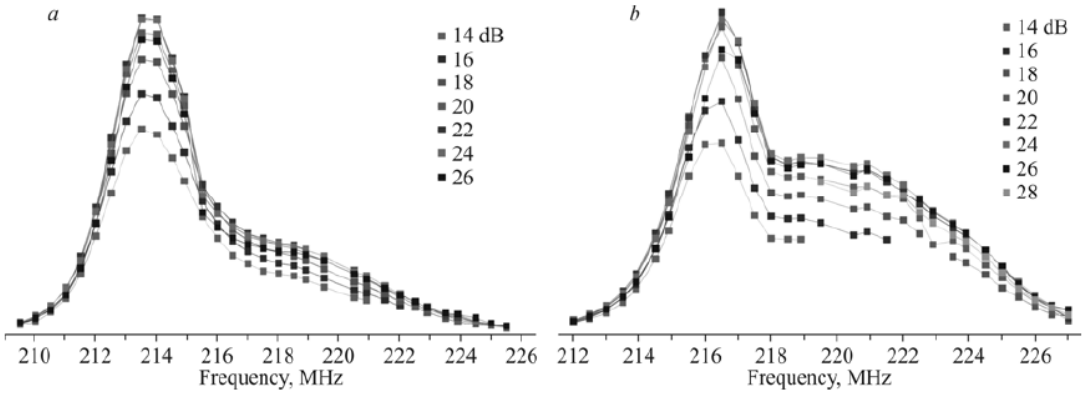

Fig. 4. The dependence of internal-field ^{59}Co NMR spectra on attenuation of the RF pulse power for Co/γ-Al_2O_3 (*a*) and Co/δ-Al_2O_3 (*b*).

This technique allowed revealing the effect of support modification on the structure of metallic cobalt. Co/δ-Al_2O_3 samples were characterized by the single-domain fcc cobalt packing and a broad line of sfs at a 1:3 ratio with the sfs prevalence. The spectrum of Co/γ-Al_2O_3 shows multidomain fcc and hcp packings, which indicate the presence of large (~70 nm) Co^0 particles on the support surface. The fcc:hcp:sfs ratio for this sample is equal to 3:5:12, respectively. Most of metallic cobalt particles have a high sfs concentration. A pronounced difference in the spin-spin relaxation time for the studied samples and non-uniformity of the T_2 value distribution over the spectrum were demonstrated.

The authors are grateful to Dr. I. I. Simentsova (Boreskov Institute of Catalysis) for affording Co-Al catalysts for the Fischer–Tropsch synthesis, and Dr. T. P. Minyukova (Boreskov Institute of Catalysis) for fruitful discussions of the work. This work was financially supported by the Russian Foundation for Basic Research (Project No. 13-03-00482A), RF President's Program for Young Scientists and Postgraduates (grant No. SP-389.2012.1), Federal Target Program "Research and Academic Professionals of Innovative Russia" (Agreement No. 8429), RAS Presidium Program V.47.3 (Project No. 3.3), and French Embassy (a scholarship within the joint postgraduate study).

REFERENCES

1. S. Wurmehl, J. T. Kohlhepp, H. J. M. Swagten, and B. Koopmans, *J. Phys. D: Appl. Phys*., **41**, 1 (2008).
2. S. Wurmehl, G. H. Fecher, K. Kroth, F. Kronast, H. A. Dürr, Y. Takeda, Y. Saitoh, K. Kobayashi, H.-J. Lin, G. Schönhense, and C. Felser, *J. Phys. D: Appl. Phys*., **39**, No. 5, 803 (2006).
3. C. Meny, E. Jedryka, and P. Panissod, *J. Phys.: Condens. Matter*., **5**, No. 10, 1547 (1993).
4. R. C. La Force and G. F. Day, *Phys. Rev. Lett*., **6**, No. 5, 226 (1961).
5. H. Yasuoka, S. Hoshinouchi, Y. Nakamura, M. Matsui, and K. Adachi, *Phys. Status Solidi B*, **46**, No. 2, K81 (1971).
6. J. Durand and M. F. Lapierre, *J. Phys. F: Metall. Phys*., **6**, No. 6, 1185 (1976).
7. P. Panissod and C. Mény, *Appl. Magn. Res*., **19**, Nos. 3/4, 447 (2000).
8. P. Panissod, J. P. Jay, C. Meny, M. V., E. Jedrica, *Hyperfine Interact*., **97/98**, 75 (1996).
9. P. Panissod, in: *Structural and Magnetic Investigations of Ferromagnets by NMR. Application to Magnetic Metallic Multilayers, in*: *Frontiers in Magnetism of Reduced Dimension Systems*, V. G. Bar'yakhtar, P. E. Wigen, and N. A. Lesnik (eds.), Kluwer Academic (1998).
10. G. J. Strijkers, J. T. Kohlhepp, H. J. M. Swagten, and W. J. M. Jonge, *Appl. Magn. Res*., **19**, Nos. 3/4, 461 (2000).
11. T. Thomson, P. C. Riedi, Q. Wang, and H. Zabe, *J. Appl. Phys*., **79**, No. 8, 6300 (1996).
12. E. Jedryka, M. Wojcik, S. Nadolski, D. Kubinski, M. Parsons, and H. Holloway, *J. Appl. Phys*., **91**, No. 10, 7191 (2002).

13. M. Wojcik, C. Christides, E. Jedryka, S. Nadolski, and I. Panagiotopoulos, *Phys. Rev. B*, **63**, No. 1, 012102 (2001).
14. T. Thomson, P. C. Riedi, and D. Greig, *Phys. Rev. B*, **50**, No. 14, 10319 (1994).
15. A. A. Sidorenko, C. Pernechele, P. Lupo, M. Ghidini, M. Solzi, R. De Renzi, I. Bergenti, P. Graziosi, V. Dediu, L. Hueso, and A. T. Hindmarch, *Appl. Phys. Lett.*, **97**, No. 16, 162503 (2010).
16. Y. D. Zhang, J. I. Budnick, W. A. Hines, S. A. Majetich, and E. M. Kirkpatrick, *Appl. Phys. Lett.*, **76**, No. 1, 94 (2000).
17. M. Shiraishi, H. Kusai, R. Nouchi, T. Nozaki, T. Shinjo, Y. Suzuki, M. Yoshida, and M. Takigawa, *Appl. Phys. Lett.*, **93**, No. 5, 53103 (2008).
18. Y. D. Zhang, W. A. Hines, J. I. Budnick, Z. Zhang, and W. M. H. Sachtler, *J. Appl. Phys*., **76**, No. 10, 6576 (1994).
19. T. Thomson, P. C. Riedi, S. Sankar, and A. E. Berkowitz, *J. Appl. Phys*., **81**, No. 8, 5549 (1997).
20. E. Jedryka, M. Wojcik, S. Nadolski, H. Pattyn, J. Verheyden, J. Dekoster, and A. Vantomme, *J. Appl. Phys*., **95**, No. 5, 2770 (2004).
21. W. Hines, J. Budnick, D. Perry, S. Majetich, R. Booth, and M. Sachan, *Phys. Status Solidi B*, **248**, No. 3, 741 (2011).
22. A. Y. Khodakov, W. Chu, and P. Fongarland, *Chem. Rev*., **107**, No. 5, 1692 (2007).
23. N. E. Tsakoumis, M. Rønning, Ø. Borg, E. Rytter, and A. Holmen, *Catal. Today*, **154**, Nos. 3/4, 162 (2010).
24. M. Sadeqzadeh, H. Karaca, O. V. Safonova, P. Fongarland, S. Chambrey, P. Roussel, A. Griboval-Constant, M. Lacroix, D. Curulla-Ferré, F. Luck, and A. Y. Khodakov, *Catal. Today*, **164**, No. 1, 62 (2011).
25. A. N. Murty, M. Seamster, A. N. Thorpe, R. T. Obermyer, and V. U. S. Rao, *J. Appl. Phys*., **67**, No. 9, 5847 (1990).
26. A. N. Murty, A. A. Williams, R. T. Obermyer, and V. U. S. Rao, *J. Appl. Phys*., **61**, No. 8, 4361 (1987).
27. A. Andreev, A. Salanov, S. Tikhov, S. Cherepanova, V. Zaikovskii, V. Usoltsev, V. Sadykov, and O. Lapina, *J. Mater. Sci. Eng. A*, **2**, No. 2, 121 (2012).
28. A. S. Andreev, S. F. Tikhov, A. N. Salanov, S. V. Cherepanova, O. B. Lapina, V. A. Bolotov, Y. Y. Tanashev, J.-B. d'Espinose de Lacaillerie, and V. A. Sadykov, *Adv. Mat. Res.,* **702**, 79 (2013).
29. B. Ernst, S. Libs, P. Chaumette, and A. Kiennemann, *Appl. Catal. A: General*, **186**, Nos. 1/2, 145 (1999).
30. W.-J. Wang and Y.-W Chen, *Appl. Catal*., **77**, No. 2, 223 (1991).
31. J. Li, G. Jacobs, Y. Zhang, T. Das, B. H. Davis, and R. C. La Force, *Appl. Catal. A: General*, **223**, 195 (2002).
32. R. Reuel, *J. Catal*., **85**, No. 1, 78 (1984).
33. I. I. Simentsova, A. A. Khassin, G. A. Filonenko, G. K. Chermashentseva, O. A. Bulavchenko, S. V. Cherepanova, and T. M. Yurieva, *Russ. Chem. Bull.*, **63**, No. 9, 1796 (2011).
34. V. I. Chizhik, *Quantum Radiophysics*. St. Petersburg Publ., St. Petersburg (2004).
35. A. M. Portis and A. C. Gossard, *J. Appl. Phys*., **31**, No. 5, S205 (1960).
36. M. Malinowska, M. Wojcik, S. Nadolski, E. Jedryka, C. Meny, P. Panissod, M. Knobel, A. D. C. Viegas, and J. E. Schmidt, *J. Magn. Magn. Mater*., **198/199**, 599 (1999).
37. J. Sort, S. Surinach, J. S. Munoz, M. D. Baro, M. Wojcik, E. Jedrica, S. Nadolski, N. Sheludko, and J. Nogues, *Phys. Rev. B*, **68**, 14421 (2003).
38. R. Speight, A. Wong, P. Ellis, P. T. Bishop, T. I. Hyde, T. J. Bastow, and M. E. Smith, *Phys. Rev. B*, **79**, No. 5, 054102 (2009).
39. A. C. Gossard and A. M. Portis, *Phys. Rev. Lett*., **3**, No. 4, 164 (1959).
40. Y. Koi, A. Tsujimura, and T. Kushida, *J. Phys. Soc. Jpn*., **15**, 2100 (1960).
41. W. A. Hardy, *J. Appl. Phys*., **32**, No. 3, S122 (1961).
42. L. E. Toth and S. F. Ravitz, *J. Phys. Chem. Solids*, **24**, No. 10, 1203 (1963).
43. L. E. Toth, G. F. Day, R. C. La Force, and S. F. Ravitz, *Acta Metall*., **12**, 311 (1964).
44. J. L. Bubendorff, E. Beaurepaire, C. Mény, P. Panissod, and J. P. Bucher, *Phys. Rev. B*, **56**, No. 12, R7120 (1997).
45. S. Colis, A. Dinia, C. Mény, P. Panissod, C. Ulhaq-Bouillet, and G. Schmerber, *Phys. Rev. B*. **62**, No. 17, 11709 (2000).
46. E. Jedryka, M. Wojcik, S. Nadolski, D. J. Kubinski, H. Holloway, and P. Panissod, *J. Appl. Phys*., **81**, No. 8, 4776 (1997).

47. M. Malinowska, C. Meny, E. Jedryka, and P. Panissod, *J. Phys.: Condens. Matter*., **10**, No. 22, 4919 (1998).
48. P. Panissod, M. Malinowska, E. Jedrica, M. Wojcik, S. Nadolski, M. Knobel, and J. E. Schmidt, *Phys. Rev. B*, **63**, No. 1, 14408 (2000).
49. R. Speight, A. Wong, P. Ellis, T. Hyde, P. T. Bishop, and M. E. Smith, *Solid State Nucl. Magn. Res*., **35**, No. 2, 67 (2009).
50. M. Cerisier, K. Attenborough, E. Jedryka, M. Wojcik, S. Nadolski, C. Van Haesendonck, and J. P. Celis, *J. Appl. Phys*., **89**, No. 11, 7083 (2001).
51. C. Christides, S. Stavroyiannis, D. Niarchos, M. Wojcik, S. Nadolski, and E. Jedryka, *Phys. Rev. B*. **59**, No. 13, 8812 (1999).
52. E. Jedryka, W. E. Bailey, M. Wojcik, S. Nadolski, and S. X. Wang, *J. Appl. Phys*., **85**, No. 8, 4439 (1999).
53. E. Jedryka, M. Wojcik, S. Nadolski, D. J. Kubinski, and H. Holloway, *J. Magn. Magn. Mater*., **165**, Nos. 1-3, 292 (1997).
54. E. Jedryka, M. Wojcik, S. Nadolski, D. J. Kubinski, and H. Holloway, *J. Magn. Magn. Mater*., **177**, 1183 (1998).
55. E. Jedryka, M. Wojcik, S. Nadolski, T. Stobiecki, and M. Czapkiewicz, *J. Magn. Magn. Mater*., **156**, Nos. 1-3, 38 (1996).
56. M. Wojcik, E. Jedryka, S. Nadolski, D. Kubinski, M. Parsons, and H. Holloway, *Acta Phys. Pol., A*, **97**, No. 3, 551 (2000).
57. M. Wojcik, E. Jedryka, S. Nadolski, T. Stobiecki, and M. Czapkiewicz, *J. Magn. Magn. Mater*., **157**, 220 (1996).
58. C. Meny, P. Panissod, P. Humbert, J. P. Nozieres, V. S. Speriosu, B. A. Gurney, and R. Zehringer, *J. Magn. Magn. Mater*., **121**, Nos. 1-3, 406 (1993).
59. A. C. Gossard, A. M. Portis, M. Rubinstein, and R. H. Lindquist, *Phys. Rev*., **138**, No. 5A, A1415 (1965).
60. H. Yasuoka and R. T. Lewis, *Phys. Rev*., **183**, No. 2, 559 (1969).
61. M. Kawakami, T. Hihara, and Y. Koi, *J. Phys. Soc. Jpn*., **33**, No. 6, 1591 (1972).
62. R. F. Jackson, R. G. Scurlock, D. B. Utton, and T. H. Wilmshurst, in: *Proc. Intern. Conf. Magnetism*, Nottingham (1964), p. 384.
63. R. E. Walstedt, J. H. Wernick, and V. Jaccarino, *Phys. Rev*., **162**, No. 2, 301 (1967).
64. E. A. Turov, A. P. Tankeev, and M. I. Kurkin, *Physics of Metals and Metallography*, **28**, No. 3, 385 (1969).
65. E. A. Turov, A. P. Tankeev, and M. I. Kurkin, *Physics of Metals and Metallography*, **29**, No. 4, 747 (1970).
66. M. Kawakami and H. Enokiya, *J. Phys. Soc. Jpn*., **55**, No. 11, 4038 (1986).
67. S. G. Bailey, D. C. Creagh, and G. V. H. Wilson, *Phys. Lett. A*, **44**, No. 3, 229 (1973).
68. H. Enokiya, *J. Phys. Soc. Jpn*., **42**, No. 3, 796.
69. D. Fekete, H. Boasson, A. Grayevski, V. Zevin, and N. Kaplan, *Phys. Rev. B*, **17**, No. 1, 347 (1978).
70. H. P. Kunkel and C. W. Searle, *Phys. Rev. B*, **23**, No. 1, 65 (1981).
71. H. Brömer and H. L. Huber, *J. Magn. Magn. Mater*., **8**, No. 1, 61 (1978).
72. R. Street, D. S. Rodbell, and W. L. Roth, *Phys. Rev*., **121**, No. 1, 84 (1961).
73. D. C. Creagh, S. G. Bailey, and G. V. H. Wilson, *Philos. Mag*., **32**, No. 2, 405 (1975).
74. P. A. Chernavsky, *Russ. Chem. J.*, **XLVI**, No. 3, 19.
75. D. L. Leslie-Pelecky and R. D. Rieke, *Chem. Mater*., **8**, No. 8, 1770 (1996).
76. V. S. Pokatilov, *Russ. J. Solid State Physics*, **48**, No. 8, 1436 (2006).

4.3.2. High temperature strong CoAlO/Co-Al cermets

In this chapter, the internal filed ^{59}Co NMR application to ceramic Co-Al-O materials is shown. The chapter is based on our earliest publication in *Journal of Material Science and Engineering A* [4]. First of all, the author apologizes for the "Russian" English used in this article. The NMR interpretation in this work has been carried out in accordance with conventional sf_1-sf_5 defects observation. During the course of this PhD work, this point of view has been re-considered. Nevertheless, the work is of importance since the application of internal field NMR to study cermets (as construction or catalysis related materials) has been reported here for the first time.

Journal of Materials Science and Engineering A 2 (2) (2012) 121-136

Formation of Micro, Nano and Atomic-Level Structure of CoAlO/Co-Al Cermets Prepared by Mechanical Alloying

Andrey Andreev, Aleksey Salanov, Serguei Tikhov, Svetlana Cherepanova, Vladimir Zaikovskii, Vladimir Usoltsev, Vladislav Sadykov and Olga Lapina

Boreskov Institute of Catalysis SB RAS, 630090, pr. Lavrentieva 5, Novosibirsk, Russian Federation

Received: November 26, 2011 / Accepted: December 16, 2011 / Published: February 10, 2012.

Abstract: Micro, nano and atomic scale structure of Co-Al cermet prepared by mechanical alloying of Co-Al powders followed by hydrothermal treatment and calcination in the air were studied by X-Ray diffraction pattern (XRD), scanning electron microscopy (SEM), transmission electron microscopy (TEM), energy-dispersive X-Ray spectroscopy (EDX) and internal field ^{59}Co NMR techniques. The set of physicochemical methods revealed that the cermet metallic part of their particles includes regions comprised of Co and Co-Al alloy with the average Co: Al ratio~ 2. In turn, the oxide matrix is contained the mixture of cobalt aluminates (Co_2AlO_4 and $CoAl_2O_4$) and cobalt oxides (Co_3O_4, CoO). The interface between these two cermet parts is represented by aluminum oxide Al_2O_3 shell protecting the metallic core against further oxidation. The presence of metallic cores containing Co and Co-Al alloy increases CoAlO/Co-Al cermets crushing strength up to 700-800 kg/cm^2 that greatly exceeds Al_2O_3/Al cermet crushing resistance (10-100 kg/cm^2).

Key words: Co-Al alloy, CoAlO/Co-Al cermet, structure, microstructure.

1. Introduction

Ceramometals (cermets) comprised of oxide matrix with uniformly distributed metallic particles have been discovered more than fifty years ago [1-3]. These systems attract a lot of interest due to their application in electrical engineering and constructional materials as well as catalysts of different heat-demanding processes [4-14]. Thus, systems based on Ni-Al/Al_2O_3 cermets are promising catalysts of CH_4 dry reforming [11] or partial oxidation into syngas [12]. Fe- or Co-containing cermets are promising as catalysts of Fischer-Tropsch synthesis [13-14].

Traditionally cermets are manufactured by mixing powders of oxides and metals followed by pressing and sintering at high temperatures [15]. Another way of cermets preparation is based upon chemical self-propagating combustion reaction, i.e., Al + Co_2O_3 → Co + Al_2O_3. This technique includes stages of ball milling of powdered oxides and metallic aluminum, pressing without oxygen access and ignition [7-8].

Recently, the method of cermets preparation based on mechanical alloying of various metals with aluminum followed by subsequent hydrothermal treatment in special dies providing consolidation of powders into monolithic bodies due to partial oxidation of aluminum and hydration of the products of oxidation was developed [16]. This method allows to produce mechanically strong ceramic/cermet materials of complex shapes with phase composition, microstructure and porosity controlled by their chemical composition and specificity of synthesis procedures including thermal treatment of consolidated monoliths in specific environment (under air, N_2 etc) [17]. Mechanical, magnetic, catalytic and other characteristics of cermets depend also substantially on the spatial distribution of individual components in solids and their structural/microstructural

Corresponding author: Serguei Tikhov, professor, research fields: heterogeneous catalysis, porous ceramometals, surface chemistry of oxides. E-mail: Tikhov@catalysis.ru.

characteristics.

This work presents results of detailed studies of structural features of Co-Al cermets by using a combination of such techniques as XRD, SEM, EDX, and internal field ^{59}Co NMR. This approach allows elucidating structural features of Co-Al cermets on micro, nano and atomic levels.

The techniques which are usually used for such investigations include a combination of SEM (permits to analyze microstructure of materials) and XRD (characterizes phase composition and real/defect structure of phases, including estimation of point and extended defects (stacking faults, etc) concentrations). In addition, EDX allows estimating distribution of each element at the sample surface as well as stoichiometry of phases in separate points [7, 16]. After superposition of all separate element maps, the distribution of different phases in the surface region can be obtained.

The internal field ^{59}Co NMR technique allows to characterize the local structure of metallic Co. It can distinguish fcc and hcp phases of metallic cobalt and different types of stacking faults (sfs) present in these phases [18-19]. Moreover, presence of foreign atom (i.e., Al) in the coordination sphere of a ferromagnetic atom is known to affect its local magnetic field, which is reflected in spectra as a shift of resonance frequency [20].

All of these methods supplement each other allowing to elucidate comprehensively the multiscale bulk and surface structure of phases present in Co-Al cermet as well as to clarify the details of its genesis from pure Co and Al metals to Co-Al alloyed precursor [9] and finally, to CoAlO/Co-Al cermet. The methods were applied earlier for process study of Co-Al alloys formation after mechanical alloying (MA) and calcination at the inert atmosphere [21-23]. In our case, the processes taking place during cermet formation are more complicated and they include in particular hydrothermal oxidation (HTO) and as well as partial oxidation of MA products in the air which were not studied for Co-Al systems yet.

2. Experiment

2.1 Preparation Process

Commercial grade aluminum PAP-2 (GOST 5499-71) and commercial grade cobalt PK-IY (GOST 9721-79) powders were used as source materials. The powdered aluminum particles have a platelets shape up to few tens of microns in diameter [24]. The shape of cobalt particles is more irregular (vide infra).

The procedure of porous cermets preparation included three steps:

(1) Mechanical activation (MA) of the mixture containing 80 wt.% Co and 20 wt.% Al was used to synthesize the powdered precursor. MA was carried out in a high-power planetary ball mill APF. The acceleration of the balls was 65 g. The balls: powder weight ratio was 20, the ball diameter 5 mm, activation time 5 min.

(2) The product of mechanical activation was loaded into a stainless steel die specially designed to ensure free access of water and hydrogen release [25]. For hydrothermal treatment (HTT), the loaded die was placed in boiling water and kept there for 4 h producing a strong monolith (diameter 1 cm, length 8 cm).

(3) The product of HTT was removed from the die, dried for 1 hour at 120 °C and calcined under air slowly increasing temperature up to 900 °C (4 h). The calcination yielded a mechanically strong material.

The crushing (mechanical) strength was determined by crushing pellets (diameter ~10 mm, height ~3 mm) between two parallel plates in static conditions using a PK-2-1 instrument. The value was calculated as a ratio of the loaded stress at a crushing point to the section of the area of pellets.

2.2 SEM, TEM, EDX

Details of the microstructure were studied with the scanning electron microscope JEOL JSM-6460LV equipped with an EDX-INCA Energy-350 (Oxford Inst.) spectrometer. For SEM studies, the cermet sample was polished to obtain a flat cross-section. The

accelerating voltage used for registration of SEM images and EDX analysis of surface segments was equal to 20 keV. The values of atomic concentrations obtained after the standard computer processing included decimal values, though the actual errors, caused by difference in the dimensions of the analysis regions for the light and heavy elements, may be as high as few rel.%. X-ray color compositional mapping has been used as a critical tool for combining information from X-Ray maps of a different elements [26]. Phase mapping allows to construct spatial distribution of a given phase for all analyzed area (100 × 100 microns) [27]. The mapping was performed with E_p = 15 keV and the matrix size equal to 256 × 210 points. Total time of accumulation was 1 h. Elemental maps were obtained with energy equal to 1.49 keV for Al, 6.93 keV for Co, and 0.53 keV for O. The content of each element was determined from these peaks in each point. Elements content corresponds to a definite brightness level of white and black or intensity of a given color with spatial resolution of microstructure ~ 1 micron.

To determine cermet phase composition and phase distribution in its surface layer, scattering diagram analysis was performed. For three elements it represents triangle field where intensities of $K_{\alpha 1}$ peak chemical elements are located at the apexes of triangle. Each point in scattering diagram roughly corresponds to the points of the relative element content. At the apexes of triangles the content of the elements is 100 wt.%. Each element concentration in each point is determined by following way. First, it is necessary to draw a line through the given point that is parallel to side of triangle which is opposite to the element (Co, O, Al) which content needs to know. Second, the cross point of drawn lines and the corresponding triangle side (for Co is Co-O side, for O is O-Al side, and for Al is Al-Co side) divides the side into the two sections. The ratio of segment length not including the required element apex to the corresponding side length gives the desired element content.

TEM micrographs were obtained using JEM 2010 instrument with the lattice resolution 1.4 Å and acceleration voltage 200 kV.

2.3 Internal Field ^{59}Co NMR

The internal field ^{59}Co NMR spectra were recorded at room temperature on a Bruker Avance 400 spectrometer (magnetic field 9.4 T) without applying any external magnetic field using frequency-stepped and point by point methods with 8000 scans in each point. The pulse length was 4 μs, i.e., the width of exciting zone was 250 kHz.

The signal intensity of ferromagnetic materials is not directly proportional to the applied radiofrequency field (h_1). The Hamiltonian for NMR transitions in ferromagnetics does not contain Zeeman summand because the external magnetic field is not applied. So the summand for hyperfine interaction provides the main contribution. All transitions are induced by variable component of the transverse part of hyperfine field $(H_{hf})_\perp$ which is created by RF field (h_1). The rotation of nuclei magnetization is related to the enhancement factor η in domains, while displacement of domain walls is reflected in the enhancement factor in domain boundaries [28]. Equation taken from [29] expresses the relationships between the observed NMR signal $S(h_1,\omega)$ at a given frequency ω, applied RF field h_1 and the "real" corrected intensity $I_0(\omega)$

$$S(h_1,\omega) = \eta I_0(\omega)\exp[-\frac{\lg^2(h_1/h_{1opt})}{2\sigma^2}] \quad (1)$$

here h_{1opt} is the RF field at a signal maximum, and σ is the width of Gaussian distribution. If $h_1 = h_{1opt}$, the Eq. (1) transforms into

$$S(h_1,\omega) = \eta I_0(\omega) \quad (2)$$

It has been demonstrated [30] that $1/\eta$ is proportional to h_{1opt}. So the corrected intensity could be obtained from Eq. (3)

$$I_0(\omega) \propto h_{1opt} \cdot S(h_1,\omega) \quad (3)$$

To get corrected intensities $S(h_{1opt}, \omega)$, two-dimensional (2D) spectra are to be acquired [19].

The effect of different substitutions in cobalt

coordination sphere on ^{59}Co NMR resonance frequency was studied in details for alloys ([18, 20, 31-32]). Since extended defects in the pure Co lattice, first of all, stacking faults and twins, also change Co coordination sphere, respective variation of ^{59}Co NMR frequencies was observed as well [33-34].

From this corrected NMR spectrum Gaussian peaks were fitted to within 0.3 MHz of the literature values and the relative number of nuclei in each site is then equivalent to the relative areas under the Gaussians used to fit each site. The frequency was allowed to vary a little due to the effect of strain in the crystal lattice.

2.4 XRD

The X-ray diffraction (XRD) patterns were registered using a X'TRA (Thermo ARL) diffractometer (Bragg-Brentano geometry, CuK radiation, energy dispersed detector, step scan mode). Data registration was made in the 2θ angle range from 15° to 120° with step of 0.05° and accumulation time of 40 s in each point. Quantitative phase analysis was carried out by Rietveld refinement with use of PCW software [35].

Simulation of XRD patterns for disordered metallic cobalt particles was carried out using the program [36]. The calculations were performed using the model of a crystal disordered in one dimension (1D). The model is built as a statistical sequence of a finite number of 2D periodic layers. The Markov chain is used as a generation rule for the statistical stacking sequence. Stacking sequences were simulated as consisting of identical hexagonally close packed (hcp, or AB type) layers. In this AB-AB-AB-AB… structure, there is no shift between AB layers (the first type of superposition). In the cubic close packed (fcc) structure, AB layers are shifted on the (1/3, 2/3) vector (the second type of superposition) to provide AB-CA-BC-AB-… sequence.

Deformation stacking faults mean statistical appearance of the extrinsic type of superposition which creates fcc fragments (AB-CA) in hcp structure and hcp fragments (AB-AB) in fcc structure. Such kind of disorder can be described by using one parameter which defines the probability of appearance of extrinsic type of superposition.

Microdomain structure consisting of slabs having fcc and hcp structures can be defined by using two probabilistic coefficients. The first one is the probability W_1 of appearance of the first type of superposition between AB layers (W_2 is calculated as $1-W_1$). The second coefficient is conditional probability P_{11} of following the first type of superposition by the first type of superposition. P_{11} determines the average thickness of fcc slabs $\langle L_{fcc} \rangle$. The ratio W_2/W_1 gives relation between the average thicknesses of hcp and fcc slabs. So the average thickness of hcp slabs $\langle L_{hcp} \rangle$ can also be calculated.

The average crystallite sizes within and normal to densely packed layers $\langle D_{xy} \rangle$ and $\langle D_z \rangle$ are also variable parameters of the model.

3. Results and Discussion

3.1 Source of Co Powder

Fig. 1 presents XRD pattern of the initial sample which is similar to hcp modification of metallic cobalt but there are some peculiarities. One can see that 101 and 102 peaks are broader than 100 and 002 ones.

These features can be assigned to the presence of stacking faults in the hcp structure [37]. In addition, very small and broad 200 peak of fcc modification of metallic Co is observed. Such XRD pattern is fitted within a model of scattering on crystallites consisting of alternating slabs with hcp and fcc structure with average hcp and fcc layers: thickness $\langle L_{fcc} \rangle = 2$ nm and $\langle L_{hcp} \rangle = 8$ nm. X-ray particle sizes were found to be 60 nm in normal to layers direction and 30 nm within the layers.

Corrected internal field ^{59}Co NMR spectrum of metallic cobalt particles is given in Fig. 2. The observed spectrum has a huge width that is usual for ferromagnetics. First of all, the spectrum contains components corresponding to unfaulted fcc and hcp Co

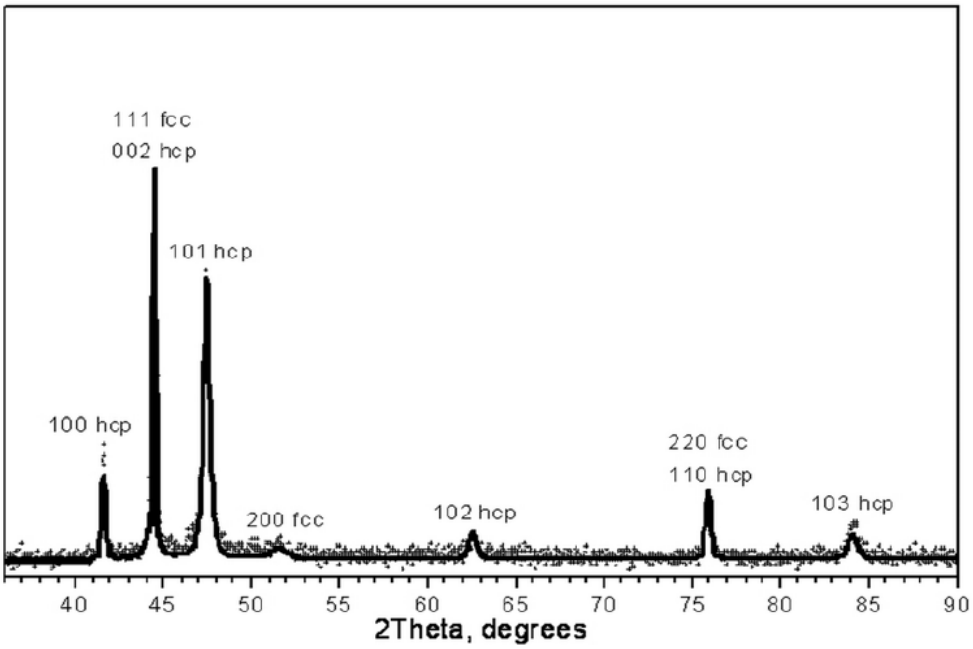

Fig. 1 XRD pattern of the initial sample of metallic Co (points) and its simulation for hcp-fcc domain structure (line) with parameters: $\langle L_{hcp} \rangle$ = 8 nm, $\langle L_{fcc} \rangle$ = 2 nm, $\langle D_z \rangle$ = 60 nm, $\langle D_{xy} \rangle$ = 30 nm.

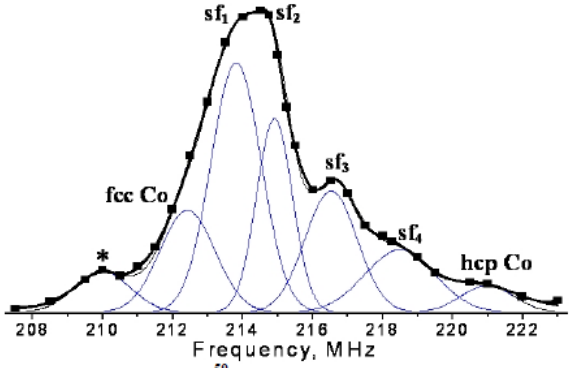

Fig. 2 Internal field ^{59}Co NMR spectrum of pure metallic cobalt. Experimental points: black squares (■), thin lines: fitting Gaussian peaks, bold solid line: cubic spline; *: atoms in magnetic domain boundaries.

phases at 212.2 MHz and 220.9 MHz, respectively. The total content of unfaulted phases (Table 1) is 15.5%, so the main part of spectrum corresponds to various Co stacking faults. These stacking faults are usually assigned as follows: sf_1 and sf_2, one stacking error in the fcc sequence, i.e., fcc twin faults or, alternatively, two consecutive stacking faults in the hcp sequence, i.e., deformation faults in hcp; sf_3 and sf_4 correspond to one stacking fault in hcp sequence, i.e., twin faults in hcp, or two stacking faults in fcc, i.e., deformation faults in fcc; sf_5 is not unambiguously assigned to any stacking sequence, although these sequences are often related to stacking faults in hcp structure [33-34, 38]. As follows from Fig. 2, the main part of cobalt atoms corresponds to sf_1 and sf_2 (Table 1) (peaks at 214.2 MHz and 214.9 MHz). Spectral components observed at 216.7 MHz and 218 MHz correspond to Co atoms in sf_3 and sf_4 while the component assigned to sf_5 (~ 224 MHz) was not detected (Table 1). The peak at 209.9 MHz (Fig. 1) can be assigned to Co atoms in a loose coordination environment (i.e., such as in grain boundaries) or having in their coordination sphere some impurities (traces of oxygen and carbon trapped from the air or admixed cations). To calculate the total amount of Co atoms in hcp or fcc phase, contributions from Co atoms in the regular phase and respected defects were summed up. In fact, the ratio of Co atoms in hcp and fcc phase close to 2:1 was obtained. The assignment of various stacking faults to hcp or fcc package was performed according [18].

This ratio differs from that estimated from XRD data

Table 1 Relative content of Co atoms in different packages by internal field ^{59}Co NMR.

	fcc Co			hcp Co			
Co phases	perfect	sf_3	sf_4	sf_1	sf_2	perfect	sf_5
Relative amount (%)	11.9	16.1	10.0	30.8	21.5	3.6	0
NMR frequency (MHz)	212.2	216.7	218	214.2	214.9	220.9	224

(~4), which is explained by the different information obtained by each method – local structure of Co atoms by NMR and structural features of extended slabs along with their packing sequence by XRD. With a due regard for big (~microns) sizes of both separate metallic Co particles and their irregular aggregates observed by SEM (Fig. 3) as well as much smaller X-ray particle sizes (vide supra), the density of various types of extended defects, and, hence, concentration of Co atoms in distorted coordination environment could be really high.

3.2 Co-Al Powdered Precursor

The first stage of cermet preparation is MA of the mixture of initial Co and Al powders (see Experimental). As follows from XRD pattern of activated sample (Fig. 4), a part of metallic Al remains after MA. Reflections corresponding to $CoAl_x$ alloy are not observed due to its amorphous state at early MA stages [9]. As in the initial sample, cobalt crystallites are comprised of hcp and fcc domains with smaller X-ray sizes ($<D_z>$ = 20 nm and $<D_{xy}$ = 15 nm) as well as the average thickness of fcc and hcp slabs ($<L_{hcp}>$ = 2.4 nm, $<L_{fcc}>$ = 1.2 nm).

Fig. 5 shows the internal field ^{59}Co NMR spectrum of Co-Al powdered sample activated for 5 minutes. The width of spectrum for activated sample increases in comparison with the metallic Co. It contains the same fcc, hcp and sf1-sf4 components as for pure metallic cobalt. In addition, new sf5 component appears at higher frequencies, and a low-frequency tail corresponding to Co-Al alloy emerges. The intensity of components corresponding to "perfect" hcp and fcc phases increases as well. All components in the activated sample spectrum are strongly overlapped due to general disordering of particles caused by mechanical activation and alloying.

TEM data confirm a complex character of MA Co-Al sample structure at nano- and atomic scale. Bulky heterophase particles with sizes in the range of 2 -5 microns are observed (Fig. 6a), their composition and structure varying from the middle of particle to its periphery. Aggregates of relatively large metallic Co domains are separated by more loose Al-containing areas (Fig. 6b). Large domains of Co possessing the fcc structure (d_{111} spacing 0.2 nm) are rather disordered due to microstrains as revealed by Moire pattern in HRTEM image (Fig. 6c). Loose areas include Co nanoparticles with sizes in the range of 10-30 nm similar to those earlier observed for Co -Al mixture

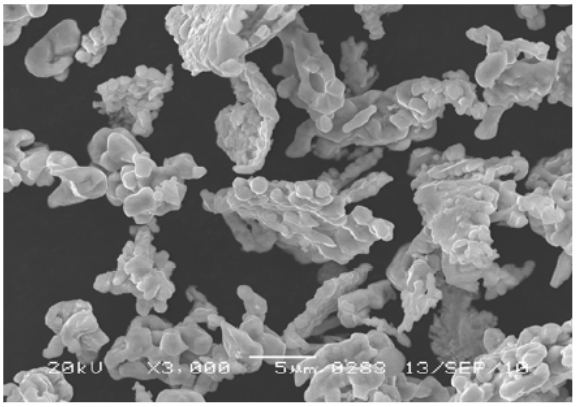

Fig. 3 SEM micrograph of initial cobalt powder particles.

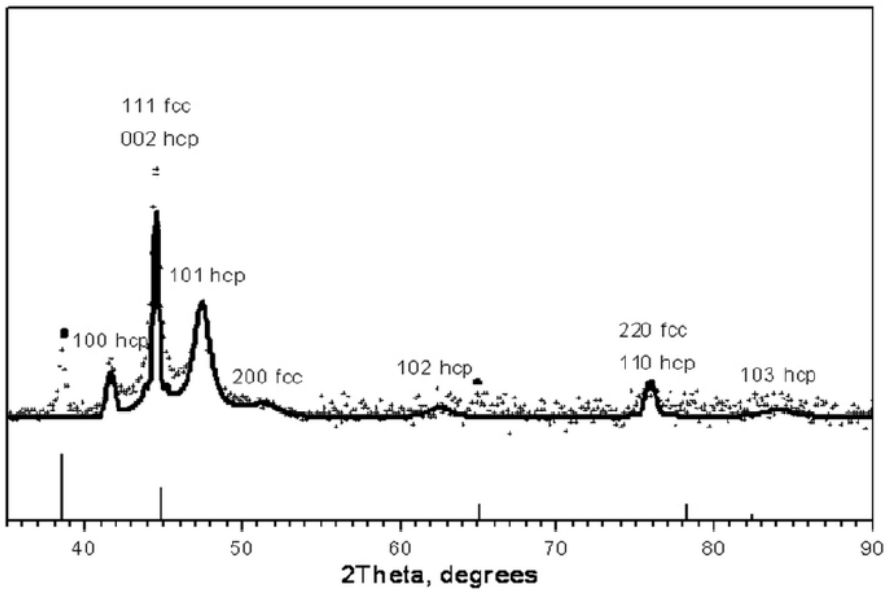

Fig. 4 XRD pattern of ball milled Co-Al sample (points) and its fitting (line) with parameters $\langle L_{hcp} \rangle$= 2.4 nm, $\langle L_{fcc} \rangle$= 1.2 nm, $\langle D_z \rangle$= 20 nm, $\langle D_{xy} \rangle$= 15 nm (top). Diffraction peaks of metallic Al are marked by vertical lines.

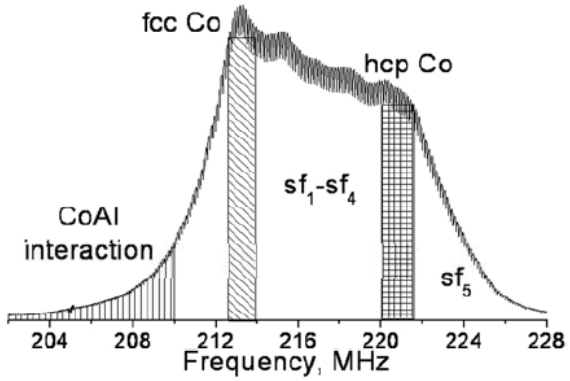

Fig. 5 Internal field ^{59}Co NMR spectrum of Co-Al ball milled sample.

with 1:2 atomic ratio mechanically activated for 9-20 minutes [9]. These nanoparticles have a multiply (111) twinned fcc structure (Fig. 6d-e), which agrees with results of XRD and internal field ^{59}Co NMR. Such Co particles were not revealed earlier in Co-Al alloys [9], though being observed in some Co catalysts [39].

The lattice image from loose areas containing both Co and Al is presented in Fig. 6f. The reflections in digital diffraction pattern (DDP) correspond to Co_2Al_9 alloy [40]. Due to a small size, these alloy nanoparticles were not detected by XRD. However, their presence is confirmed by the internal field ^{59}Co NMR data. Earlier products of Co and Al mechanical alloying with high (75 at.%) Al concentration were shown to be amorphous Co_2Al_5 phase [9].

SEM data (Fig. 7a) show that mechanical activation drastically changes the shape and size of particles on the micron scale. Not only large aggregates with size comparable with that of initial Co and Al particles are observed but also small particles appear due to grinding.

The internal microstructure of large aggregates has a complex character (Fig. 7b). Two types of microstructure are observed: (1) disordered aggregates containing Co and Al in atomic ratio 45:55 by EDX data; (2) regions containing only Co. A part of disordered Co-Al aggregates combines with metallic Co particles to form large (up to tens of microns) particles. Hence, all applied methods demonstrate that mechanical activation has not resulted in complete Co and Al intermixing at the atomic level.

All EDX data points are characterized by noticeable content of oxygen (from 2 to 10 at.%) associated with the surface oxidation after contact with air or during MA process.

Hence, after ball milling we still have both metallic

Co and Al particles and, in addition, Co-Al alloy appears. In general, the structure of activated product is more disordered as compared with that of Co powder due to heterogeneous intermixing with Al.

3.3 CoAlO/Co-Al Cermet

3.3.1 XRD

XRD cermet pattern after hydrothermal treatment and calcination at 900 °C in the air (Fig. 8) shows presence of several phases including Co3-xAlxO4 spinel, metallic Co, CoAl intermetallide, CoO oxide and alumina.

The main part of cermets (66 wt.%) is comprised of $Co_{3-x}Al_xO_4$ spinel type phases. It is hard to distinguish composition of spinel type compound because Co_3O_4, Co_2AlO_4 and $CoAl_2O_4$ have very close lattice constants 8.083, 8.086 and 8.104 Å, resp. The lattice constant of $Co_{3-x}Al_xO_4$ obtained from XRD data is equal to 8.099 Å, so x is close to 2.

The content of metallic Co and Co-Al alloy is equal to 12 and 17 wt.%, resp. Hence, a part of metallic Co is not oxidized after HTT and sintering under air at 900 °C, which is not expected. Metallic cobalt has a perfect high-temperature fcc structure with the average crystalline size about 30 nm. It means that Co particles are partially sintered during annealing because their average size in ball milled precursor is about 5-20 nm. The content of CoO oxide in cermet is ~ 5 wt. %.

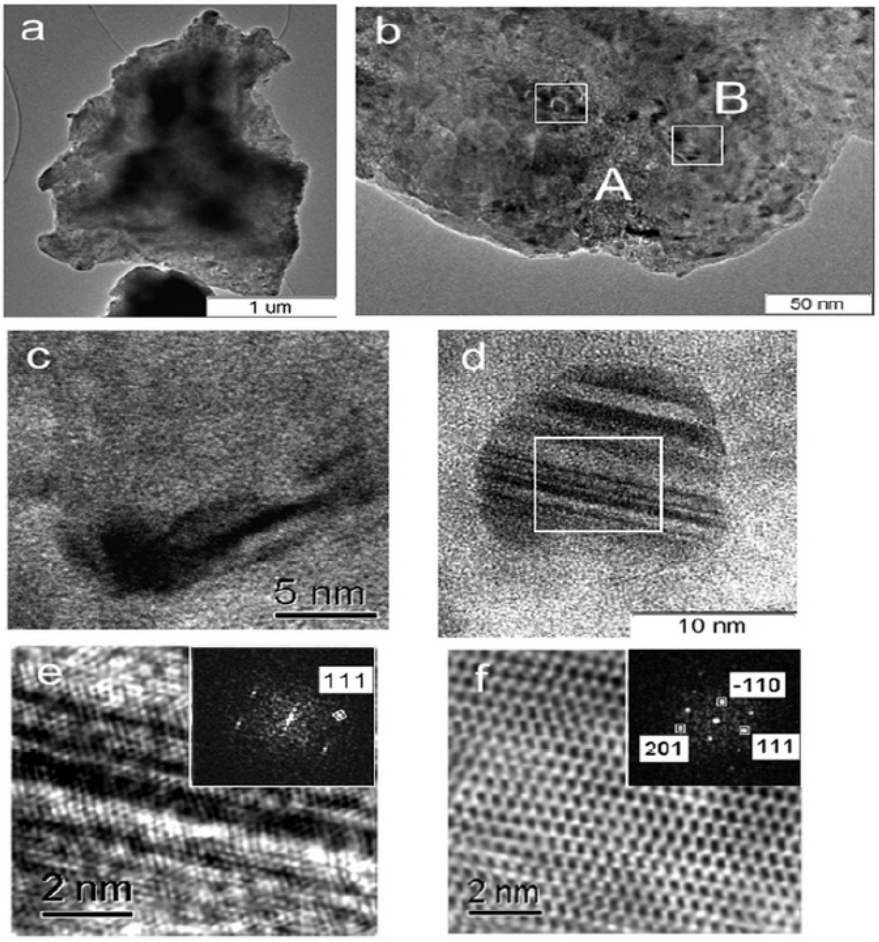

Fig. 6 (a) Morphology of a bulky Co-Al-O heterophase particle; (b) Areas containing Al phase (A) and metallic Co phase (B); (c) Moire pattern in HRTEM image; (d) multiple twinned Co nanoparticle, (e) HRTEM image of Co twinned nanoparticle and digital diffraction pattern (DDP) (inset) with elongated reflections from fcc Co; (f) HRTEM image of Co_2Al_9 alloy lattice and DDP (inset) with reflections corresponding to d_{110} = 0.507 nm; d_{111} = 0.382 nm; d_{201} = 0.337 nm.

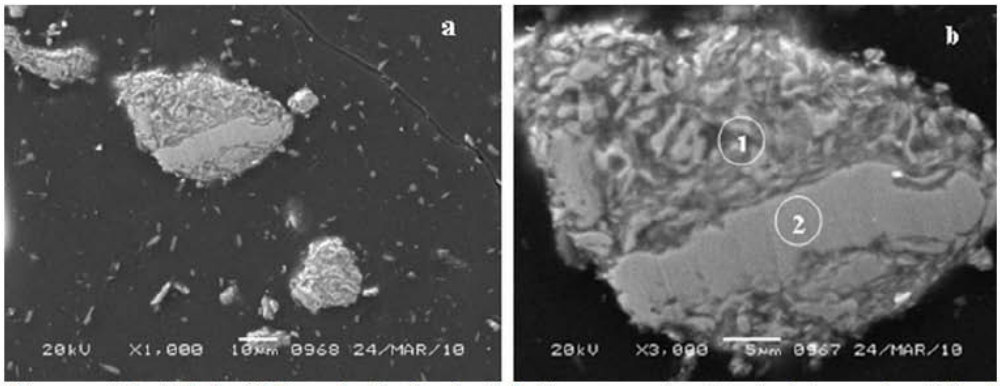

Fig. 7 SEM images of Co-Al ball milled powder fixed and polished in epoxy resin: (a) typical shapes of particles, (b) enlarged image of a particle comprised of disordered Co-Al aggregates (1) and sintered metallic Co particles with a low O content (2).

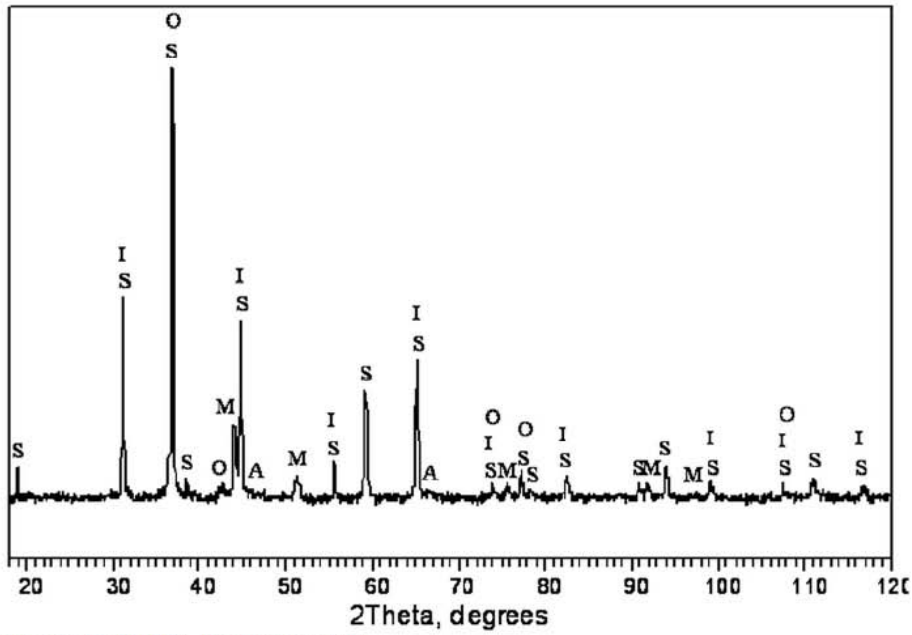

Fig. 8 XRD pattern of CoAlO/Co-Al cermet sample.

S: $Co_{3-x}Al_xO_4$ spinel, I: CoAl intermetallide, M: metallic Co, O: CoO oxide, A: alumina.

A small (~ 1 wt.%) amount of alumina has also been detected as a halo at $2\theta \sim 67^{\circ}$.

To compare XRD data with those of NMR, atomic percentage of Co atoms in pure Co phase (49%) and in Co-Al alloy (51%) was estimated.

3.3.2 Internal field ^{59}Co NMR

Internal field ^{59}Co NMR data present detailed structure of the non-oxidized metallic Co part of the cermet.

NMR spectrum (Fig. 9) can be divided into two main parts. The first one corresponds to pure fcc Co (212.2 MHz) and the second one to Co-Al alloy (below 209 MHz) [20]. Domination of the first component clearly correlates with the Co excess in the initial mixture. Comparison of this spectrum with those of initial and mechanically activated sample shows that peaks corresponding to hcp phase and sfs disappear as it was expected after high-temperature treatment. Spectral line broadening to low frequencies suggests that substitution Al for Co occurs continuously (from 0 to 7 Al atoms in Co coordination sphere). However, the spectrum exhibits presence only from 1 to 5 Al atoms

that is associated with not fully recorded spectrum due to the tuning frequency problems in the frequency range below 195 MHz. The all substitution peaks (Table 2) are equidistant with a step of 3 MHz. The intensity of these peaks reflects the probability of each substitution type decreasing with increasing the number of substituent Al atoms.

Data of Table 2 allow to estimate the atomic ratio of Co atoms in a pure metal (46 at.%) and in Al-Co alloys (54 at.%). These results are in a good agreement with XRD data. Hence, the contribution of unregistered peaks is small because the intensity of each subsequent peak is less than previous.

3.3.3 SEM Analysis

A spatial distribution of elements in the cermet characterized by SEM and EDX methods helps to obtain comprehensive picture of CoAlO/Co-Al cermet microstructure. Fig. 10 shows the SEM micrograph for the polished surface of CoAlO/Co-Al cermet with a complex microstructure. In fact, SEM micrograph provides 2D image but the choice of polishing surface is arbitrary so we can suppose that 2D image represents the same information as 3D one.

The main characteristic features are indicated in Fig. 10. There are dark regions of various shapes (typical size 5-10 microns) with brighter patches situated at their boundaries. These regions correspond to pores distributed in the bulk of sample (marked by 0 in Fig. 10). The main contribution to brightness variation during probe shift corresponds to changing the local chemical composition of cermet. The secondary emission coefficient of material increases with the element atomic number (Z) so regions with a higher average Z are characterized by a brighter image. The regions with similar brightness can be assigned to phases of the same chemical composition. So, in addition to pores, two characteristic types of phases can be distinguished in Fig. 10. One of them (marked by 1) with typical size 10-50 microns corresponds to Co-rich cores. These cores have a sandwich-type structure with alternating bright and dark domains. They are covered by a darker shell with thickness ~ 1 μm. Another characteristic fragment (marked by 2) of a dark appearance (and, hence, possessing a smaller average Z) is an oxide matrix where metallic cores (1) are distributed.

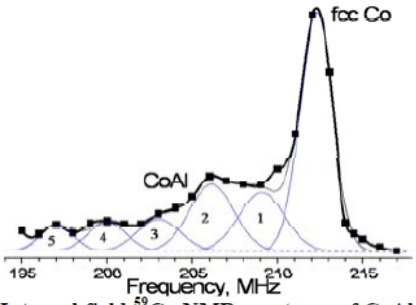

Fig. 9 Internal field ^{59}Co NMR spectrum of CoAlO/Co-Al cermet corrected for the enhancement factor and fitted Gaussian peaks corresponding to a number of Al atoms replacing Co atoms in the first coordination sphere (signed by numbers). Black squares (■) indicate experimental points, bold line is extrapolation, and thin line is the fitted peak sum.

Fig. 10 SEM micrograph of polished surface of CoAlO/Co-Al cermet.

0: pores; 1: sandwich-type cores enclosed by well-defined boundary line; 2: porous fragments with more uniform grey color.

Table 2 Relative content of Co atoms in different packages by internal field ^{59}Co NMR (indicated by numbers of Al atoms in Co coordination sphere) for CoAlO/Co-Al cermet.

Phase	fcc Co	1	2	3	4	5
Relative amount (%)	46.4	16.1	17.8	8.1	6.5	5.1
NMR frequency(MHz)	212.2	209	206	203	200	197

3.3.4 SEM Analysis: Elemental Mapping and Scattering Diagram

To precise further chemical composition of phases present in cermet, elemental mapping technique was applied. All data from the maps of the individual element distributions were transferred into scattering diagram. This diagram gives more objective information about stoichiometry of different fragments and their distribution in monolith cermet. The diagram (Fig. 11) consists of dots which are located in total distribution map of the all elements. One dot in scattering diagram corresponds to the all points with the equal stoichiometry at the microscopic image. So the scattering diagram was divided into five fragments (Fig. 11 and Table 3) with similar stoichiometry because they have similar tints.

First of all, one two groups of points can be selected corresponding to a constant high O content (fragments a and b in Fig. 11) and constant low O content (fragments d and e in Fig. 11). There are no clear areas with a narrow Co, Al, O stoichiometric interval since this case supposes separate definite points in the diagram. There are only two broad almost parallel lines (with high and low O concentration) intersecting in high Al concentration region (fragment c in Fig. 11). The ratio Co/Al varies in a broad range for both groups of point i.e., from Co surplus to Al excess. It means that, in agreement with XRD and NMR data, continuous variation of Co/Al stoichiometry takes place for both oxide and metallic cermet parts.

Average atomic ratio was calculated in each quadrangle (regions a-e) in Fig. 11. All data are placed in Table 3. First of all, it is very important to underline relative character of values given in Table 3 since they characterize tendencies but not absolute stoichiometry of possible compounds.

According to this Table 3, several specific features can be underlined:

(1) The absence of pure Co or Al areas on a microscopic scale. In each quadrangle, concentration of elements changes continuously.

(2) Co and Al ratio changes non-monotonously. Al maximum corresponds to Co minimum and vice versa (region c).

(3) O concentration slightly increases from a to b and monotonously decreases from b to e.

(4) The fragment e, probably, does not contain O, it is only metallic cermet part, so the overall oxygen concentration in d-e regions seems to be overestimated by 10-12% due to surface oxidation during sample polishing.

Firstly high O content group of points (fragments a and b in Fig. 11) was analyzed. The first region (quadrangle a in the scattering diagram) with a low Al content contain mainly CoO or Co_3O_4 since these cobalt oxides have rather close stoichiometry. It is in agreement with XRD data for the reason that the X-ray pattern contains CoO and cobalt spinel peaks. The next fragment with a high O concentration (quadrangle b of the scattering diagram) demonstrates Co-Al-O phase distribution with Co to Al ratio close to 1. These data are also in a good agreement with XRD analysis which detects spinel $Co_{3-x}Al_xO_4$ structures with a broad range of stoichiometry in the oxide part of cermet (Fig. 8).

The two fragments a and b (emerald and scarlet colors in Fig. 11) with a high O content constitute the oxide matrix of cermet. The middle fragment (quadrangle c of the scattering diagram) contains a high Al and a low Co concentration. It is clear that Al is basically located at the boundary between the metallic cores and oxide matrix. Apparently, the interface oxide film comprised mainly of Al_2O_3 (Figs. 10 and 11). Some admixtures of alumina are also present within the core, but it may be caused by oxidation of metallic Al particles during sample preparation for analysis. We should note that the EDX measurements resolution is about 1 μm^2, and the region c in Fig. 11 is characterized by a small Co content (Table 3 fragment c). If the size of alumina particles is less than 1 μ, Co-containing fragments will always be captured as well, which could explain Co presence in region c.

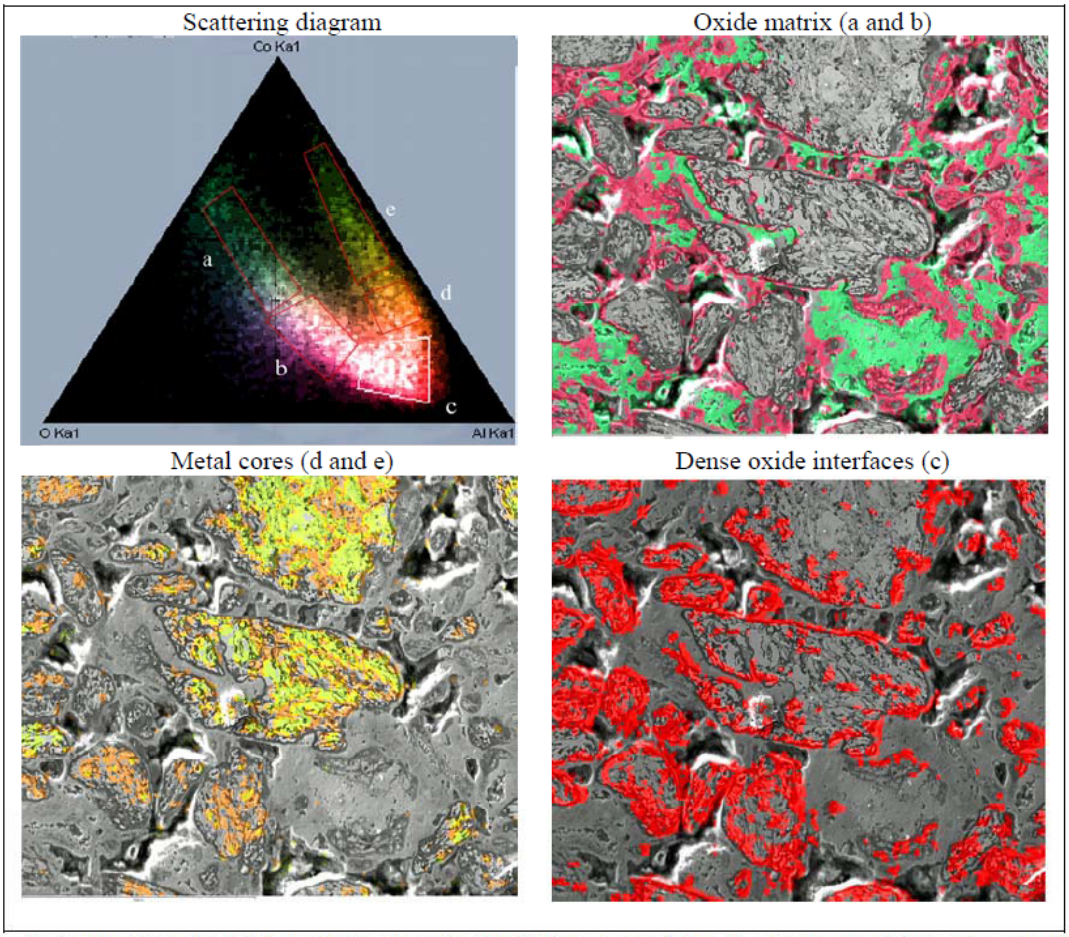

Fig. 11 Scattering diagram calculated from elements distribution maps of Co, Al, and O and various phases distribution marked out in the scattering diagram: oxide matrix, dense oxide interface, metal cores.

Table 3 Composition of different fragments shown in Fig. 11.

Fragments in Fig. 11	O (%)	Al (%)	Co (%)
a (emerald)	45.1	9.3	45.5
b (scarlet)	52.7	23.5	23.8
c (red)	42.2	39.8	18.1
d (orange)	20.1	36.7	43.2
e (green)	11.5	24.8	63.7

At last, low O-containing group of points within sandwich-type core fragments was analyzed. The first fragment inside cores (quadrangle d in the scattering diagram) corresponds mainly to Co-Al alloy. However, comparison of Fig. 11 and 10 shows that Co and Al interlayers are localized not only at the core boundary but also inside the cores. The average Co:Al ratio in these cores is ~2, that is in agreement with XRD measurements giving near the same average stoichiometry. Fragment e represents big metallic Co excess (Table 3). Apparently, it is the region for the fragment with a high content of metallic Co which was not oxidized during annealing at 900 °C. Most probably, $Co_{8-n}Al_n$ stoichiometry is changed continuously because each type gives the contribution to NMR spectrum (Gaussian components fitting, Fig. 9). The fragments containing metallic Co were shown to alternate with thin oxide interlayers (orange and

green, Fig. 11) during spatial distribution analysis (Fig. 11). Apparently, the oxide strata on the surface prevent Co from bulk oxidation. The average fragment size inside the cores is less than in the oxide matrix (Figs. 8d, 8e and 10).

Thereby, metallic cores are surrounded by redundant alumina which, probably, prevents oxidation of metallic Co. On the other hand, another reason of metallic Co protection is the formation of CoAl intermetallide particles with sandwich-type microstructure. The fact that XRD registered very small amounts of metallic Co in contrast to internal field ^{59}Co NMR could be explained by the amorphous character of Co-Al alloys or very small size of Co particles. Consecutive change in Co-Al-O stoichiometry from Co excess to Al excess leads to formation of spinel-like Co-Al-O structures. In the same way as in MA sample, CoAl intermetallide is built into metallic domains.

3.3.5 Specificity of the CoAlO/CoAl cermet formation

Being based on obtained results we may suppose the following processes which occur during MA stage of Co (80 wt.%) and Al (20 wt.%) mixture. Partial phase transformation to less thermostable phase $Co_{fcc} \rightarrow Co_{hcp}$ happens. The decrease of initial Co crystalline sizes due to ball milling and increase the sfs concentration occurs. Partial Al amorphization occurs and Al and Co composites are formed at both nano and micro scale. Co and Al interaction occurs with the formation of amorphous CoAl intermetallide including Al_2Co_9 and etc..

The main conclusions concerning MA influence to Co-Al blends obtained in this paper agree with published earlier [21-23]. For example, the main deduction about nanocomposite formation, Al amorphization, and transformation from α-Co (fcc Co) to β-Co (hcp Co) in our work coincides with the paper [9]. The formation of twins and decrease of Co particles size were observed in [21] and of nanostructurated alloys in [9, 23]. The several types of intermetallic particles were detected during long time MA [9, 21, 23].

Unlike the published papers the present work has the MA time which is substantially lower (5 min). It is not sufficient to form well-crystallized intermetallic particles but it is quite enough to use MA product at the synthesis of solid cermet. Also we do not measure stoichiometry of X-ray amorphous intermetallides but XRD analysis and internal field ^{59}Co NMR allow to detect several types of $CoAl_x$ compounds with various stoichiometry.

HTO stage was not studied in detail. However, the fact that strong monolith is formed after HTO proves the presence of Al oxidation and hydration: $Al + H_2O \rightarrow AlO(OH)_y + H_2$. Aluminum hydration products cement the composite particles into porous monolith.

The last stage including the calcination in the air of MA and HTO products is more complex process than conventional annealing under an the inert atmosphere of MA products described earlier [9, 21-23]. It consists of not only solid state reaction like Co-Al interaction or various intermetallides crystallization [9, 21-22] but also includes partial oxidation of solids by oxygen. However, it is necessary to underline that most of intermetallides crystallization processes go at the temperatures that are considerably lower than melting temperature of aluminum [21]. Therefore, the formation starts from metallic cores which are stable to oxidation and then the bulk oxidation of cermet begins during the temperature growth. The primary intermetallic particles creation prevents further Co oxidation in the bulk of metallic cores due to formation of protecting oxide film based on the alumina [41].

3.3.6 Structure model of CoAlO/Co-Al cermet and its relation with Co-Al powdered precursor

On micron level, the structure of Co-Al cermet could be described as metallic cores with sizes in the range of 10-50 microns dispersed within composite oxide matrix. More precise atomic structure given by internal field ^{59}Co NMR revealed these cores to consist of metallic Co and Co-Al alloy of variable composition

$Co_{8-n}Al_n$ (n = 0-7) with average Co/Al ratio ~2. Both Co and Co-Al alloy are uniformly distributed inside very densely packed cores which prevent full oxidation of the phase of metallic cobalt.

The atomic structure characterized by internal field ^{59}Co NMR and XRD is represented by the high temperature fcc Co phase (hcp Co and all sfs were transformed to regular fcc structure during annealing at 900 °C because of the phase transition at T = 420 °C) with particle size 1-5 microns. The ratio of fcc Co to Co-Al alloy is close to 1:1, which is in a good agreement with XRD data. The ceramic part (matrix) of cermet contains $Co_xAl_{3-x}O_4$ oxides with Co:Al ratio ≈1:1 by EDX analysis. Metallic cores appear to be sited into oxide matrix consisting of the mixture of cobalt aluminates Co_2AlO_4 and $CoAl_2O_4$ with the average Co:Al ratio ~1 and cobalt oxides - Co_3O_4 spinel and CoO monoxide.

It is important to clarify the relationship between the structures of cermet and powdered MA Co-Al precursor to control cermet properties. The fragments consisting of metallic Co (Fig. 7b-2) are expected to be fully oxidized to cobalt oxides (Figs. 11 a and 11b) after calcination in the air. Micron-size composites containing both Co and Al (Fig. 7b-1) most probably form the oxide matrix consisting of $CoAlO_x$, CoO_x (Fig. 11). The nanocomposite fragments (Fig. 7a) appear to generate $CoAl_x$ intermetallides which alternate with metallic Co particles preventing fragments oxidation (Fig. 11). The interaction between Co and Al apparently occurs during sintering via self-propagating process when temperature is increased up to the Al melting temperature (660 °C), i.e. before bulk oxidation of Co particles begins. This clearly helps to stabilize metallic cores via subsequent formation of protective alumina layer on the metallic cores surface at temperatures higher than aluminum melting temperature similar to processes found for FeCrAl steels [42-43].

3.3.7 Mechanical properties of CoAlO/Co-Al cermet

Presence of metallic Co inside the cores of cermets greatly reinforces cermets increasing the crushing strength up to 700-800 kg/cm^2, which is much higher than that for Al_2O_3/Al cermet (crushing strength 10-100 kg/cm^2 [17, 24]).

4. Conclusions

Application of several advanced method (XRD, TEM, SEM with X-ray elemental mapping for construction of scattering diagram of different fragment types, internal field ^{59}Co NMR) for elucidation of the structural features of Co-Al cermet prepared via mechanical alloying followed by hydrothermal treatment and annealing in the air revealed pronounced non-uniformity of phase and elements distribution. Metallic phase includes metallic Co and Co-Al alloy covered by Al_2O_3 oxide film which protects this phase from oxidation. The oxide matrix surrounding metallic domains consists of cobalt aluminates and cobalt oxides phases. The presence of metallic cores greatly improves the cermet mechanical strength.

Acknowledgments

This work was supported by RFBR 11-08 00704 Project. The authors thank G.V. Golubkova and O.I. Lomovsky for mechanical alloying of Co and Al metals.

References

[1] P. Patent, Schwarzkopf 1929 (issued 1942) Germany N 750502.

[2] P. Schwarzkopf, R. Kieffer, Cemented Carbides, The Macmillan Co., New York, 1960.

[3] R. Kieffer, F. Benesovsky, Hartmetalle, Springer-Verlag Wien/New York, 1965.

[4] Y.H. Yun, S.W. Hong, S.C. Choi, Metal penetration processing and mechanical properties of Al/Al_2O_3 composite system, Journal of Materials Science Letters 21 (2002) 1297-1299.

[5] S.T. Oh, T. Sekino, K. Niihara, Fabrication and mechanical properties of 5 vol% copper dispersed alumina nanocomposite, J. Eu. Ceram. Soc. 18 (1998) 31-37.

[6] X.Y. Qin, R. Cao, J. Zhang, Mechanical and magnetic properties of gamma-Ni$_x$Fe/Al_2O_3 composites, Composites Science and Technology 67 (2007) 1530-1540.

[7] O. Aharon, S. Bar-Ziv, D. Gorni, T. Cohen-Hyams, W.D. Kaplan, Residual stresses and magnetic properties of alumina-nickel nanocomposites, Scripta Materialia 50 (2004) 1209-1213.

[8] T. Lu, Y. Pan, Combustion synthesis of ferromagnetic Al_2O_3-based cermets in thermal explosion mode, J. Mater. Sci. 45 (2010) 5923-5928.

[9] G.V. Golubkova, O.I. Lomovsky, Y.S. Kwon, A.A. Vlasov, A.L. Chuvilin, Formation of nanocrystalline structures in a Co-Al system by mechanical alloying and leaching, Journal of Alloys and Compounds 351 (2003) 101-105.

[10] E.V. Pugacheva, V.N. Borshch, S.Y. Zhuk, D.E. Andreev, V.N. Sanin, V.I. Yukhvid, SHS-Produced intermetallides as catalysts for deep oxidation of carbon monoxide and hydrocarbons, Int. J. Self-Prop. High-Temp. Syn. 19 (2010) 65-69.

[11] L.A. Arkatova, The deposition of coke during carbon dioxide reforming of methane over intermetallides, Catalysis Today 157 (2010) 170-176.

[12] S. Pavlova, S. Tikhov, V. Sadykov, Y. Dyatlova, O. Snegurenko, V. Rogov, et al., Monolith composite catalysts based on ceramometals for partial oxidation of hydrocarbons to synthesis gas, Natural Gas Conversion 147 (2004) 223-228.

[13] S.F. Tikhov, V.I. Kurkin, V.A. Sadykov, E.V. Slivinsky, Y.N. Dyatlova, A.E. Kuz'min, et al., Hydrogenated Zr-Fe alloys encapsulated in Al_2O_3/Al matrix as catalysts for Fischer-Tropsch synthesis, Natural Gas Conversion 147 (2004) 337-342.

[14] A.Y. Khodakov, W. Chu, P. Fongarland, Advances in the development of novel cobalt Fischer-Tropsch catalysts for synthesis of long-chain hydrocarbons and clean fuels, Chemical Reviews 107 (2007) 1692-1744.

[15] Patent USA N 546903.

[16] S. Tikhov, V. Usoltsev, A. Salanov, S. Tsybulya, Y. Chesalov, G. Kustova, et al., Design of composite porous cermets synthesized by hydrothermal treatment of CrAl powder followed by calcination, Journal of Materials Science 45 (2010) 3160-3168.

[17] V. Sadykov, V. Parmon, S. Tikhov, Design of some oxide/metal composite supports and catalysts, Composite Interfaces 16 (2009) 457-476.

[18] R. Speight, A. Wong, P. Ellis, T. Hyde, P.T. Bishop, M.E. Smith, A ^{59}Co NMR study to observe the effects of ball milling on small ferromagnetic cobalt particles, Solid State Nuclear Magnetic Resonance 35 (2009) 67-73.

[19] R. Speight, A. Wong, P. Ellis, P.T. Bishop, T.I .Hyde, T.J. Bastow, et al., ^{59}Co NMR study of the allotropic phase transformation in small ferromagnetic cobalt particles, Physical Review B 79 (2009).

[20] Y. Koi, A. Tsujimura, NMR of ^{59}Co in Ferromagnetic Cobalt Alloys, J. Phys. Soc. Jpn. 16 (1961) 574-574.

[21] V.K. Portnoi, K.V. Tret'yakov, V.I. Fadeeva, Structural transformations during the mechanochemical synthesis and heating of Co-Al alloys, Inorganic Materials 40 (2004) 937-944.

[22] Y. Kimura, H. Kuriyama, T. Suzuki, Y. Mishima, Microstructure control and mechanical-properties of binary Co-Al alloys based on B2 intermetallic compound coal, Materials Transactions Jim 35 (1994) 182-188.

[23] S.N. Hosseini, T. Mousavi, F. Karimzadeh, M.H. Enayati, Thermodynamic aspects of nanostructured CoAl intermetallic compound during mechanical alloying, Journal of Materials Science & Technology 27 (2011) 601-606.

[24] S.F. Tikhov, V.E. Romanenkov, V.A. Sadykov, V.N. Parmon, A.I. Rat'ko, Physicochemical principles of the synthesis of porous composite materials through the hydrothermal oxidation of aluminum powder, Kinetics and Catalysis 46 (2005) 641-659.

[25] S.F. Tikhov, Y.V. Potapova, V.A. Sadykov, V.B. Fenelonov, I.V. Yudaev, O. Lapina, Aet al., Synthesis of alumina through hydrothermal oxidation of aluminum powder conjugated with surfactant-directed oriented growth, Mat. Res. In. online 9 (2005) 431-446.

[26] J. Goldstein, D. Newbury, D. Joy, C. Lyman, P. Echlin, L. Sawyer, J.M. Michael, Scanning Electron Microscopy in X-Ray Microanalysis, Springer, New York, 2008, pp. 485-499.

[27] OIA INCA Energy Operation Manual, UK, 2004.

[28] A.M. Portis, A.C. Gossard, Nuclear resonace in ferromagnet cobalt, J. Appl. Phys. 31 (1960) 205-213.

[29] M. Malinowska, M. Wojcik, S. Nadolski, E. Jedryka, C. Meny, P. Panissod, et al., Identification of magnetic phases in granular Co10Cu90 alloy using ^{59}Co NMR method, J. Magn. Magn. Mater. 198-199 (1999) 599-601.

[30] P. Panissod, J.P. Jay, C. Meny, E. Jedrica, NMR analysis of buried metallic interfaces, Hyperfine Interact. 97-98 (1996) 75-98.

[31] P.C. Riedi, R.G. Scurlock, Satellite lines in the ^{59}Co resonans in cobalt-nickel alloys, J. Appl. Phys. 39 (1968) 1241-1242.

[32] P. Panissod, M. Malinowska, E. Jedrica, M. Wojcik, S. Nadolski, M. Knobel, J.E. Schmidt, Inhomogeneous structure and magnetic properties of granular $Co_{10}Cu_{90}$ alloys, Phys. Rev. B 63 (2000) 014408-014401-014408-014410.

[33] L.E. Toth, S.F. Ravitz, Ferromagnetic nuclear resonance in cobalt nuclei in stacking faults and twins, J. Phys. Chem Solids 24 (1963) 1203-1206.

[34] J. Sort, S. Surinach, J.S. Munoz, M.D. Baro, M. Wojcik, E. Jedrica, et al., Role of stacking faults in the structural and magnetic properties of ball-milled cobalt, Phys. Rev. B 68

(2003) 014421-014421-014421-014427.

[35] W. Kraus, G. Nolze, Powder Cell: A program for the representation and manipulation of crystal structures and calculation of the resulting X-ray powder patterns, Journal of Applied Crystallography 29 (1996) 301-303.

[36] S. Cherepanova, S. Tsybulya, Simulation of X-ray powder diffraction patterns for one-dimensionally disordered crystals, European Powder Diffraction Epdic 8 443-4 (2004) 87-90.

[37] O.A. Bulavchenko, S.V. Cherepanova, S.V. Tsybulya, *In situ* XRD investigation of Co_3O_4 reduction, Zeitschrift Fur Kristallographie (2009) 329-334.

[38] H. Brömer, H.L. Huber, Nuclear magnetic resonance in ferromagnetic HCP and FCC ^{59}Co, J. Magn. Magn. Mater. 8 (1978) 61-64.

[39] S.V. Tsybulya, S.V. Cherepanova, A.A. Khasin, V.I. Zaikovskii, V.N. Parmon, The structure of the heterogeneous coherent states in high-dispersed particles of metallic cobalt, Doklady Akademii Nauk 366 (1999) 216-220.

[40] DataBase, PDF-2 N.06-0699.

[41] A.H. Heuer, D.B. Hovis, J.L. Smialek, B. Gleeson, Alumina scale formation: A new perspective, Journal of the American Ceramic Society 94 (2011) S146-S153.

[42] J. Camra, E. Bielanska, A. Bernasik, K. Kowalski, M. Zimowska, A. Bialas, et al., Role of Al segregation and high affinity to oxygen in formation of adhesive alumina layers on FeCr alloy support, Catalysis Today 105 (2005) 629-633.

[43] D. Ugues, S. Specchia, G. Saracco, Optimal microstructural design of a catalytic premixed FeCrAlloy fiber burner for methane combustion, Industrial and Engineering Chemistry Research 43 (2004) 1990-1998.

4.3.3. Low-temperature Al_2O_3/CoAlO/CoAl cermet

In this chapter, Al_2O_3/CoAlO/CoAl cermet is studied by a set of methods including internal field ^{59}Co NMR. This cermet has more catalytic relevance than the material studied in the previous chapter due to its high specific surface area (SSA), which was enhanced by the addition of gibbsite during its preparation. The microwave absorption of the cermet has been studied as well, which can be used in catalytic reactor as a source of heating. The content of this chapter is published in *Advanced Materials Research* vol. 702 [5], which was a proceeding of the *2013 International Conference on Solid State and Materials* (ICSSM 2013), January 30-31, 2013, Los Angeles, CA, USA.

Regarding this publication, the author also apologizes for the "Russian" English used in this article. The NMR assignment in this article consists of a mixture of conventional sf_1-sf_5 defects and an early attempt to account for magnetic contributions. The NMR spectra description should not be used as such since our full view of the issues was refined later (see section 4.2.1).

Advanced Materials Research Vol. 702 (2013) pp 79-87
© (2013) Trans Tech Publications, Switzerland
doi:10.4028/www.scientific.net/AMR.702.79

Design of Al_2O_3/CoAlO/CoAl Porous Ceramometal for Multiple Applications as Catalytic Supports

Andrey S. Andreev[1, 2, 3, a], Serguey F. Tikhov[1, b], Aleksey N. Salanov[1], Svetlana V. Cherepanova[1], Olga B. Lapina[1, 2], Vasiliy A. Bolotov[1], Yuriy Yu. Tanashev[1], Jean-Baptiste d'Espinose de Lacaillerie[3], and Vladislav A. Sadykov[1, 2]

[1] Boreskov Institute of Catalysis, pr. Lavrentieva 5, Novosibirsk, Russian Federation, 630090

[2] Novosibirsk State University, 2 Pirogova str., Novosibirsk, Russian Federation, 630090

[3] Soft Matter Sciences and Engineering Laboratory, UMR 7615 CNRS UPMC, ESPCI ParisTech, 10 rue Vauquelin, 75005 Paris, France

[a] aandreev@catalysis.ru, [b] tikhov@catalysis.ru

Keywords: Al_2O_3/CoAlO/CoAl cermet, XRD, SEM, Internal field ^{59}Co and ^{27}Al MAS NMR, Microwave irradiation.

Abstract. Porous ceramometal Al_2O_3/CoAlO/CoAl was studied by set of physicochemical techniques such as XRD, SEM, internal field ^{59}Co and ^{27}Al MAS NMR, and porosity measurements. They revealed the cermet containing three parts. First, cobalt-free large porous alumina particles which surrounded by the second oxide part representing spinel $Co_xAl_{3-x}O_4$ (x=1,2,3) oxides. And third, oxygen-free metallic part consists of cobalt metal particles covered by Co-Al oxide protecting the metallic part from oxidation. Porosity measurements ascertained high porosity (60%) and good SSA (122 m^2/g). Also the enhanced adsorption of microwaves due to metallic particles randomly distributed in oxides was found.

Introduction

Ceramometals (cermets) comprised of oxide matrix with uniformly distributed metallic particles have been discovered more than fifty years ago [1, 2]. Porous cermets are promising catalysts for different processes [3-7] and as filter systems [8]. Also, these materials can be used as supports or catalysts for processes of microwave (MW) chemistry due to possibility of selective heating of metal components [9].

Traditionally cermets are manufactured by mixing powders of oxides and metals followed by pressing and sintering at high temperatures [10]. Another way of cermets preparation is based upon chemical self-propagating combustion reaction, i.e. $Al + Co_2O_3 \rightarrow Co + Al_2O_3$ and other techniques include stages of ball milling of powdered oxides and metallic aluminum, pressing without oxygen access and ignition [11-15].

Recently, the pressureless method of porous cermets preparation based on mechanical alloying of various metals with aluminum, loading into a special stainless steel die followed by subsequent hydrothermal treatment providing consolidation of powders into monolithic bodies due to partial oxidation of aluminum and hydration of the products of oxidation was developed [16]. This method allows producing mechanically strong ceramic/cermet materials of complex shapes with phase composition, microstructure and porosity controlled by their chemical composition and specificity of synthesis procedures including thermal treatment of consolidated monoliths in specific environment. For example, CoAl-based cermet was prepared and studied earlier [17]. This cermet had a relatively high crushing strength but its drawback was low specific surface area (SSA) which is important for heterogeneous catalyst preparation. This work presents a new type of CoAl-based cermet with mesoporous alumina consolidated inside ceramometal monolith. The spatial distribution of individual components in solids and their structural/microstructural characteristics

are discussed by using a combination of such techniques as XRD, SEM, EDX [18, 19], and solid-state NMR (SSNMR)[20, 21]. This approach allows elucidating structural features of Co-Al cermets on micro, nano and atomic levels.

Experimental

Preparation procedure. Commercial grade aluminum PAP-2 (GOST 5499-71) and commercial grade cobalt PK-IY (GOST 9721-79) powders were used as source materials. The powdered aluminum particles have a platelets shape up to few tens of microns in diameter [22]. The shape of cobalt particles is more irregular (vide infra).

The procedure of porous cermets preparation included few steps:

a) Mechanical activation (MA) of the mixture containing 80 wt.% Co and 20 wt.% Al was used to synthesize the powdered precursor. MA was carried out in a high-power planetary ball mill APF. The acceleration of the balls was 65 g. The balls: powder weight ratio was 20, the ball diameter 5 mm, activation time 5 min.

b) The product of mechanical activation was blended together with powdered product of thermal activation of gibbsite (TCA) [8, 23] loaded into a stainless steel die specially designed to ensure free access of water and hydrogen release [24].

c) For hydrothermal treatment (HTT), the loaded die was placed in boiling water and kept there for 4 hours producing a strong monolith (diameter 1 cm, length 8 cm).

d) The product of HTT was removed from the die, dried for 1 hour at 120°C and calcined under air slowly increasing temperature up to 600°C (4 hours). The calcination yielded a mechanically strong material.

The crushing (compressing) strength was determined by crushing pellets (diameter ~10 mm, height ~3 mm) between two parallel plates in static conditions using a PK-2-1 instrument. The value was calculated as a ratio of the loaded stress at a crushing point to the section of the area of pellets. The porosity was estimated from the values of true and apparent densities of the granulated cermets. The true densities of the samples were measured using a helium pycnometer – Autopycnometer 1320 (Micromeritics). SSA was determined by low temperature (77 K) nitrogen adsorption on the ASAP-2400 Micromeritics instrument.

As criteria of MW adsorption, the dimensionless parameters ε (dielectric constant) and $\mathrm{tg}\delta$ (tangent of dielectric losses) were measured using analyzer Agilent CSA, series N1996A. The measurements also were performed for the sample of pure γ-Al_2O_3 obtained from pseudoboehmite by calcination at 823K. Also, the efficiency of MW power-to-heat conversion that can be achieved by use of the samples under study was estimated by the method presented in [25].

Structural characterization

Internal field ^{59}Co NMR. The internal field ^{59}Co NMR spectra were recorded at room temperature on a Bruker Avance 400 spectrometer (magnetic field 9.4 T) without applying external magnetic field and using point by point methods with 512 scans in each point. The solidecho pulse program was used in echo experiment with the pulse length of 4 μs (i.e. the width of exciting zone was 250 kHz) and interpulse delay was 16 μs. All details of such approach were described earlier in [17].

Since Gossard and Portis in 1959 were found resonance in ferromagnetic Co [26] the intensive development of this area had begun. In our days the resonance line position of metallic Co is well known [20], but their interpretation is different according to different authors. We used the following peak matching in given paper for room temperature experiments. Multi-domain fcc Co gives resonance from domain wall edge (d.w.e) at 213 MHz [26] and from domain center (d.w.c.) at ~217 MHz [27] and multi-domain hcp Co metal gives resonance from d.w.c. at 221 MHz [28] and from d.w.e. at 214 MHz [29]. In addition, three defects are observable in bulk cobalt metal at 215.5, ~218.5, and ~223.5 MHz [30]. The effect of different substitutions in cobalt coordination sphere on ^{59}Co NMR resonance frequency was studied in details for alloys [21, 31, 32].

From this corrected NMR spectrum Gaussian peaks were fitted to within 0.2MHz of the literature values and the relative number of nuclei in each site is then equivalent to the relative areas under the Gaussians used to fit each site. The frequency was allowed to vary a little due to the effect of strain in the crystal lattice.

^{27}Al MAS NMR. The ^{27}Al MAS NMR experiments were performed at room temperature on a Bruker Avance-400 spectrometer at the resonance frequency of 104.26 MHz using a 4-mm probe with ZrO_2 rotors at spinning frequencies of 15 kHz. The pulse length of 1 μs (π/12) and recycle delay of 0.1 s were used for the night acquisition of all the ^{27}Al spectra. The spectra were referenced to external $Al(H_2O)^{3+}$.

XRD. The X-ray diffraction (XRD) patterns were registered using a Siemens diffractometer. Data registration was made in the 2θ angle range from 25° to 70° with step of 0.05° and accumulation time of 40 s in each point.

Experimental results

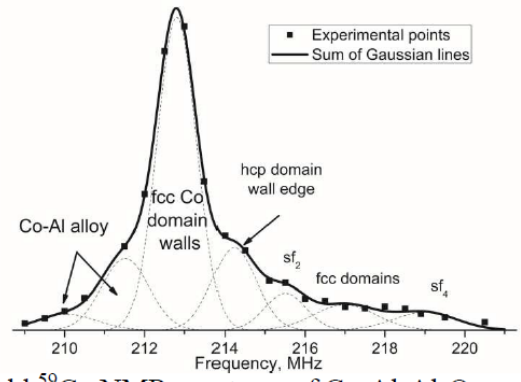

Fig. 1. Corrected internal field ^{59}Co NMR spectrum of Co-Al-Al_2O_3 cermet. Black squares indicates experimental points and the solid line shows the sum of Gaussian lines in the decomposition.

Internal field ^{59}Co NMR. Figure 1 represents corrected internal field ^{59}Co NMR spectrum of Al_2O_3/CoAlO/CoAl cermet. It is clearly seen the prevalence of multidomain fcc phase (212.8 MHz) over the other cobalt packages. Another noticeable feature is the absence of domain wall center hcp Co phase (221 MHz) but it is easy to understand because metallic Co has the allotropic phase transformation from hcp to fcc package at nearly 420°C [33] and the annealing temperature was 600°C (see preparation). Also spectra exhibits sf_2 and sf_4 stacking faults, in addition, sf_2 can be locally classified as two consecutive deformation fault in hcp and sf_4 as two consecutive deformation faults in fcc [20]. In comparison with our previous work [17] where due to high-temperature annealing (900°C) there were no peaks corresponding to any sfs since the annealing of defects happened**.** The main cause that the sfs and d.w.e. hcp resonances are still present in Al_2O_3/CoAlO/CoAl cermet is nonsufficient time of annealing for the sample at given temperature (600°C). Also another remarkable specificity of the sample is the spectrum broadening to the area of low frequencies which indicates that Co strongly interacts with Al to form Co-Al alloy. Another consideration which instigates us to Co-Al alloy idea is the slight shift of fcc Co resonance peak from 213 MHz to 212.8 MHz due to strain effect [34]. The same type of displacement (from 213 MHz to 212.2 MHz) was detected in our previous work [17] but the value of such shift was larger. The quantity of the shift can point to the strength of Co and Al interaction. It is become hard to correlate fitted Gaussian lines to the number of Al in Co coordination sphere so it is more correct to regard only the sum of Co-Al alloy Gaussian peaks because the peaks placement was chosen in the way to receive the best fit. According Table 1 the major of cermets metallic part is the unfaulted fcc Co (~ 57 at.%). In turn the percentage of sfs do not exceed 11 at.% , hcp phase does not exceed 15 at.% and the Co-Al alloy is only ~ 17 at.% that is much lower than Al_2O_3/CoAlO/CoAl cermet had [17] but it is sufficient to protect metallic Co preventing its oxidation during annealing.

Table 1. Relative phases shown at Figure 1.

Phase	Co-Al alloy	fcc d.w.*	hcp d.w.e.*	sf_2	fcc d.*	sf_4
Frequency, [MHz]	210.1 + 211.5	212.8	214.3	215.5	217	219
Relative phase content, [at.%]	17.4	50.5	14.8	6.2	6.5	4.6

*d.w. – domain wall, d.w.e. – domain wall edge, d. –domain

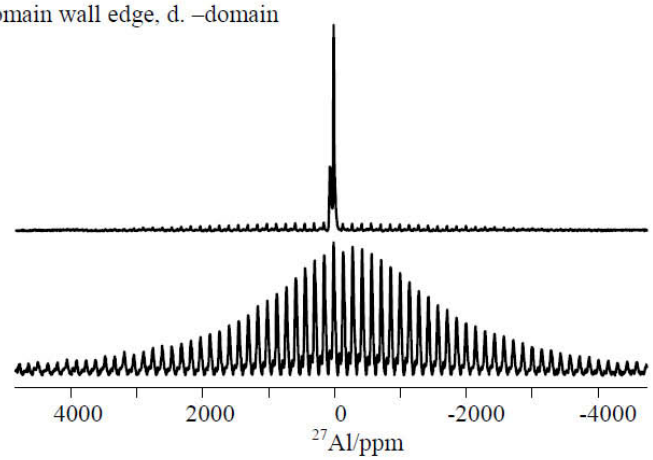

Fig. 2. 15kHz ^{27}Al MAS spectra of γ-Al_2O_3 (top) and Co-Al-Al_2O_3 cermet (bottom).

^{27}Al MAS NMR. Figure 2 exhibits 15 kHz ^{27}Al MAS NMR spectra of Al_2O_3/CoAlO/CoAl cermet and for comparison pure γ-alumina. The distinctions between these two spectra are obvious and tremendous. The bottom spectrum presents broadened central transition of alumina spectrum due to ferromagnetic cobalt effect which is located near alumina. The similar effect was observed on aluminosilicates with supported NiO [35]. Nickel oxide was found to locate on the SiO_2-Al_2O_3 surface but not incorporated into matrix. Thus, authors proved the existence of not only paramagnetic NiO but also metallic nickel that is ferromagnetic. The broadening effect in cited article was weaker so it can be associated with a lower local magnetic field of metallic Ni [36] compared to metallic Co.

Central transition in γ-Al_2O_3 ^{27}Al MAS spectrum is two most intensive resonance lines representing tetrahedral (63 ppm) and octahedral coordinate (7 ppm) aluminum. It should be noted that such ferromagnetic Co influence to Al spectrum does not mean formation of Co-Al alloy. The main reason is that the cermet spectrum exhibits both octahedral and tetrahedral Al sites which are typical for non-perfect aluminum oxides (not α-alumina) but the unusual ratio between octahedral and tetrahedral aluminum ($Al_O/Al_T \approx 6$ instead of non-perfect alumina $Al_O/Al_T \approx 3$) induces that spectrum consists of a mixture of different aluminas. However, Co-Al alloy is invisible for ^{27}Al MAS NMR due to strong interaction with Co that results as high broadening but its presence in Al_2O_3/CoAlO/CoAl cermet was proved by the all other techniques used in this work. The similar broadened spectra were observed on the other object such as supported on alumina metallic cobalt particles. Drawing analogies we can assume that in the case of Al_2O_3/CoAlO/CoAl cermet the location of cobalt and alumina is similar, i.e. the contact between metallic Co and alumina happens. So it can be interpreted as surrounding of cobalt particles by the alumina.

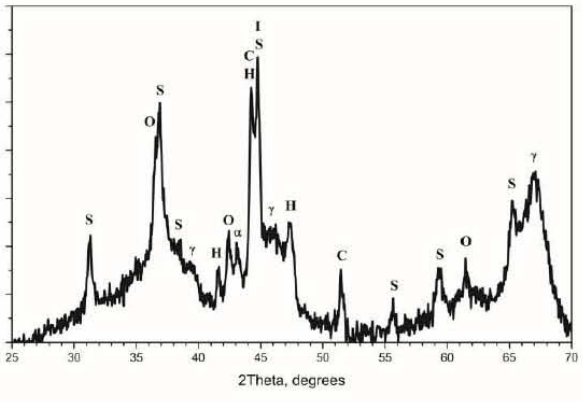

Fig. 3. XRD pattern of cermet sample (**S** – $Co_{3-x}Al_xO_4$ spinel, x=0-2, **I** – CoAl intermetallide, **C**– cubic Co, **H**- hexagonal Co, **O** – CoO oxide, **γ** – γ -alumina, **α** – α-alumina).

XRD. The Al_2O_3/CoAlO/CoAl cermet XRD pattern corresponds to multiphase system (Fig. 3). Presence of γ- and α-alumina peaks can support the ^{27}Al MAS data where spectrum, at least, of two alumina (perfect (α-Al_2O_3) and non-perfect (any other)). The Fig. 3 clearly exhibits lines corresponding to fcc metallic Co and CoAl alloy that is in a good agreement with internal field ^{59}Co NMR data. The presence of hcp Co in the XRD pattern also supports NMR data but it should be mentioned that these two techniques gives slightly different information. The NMR is a molecular (or atomic) level technique giving information about the local environment of the atoms however XRD is a more technique rendering more long-range information [20]. So the NMR hexagonal stacking faults on the microscopic range can be determined by XRD as a pseudo – ordered hcp sequence. The last that NMR in this sort of materials cannot observe is oxide compound such as cobalt aluminates and cobalt oxide. The content of these phases conforms to our previous work [17] where the existence of cobalt aluminates and cobalt oxide was proved by both XRD and EDX techniques.

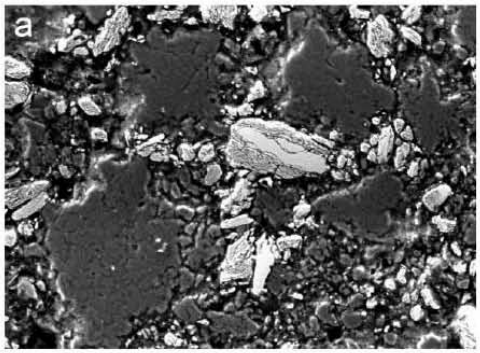

Fig.4. SEM-micrograph of the polished surface of Al_2O_3/CoAlO/CoAl cermet

SEM analysis, mapping and scattering diagram. Fig. 4 shows the SEM-micrograph of polished surface of cermet. The micrograph has complicated microstructure where can be emphasized two characteristic fragments in the image. The first part is dark areas roughly circular shape which size in cross-section is near 50 – 200 μm. Another part is linked to regions between spherical-like particles enveloping them. The average size of particles in this covering environment is 1-50 μm which looks brighter in comparison with the spherical-like particles. Probably, the surroundings have other chemistry.

SEM cermet image exhibits fragments which are distinguished each other by brightness value. These fragments can be connected to range of phases such as Co, Co-Al, Co-Al-O spinel, and alumina Al2O3. Mapping technique was used for obtaining more detailed microstructure. The procedure was described earlier for CoAlO/Co-Al cermets [17].

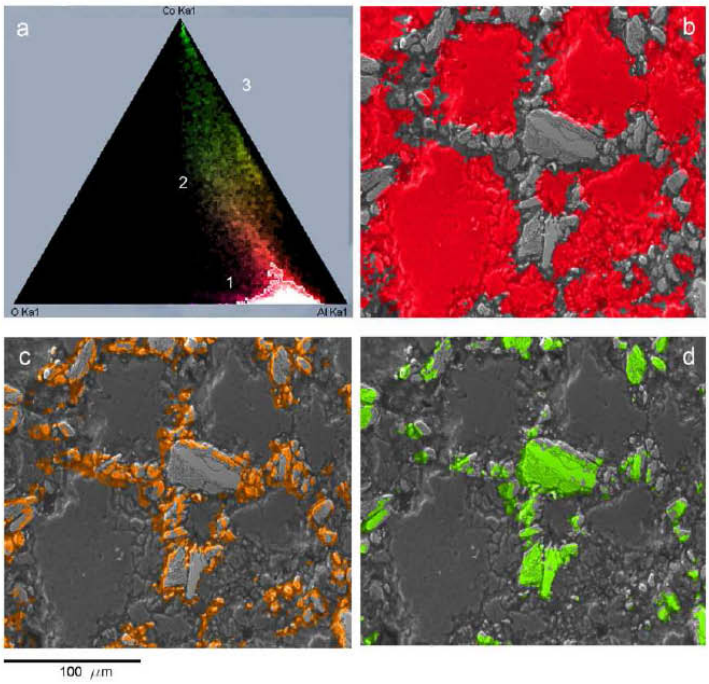

Fig. 5. Scattering diagram obtained from maps of separate elements (Co, Al, and O) distribution (a) and distribution of various phases marked out in the scattering diagram; (b) – alumina (signed by 1 in *a*); (c) CoAlO oxides (signed by 2 in *a*); (d) Co-Al alloy and cobalt metal particles (signed by 3 in *a*).

Fig. 5a exhibits scattering diagram for Co, Al, and O derived from distribution cards of these elements. The main part of dots in scattering diagram are concentrated in a quite narrow strip that is extended from Co apex to Al one. The analysis of the strip helps indicating to three main phases of the cermet. The first phase (signed as 1 at the diagram) contains only Al and O in definite proportion moreover Co concentration is negligible (Table 2). The second one (marked out by number 2 in the scattering diagram) comprises significant amount of Co Al, O and the third part (number 3 at the diagram) consist of variable Co and Al amount together with minute O concentration (see also Table 2). Fig. 5 shows microscopic section of the cermet where regions corresponding to parts of the strip numbered in the scattering diagram are colored. The each region in the scattering diagram characterized by definite ratio of Co, Al, and O is presented in microscopic image as set off parts in color. This correspondence allows determining the location of regions with certain chemistry in the image of the material. One can see in Fig. 5 the region 1 in the scattering diagram corresponds to cross-section of spherical particles of Al_2O_3 globules (Fig. 5b, red color). The region 3 is a metal streak between the spherical particles (Fig. 5d, green color). Finally, the region 2 represents an oxide boundary layer between first and third parts (Fig. 5c, yellow tints).

Table 2. Relative content of Co, Al, and O in phases marked out in the scattering diagram and the summed up spectrum.

Phase	Phase number	Relative concentration of elements, [at.%]		
		O	Al	Co
Al_2O_3	1	58.8	40.5	0.7
Al-Co-O	2	48.4	29.9	21.7
Co	3	21.7	30.3	48

Porosity measurements. The Al_2O_3/CoAlO/CoAl cermet shows great improvement of porosity in comparison with previously studied CoAlO/Co-Al cermet [17]. Addition of aluminum in the first preparation stage hydroxide extremely increases the specific surface area (SSA) in final product from 1 to 122 m^2/g. Also porosity of samples was transformed from low (~5%) in CoAlO/Co-Al cermet [17] to high (~60%) in Al_2O_3/CoAlO/CoAl cermet. So such development of material allows

using Al_2O_3/CoAlO/CoAl cermet in catalysis due to appropriate SSA and porosity. The mechanical strength (~5 MPa) of new Al_2O_3/CoAlO/CoAl cermet remains satisfactory for granulated catalysts and supports.

Dielectric properties/microwave absorption. The main dielectric parameters were measured as following: ε = 2.03, tg δ = 0.016 for γ-Al_2O_3 versus ε = 3.06, tg δ = 0.065 for the Al_2O_3/CoAlO/CoAl. It means that the MW absorbency of cermet is sufficiently higher than that of pure oxide. Thus, the cermet can be used as efficient absorber of microwave power in MW cavities when they are placed into the maximum of electric component of the electromagnetic field. Moreover, the difference in MW absorbency between γ-Al_2O_3 and Al_2O_3/CoAlO/CoAl is even greater when the samples are located in the MW cavity in the maximum of magnetic component. The measured efficiency η of MW power-to-heat conversion for γ-Al_2O_3 is about 1.5% whereas for Al_2O_3/CoAlO/CoAl under the same conditions η = 26%; the procedure of cavity tuning, in principle, can rise this parameter to 85%.

Discussion

One can conclude that obtained Al_2O_3/CoAlO/CoAl cermet has complex solid structure. It includes metallic particles like fcc Co with developed stacking faults (according to NMR) uniting in hexagonal structures (XRD) as well as CoAl intermetallide. The oxides like α-Al_2O_3, spinel $Co_{3-x}Al_xO_4$ and CoO with the metal particles form the sort of skeleton where the mesoporous γ-Al_2O_3 globules are randomly distributed. The straight contact between the metal particles and mesoporous alumina was evidenced from NMR. So the MW power adsorbed as heat can be transferred to alumina faster comparing with conventional heating from the wall of oven. It is very important for the endothermic catalytic processes like dehydrogenation and cracking of hydrocarbons, steam reforming, etc. It can decrease energy losses and increase the efficiency of the catalytic processes.

The Al_2O_3/CoAlO/CoAl cermet can be utilized as a model system for other type of MeAl-based cermets with incorporated mesoporous materials.

Conclusions

New approach of preparation porous ceramometalic materials allows obtaining both sufficient crushing strength and high SSA. According to all techniques used for characterization cermet structure seems following. The main part of Al_2O_3/CoAlO/CoAl cermet is alumina that represented by mixture of γ-Al_2O_3 and α- Al_2O_3 modifications. Huge blocks of alumina coated by CoAl alloy and $Co_{3-x}Al_xO_4$ (x = 0; 1; 2) and outer part of material is metallic Co that is still present after 600°C calcination under air atmosphere. Cobalt is mainly in fcc stacking but also one can see set of defects and part of them can be associated with hcp Co. High SSA propose using this system as promising catalyst support. The enhanced adsorption of MW irradiation permits utilizing this type of cermets in endothermic catalytic processes.

Acknowledgements

Authors thank grants RFBR #11-08-00704-a, # 10-03-00667-a, President Program "Leading Scientific Schools" (grant 524.2012.3), President program of PhD students scholarships SP-389.2012.1, and The Ministry of education and science of Russian Federation (project 8429) for financial support.

References

[1] Shelvin, S.S., *Cermets* ed. J.R. Tinkelpaugh and W.B. Grandall. 1966, New York: Reinold Publ.Corp.

[2] Kaplan, W.D. and A. Avishai, *Ceramic matrix composites (Microstructure, properties and applications)*, ed. I.M. Low. 2006, Cambridge, England: Woodhead Publ.Ltd.

[3] Pugacheva, E.V., et al., *SHS-Produced Intermetallides as Catalysts for Deep Oxidation of Carbon Monoxide and Hydrocarbons.* Int. J. Self-Prop. High-Temp. Syn., 2010. **19**(1): p. 65.

[4] Arkatova, L.A., *The deposition of coke during carbon dioxide reforming of methane over intermetallides.* Catalysis Today, 2010. **157**(1-4): p. 170.

[5] Pavlova, S., et al., *Monolith composite catalysts based on ceramometals for partial oxidation of hydrocarbons to synthesis gas.* Natural Gas Conversion Vii, 2004. **147**: p. 223.

[6] Tikhov, S.F., et al., *Hydrogenated Zr-Fe alloys encapsulated in Al_2O_3/Al matrix as catalysts for Fischer-Tropsch synthesis.* Natural Gas Conversion Vii, 2004. **147**: p. 337.

[7] Khodakov, A.Y., W. Chu, and P. Fongarland, *Advances in the Development of Novel Cobalt Fischer−Tropsch Catalysts for Synthesis of Long-Chain Hydrocarbons and Clean Fuels.* Chemical Reviews, 2007. **107**(5): p. 1692.

[8] Tikhov, S.F., et al., *Porous ceramic matrix Al_2O_3/Al composites as supports and precursors for catalysts and permeable materials*, in *Metal, ceramic and polymeric composites for various uses*, J. Cuppoletti, Editor. 2011, INTECH: Croatia. p. 195.

[9] Bolotov, V.A., et al., *Pyrolysis of Heavy Hydrocarbons Under Microwave Heating of Catalysts and Adsorbents.* Journal of Microwave Power and Electromagnetic Energy, 2012. **46**(1): p. 39.

[10] Patent, USA, N 5462903, 1955

[11] Aharon, O., et al., *Residual stresses and magnetic properties of alumina-nickel nanocomposites.* Scripta Materialia, 2004. **50**(9): p. 1209.

[12] Lu, T. and Y. Pan, *Combustion synthesis of ferromagnetic Al_2O_3-based cermets in thermal explosion mode.* J. Mater. Sci., 2010. **45**: p. 5923.

[13] Portnoi, V.K., K.V. Tret'yakov, and V.I. Fadeeva, *Structural transformations during the mechanochemical synthesis and heating of Co-Al alloys.* Inorganic Materials, 2004. **40**(9): p. 937.

[14] Kimura, Y., et al., *Microstructure Control and Mechanical-Properties of Binary Co-Al Alloys Based on B2 Intermetallic Compound Coal.* Materials Transactions Jim, 1994. **35**(3): p. 182.

[15] Hosseini, S.N., et al., *Thermodynamic Aspects of Nanostructured CoAl Intermetallic Compound during Mechanical Alloying.* Journal of Materials Science & Technology, 2011. **27**(7): p. 601.

[16] Tikhov, S., et al., *Design of composite porous cermets synthesized by hydrothermal treatment of CrAl powder followed by calcination.* Journal of Materials Science, 2010. **45**(12): p. 3160.

[17] Andreev, A., et al., *Formation of Micro, Nano and Atomic-Level Structure of CoAlO/Co-Al Cermets Prepared by Mechanical Alloying.* J. Mater. Sci. Eng. A, 2012. **2**(2): p. 121.

[18] Goldstein, J., et al., *Scanning Electron Microscopy in X-Ray Microanalysis*. 3rd ed. 2008, New York: Springer.

[19] INCA Energy Operation Manual, O.I.A., UK, 2004.

[20] Sort, J., et al., *Role of stacking faults in the structural and magnetic properties of ball-milled cobalt* Phys. Rev. B, 2003. **68**: p. 014421.

[21] Koi, Y. and A. Tsujimura, *NMR of Co^{59} in Ferromagnetic Cobalt Alloys.* J. Phys. Soc. Jpn., 1961. **16**: p. 574.

[22] Tikhov, S.F., et al., *Physicochemical principles of the synthesis of porous composite materials through the hydrothermal oxidation of aluminum powder.* Kinet Catal+, 2005. **46**(5): p. 641.

[23] Zolotovskii, B., et al., *Development of the technology and production of spherical alumina for catalysts supports and adsorbents.* Russian Journal of Applied Chemistry, 1997. **70**(1): p. 299.

[24] Tikhov, S.F., et al., *Synthesis of alumina through hydrothermal oxidation of aluminum powder conjugated with surfactant-directed oriented growth* Mat. Res. In. online, 2005. **9**: p. 431.

[25] Chernousov, Y.D., et al., *Characteristics of a chemical reactor that is a loaded microwave resonator.* Journal of Communications Technology and Electronics, 2009. **54**(2): p. 231.

[26] Gossard, A.C. and A.M. Portis, *Observation of nuclear resonanse in a ferromagnet.* Phys. Rev. Lett., 1959. **3**(4): p. 164.

[27] Gossard, A.C., et al., *Ferromagnetic Nuclear Resonance of Single-Domain Cobalt Particles.* Physical Review, 1965. **138**(5A): p. A1415.

[28] Koi, Y., A. Tsujimura, and T. Kushida, *NMR of Co^{59} in Ferromagnetic Hexagonal Cobalt Metal.* J. Phys. Soc. Jpn., 1960. **15**: p. 2100.

[29] Kawakami, M., T. Hihara, and Y. Koi, *The Co^{59} Nuclear Magnetic Resonance in Hexagonal Cobalt.* J. Phys. Soc. Jpn., 1972. **33**(6): p. 1591.

[30] Hardy, W.A., *Nuclear Resonances in Cubic, Hexagonal, and Mixed Phase Cobalt Powders and Thin Films.* J. Appl. Phys., 1961. **32**(3): p. S122.

[31] Panissod, P., et al., *NMR analysis of buried metallic interfaces.* Hyperfine Interact., 1996. **97-98**: p. 75.

[32] Panissod, P., *Structural and magnetic investigations of ferromagnets by NMR. Application to magnetic metallic multilayers*, in *Frontiers in Magnetism of Reduced Dimension systems*, V.G. Bar'yakhtar, P.E. Wigen, and N.A. Lesnik, Editors. 1998, Kluwer Academic. p. 225.

[33] Bibring, H. and F. Sebilleau, Rev. Met., 1955. **52**.

[34] Wieldraaijer, H., W.J.M. de Jonge, and J.T. Kohlhepp, *Electric-field gradients in thin face-centered-tetragonal Co films observed by nuclear magnetic resonance.* Physical Review B, 2005. **72**(15): p. 155409.

[35] Bakhmutov, V.I., et al., *Supermicroporous silica-based SiO_2-Al_2O_3-NiO materials: Solid-state NMR, NMR relaxation and magnetic susceptibility.* Microporous and Mesoporous Materials, 2009. **118**(1-3): p. 78.

[36] Cowan, D.L. and L.W. Anderson, *Nuclear Magnetic Resonance of ^{61}Ni in Nickel Metal.* Physical Review, 1965. **139**(2A): p. A424.

4.4. Co/MWCNT hybrids

Metallic cobalt nanoparticles of high aspect ratios were cast into carbon nanotubes. The original magnetic properties of the ferromagnetic hybrid are revealed by internal field ^{59}Co nuclear magnetic resonance. The content of this chapter will be submitted to *Journal of Materials Chemistry A*.

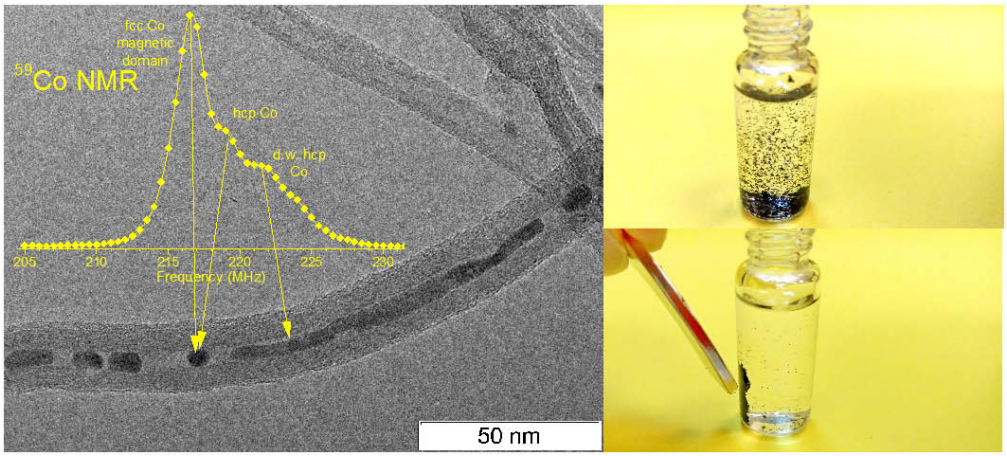

In this study, several important questions are still not solved. It is no doubt that lines at 219 and 221 MHz belong to hcp stacking, but it is still not clear if the creation of domain walls can occur here. On the one hand, prolonged particles and nanowires should have preferred direction of magnetization (along the axis of cylinder), and the domain wall formation requires high anisotropy field that cannot be achieved in nanoparticles. On the other hand, these "quasi nanocylinders" have distorted shapes as can be seen from figures, and the creation of specific domain walls cannot be excluded.

The second main point is room-temperature ferromagnetism of such particles. According to simple calculations, the Co metal particles of 3-4 nm size should be superparamagnetic. And NMR signal can come from residual large "blocked" particles. However, no particles outside the nanotubes were observed by TEM, and XRD crystalline size was less 8 nm, i.e. no large particles with high Co metal content is observed that can give appropriate NMR signal.

To solve these uncertainties, additional experiments with the samples at lower temperatures (77 K and 4.2 K) should be done to see if the intensity increases enormously compared to the usual behavior of nuclear magnetization. The second possibility is to perform the experiments in a static external field to saturate the superparamagnetic Co metal particles.

Templating ferromagnetic Cobalt nanoparticles and wires within Carbon Nanotubes

Andrey S. Andreev[†, ‡, §],Mariya A. Kazakova[†, ‡], Arcady V. Ishchenko[†, ‡], Alexander G. Selyutin[†], Olga B. Lapina[†, ‡], Vladimir L. Kuznetsov[†, ‡], Jean-Baptiste d'Espinose de Lacaillerie*[, §]

[†] Boreskov Institute of Catalysis, SB RAS, Lavrentieva 5, Novosibirsk 630090, Russia

[‡] Novosibirsk State University, Pirogova 2, Novosibirsk, 630090, Russia

[§] Soft Matter Sciences and Engineering (SIMM), UMR CNRS 7615, PSL Research University, ESPCI ParisTech, 75005, Paris, France

* Corresponding Author: jean-baptiste.despinose@espci.fr

KEYWORDS: Ferromagnetism, hybrid structures, multi-wall carbon nanotubes, internal field NMR, ^{59}Co NMR, HRTEM, Cobalt metal

ABSTRACT

Obtaining ferromagnetic metal particles in the nanometer range can be experimentally very elaborate but is of high interest in various fields varying from catalysis to electro-magnetic devices. Ferromagnetic cobalt/multi-walled carbon nanotubes (MWCNT) hybrids were formed by casting Co nanoparticles of high aspect ratios as well as short nanowires within the internal space of porous MWCNTs. The Co particles localization and size distributions were analyzed by high-resolution transmission electron microscopy, *in situ* synchrotron x-ray diffraction, and ^{59}Co internal field nuclear magnetic resonance. The magnetic features of the cobalt nanoparticles provided original information about the structure, face centered cubic (fcc) or hexagonal close-packed (hcp), and the shape, anisotropy, of the nanoparticles. Depending on the Co concentration, cobalt particles formed either inside the nanotube channels or on the external surface. Samples with Co concentration up to 10 wt.% mainly contained Co particles of elongated shapes (3–5 nm effective diameters) within the MWCNT channels. The confinement was responsible for the ferromagnetism of the particles at room temperature. The hcp/fcc ratio varies within 0.6 and 1.2 depending on the concentration. The

reduction of CoO to Co particles in H_2 flow occurred at 350°C but intensive sintering of Co metal particles started only at temperature higher than 550°C, thus demonstrating a stabilization effect of the MWCNTs on the Co particles. MWCNT modification by Co metal nanoparticles can potentially alter the dielectric and magnetic permeability of the carbon nanotubes thus making Co/MWCNT hybrids a new material for electro-magnetic applications such as radiofrequency shielding.

Over the last decade, magnetic nanoparticles (NPs) and their composites, especially cobalt based, found wide application in different technological spheres.[1–5] One of the most promising matrix consist of carbon nanotubes (CNTs), a material which gained a large public interest after the publication by Iijima in 1991.[6,7] The combination of these two types of materials (CNTs and NPs) significantly modifies their intrinsic properties, and the development of hybrid structures for specific applications is of extremely high interest. New synthetic techniques, which control the size, structure and magnetic properties of Co particles, have resulted in composites with physical and chemical properties significantly different from the bulk materials. These composites are now utilized as Fischer-Tropsch synthesis catalysts,[8–10] in biomedicine applications,[11–13] in Li-ion Co based battery materials,[14,15] and for thermoelectric applications.[16]

A potential advantage of magnetic NP/CNT composite over "raw" magnetic NP is an added resistance towards oxidation and sintering even for high metal loading due to the large specific surface area of CNT, up 1100 m^2/g, which can be modulated according to their diameter and wall thickness.[17,18] Additionally, CNTs in their own right possess unique thermal,[19–21] electrical,[22–24] and mechanical[25–27] properties. Consequently, the insertion of superparamagnetic or ferromagnetic Co metal particles within the CNTs provides a unique possibility to synthesize hybrid materials with a large diversity of tunable electro-magnetic properties. Finally, the steric control exerted by the well-defined tubular geometry of CNT at the nanoscale open the possibility to stabilize magnetic NPs of original shapes and structures.[28] This in particular, is a key to control of performance of ternary composites such magnetic NPs/CNT/polymers, a material of tremendous potential for radio-frequency shielding.[29–31]

A common synthetic route to produce Co/CNT composites and hybrids is incipient wetness impregnation with cobalt salt solutions.[9,10] This technique is most simple and easily upscaled. Nevertheless, some more exotic technique also have been explored,[32,33] with specific advantages such as the solvothermal method which can reach Co loadings up to 60 wt.%.[28,34] The majority of studies have so far been performed on multi-wall CNT of average diameter in the 50 to 70 nm range. However, multi-wall CNT of smaller diameter are in some cases of higher interest because they exhibit larger surface areas and much larger elastic moduli.[35] Furthermore, smaller tube diameters offer the potential to cast particles of even smaller sizes. An important step of hybrid preparation is the necessity of opening up the CNT to fill their

internal space with the Co phase. This can be achieved by treatment with concentrated nitric acid, with the added benefit of creating anchoring sites for Co on the CNTs surface.[36,37]

Whatever the chosen synthetic route, the Co precursors loaded on, or in, the CNT (thus forming a true hybrid structure) must be reduced to its metallic state. This is most commonly achieved by exposure to a hydrogen gas flow at elevated temperatures. This reduction procedure is known to proceed in two steps as the spinel Co_3O_4 phase, Co(II) and Co(III), stable under atmospheric conditions, is first reduced into CoO, Co(II), and then into Co(0) metal. Since the reverse oxidation reaction occurs easily even at room temperature and is auto-catalytic and pyrophoric in NPs, the Co metal surface is usually passivated by creating a thin oxidized layer through a final treatment with a dilute oxygen stream (1 % of O_2 in the inert gas).[28,38] While this is legitimate when one is concerned only with the shape and internal structure of the metal NPs, it is not clear how much properties dependent on the surface state such as magnetism or sintering resistance are modified by this passivation treatment. To study the intrinsic properties of reduced Co metal, it would be preferable to maintain the surface in its native reduced state.

In this paper, the structure of Co metal / multi-wall CNT (Co/MWCNT) hybrids is reported with different Co contents. As the MWCNTs internal geometry is used to template and to stabilize Co magnetic NPs below the 10 nm range (something that is particularly challenging for *3d* metals), a precise control of the MWCNTs properties is essential. To that respect, we used MWCNTs of 3-4 nm internal average diameter and of 4-6 nm average wall thickness carefully characterized by some of us in previous works.[39,40] The reduction of the precursors is followed by temperature programmed reduction (TPR) and *in situ* synchrotron X-ray diffraction (XRD). High-Resolution Transmission Electron Microscopy (HRTEM), and state-of-the-art ^{59}Co internal field nuclear magnetic resonance (IF-NMR)[41] were combined to probe the shape and structure of the Cobalt phase after reduction. IF-NMR is particularly valuable as it reveals quantitatively the different Co metal magnetic NP structures and provides size estimations without exposure to oxygen, information not available by other methods.[38,42–47] In this way, we demonstrate that Co(0) phase in the nanometer range can be cast into the CNTs as magnetic NPs of high aspect ratios or short nanowires.

Results and discussion

Assessing reduction and sintering by *in situ* synchrotron XRD. *In situ* synchrotron XRD reveals the processes occurring during the reduction of the samples. The actual reduction temperature program was mimicked but for a faster heating rate to 350°C to allow for limited beam-time, as displayed as an inset of Figure 1.

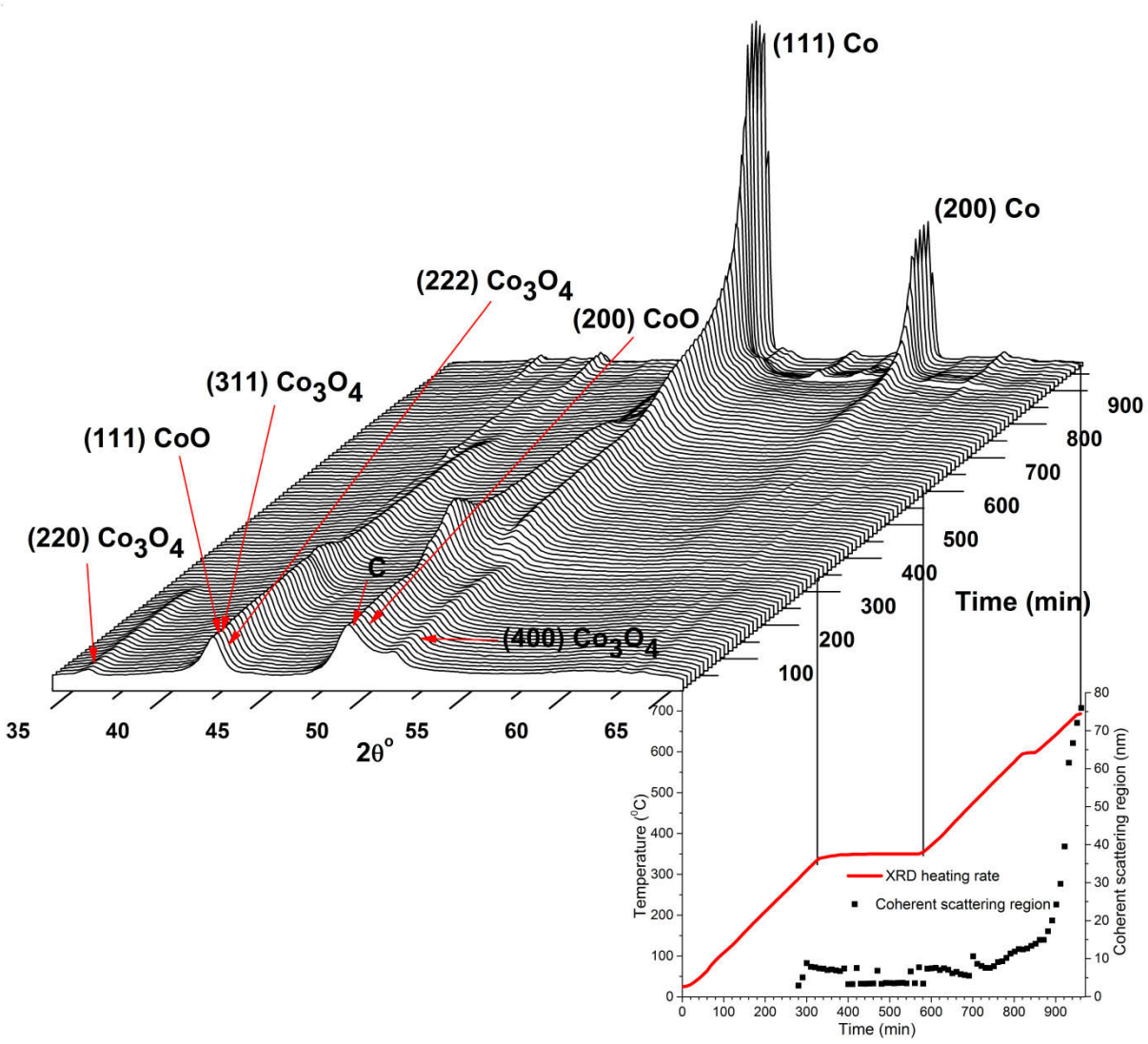

Figure 1. Time-resolved XRD patterns of the cobalt phases impregnated on MWCNTs (7.5% Co/MWCNT) during reduction under diluted hydrogen and temperature sintering. The temperature ramps and coherence size domains derived from the Sherrer approximation are also displayed. Co metal (PDF 15-806), CoO (PDF 48-1719), Co_3O_4 (PDF 42-1467), C (PDF 43-1104). The successive reduction of steps of the cobalt spinel into cobalt metal were evidenced but only particles with coherent domain sizes above 10 nm are visible by XRD . Reduction, complete after the 350°C stage, was followed by temperature sintering up to

700°C. Sintering, as revealed by the increase of the coherent domain size, occurred only after about 550°C.

In Figure 1, the reduction of the 7.5% Co/MWCNT sample is displayed. The Co phase in the precursor sample initially consisted of a mixture of CoO and Co_3O_4 oxides. As the temperature increased, the characteristic peaks of Co_3O_4 progressively disappeared. The growth of the CoO (111) diffraction line revealed that the first step of Co_3O_4 reduction (from Co_3O_4 to CoO) occurred. Around 320°C, all reflections from the Co_3O_4 phase disappeared. Simultaneously, the Co^0 (111) peak emerged. Clearly, at this temperature, the second stage of Co^0 reduction (from CoO oxide to Co metal) had started and proceeded during the 350°C stage. An assessment of the size of the metal particles seen by XRD can be obtained from the breadth of the (111) Co diffraction line using the Scherrer approximation (the face centered cubic (fcc) (111) reflection is used as it is less influenced by stacking faults than the (200) one).[48] The coherent domain size remained roughly constant at 7-8 nm during the 350°C reduction stage. Sintering was then probed by raising the temperature to 700°C. Starting at 550°C, the coherent domain size increased to reach almost 80 nm at the final temperature of 700°C. Simultaneously, the Co metal reflections dramatically grew. This meant that due to sintering, more and more Co reached the minimum size to diffract coherently and implied that, in the 7.5% Co/MWCNT sample after reduction at 350°C, a significant number of Co NPs were small enough to escape XRD detection, *i.e.* their size was 10 nm at the very most. These small particles resisted sintering until 550°C, that is well above the Tammann temperature of Cobalt metal (405°C),[49] suggesting a stabilizing effect from the MWCNTs.

Particles morphology and localization by HRTEM. HRTEM images of reduced Co/MWCNTs of different Co contents are shown in Figure 2. The localization and size of the Co NP was clearly revealed and depended on the total Co loading. The 3.5 wt.% sample exhibited only small Co particles inside the CNT channels while, at higher loading a second population of larger sizes appeared outside of the MWCNTs.

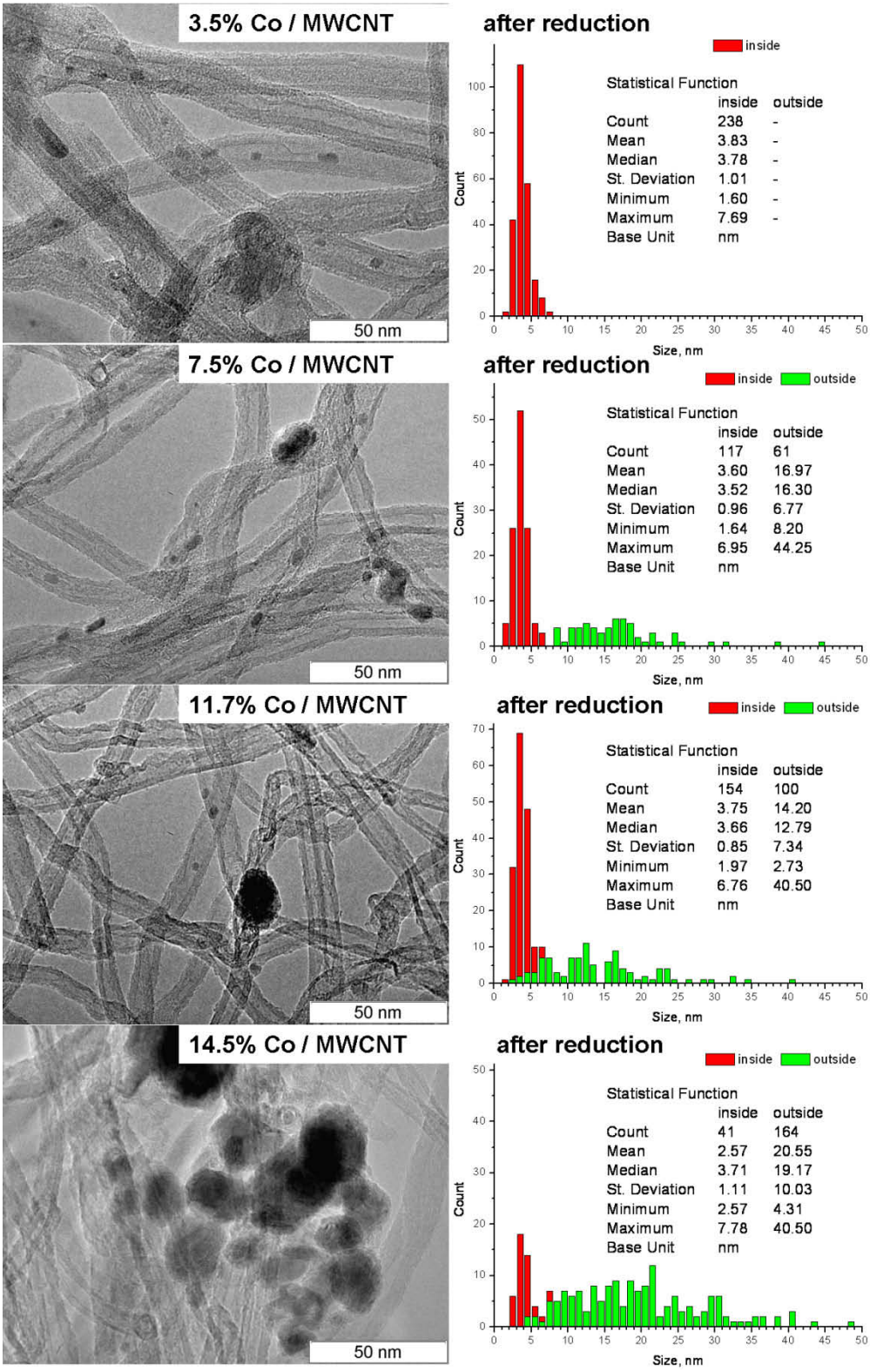

Figure 2. HRTEM images and particle size histograms of Co / MWCNT hybrids of different Co content (3.5, 7.5, 11.7, and 14.5 wt.% Co) after reduction treatment. At low Co loading (3.5%wt.) particles were only present within the nanotube channels; their size histogram (in red) was very sharp and centered below 4 nm, that is with lateral extensions determined by

the internal diameter of the MWCNTs. Up to about 10%wt. Co this population remained predominant but a new population of particles outside of the nanotubes and of larger size appeared (in green).

The presence of Co NPs inside the MWCNTs thus forming a true Co/MWCNT hybrid was a direct consequence of the nitric acid pre-treatment whose effect could be visualized by HRTEM (Fig. S1). Despite, the fact that the nanotubes were closed at their ends, the treatment with nitric acid opened pores within the walls. Consequently, the Co ions could diffuse or be driven inside the tubes during impregnation and drying. The most striking feature from Figure 2 was that the first population, constrained by the internal dimensions of the nanotubes, was relatively narrow with a constant number average diameter of 3.6 to 4.0 nm and a standard deviation of 1 nm, well in line with the internal nanotube diameter of ~ 4 nm. Furthermore, the localization of the small NPs population inside the MWCNT might explain the resistance to sintering observed by XRD for the small particles in the 7.5% Co/MWCNT hybrid.

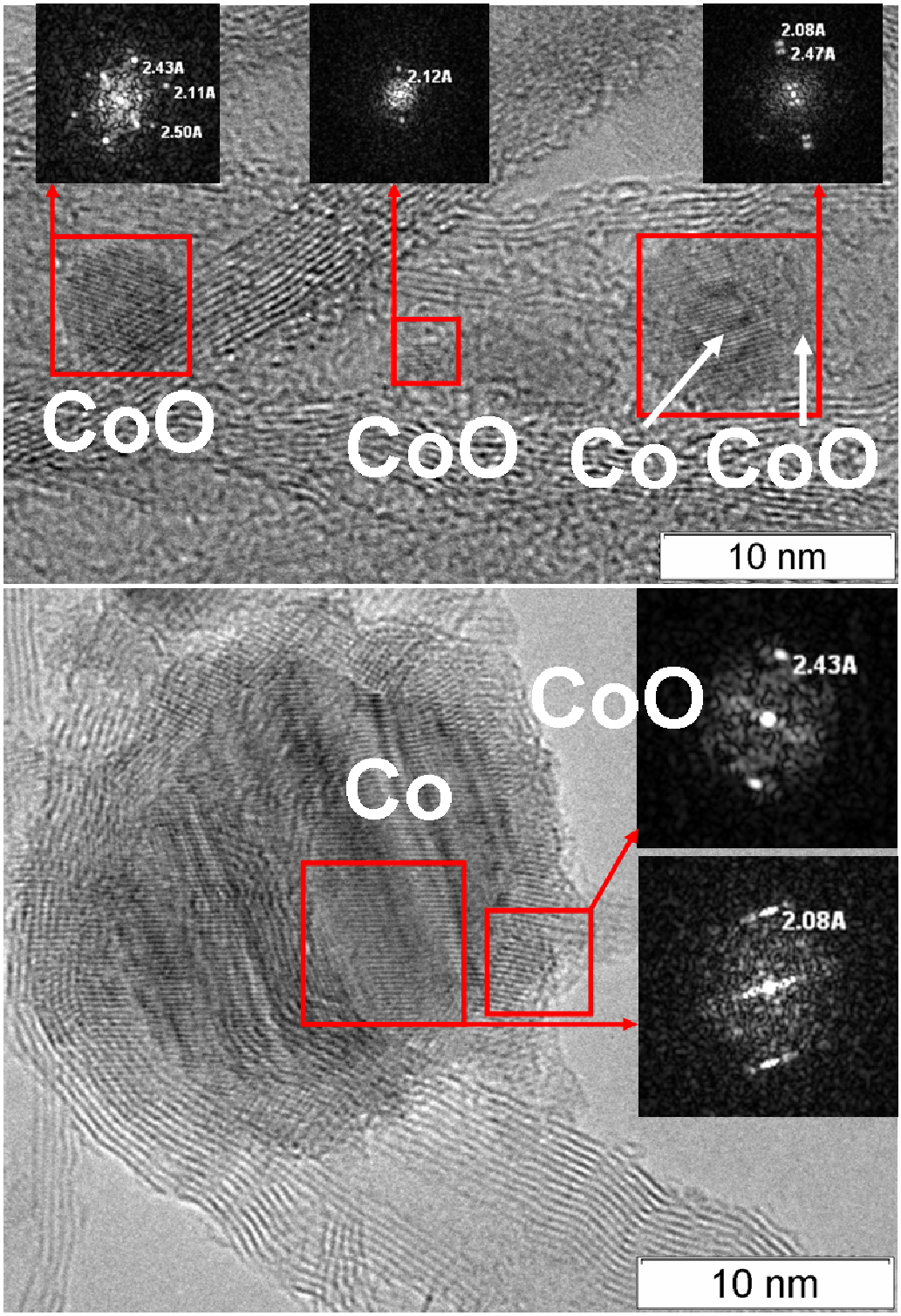

Figure 3. HRTEM images of 7.5% (above) and 11.7% (below) Co/MWCNT hybrids after reducing treatment with electron diffraction patterns. The particles of the small inside population appeared fully oxidized while the larger outside ones had a Co-CoO core-shell structures.

As the Co load increased, the inside population remained constant (Fig. 2) but the size distribution of the outside population increased, widened, and shifted toward higher values reaching a number average of about 21 nm at 14.5 % loading. Analysis of the electron diffraction patterns of selected nano particles shown in Figure 3 revealed that, in apparent contradiction with TPR results (Fig. S2), the Co phase present in the HRTEM chamber was partially oxidized. The large particles outside of the tubes had a Co-CoO core-shell structure with a shell thickness of ~2-3 nm. Consistently, the small particles inside the tubes, being of diameters of less than twice the oxidized shell thickness, were fully oxidized. The discrepancy between the TPR, showing unambiguously that the samples were fully reduced, and electron diffraction data, showing the partial oxidation of the samples analyzed in the HRTEM chamber, likely resulted from a well-known limitation of HRTEM: despite the protection provided by the glove box and then suspension in hexane, the standard sample preparation inevitably resulted in some fractional exposure to air. Nevertheless, this did not alter the validity of the conclusions regarding the particle sizes and localization obtained by HRTEM. Actually, this incidental oxidation revealed that the Co NPs inside the MWCNTs were not particularly protected from oxidation. This behavior contrasted with recent observations by Baaziz *et al.*[28] concerning clusters of Co NPs of similar sizes (5 nm) but confined inside non-porous MWCNTs with a wall thickness an order of magnitude larger (about 20 nm), for which an extremely high resistance to oxidation was reported.

Particles sizes, shapes and structures by IF-NMR. Small particles escape XRD detection, and HRTEM is difficult to perform without a minimum level of oxidation. Taking advantage of the magnetic properties of Cobalt metal, these measurements can thus be usefully complemented by ^{59}Co IF-NMR. Before even analyzing the ^{59}Co IF-NMR spectra, the fact that all samples provided a strong ferromagnetic signal was very informative (Figure 4). First, it demonstrated further that a significant part, if not all, of the cobalt was indeed in a metallic state since it is the only one that can exhibit ferromagnetism.

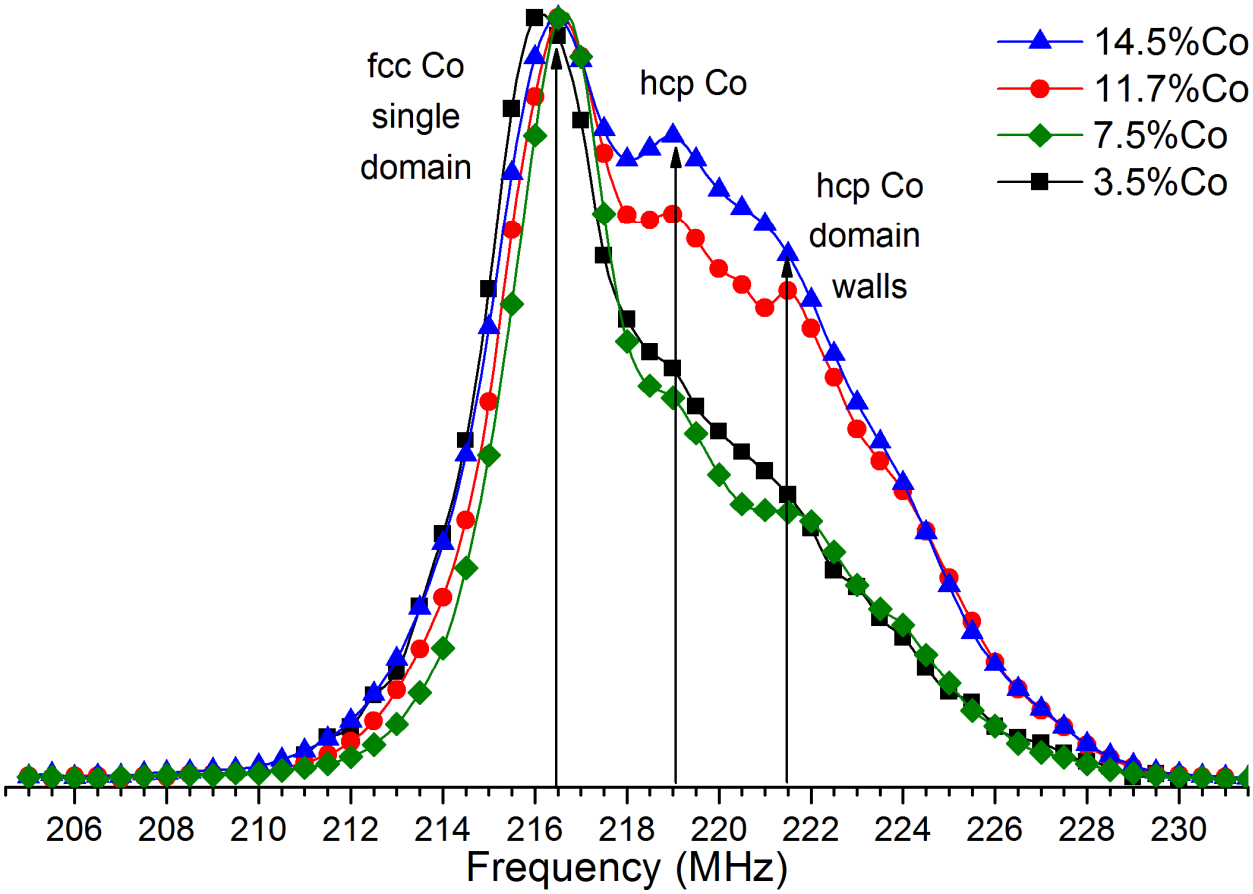

Figure 4. Optimal ^{59}Co IF-NMR spectra of all Co/MWCNT hybrids (3.5, 7.5, 11.7, 14.5 wt.% Co) after reduction. No contribution from multi domain fcc particles could be seen at 213 MHz proving that no fcc particles exceeded the critical domain size (about 50-70 nm). For the resonances attributed to the hcp system, a contribution from domain walls occurred despite the small size seen by HRTEM (less than 50 nm in all cases). This was related to the anisotropy of the particles cast inside carbon nanotube channels.

In the HRTEM electron diffraction pattern, all the particles in the 3.5% Co/MWCNT sample appeared oxidized; hence, they should not have provided a ^{59}Co IF-NMR resonance. This further proved that the partial oxidation observed in HRTEM occurred after the reduction treatment and did not reflect the true state of the as-reduced Co/MWCNT hybrids. Second, for such small particles, the occurrence of a ferromagnetic behavior at room temperature was a signature of a significant aspect ratio. According to ref.,[50] the blocking temperature T_B for the superpara- to ferro-magnetic transition is given by

$$T_B = \frac{1}{k_B \ln(\tau_m / \tau_0)} V K_{ef} \quad , \qquad (1)$$

where V is the particle volume; τ_m is the time of the experimental measurements (10–20 μs in our case); τ_0 is the characteristic relaxation time, in the range of 10^{-9} – 10^{-11} s; and K_{ef} is the magnetic anisotropy which results not only from magnetocrystalline anisotropy but also in part from shape anisotropy. For spherical Co particles, $K_{ef} = 5\times10^6$ Erg·cm^{-3}, a value leading to a critical volume of 12.10^2 nm^3 at room temperature, that is to a diameter of about 13 nm. For the 3.5% Co/MWCNT sample, the observation of a ferromagnetic behavior for particles that are all of equivalent diameter inferior to 8 nm established that K_{ef} was significantly lower than in spherical particles, *i.e.* that the Cobalt particles had significant shape or magnetic anisotropy caused by the interaction with MWCNTs.[51] Indeed, as shown in Figure 5 (and Fig. S1), inside the MWCNTs, oblong particles and even nanowires could be detected by HRTEM.

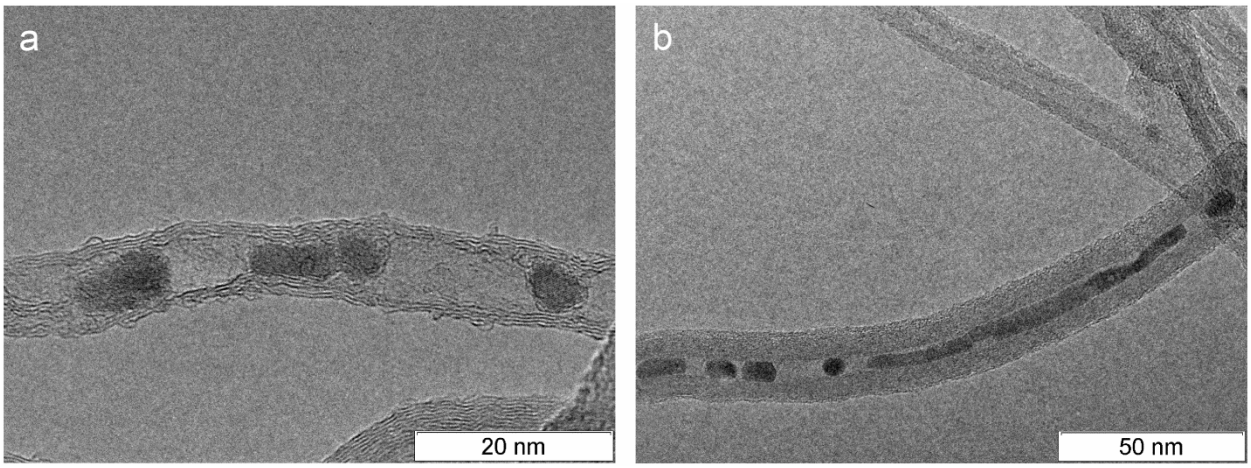

Figure 5. **(a)** HRTEM image of 3.5% Co/MWCNT showing oblong Co particles within the nanotubes; **(b)** HRTEM image of 7.5% Co/MWCNT showing a Co particle of very high aspect ratio, a Co nanowire inside a carbon nanotube.

A deeper understanding could be obtained by analyzing the spectral response of the cobalt magnetic NPs. The room temperature corrected ^{59}Co IF-NMR spectrum of the reduced 11.7% Co/MWCNT samples is shown in Figure 6 together with the variation of the enhancement factor with frequency. The optimal spectra of all the samples are represented in Figure 4. Further explanations concerning the notions of optimal and enhancement factor corrections of

IF-NMR spectra in ferromagnetic materials are provided in the Supporting Information. Briefly stated, the optimal spectra are obtained by varying the radio-frequency (rf) pulse power and recording for each sampled frequency the point of maximum intensity. The advantage of this representation is that it is independent of the acquisition conditions and is thus fully reproducible. Its disadvantage is that, because the rf field is enhanced differently by different magnetic structures, it is not quantitative. A correction by an enhancement factor is thus necessary to quantify the contributions of the different Co ferromagnetic structures. Whatever the chosen representation, the contributions of face centered cubic (fcc) and hexagonal closed-packed (hcp) phases to a ^{59}Co IF-NMR spectrum are very different. The fcc structure being cubic, there is no difference between the resonance frequencies from magnetic domains and from domain walls. The resonances are thus sharp and an easy distinction can be made between the resonances of the fcc multi-domain (213 MHz) and the one from the fcc single-domain particles (216.5 MHz) separated by the contribution of the demagnetization field to the internal field. In contrast, in hcp structures, the resonance are distributed over a wide range of frequencies to account for the contributions of Co in domain walls (221.5 MHz), domain wall edges (214 MHz), and domains. The resonance frequency of the latter is poorly defined as it is broadened simultaneously by a large internal field anisotropy and by a dispersion of internal field values that is not predictable *a priori* since it depends on the particle shapes and sizes.[41] (Note that the resonances of Co in fcc structures with stacking faults cannot be distinguished from the ones in hcp structures as the internal environment of Co are similar in both cases).

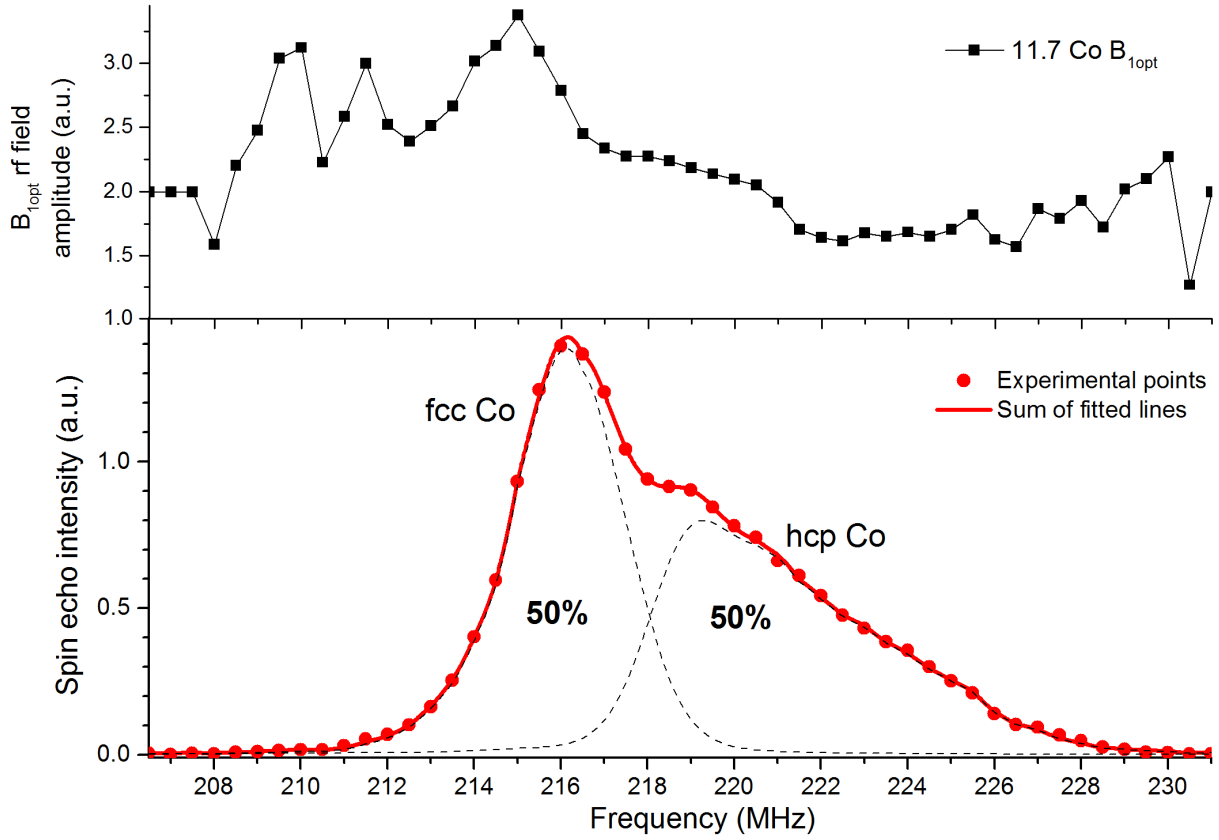

Figure 6. Corrected ^{59}Co IF-NMR of 11.7% Co/MWCNT hybrid sample after reduction. Also shown is the decomposition into two contributions, fcc and hcp **(bottom).** The optimal B_{1opt} field distribution through the spectrum giving information regarding the relative enhancement factors **(top)**. The exact line shape of the hcp resonance was obtained empirically by subtracting the fcc Gaussian line shape.

On this basis, the relative contribution of the fcc and hcp phases was simply obtained by subtracting the contribution of the two fcc 213 MHz and 216.5 MHz resonances from the spectra (see an example in Fig. 6, the results of the decompositions being summarized in Table 1). The first observation is that the multi-domain 213 MHz resonance was systematically absent in our samples. All the fcc particles had thus a single ferromagnetic domain resonating at 216.5 MHz, *i.e.* they were all smaller than the critical size of Co magnetic domains at room temperature namely ~50-70 nm.[52] This was perfectly in line with the HRTEM images where no particles with a diameter larger than 50 nm were observed and very few reported above 30 nm. The second observation was that the relative proportion of the hcp phase increased with the Co loading (Figure 5 and Table 1). This could be related to

the development of the outside population of particles of larger sizes evidenced by HRTEM. Kitakami *et.al.* have evidenced that in small particles, the high-temperature fcc structure is stabilized by the contribution of the surface free energy.[53]

Table 1. hcp/fcc ratio recalculated from the fit of IF-NMR spectra. An example is provided in Figure 6. The accuracy of the total fcc (hcp) phase determination is ±4%.

Sample Co weight content	3.5%	7.5%	11.7%	14.5%
hcp/fcc ratio	0.75 ± 0.12	0.58 ± 0.10	1.00 ± 0.16	1.17 ± 0.19

Consequently, as the particle sizes increased, the fcc phase was less stable and its proportion decreased with regards to the hcp structure. The growth of the hcp resonance was especially marked around 221.5 MHz (Figure 4). Such a resonance frequency is typically attributed to Co metal at the center of domain walls in multi domain hcp particles.[54,55] This line was barely resolved in the optimal spectrum representation of Figure 6 but due to its high enhancement factor was clearly evidenced at low rf field intensity (Fig. S3). The development of magnetic domain walls for particles of effective diameters inferior to the theoretical critical magnetic domain size for spherical particles was further proof that particles of high aspect ratio formed. This 221.5 MHz resonance was thus a signature of the bi-dimensional Co metal structures (nanowires) filling the MWCNTs observed in HRTEM (Fig. 4b).

Conclusion

Obtaining metal particles in the nanometer range can be experimentally very elaborate. Here, we showed that porous MWCNTs can act as templates to cast Co metal particles of elongated shapes following a simple incipient wetness procedure. Using MWCNTs of small internal diameter allowed the stabilization of particles with a diameter of less than 4 nm but with high aspect ratios. Small metallic particles are not expected to be ferromagnetic at room temperature but because of the tubular geometry into which they were cast, they had a high aspect ratio and magnetic anisotropy factor. This peculiar magnetic property meant that a true ferromagnetic Co/MWCNT nano-hybrid could be synthesized. Depending on the Co loading, particles with diameters an order of magnitude larger could also be deposited on the outside of the tubes. Quantification of each population was performed by HRTEM but this technique

does not preserve the oxidation state and phase structure of the particles. On the contrary, IF-NMR provided an original mean to characterize the magnetic NPs in their fully reduced state. Based on the different resonances of ferromagnetic single domains and of domain walls, the absence of large particles and the high aspect ratio of the particles inside the MWCNTs were confirmed. Furthermore, the relative amounts of fcc and hcp crystalline phases could be quantified, an information which can be of high interest for catalysis[56] and batteries[14] applications and cannot be obtained by other methods.

The Co magnetic NPs were not protected from oxidation but synchrotron XRD showed that they resisted sintering up to 550°C. This property is of high interest in catalysis. However, beyond this, the possibility to exploit simultaneously the original transport properties of CNTs and the magnetism of Co NPs also opens the way to use the Co/MWCNT hybrid as a component for polymer composites with new electro-magnetic properties such as improved radio-frequency shielding.[24] Elongated Co magnetic particles have been predicted to absorb in a wide range of frequencies (GHz to THz). Work is ongoing to understand the maximum Co intake inside the CNTs, and how to control the formation of magnetically coupled chains or of long nanowires.

Experimental Section

Synthesis of MWCNTs and functionalization. . MWCNTs were synthesized by ethylene decomposition over bimetallic Fe-Co catalysts at 680°C. Conditions were chosen according to ref.[39,40] to target an internal diameter of 3-4 nm and a wall thickness of 4-6 nm. These characteristics were controlled by statistical analysis of HRTEM images (see below). The Nitrogen BET surface area, measured on the ASAP-2400 Micromeritics instrument, was 305 m^2/g. Carbon nanotube pre-treatment was performed by reflux of 1–2 g in an excess of concentrated nitric acid during 90 min. This resulted in the formation of about 0.8 carboxylic groups per 1 nm,[39] while the surface area decreased slightly to 300 m^2/g.

Co/MWCNT preparation. Co-containing samples were prepared by incipient wetness impregnation of MWCNTs with aqua solutions of cobalt nitrate. After impregnation for 2 h, the sample precursors were dried at 110°C for 12 hours followed by calcination at 350°C for 4 hours under an argon atmosphere. They were then reduced in a stream of pure hydrogen (40 ml / min) at 350°C for 3 hours with a heating rate of 2°C/min. Varying the concentration of the cobalt nitrate solutions, samples of 3.5, 7.5, 11.7 and 14.5 wt. % Co loading were

obtained. This was controlled by X-ray fluorescence (XRF) using a sequential spectrometer ARL Perform'X with a Rh anode X-ray tube. The prepared samples were denoted as *x*% Co/MWCNT, the number *x* standing for the cobalt load (wt. %). The completeness of the reduction process was verified by temperature programmed reduction (TPR) (Fig. S2). Reduced samples were transferred into NMR ampoules, which were sealed without contact with air immediately after the reduction procedure.

***In situ* synchrotron X-ray diffraction (XRD).** The crystal phase transformations of the cobalt phase during the reduction of impregnated MWCNT precursors were monitored *in situ* by XRD on the VEPP 3 Precision Diffractometry station at the Siberian Center of Synchrotron and Terahertz Radiation. The samples were placed in an XRK 900 X-ray reaction chamber (Anton Paar, Austria). Heating was performed from room temperature to 700°C at a speed of 10°C/min under a flow of diluted H_2 (H_2 rate of 150 ml / sec). An intermediate stage at 350°C for 200 min was observed. The X ray patterns were recorded in near real time (60 s per frame) with an OD 3M 350 position sensitive detector in a 2θ range of 33°–65° with steps of ~0.01° (operating wavelength, 0.1731 nm), so as to capture the main reflections of Co, Co_3O_4 and CoO. The X-ray patterns were interpreted using the Topas full profile analysis program. The contribution of the baseline was eliminated by conducting additional experiments on the original nanotubes.

High Resolution Transmission Electron Microscopy (HRTEM). Morphologies of the CNT supports and of the Co/MWCNT hybrids were characterized using a JEOL JEM-2010 microscope operating at 200 kV accelerating voltage which allows a nominal resolution of 1.4 Å. Sample specimens for TEM studies were prepared by dispersion of the powder in hexane in a glove box under Argon. The hexane suspension was removed from the box and a drop deposited onto a Micro-mesh copper grid and then quickly transferred to the TEM vacuum chamber where it evaporated. The total time of exposure of the hexane suspension to atmosphere was 20 s. The MWCNT mean diameters and Co particle size distributions were estimated from a statistical count of the nanotubes from several frames taken on different parts of the samples.

Internal Field ^{59}Co nuclear magnetic resonance (IF-NMR). All IF ^{59}Co NMR experiments were carried out using a Bruker Avance NMR console without external magnetic field application, *i.e.* outside of the NMR magnet, and at ambient temperature. A commercial broadband static low Q NMR probe head with tuning and matching capacitors was used.

Although the measurements were not performed *in situ*, the samples were sealed on-line in the glass reactor used for reduction. Thus, during analysis, the samples did not evolve from the state they reached in the reactor, *i.e.* they were characterized in the same state of reduction and dispersion. The spectra were acquired using the spin-echo Fourier transform point by point method, described elsewhere.[46] The pulse train consisted of two identical pulses of 1 μs duration with an interpulse delay of 8 μs. The number of transients varied from 1k to 8k. The sequence repetition rate was 33 Hz due to the very short T_1 relaxation time of ferromagnetic cobalt. Low pulse powers were implemented (10 to 100 mW delivered at the radio-frequency coil) due to the high enhancement factor of metallic Co.[48] All Gaussian peak positions were determined from the ‘‘optimal’’ spectra (see Supporting Information for the definition of an “optimal” spectrum) and were in agreement with previous literature results. Only line widths and line intensities were varied, the peak positions remaining fixed during the spectral decompositions. Small manual deviation from the fixed line positions within 0.2 MHz were allowed to optimize the fit. The details of decomposition procedure can be found elsewhere.[48]

SUPPORTING INFORMATION.

Additional HRTEM images, TPR profiles, IF-NMR details, 2D NMR spectrum

Conflict of Interest: The authors declare no competing financial interest.

ACKNOWLEDGMENT

The NMR study is made possible by grant RFBR #14-03-31684. The sample preparation and treatment is supported by RAS Project V.44.1.17. A. Andreev was supported in part by a PhD grant from the French Embassy in Moscow and by the *Société des Amis de l'ESPCI*. The authors thank A. S. Lisitsyn from BIC SB RAS for the TPR analysis and discussion.

REFERENCES

(1) Lu, A.-H.; Salabas, E. L.; Schüth, F. Magnetic Nanoparticles: Synthesis, Protection, Functionalization, and Application. *Angew. Chemie Int. Ed.* **2007**, *46*, 1222–1244.

(2) Akbarzadeh, A.; Samiei, M.; Davaran, S. Magnetic Nanoparticles: Preparation, Physical Properties, and Applications in Biomedicine. *Nanoscale Res. Lett.* **2012**, *7*, 144.

(3) Pankhurst, Q. A.; Connolly, J.; Jones, S. K.; Dobson, J. Applications of Magnetic Nanoparticles in Biomedicine. *J. Phys. D. Appl. Phys.* **2003**, *36*, R167–R181.

(4) Ito, A.; Shinkai, M.; Honda, H.; Kobayashi, T. Medical Application of Functionalized Magnetic Nanoparticles. *J. Biosci. Bioeng.* **2005**, *100*, 1–11.

(5) Gao, J.; Gu, H.; Xu, B. Multifunctional Magnetic Nanoparticles: Design, Synthesis, and Biomedical Applications. *Acc. Chem. Res.* **2009**, *42*, 1097–1107.

(6) Iijima, S. Helical Microtubules of Graphitic Carbon. *Nature* **1991**, *354*, 56–58.

(7) Monthioux, M.; Kuznetsov, V. L. Who Should Be given the Credit for the Discovery of Carbon Nanotubes? *Carbon N. Y.* **2006**, *44*, 1621–1623.

(8) Bartling, S.; Yin, C.; Barke, I.; Oldenburg, K.; Hartmann, H.; von Oeynhausen, V.; Pohl, M.-M.; Houben, K.; Tyo, E. C.; Seifert, S.; *et al.* Pronounced Size Dependence in Structure and Morphology of Gas-Phase Produced, Partially Oxidized Cobalt Nanoparticles under Catalytic Reaction Conditions. *ACS Nano* **2015**, *9*, 5984–5998.

(9) Zhang, H.; Lancelot, C.; Chu, W.; Hong, J.; Khodakov, A. Y.; Chernavskii, P. A.; Zheng, J.; Tong, D. The Nature of Cobalt Species in Carbon Nanotubes and Their Catalytic Performance in Fischer–Tropsch Reaction. *J. Mater. Chem.* **2009**, *19*, 9241–9249.

(10) Xiong, H.; Motchelaho, M. A. M.; Moyo, M.; Jewell, L. L.; Coville, N. J. Correlating the Preparation and Performance of Cobalt Catalysts Supported on Carbon Nanotubes and Carbon Spheres in the Fischer–Tropsch Synthesis. *J. Catal.* **2011**, *278*, 26–40.

(11) Lentijo-Mozo, S.; Tan, R. P.; Garcia-Marcelot, C.; Altantzis, T.; Fazzini, P.-F.; Hungria, T.; Cormary, B.; Gallagher, J. R.; Miller, J. T.; Martinez, H.; *et al.* Air- and Water-Resistant Noble Metal Coated Ferromagnetic Cobalt Nanorods. *ACS Nano* **2015**, *9*, 2792–2804.

(12) Kim, J.; Piao, Y.; Hyeon, T. Multifunctional Nanostructured Materials for Multimodal Imaging, and Simultaneous Imaging and Therapy. *Chem. Soc. Rev.* **2009**, *38*, 372–390.

(13) Xu, Y.; Mahmood, M.; Li, Z.; Dervishi, E.; Trigwell, S.; Zharov, V. P.; Ali, N.; Saini, V.; Biris, A. R.; Lupu, D.; *et al.* Cobalt Nanoparticles Coated with Graphitic Shells as Localized Radio Frequency Absorbers for Cancer Therapy. *Nanotechnology* **2008**, *19*, 435102.

(14) Rosant, C.; Avalle, B.; Larcher, D.; Dupont, L.; Friboulet, A.; Tarascon, J.-M. Biosynthesis of Co3O4 Electrode Materials by Peptide and Phage Engineering: Comprehension and Future. *Energy Environ. Sci.* **2012**, *5*, 9936–9943.

(15) Cabana, J.; Monconduit, L.; Larcher, D.; Palacín, M. R. Beyond Intercalation-Based Li-Ion Batteries: The State of the Art and Challenges of Electrode Materials Reacting through Conversion Reactions. *Adv. Mater.* **2010**, *22*, E170–E192.

(16) Fukumaru, T.; Fujigaya, T.; Nakashima, N. Development of N-Type Cobaltocene-Encapsulated Carbon Nanotubes with Remarkable Thermoelectric Property. *Sci. Rep.* **2015**, *5*, 7951.

(17) Peigney, A.; Laurent, C.; Flahaut, E.; Bacsa, R. R.; Rousset, A. Specific Surface Area of Carbon Nanotubes and Bundles of Carbon Nanotubes. *Carbon N. Y.* **2001**, *39*, 507–514.

(18) Chakraborty, S.; Chattopadhyay, J.; Peng, H.; Chen, Z.; Mukherjee, A.; Arvidson, R. S.; Hauge, R. H.; Billups, W. E. Surface Area Measurement of Functionalized Single-Walled Carbon Nanotubes. *J. Phys. Chem. B* **2006**, *110*, 24812–24815.

(19) Aliev, A. E.; Lima, M. H.; Silverman, E. M.; Baughman, R. H. Thermal Conductivity of Multi-Walled Carbon Nanotube Sheets: Radiation Losses and Quenching of Phonon Modes. *Nanotechnology* **2010**, *21*, 035709.

(20) Yang, D. J.; Zhang, Q.; Chen, G.; Yoon, S. F.; Ahn, J.; Wang, S. G.; Zhou, Q.; Wang, Q.; Li, J. Q. Thermal Conductivity of Multiwalled Carbon Nanotubes. *Phys. Rev. B* **2002**, *66*, 165440.

(21) Prasher, R. Thermal Boundary Resistance and Thermal Conductivity of Multiwalled Carbon Nanotubes. *Phys. Rev. B* **2008**, *77*, 075424.

(22) Chang, C.-M.; Liu, Y.-L. Electrical Conductivity Enhancement of Polymer/Multiwalled Carbon Nanotube (MWCNT) Composites by Thermally-Induced Defunctionalization of MWCNTs. *ACS Appl. Mater. Interfaces* **2011**, *3*, 2204–2208.

(23) Ra, E. J.; An, K. H.; Kim, K. K.; Jeong, S. Y.; Lee, Y. H. Anisotropic Electrical Conductivity of MWCNT/PAN Nanofiber Paper. *Chem. Phys. Lett.* **2005**, *413*, 188–193.

(24) Eletskii, A. V; Knizhnik, A. A.; Potapkin, B. V; Kenny, J. M. Electrical Characteristics of Carbon Nanotube-Doped Composites. *Physics-Uspekhi* **2015**, *58*, 209–251.

(25) Coleman, J. N.; Khan, U.; Blau, W. J.; Gun'ko, Y. K. Small but Strong: A Review of the Mechanical Properties of Carbon Nanotube–polymer Composites. *Carbon N. Y.* **2006**, *44*, 1624–1652.

(26) Arash, B.; Wang, Q.; Varadan, V. K. Mechanical Properties of Carbon Nanotube/polymer Composites. *Sci. Rep.* **2014**, *4*, 6479.

(27) Ruoff, R. S.; Qian, D.; Liu, W. K. Mechanical Properties of Carbon Nanotubes: Theoretical Predictions and Experimental Measurements. *Comptes Rendus Phys.* **2003**, *4*, 993–1008.

(28) Baaziz, W.; Florea, I.; Moldovan, S.; Papaefthimiou, V.; Zafeiratos, S.; Begin-Colin, S.; Begin, D.; Ersen, O.; Pham-Huu, C. Microscopy Investigations of the Microstructural Change and Thermal Response of Cobalt-Based Nanoparticles Confined inside a Carbon Nanotube Medium. *J. Mater. Chem. A* **2015**, *3*, 11203–11214.

(29) Keng, P. Y.; Kim, B. Y.; Shim, I.-B.; Sahoo, R.; Veneman, P. E.; Armstrong, N. R.; Yoo, H.; Pemberton, J. E.; Bull, M. M.; Griebel, J. J.; *et al.* Colloidal Polymerization of Polymer-Coated Ferromagnetic Nanoparticles into Cobalt Oxide Nanowires. *ACS Nano* **2009**, *3*, 3143–3157.

(30) Lutsev, L. V; Kazantseva, N. E.; Tchmutin, I. A.; Ryvkina, N. G.; Kalinin, Y. E.; Sitnikoff, A. V. Dielectric and Magnetic Losses of Microwave Electromagnetic Radiation in Granular Structures with Ferromagnetic Nanoparticles. *J. Phys. Condens. Matter* **2003**, *15*, 3665–3681.

(31) Lutsev, L. V. Spin Excitations in Granular Structures with Ferromagnetic Nanoparticles. *Phys. Solid State* **2002**, *44*, 102–110.

(32) Costa, P. M. F. J.; Sloan, J.; Rutherford, T.; Green, M. L. H. Encapsulation of Re_xO_y Clusters within Single-Walled Carbon Nanotubes and Their in Tubulo Reduction and Sintering to Re Metal. *Chem. Mater.* **2005**, *17*, 6579–6582.

(33) Martín-Fabiani, I.; García-Gutiérrez, M.-C.; Rueda, D. R.; Linares, A.; Hernández, J. J.; Ezquerra, T. A.; Reynolds, M. Crystallization under One-Dimensional Confinement in Alumina Nanopores of Poly(trimethylene Terephthalate) and Its Composites with Single Wall Carbon Nanotubes. *ACS Appl. Mater. Interfaces* **2013**, *5*, 5324–5329.

(34) Baaziz, W.; Begin-Colin, S.; Pichon, B. P.; Florea, I.; Ersen, O.; Zafeiratos, S.; Barbosa, R.; Begin, D.; Pham-Huu, C. High-Density Monodispersed Cobalt Nanoparticles Filled into Multiwalled Carbon Nanotubes. *Chem. Mater.* **2012**, *24*, 1549–1551.

(35) Elumeeva, K. V.; Kuznetsov, V. L.; Ischenko, A. V.; Smajda, R.; Spina, M.; Forró, L.; Magrez, A. Reinforcement of CVD Grown Multi-Walled Carbon Nanotubes by High Temperature Annealing. *AIP Adv.* **2013**, *3*, 112101.

(36) Tsang, S. C.; Chen, Y. K.; Harris, P. J. F.; Green, M. L. H. A Simple Chemical Method of Opening and Filling Carbon Nanotubes. *Nature* **1994**, *372*, 159–162.

(37) Satishkumar, B. C.; Govindaraj, A.; Mofokeng, J.; Subbanna, G. N.; Rao, C. N. R. Novel Experiments with Carbon Nanotubes: Opening, Filling, Closing and Functionalizing Nanotubes. *J. Phys. B At. Mol. Opt. Phys.* **1996**, *29*, 4925–4934.

(38) De Tymowski, B.; Liu, Y.; Mény, C.; Lefèvre, C.; Begin, D.; Nguyen, P.; Pham, C.; Edouard, D.; Luck, F.; Pham-Huu, C. Co–Ru/SiC Impregnated with Ethanol as an Effective Catalyst for the Fischer–Tropsch Synthesis. *Appl. Catal. A Gen.* **2012**, *419-420*, 31–40.

(39) Mazov, I.; Kuznetsov, V. L.; Simonova, I. A.; Stadnichenko, A. I.; Ishchenko, A. V.; Romanenko, A. I.; Tkachev, E. N.; Anikeeva, O. B. Oxidation Behavior of Multiwall Carbon Nanotubes with Different Diameters and Morphology. *Appl. Surf. Sci.* **2012**, *258*, 6272–6280.

(40) Kuznetsov, V. L. (RU); Usol'tseva, A. N. (RU). Method of Producing Fine-Grained Supported Catalysts and Synthesis of Carbon Nanotubes. Patent RU 2373995, 2008.

(41) Andreev, A. S.; d'Espinose de Lacaillerie, J.-B.; Lapina, O. B.; Gerashenko, A. Thermal Stability and Hcp-Fcc Allotropic Transformation in Supported Co Metal Catalysts Probed near Operando by Ferromagnetic NMR. *Phys. Chem. Chem. Phys.* **2015**, *17*, 14598–14604.

(42) Liu, Y.; Luo, J.; Girleanu, M.; Ersen, O.; Pham-Huu, C.; Meny, C. Efficient Hierarchically Structured Composites Containing Cobalt Catalyst for Clean Synthetic Fuel Production from Fischer–Tropsch Synthesis. *J. Catal.* **2014**, *318*, 179–192.

(43) Liu, Y.; de Tymowski, B.; Vigneron, F.; Florea, I.; Ersen, O.; Mény, C.; Nguyen, P.; Pham, C.; Luck, F.; Pham-Huu, C. Titania-Decorated Silicon Carbide-Containing Cobalt Catalyst for Fischer–Tropsch Synthesis. *ACS Catal.* **2013**, *3*, 393–404.

(44) Liu, Y.; Florea, I.; Ersen, O.; Pham-Huu, C.; Meny, C. Silicon Carbide Coated with TiO_2 with Enhanced Cobalt Active Phase Dispersion for Fischer–Tropsch Synthesis. *Chem. Commun.* **2015**, *51*, 145–148.

(45) Andreev, A. S.; Lapina, O. B.; d'Espinose de Lacaillerie, J.-B.; Khassin, A. A. Effect of Alumina Modification on the Structure of Cobalt-Containing Fischer-Tropsch Synthesis Catalysts according to Internal-Field ^{59}Co NMR Data. *J. Struct. Chem.* **2013**, *54*, 102–110.

(46) Andreev, A. S.; Tikhov, S. F.; Salanov, A. N.; Cherepanova, S. V; Lapina, O. B.; Bolotov, V. A.; Tanashev, Y. Y.; d'Espinose de Lacaillerie, J.-B.; Sadykov, V. A. Design of Al_2O_3/CoAlO/CoAl Porous Ceramometal for Multiple Applications as Catalytic Supports. *Adv. Mater. Res.* **2013**, *702*, 79–87.

(47) Belesi, M.; Panagiotopoulos, I.; Pal, S.; Hariharan, S.; Tsitrouli, D.; Papavassiliou, G.; Niarchos, D.; Boukos, N.; Fardis, M.; Tzitzios, V. Decoration of Carbon Nanotubes with CoO and Co Nanoparticles. *J. Nanomater.* **2011**, *2011*, 1–9.

(48) Andreev, A. S.; Lapina, O. B.; Cherepanova, S. V. A New Insight into Cobalt Metal Powder Internal Field ^{59}Co NMR Spectra. *Appl. Magn. Reson.* **2014**, *45*, 1009–1017.

(49) Moulijn, J. .; van Diepen, A. .; Kapteijn, F. Catalyst Deactivation: Is It Predictable? *Appl. Catal. A Gen.* **2001**, *212*, 3–16.

(50) De Julián Fernández, C. Influence of the Temperature Dependence of Anisotropy on the Magnetic Behavior of Nanoparticles. *Phys. Rev. B* **2005**, *72*, 054438.

(51) Skumryev, V.; Stoyanov, S.; Zhang, Y.; Hadjipanayis, G.; Givord, D.; Nogués, J. Beating the Superparamagnetic Limit with Exchange Bias. *Nature* **2003**, *423*, 850–853.

(52) Leslie-Pelecky, D. L.; Rieke, R. D. Magnetic Properties of Nanostructured Materials. *Chem. Mater.* **1996**, *8*, 1770–1783.

(53) Kitakami, O.; Sato, H.; Shimada, Y.; Sato, F.; Tanaka, M. Size Effect on the Crystal Phase of Cobalt Fine Particles. *Phys. Rev. B* **1997**, *56*, 13849–13854.

(54) Kawakami, M.; Hihara, T.; Koi, Y. The Co^{59} Nuclear Magnetic Resonance in Hexagonal Cobalt. *J. Phys. Soc. Jpn.* **1972**, *33*, 1591–1598.

(55) Kunkel, H. P.; Searle, C. W. Experimental Identification of Domain-Wall-Center and Domain-Wall-Edge NMR Resonances in Magnetically Ordered Materials. *Phys. Rev. B* **1981**, *23*, 65–68.

(56) Liu, J.-X.; Su, H.-Y.; Sun, D.-P.; Zhang, B.-Y.; Li, W.-X. Crystallographic Dependence of CO Activation on Cobalt Catalysts: HCP versus FCC. *J. Am. Chem. Soc.* **2013**, *135*, 16284–16287.

Supporting Information

Templating ferromagnetic Cobalt nanoparticles and wires within Carbon Nanotubes

Andrey S. Andreev[†, ‡, §],Mariya A. Kazakova[†, ‡], Arcady V. Ishchenko[†, ‡], Alexander G. Selyutin[†], Olga B. Lapina[†, ‡], Vladimir L. Kuznetsov[†, ‡], Jean-Baptiste d'Espinose de Lacaillerie*[, §]

[†] Boreskov Institute of Catalysis, SB RAS, Lavrentieva 5, Novosibirsk 630090, Russia

[‡] Novosibirsk State University, Pirogova 2, Novosibirsk, 630090, Russia

[§] Soft Matter Sciences and Engineering (SIMM), UMR CNRS 7615, PSL Research University, ESPCI ParisTech, 75005, Paris, France

* Corresponding Author: jean-baptiste.despinose@espci.fr

Additional high-resolution transmission electron microscope (HRTEM) data

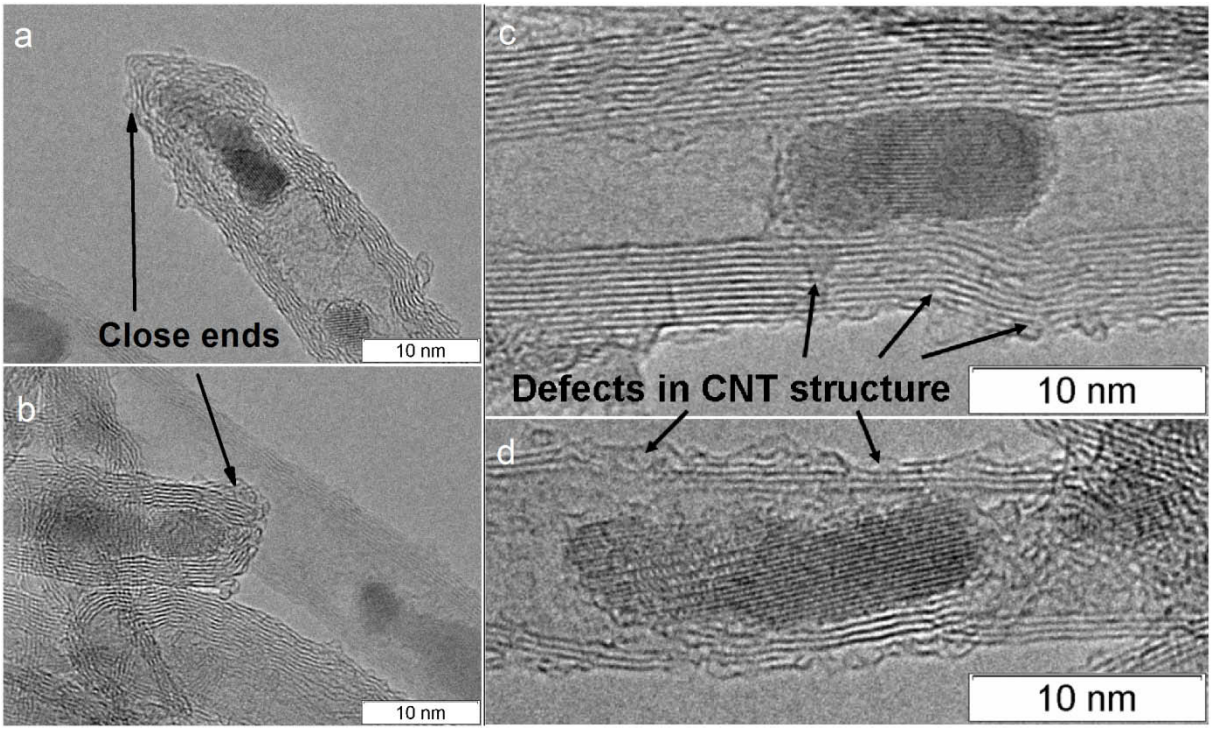

Figure S1. HRTEM images of 3.5% Co/MWCNT showing the closed ends of MWCNTs, **(a)** and **(b)**, and the defective structure of the MWCNT porous walls, **(c)** and **(d)**.

Temperature programmed reduction (TPR) data

TPR was performed using a Micromeritics ASAP 2400, system, equipped with a thermal conductivity detector (TCD). The samples were re-treated in a flow of argon at 350°C for 10 min to remove excess water, and then cooled down to room temperature. A 5% H_2/Ar mixture (25 mL/min) was then introduced and the samples heated to 700 °C with a ramp of 20 °C/min. TCD was used to record the signal linked to hydrogen consumption or adsorbed water release.

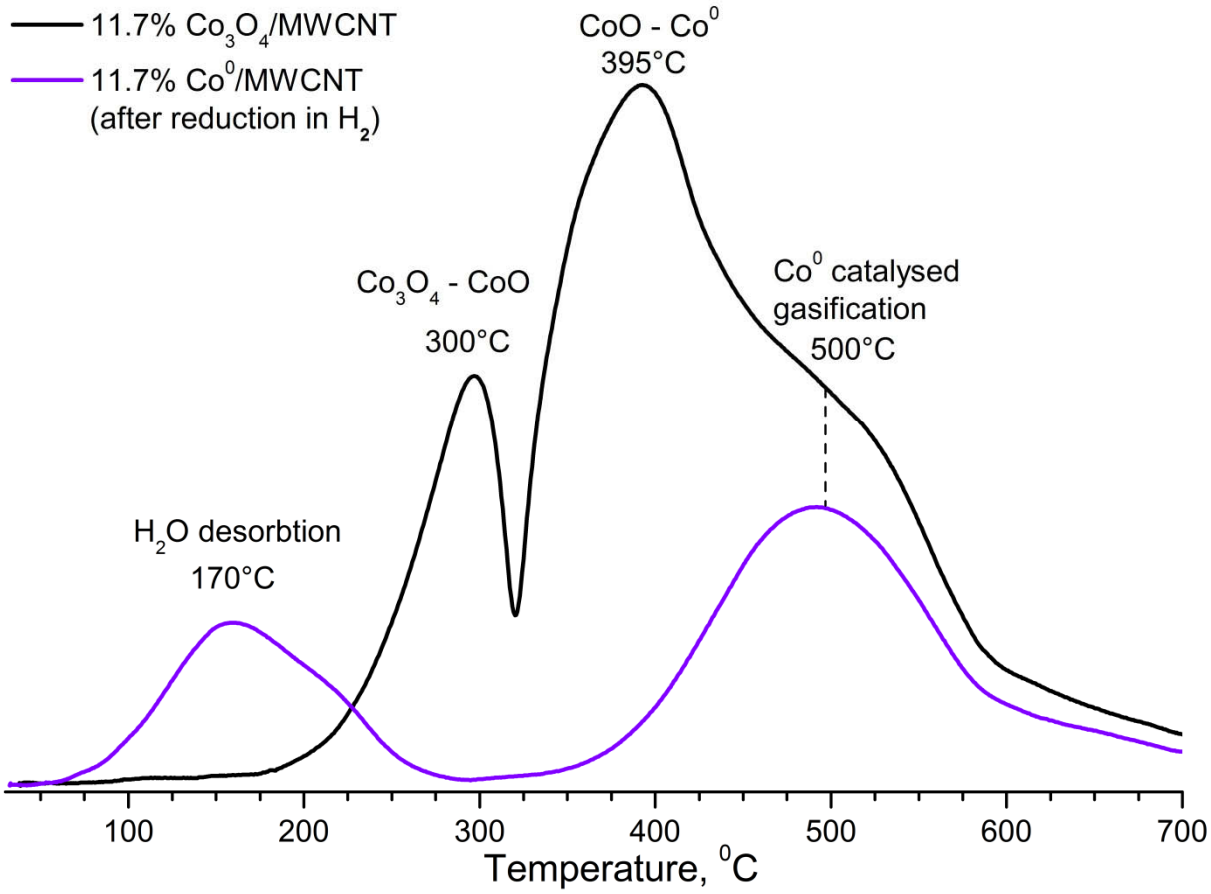

Figure S2. TPR profiles of 11.7% Co/MWCNT hybrid as synthesized and after reduction according to the experimental procedure. Intensities are not to scale.

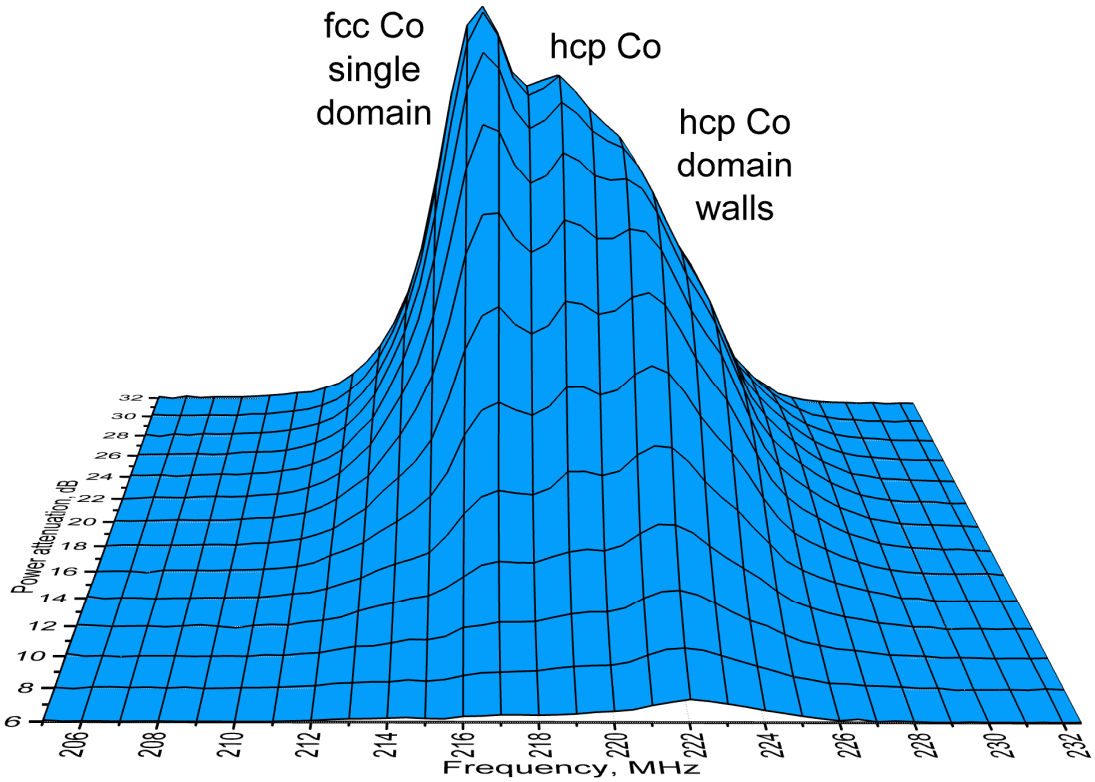

Figure S3. 3D internal field ^{59}Co NMR plot of signal intensity *versus* applied power and frequency (sample 14.5% Co/MWCNT). The dependency definitely showed that the spectrum should be decomposed into 3 lines, *i.e.* including one at 221.5 MHz.

Additional details on internal field NMR.

Different structures in internal field NMR spectra can have different enhancement factors and thus different dependence of their signal on the applied rf field intensity delivered at the nucleus which in turns cannot be known *a priori*. Consequently, the internal field NMR spectra acquired at one power level are irreproducible when different spectrometer and probes are used. Nevertheless, full reproducibility can be attained using the optimal spectra representation. This approach requires knowing the rf field dependency of the resonance at each frequency as shown by Mény, Panissod and co-workers.[1,2] These authors provided a formula of the internal field NMR signal dependence on frequency and applied power (which is true for nuclei in domains, but its relevance in domain walls requires additional justifications)[3,4]

$$S(B_1,\omega) = \eta I_0(\omega)\exp\left[-\log^2\left(B_1/B_{1opt}\right)/2\sigma^2\right] \quad (1)$$

where $S(B_1,\omega)$ is the observed intensity in the spectrum, $I_0(\omega)$ its « true » intensity, B_1 the rf field inducing the signal, B_{1opt} the applied rf field when the signal is maximal (*i.e.* optimal), σ the width of the Gaussian distribution in the units of $ln(B_1)$, and η is the enhancement factor.

Generally, a majority of studies uses a simplified expression of equation (1) working at conditions where $B_1 = B_{1opt}$. Since the applied rf field B_{1opt} causes maximal intensity in the spectra, the spectrum plotted using B_{1opt} at each frequency is called optimal. The main advantage of this approach consists in its universality, *i.e.* the optimal spectrum is not dependent on instrumental specifications (whereas attempting to correct for the enhancement factor is tainted by measurement errors of the rf field amplitude B_1). Practically, the optimal spectrum is obtained as follows. The NMR signal is acquired in two dimensions, that is intensity *versus* frequency and rf power as described elsewhere.[1,2] The optimal spectrum is simply a projection along the rf power dimension and does not require exact knowledge of the power values (hence its reproducibility).

Unfortunately, this representation is not quantitative because each point has its own enhancement factor η (*i.e.* different optimal excitation field B_{1opt}, at which the signal is maximal). To get quantitative results, a correction is required. It consists in a multiplication of the optimal spectrum by a calibration curve showing the B_{1opt} rf field frequency dependence.[5] The resulting spectral representation is called a spectrum corrected for the enhancement factor.[6]

References

(1) Panissod, P.; Jay, J. P.; Mény, C.; Wójcik, M.; Jędryka, E. NMR Analysis of Buried Metallic Interfaces. *Hyperfine Interact.* **1996**, *97-98*, 75–98.

(2) Malinowska, M.; Wójcik, M.; Nadolski, S.; Jędryka, E.; Mény, C.; Panissod, P.; Knobel, M.; Viegas, A. D. C.; Schmidt, J. E. Identification of Magnetic Phases in Granular Co10Cu90 Alloy Using ^{59}Co NMR Method. *J. Magn. Magn. Mater.* **1999**, *198-199*, 599–601.

(3) Mény, C. PhD Thesis. Etude de Multicouches Magnétiques Par RMN: Méthodologie et Application Aux Systèmes Co/Cu, Co/Cr, Co/Ru et Co/Fe. Université Louis Pasteur: Strasbourg I, 1994.

(4) Jay, J.-P. PhD Thesis. Etude Par Resonance Magnetique Nucleaire de l'Ordre à Courte Distance dans le Système Cobalt/Fer : De l'Alliage Massif à la Multicouche. Université Louis Pasteur: Strasbourg I, 1995.

(5) Panissod, P.; Mény, C. Nuclear Magnetic Resonance Investigations of the Structure and Magnetic Properties of Metallic Multilayers and Nanocomposites. *Appl. Magn. Reson.* **2000**, *19*, 447–460.

(6) Andreev, A. S.; Lapina, O. B.; Cherepanova, S. V. A New Insight into Cobalt Metal Powder Internal Field ^{59}Co NMR Spectra. *Appl. Magn. Reson.* **2014**, *45*, 1009–1017.

5. Conclusion

5.1. Summary of results

Nowadays, there are several approaches for the interpretation of the internal field ^{59}Co NMR peaks in metallic cobalt. The same resonance frequencies have been interpreted differently in the literature. To understand the roots of such disagreements, a substantial chronological examination of the literature, starting from the discovery of magnetic resonance in magnetic substances, was necessary.

Despite the fact that NMR and XRD provide different type of information (NMR probes short-range environment and XRD long-ranges order), a good agreement between both techniques can be reached regarding the quantification of Co metal hcp/fcc ratio. This requires a careful examination of the NMR spectra taking into account variations of the enhancement factor. The best approach must consider both structural (hcp, fcc, sfs) and magnetic (domains and domain walls) features. The assignment we decided to follow can be listed as follows:

211 MHz and below – resonance of particle boundaries or Co with loose coordination;

213 MHz – fcc Co resonance in multidomain particles;

~214 MHz – hcp domains;

219 - hcp Co resonance (usually attributed to domain walls)

221 MHz – hcp Co resonance in domain walls

The hcp/fcc ratio by NMR based on the assignment is 2.2, when it is equal to 2.5 by XRD within experimental errors. Finally, the optimal field B_1^{opt} distribution also gives valuable information facilitating spectral line assignment in internal field ^{59}Co NMR spectra, since it varies greatly between magnetic domain and d.w.

The temperature behavior of Co metal nanoparticles supported on β-SiC provides different type of information. The resonances of the fcc multi-domain particles, fcc single-domain

particles and hcp Co particles were clearly distinguishable. The allotropic transition was found to start in the 600-650 K temperature range, that is 50 K less than in the bulk and approximately 100 K lower than in Co metal powders according to Speight et al. [58]. A significant part of the sample remained in the hcp phase at the highest temperature considered (850 K). The hcp-fcc transformation appeared fully reversible in the 300-850 K temperature range. Our description of the Co particles stability in temperatures near *operando*, up to 600 K, might prove useful to understand and model active species in other catalytic or battery materials were the active species are above the superparamagnetic critical size. Finally, the anomalous stability of some hcp domains up to 850 K (the maximal temperature implemented in the present study) had never been reported before.

The internal field ^{59}Co NMR technique provided unique data on the composition and magnetic structure of co-precipitated FTS catalysts by distinguishing the contributions from magnetic d.w. and magnetic domains, fcc and hcp packings as well as contributions from various sfs. This technique revealed the effect of support modification on the structure of metallic cobalt. Co/δ-Al_2O_3 samples were characterized by the single-domain fcc cobalt packing and a broad line of sfs at a 1:3 ratio with the sfs prevalence. The spectrum of Co/γ-Al_2O_3 shows multidomain fcc and hcp packings, which indicate the presence of large (~70 nm) Co^0 particles on the support surface. The fcc:hcp:sfs ratio for this sample is equal to 3:5:12, respectively. Most of metallic cobalt particles have a high sfs concentration. A pronounced difference in the spin-spin relaxation time for the studied samples and non-uniformity of the T_2 value distribution over the spectrum were demonstrated.

Application of several methods (XRD, TEM, SEM with X-ray elemental mapping, internal field ^{59}Co NMR) to examine the structural features of CoAlO/Co-Al cermet prepared via mechanical alloying followed by hydrothermal treatment and annealing in the air revealed pronounced non-uniformity of phase and element distribution. Metallic phase consisted of metallic Co and Co-Al alloy covered by thin Al_2O_3 oxide film, which protected the metallic part of the cermet from oxidation. The internal field ^{59}Co NMR was found extremely powerful to study the metallic part of the cermet due to quantification of Co metal and CoAl alloy phases. Moreover, the existence of metallic cermet part was initially proved only by strong internal field NMR signal, which arose only from Co in metallic state. SEM mapping had main drawbacks, which consisted in partial surface oxidation after polishing leading to oxygen content overestimation in EDX mapping. The oxide matrix surrounding metallic

domains consisted of cobalt aluminates and cobalt oxides phases proved by XRD and SEM coupled with EDX mapping. The presence of metallic cores greatly improves the cermet mechanical strength from 10-100 kg / cm^2 in cobalt-free cermets to 700-800 kg / cm^2 in CoAlO/Co-Al cermet.

A new approach of preparation of porous ceramometalic materials allowed obtaining both sufficient crushing strength and high SSA in low temperature Al_2O_3/CoAlO/CoAl cermet. Based on structural data by XRD, NMR, and SEM coupled with EDX, the Al_2O_3/CoAlO/CoAl cermet consisted mainly alumina (mixture of γ-Al_2O_3 and α- Al_2O_3). Large blocks of alumina were coated by $Co_{3-x}Al_xO_4$ (x = 0; 1; 2) mixed oxides, which touched the metallic part of the cermet made of Co metal with some inclusions of CoAl alloy. An oxide coating protected the Co metal against full oxidation even under high temperature calcinations at 600ºC in air. The Cobalt metal structure was mainly fcc with some stacking faults associated with hcp Co. The high surface area of 122 m^2 / g was the key for using this Al_2O_3/CoAlO/CoAl cermet as a promising catalytic support or catalyst. The enhanced adsorption of microwaves can be considered as an alternative route of for heat transfer in a catalytic reactor in endothermic catalytic processes.

Porous MWCNTs can act as templates to cast Co metal particles of elongated shapes following a simple incipient wetness procedure. Using MWCNTs of small internal diameter allowed the stabilization of particles with a diameter of less than 4 nm but with high aspect ratios. Small metallic particles are not expected to be ferromagnetic at room temperature but because of the tubular geometry into which they were cast, they had a high aspect ratio and magnetic anisotropy factor. This peculiar magnetic property meant that a true ferromagnetic Co/MWCNT nano-hybrid could be synthesized. Depending on the Co loading, particles with diameters an order of magnitude larger could also be deposited on the outside of the tubes. Quantification of each population was performed by HRTEM but this technique does not preserve the oxidation state and phase structure of the particles. On the contrary, IF-NMR provided an original mean to characterize the magnetic NPs in their fully reduced state. Based on the different resonances of ferromagnetic single domains and of domain walls, the absence of large particles and the high aspect ratio of the particles inside the MWCNTs were confirmed. Furthermore, the relative amounts of fcc and hcp crystalline phases could be quantified. The Co magnetic NPs were not protected from oxidation but synchrotron XRD showed that they resisted sintering up to 550°C.

5.2. Future work

Internal field ^{59}Co NMR is a promising technique to characterize Co metal based materials. Despite some limitations in particle size due to ferromagnetism-superparamagnetism transition of fine Co metal nanoparticles, the technique is extremely powerful as we demonstrated in bi-metallic Co-Al-O cermet.

The Chapter 2.2 gives a brief classification of what has been done in different binary or even ternary Co metal alloys. Due to a large number of papers on Co metal alloys and films this scientific field can seem at first sight to have been exhausted. However, all the papers concerns samples with common structures, which can be generalized as *stochastic or perfect alloy structure.* Consequently, the application of internal field NMR is mainly limited to fully ordered/disordered or very dilute Co alloys which display distinct satellite lines in the spectra due to internalized magnetic moments. Moreover, the majority of published work aimed to give only fundamental insight into (magnetic) structure of Co alloys, film and coatings.

Nevertheless, more complex bi-metallic cobalt alloys are of high interest in more applied spheres of science and technology as catalysis and material for energy including batteries. Different Co-X alloys where X is Fe, Mo, Mn, noble metals and *etc.* are commonly utilized as supported catalysts in many technological processes. Based on Co/MWCNT study, which is a part of present manuscript, a particular interest have been paid to Co-Fe bi-metallic supported nanoparticles on CaO that are used as catalyst for MWCNT production (this work is presently in progress in our laboratory).

Unlike the majority of Co bi-metallic alloys, the catalytically active Co-Fe nanoparticles are formed during extremely short activation time varied from 30 sec up to several minutes. This short reaction/reduction time (the reduction occurs as a result of acetylene decomposition at high temperature ~650ºC) leads to creation of non-equilibrium Co-Fe alloy which exhibit simultaneously the resonance lines from both Co-rich (strong ferromagnetism) and Fe-rich (weak ferromagnetism) alloys. Moreover, an additional complication is due to alloy ordering, which is a time-dependent process: full alloy relaxation cannot be reached due to very limited reaction time. Indeed, the study of non-equilibrium alloys cannot be performed quantitatively by other technique. This makes the internal field NMR extremely powerful in study of non-equilibrium non-stochastic Co alloys.

Another large-scale field, which is not covered by internal field NMR, is Li-Co batteries that can be found today in almost everybody's pocket. Internal field NMR as technique extremely sensitive to Co metal presence and its structure can provide unique additional information on active Co metal species during charge/discharge cycles even *in situ* since internal field NMR is not restricted by the internal space of high field magnet and non-magnetic construction materials. Moreover, the temperature study of Co/SiC catalyst proved internal field NMR to have enough signal even at very high temperatures up 850 K. The main experimental perspective of internal field ^{59}Co NMR consists in building low-cost dedicated portable NMR spectrometer, which could operate at near *operando* conditions in different catalytic and related processes (such as batteries) where the problem of sample aging is crucial. The main challenge of instrument design is how to assemble the NMR coil and the catalytic reactor to ensure the highest sample filling rate and possible coil cooling to increase the sensitivity of the internal field NMR.

Despite the rather simple experimental design of internal field NMR, the theoretical issues behind of observed signal is not obvious as it is shown in Chapter 1. The theoretical insight of NMR signal in magnetic materials is done only in classical interpretation and tackles only relatively simple problems: resonance from domains, isotropic electronic magnetization, no relaxation… For example, it would be interesting to see if the magnetization dynamics derived from nuclear and electron coupled Bloch equations can be generalized if the anisotropic electron magnetization is considered (that is including the anisotropic g-factor). Moreover, more careful account of T_1 and T_2 relaxation should be introduced into the model. A careful study of the relaxation times in Co metal is also a probable route to extend our work since the relaxation process in influenced by structural parameters (for example, particle size).

Another theoretical issue is to compose the quantum theory of internal field NMR mechanism in magnetic materials, especially for the ferromagnetic case. Of cause, the pure *ab initio* quantum chemistry calculations are not immediately possible; however some semi-classical approaches as Hartree-Fock calculation might provide some additional evidence of Co metal resonance lines since the origin of many hcp Co metal resonance lines is still unknown. Also an attempt to simulate the behavior of a several thousand atom Co metal cluster appears to be extremely interesting from the magnetism theory point of view. This could shed light on internal field NMR spectra of very fine particles. Moreover, internal field NMR is a unique

technique which can probe magnetization versus temperature behavior without changing the magnetic state of the specimen.

In this manuscript, we tried to demonstrate, both by our work and by summarizing the one of our predecessors, the many possibilities of internal field NMR application to various spheres of chemistry and material science. In our opinion, once the theory behind it is demystified and when the necessary caution is used in the interpretation of the spectra, internal field NMR of ferromagnetic particles has a high potential to penetrate different scientific areas due to its instrumental simplicity.

Résumé en français

Contexte scientifique et objectifs

Les propriétés magnétiques des métaux de configuration électronique 3d sont bien établies. Ils sont ferromagnétiques à température ambiante et constitués de domaines magnétiques de tailles variables selon la température. En-deçà de cette taille critique, les particules métalliques sont nécessairement mono-domaine et il existe un seul moment magnétique macroscopique qui peut être compris comme résultant de l'alignement de tous les moments atomiques comme s'ils formaient un spin unique. De plus, pour un même métal, les différentes structures cristallines possibles se traduisent par des différences significatives d'amplitude du moment magnétique. Finalement, la forme des particules et la nature de leurs interfaces ont également un effet sur les propriétés magnétiques.

L'étude du comportement magnétique des particules de Cobalt métallique, par des mesures de résonance magnétique nucléaire (RMN) du ^{59}Co, peut donc se révéler riche d'informations relatives à leur taille, leur forme, leur structure et leur mode d'interaction avec leur support oxyde. Toutes ces informations sont particulièrement pertinentes lorsqu'on veut comprendre et maîtriser le fonctionnement de matériaux dont les propriétés d'usage sont fondées sur la présence de particules de Cobalt métallique dispersées. Dans le domaine de l'énergie, une attention toute particulière est actuellement portée vers les catalyseurs pour la synthèse Fischer-Tropsch (FT).

La synthèse Fischer-Tropsch.

Dans le contexte de réserves pétrolières déclinantes, la synthèse Fischer-Tropsch reçoit une attention renouvelée comme en témoigne par exemple l'adoption récente par la Finlande de la technologie Axens de conversion de la biomasse en fuel, technologie basée sur des catalyseurs au Cobalt. Le procédé Fischer-Tropsch est essentiellement un processus catalytique produisant des alcanes et des carburants liquides à partir d'hydrogène et de monoxyde de carbone (syngas) dérivés de combustibles fossiles ou renouvelables. Bien que le carburant produit soit peu polluant, ce n'est pas un procédé neutre en carbone mais cet inconvénient peut être atténué si le syngas est produit à partir de déchets issus de la biomasse.

Aujourd'hui, les catalyseurs Fischer-Tropsch sont des métaux du group VIII, le Cobalt étant le choix optimal pour les procédés basse température. La sélectivité de la réaction catalysée par des nanoparticules de cobalt supportées dépend fortement de la taille des particules et de leur phase. De plus, la présence d'espèces oxydées et de carbures résulte en une désactivation et favorise les réactions secondaires. En outre, les particules métalliques peuvent être modifiées lors de leur exposition au syngas dans le réacteur, par frittage ou restructuration. En conséquence, l'efficacité du procédé est considérablement réduite. **Pour pouvoir améliorer l'efficacité du procédé Fischer-Tropsch, il est donc essentiel d'obtenir une représentation de la structure et de la taille des nanoparticules de Cobalt métallique dans des conditions aussi proches de possible de celles de leur fonctionnement dans le réacteur catalytique (conditions *operando*).**

Il apparaît que les particules de Cobalt métalliques jouent un rôle important mais qu'elles ne sont stables que dans un environnement réducteur, à savoir celui résultant des gaz dans le réacteur catalytique**. Le but de ce travail est donc précisément de développer et d'appliquer la RMN du ^{59}Co pour caractériser la nature et la taille de nanoparticules de Cobalt métallique inclus dans des matériaux oxydes tels que des catalyseurs ou des batteries dans des conditions proches de leur fonctionnement (*operando*).** Ceci impose qu'un champ magnétique externe ne peut pas être appliqué. Nous prenons donc avantage du champ interne régnant dans les nanostructures ferromagnétiques de Cobalt pour réaliser une RMN du ^{59}Co en champ nul (en fait dans le champ interne des particules).

Etat de l'art

Bien que la théorie de la résonance magnétique dans les matériaux ferromagnétique soit déjà ancienne, la RMN en champ interne est une méthode encore confidentielle. Nous avons donc résumé l'essentiel de la théorie dans ce manuscrit pour permettre sa lecture par un non-spécialiste. La nature des interactions magnétiques responsable du signal RMN dans les matériaux d'ordre magnétique est discutée dans le cadre du modèle de Bloch. Les particularités de la RMN en champ interne qui ne sont pas observables en RMN des matériaux diamagnétiques en champ externe sont mises en exergue. Les étapes historiques du développement de la RMN en champ interne, les progrès et les controverses s'y afférents sont détaillées. Finalement, une brève description de la gamme de matériaux susceptibles d'être étudiés par cette méthode est fournie.

L'état de dispersion et la structure cristalline de particules de Cobalt peuvent être appréciés par diverses méthodes, les plus utilisées dans la littérature étant la microscopie électronique à transmission, les spectroscopies vibrationnelles, la DRX, les méthodes de réduction et chimisorption en températures, l'EXAFS et la magnétométrie. Ces méthodes ont toutes leurs limitations (par exemple la DRX est peu sensible pour des domaines de cohérences de moins de 5 nm, et la stœchiométrie de la chimisorption est parfois contestable).

Il est significatif que la RMN ne fasse pas partie des méthodes établies. En effet, la RMN est généralement perçue comme n'étant pas applicable aux matériaux ferromagnétiques comme le Cobalt.

Pourtant, il est connu depuis les débuts de la méthode RMN que, dans les particules de Cobalt ferromagnétiques, le champ interne est suffisamment fort pour permettre la RMN en champ externe nul à température ambiante (les particules isotropes de tailles inférieures à 5-10 nm sont ferromagnétiques mais cette taille critique est considérablement réduite pour des particules anisotropes). La levée de dégénérescence est alors assurée par le champ effectif due au couplage hyperfin du spin nucléaire avec les électrons environnant. On parle alors de RMN en champ interne (IF-NMR*, internal field NMR*). Le spectre est difficile à interpréter car le champ radiofréquence n'est pas directement absorbé par le spin nucléaire. Il excite faiblement les électrons de façon non résonante mais cela est suffisant pour induire une oscillation du champ hyperfin à la résonance avec les spins nucléaires. Une autre complication est que la résonance nucléaire est très large, couvrant plusieurs dizaines de MHz. Néanmoins, le fait que dans un matériau magnétique le champ hyperfin soit déterminé par l'environnement électronique permet d'obtenir des informations structurales à l'échelle nanométrique. En particulier, on peut remonter en principe à la phase cristalline (fcc, bcc ou hcp dans le cas du Co), la taille et la forme des domaines magnétiques, la présence d'alliage ou la nature de l'interface métallique. Avec le développement des nanosciences, ce type d'information est de plus en plus recherché et l'IF-NMR est mobilisée pour l'étude des couches minces, des semi-conducteurs, et des oxydes intermétalliques.

Le but de travail de recherche est de développer et d'adapter la méthode de RMN en champ interne à de nouveaux champs disciplinaires tels que la catalyse hétérogène et les matériaux similaires.

Nouveauté expérimentale

L'avantage principal la RMN en champ interne est qu'elle ne nécessite pas de champ externe, donc d'aimant permanent. La géométrie des sondes est donc très ouverte ce qui permet d'adapter l'appareillage aux contraintes géométriques du système à étudier (réacteur catalytique ou batterie par exemple). Comparé aux autres méthodes (dont la RMN traditionnelle), il est beaucoup plus facile de s'adapter à la présence de lignes de vide, à des flux de gaz et à des hautes températures. Dans cette étude, la difficulté principale a été la largeur du signal qui s'étend sur des dizaines de MHz. Néanmoins, nous avons conçu un système d'accord automatique qui permet d'acquérir des spectres sur une très large gamme spectrale.

Résultats

Etude de poudre de Co métal et de nanoparticules.

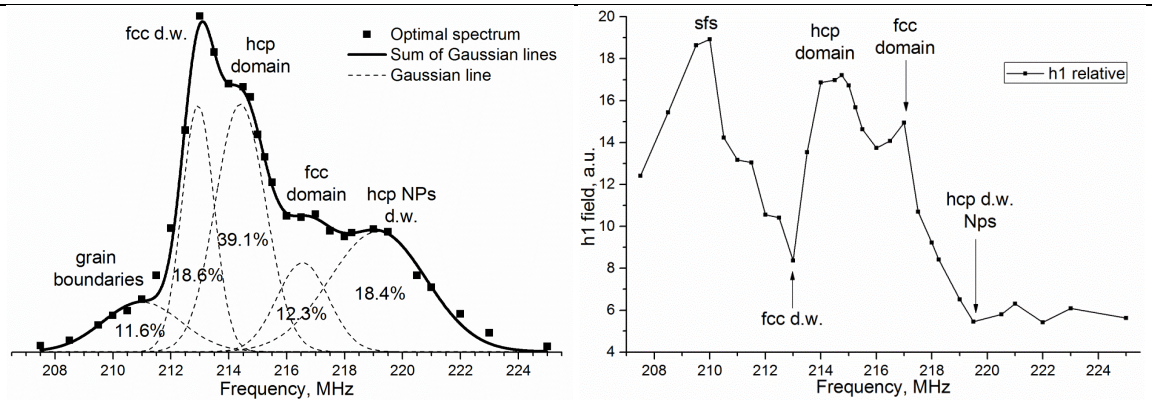

(gauche) Spectre optimisé IF ^{59}Co NMR d'une poudre de cobalt métal pure. Une décomposition quantitative du spectre est proposée en pointillé. La représentation optimisée permet de s'affranchir des variations d'intensité effective des impulsions.

(droite) Distribution en fréquence du champ radio-fréquence optimal.

Compte-tenu des contradictions régnant dans la littérature, il est apparu nécessaire de commencer notre étude par un examen de la réponse de poudre de Co métallique par IF ^{59}Co NMR. Dans ce chapitre, les rapports hcp/fcc obtenus par IF NMR sont comparés à la DRX. Une méthode pour représenter les spectres IF NMR de façon universelle est

présentée ainsi que l'attribution des lignes de résonance. La représentation la plus appropriée est une projection de spectres 2D intensité radio-fréquence / fréquence car cette représentation est indépendante de l'instrument utilisé. La distribution du champ radio-fréquence optimal est aussi une source précieuse d'information. Les minima correspondent aux résonances du cobalt dans les parois de domaine et les maxima à ceux au cœur des domaines (ou dans des mono-domaines). Concernant l'attribution des fréquences de résonance, nous proposons un modèle tenant compte des effets structuraux (fcc, hcp, et sfs) et magnétiques (domaines, parois de domaines, et mono-domaines). Un bon agreement avec la DRX est obtenu. Ce travail a été publié dans *Applied Magnetic Resonance*.

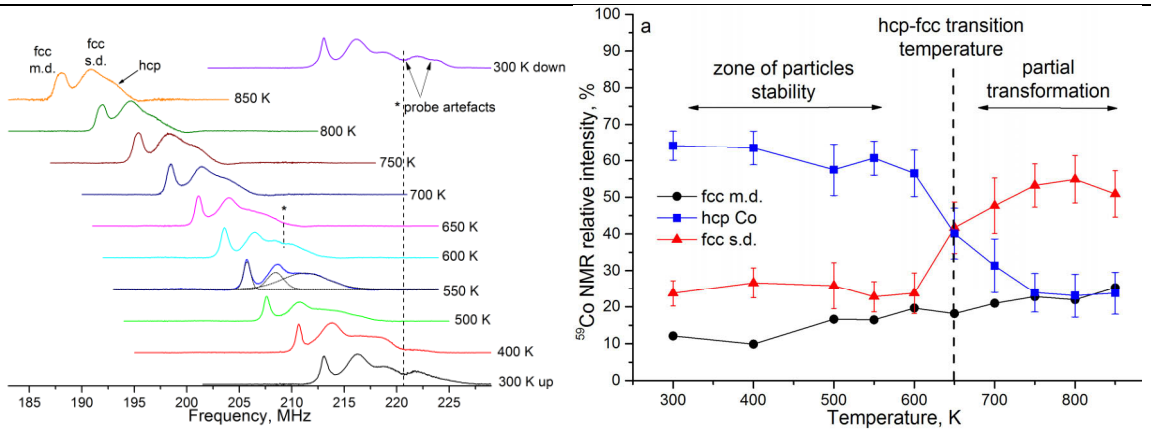

(gauche) Spectres IF ^{59}Co NMR en température variable de nanoparticules de cobalt supportées. Les intensités sont normalisées à leur maxima

(droite) Variation en température des intensités intégrées obtenues par décomposition des spectres présentés à gauche.

Nous sommes ensuite passés sur des nanoparticules supportées. Plus précisément, nous avons étudié l'évolution en température du spectre de nanoparticules supportés sur β-SiC dans la gammee 300-850 K. Nous avons fourni une analyse complète en termes de position, largeur et intensité des résonances. La position est essentiellement déterminée par les propriétés magnétiques (c'est-à-dire la magnétisation électronique) alors que les intensités relatives et absolues fournissent les informations structurales recherchées sur la stabilité des particules de Co et la transition de phase allotropique de hcp à fcc. Cette

dernière est observée en l'espèce entre 600 et 650 K, révélant un effet de taille et/ou de support.

Ce travail a été publié dans *Physical Chemistry Chemical Physics*.

Catalyseurs et structures similaires

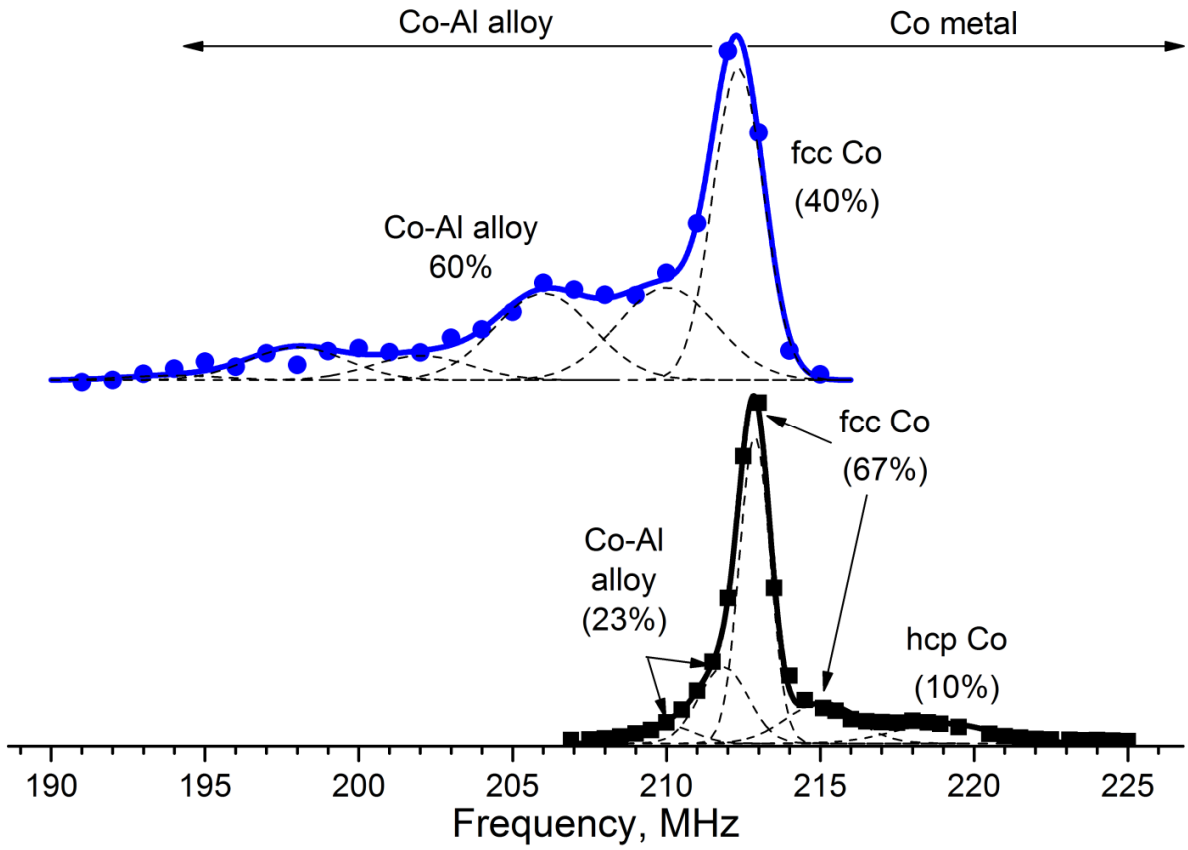

RMN du ^{59}Co en champ interne de cermets CoAlO/CoAl **(en haut)** et Al_2O_3/CoAlO/CoAl **(en bas)**. La decomposition en gaussiennes pezrmet d'obtenir la proportion de chaque phase métallique.

Tout d'abord, nous avons étudié un catalyseur Fischer-Tropsch synthétisé par co-précipitation sur divers oxides d'aluminium. Ce travail a été publié dans *Journal of Structural Chemistry* (doi: 10.1134/S0022476613070093).

Ensuite, un matériau céramique (cermet) CoAlO/CoAl a été étudié par un ensemble de techniques de caractérisation dont la RMN en champ interne. Les catalyseurs sont préparés

par un alliage mécanique suivi d'un traitement hydrothermal et d'un recuit sous air. La RMN révèle une hétérogénéité significative de phase et de composition. La partie métallique consiste en Co et en alliage Co-Al recouverts d'une couche mince d'oxyde Al_2O_3 qui la protège de l'oxydation.

La RMN en champ interne du ^{59}Co s'est révélée très riche d'informations concernant la partie métallique du cermet : il a même été possible de quantifier la proportion des phases Co métal et alliage Co-Al. En fait, l'existence même de parties métalliques dans le cermet a été établie par l'existence de la résonance ferromagnétique intense qui ne peut provenir que de Co à l'état métallique (la cartographie EDX sous MEB surestime systématiquement la quantité d'oxygène du fait de l'oxydation de surface lors du polissage). La matrice oxyde entourant les domaines métalliques est constituée d'aluminates de cobalt et d'oxydes de cobalt révélés par DRX et EDX-MEB.

La présence d'un cœur métallique augmente grandement la résistance mécanique qui passe de 10-100 kg / cm^2 dans un cermet sans cobalt à 700-800 kg / cm^2 dans le cermet CoAlO/Co-Al.

Ce travail a été publié dans *Journal of Materials Science and Engineering A*.

Finalement, nous avons étudié la structure d'un cermet Al_2O_3/CoAlO/CoAl modifié pour augmenter sa surface spécifique (112 m2 / g) ce qui en fait un candidat idéal comme support de catalyseur dans des réacteurs non-conventionnels chauffés par irradiation micro-onde.

Cette nouvelle approche pour la préparation de ceramometalic poreuses permet de combiner haute surface spécifique et résistance mécanique à la compression dans des cermets basse température Al_2O_3/CoAlO/CoAl.

Sur la base de caractérisations structurales par DRX, RMN et EDX-MEB, il est montré que ce matériau consiste essentiellement en alumine (un mélange de γ-Al_2O_3 et de α- Al_2O_3). Les alumines sont recouvertes d'oxydes mixtes $Co_{3-x}Al_xO_4$ (x = 0; 1; 2), qui sont en contacts avec la partie Co métal du cermet, qui elle-même contient des inclusions d'alliage Co-Al. Un film oxide protège le métal de l'oxydation même lors d'une calcination à 600°C sous air. La Co métal a une structure fcc avec des défauts d'empilement de type hcp.

Ce travail a été publié dans *Advance Materials Research* (doi: 10.4028/www.scientific.net/AMR.702.79) [5]

Hybrides de Co/MWCNT

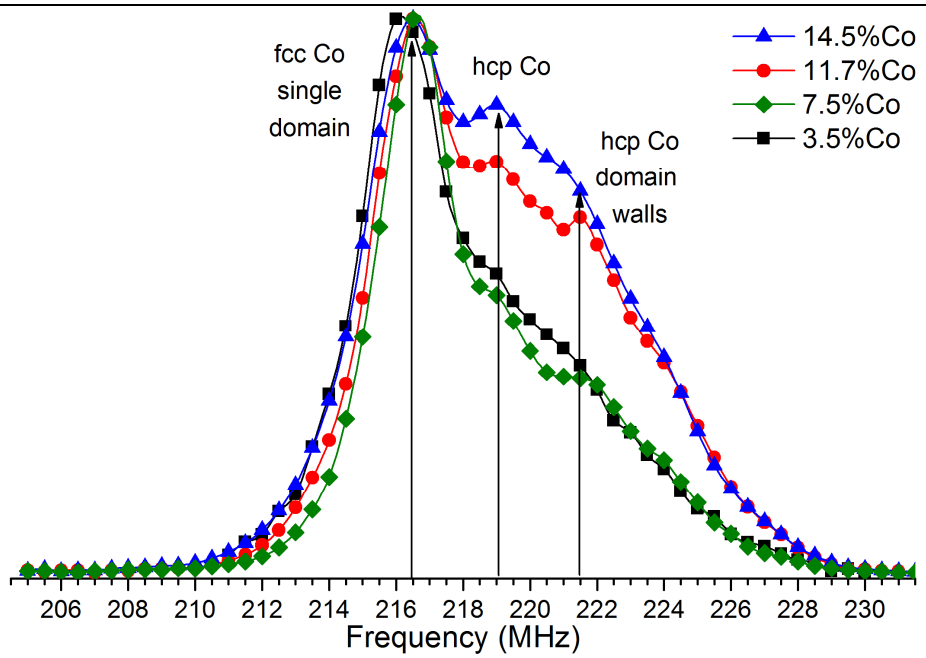

Spectres de RMN en champ interne du ^{59}Co d'hybrides de Co/MWCNT (3.5, 7.5, 11.7, 14.5 wt.% Co) après réduction. L'absence de contribution attribuable à des particules de Co fcc multi-domaines à 213 MHz prouve qu'aucune particule de structure fcc n'excède la taille d'un domaine critique (environ 50-70 nm). Pour la résonance attribuée au système hcp, une contribution due aux parois de domaine est observée malgré la petite taille des particules vues en MET haute résolution (moins de 50 nm dans tous les cas). Ceci est à mettre en rapport avec l'anisotropie des particules précipitées à l'intérieur des nanotubes de carbone.

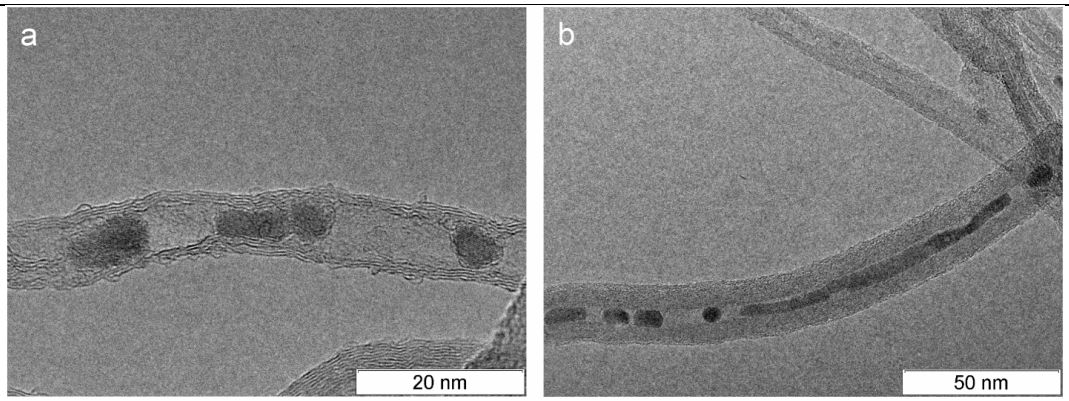

(gauche) TEM haute resolution de 3.5% Co/MWCNT montrant des particules de Co allongées à l'intérieur des nanotubes de carbone;

(droite) 7.5% Co/MWCNT montrant une particule de très haut facteur d'aspect, un nanofil à l'intérieur d'un nanotube de carbone.

Les nanotubes de carbone à plusieurs couches poreux peuvent servir de gabarit pour déposer des particules de Co métallique de haut facteur de forme par simple imprégnation à sec. L'utilisation de nanotubes de petit diamètre interne a permis la stabilisation de particules de diamètre inférieur à 4 nm mais très allongées.

Les petites particules de cobalt sont en général ferromagnétiques à température ambiante mais du fait de la géométrie en tube dans laquelle elles sont formées, elles ont forcément un facteur de forme élevé ce qui se traduit par une forte anisotropie magnétique. Cette particularité magnétique signifie que de véritable nano-hybrides ferromagnétiques à base de Co/MWCNT ont pu être préparés.

Selon la charge en cobalt, des particules avec des diamètres plus élevés par un ordre de grandeur sont également déposées sur la surface externe des nanotubes.

La distribution en taille des particules et une statistique sur leur localisation en surface ou dans les nanotubes peut être obtenue par MET haute résolution. Cependant, cette technique ne préserve pas l'état d'oxydation et la structure cristalline des particules. La RMN en champ interne apparaît donc très complémentaire. Sur la base des différentes résonances des mono domaines et des parois de domaines ferromagnétiques, l'absence de grandes particules à l'intérieur des canaux et le haut facteur de forme de ces particules peut être confirmé. De plus, la proportion relative des phases fcc et hcp est obtenue. Les nanoparticules de Co ne sont stabilisées contre l'oxydation à l'intérieur des nanotubes poreux mais la DRX sous rayonnement synchrotron a révélé leur résistance au frittage jusqu'à des températures de 550°C.

Ce travail est en cours de soumission.

Bibliographie

1. Andreev A.S., Lapina O.B., Cherepanova S. V. "*A New Insight into Cobalt Metal Powder Internal Field 59Co NMR Spectra*." Appl. Magn. Reson., 2014, vol. 45 (10), pp. 1009–1017.

2. Andreev A.S., d'Espinose de Lacaillerie J.-B., Lapina O.B., Gerashenko A. "*Thermal stability and hcp-fcc allotropic transformation in supported Co metal catalysts probed near operando by ferromagnetic NMR*." Phys. Chem. Chem. Phys., 2015, vol. 17, pp. 14598–14604.

3. Andreev A.S., Lapina O.B., d'Espinose de Lacaillerie J.-B., Khassin A.A. "*Effect of alumina modification on the structure of cobalt-containing Fischer-Tropsch synthesis catalysts according to internal-field 59Co NMR data*." J. Struct. Chem., 2013, vol. 54 (S1), pp. 102–110.

4. Andreev A., Salanov A., Tikhov S., Cherepanova S., Zaikovskii V., Usoltsev V., Sadykov V., Lapina O. "*Formation of Micro, Nano and Atomic-Level Structure of CoAlO/Co-Al Cermets Prepared by Mechanical Alloying*." J. Mater. Sci. Eng. A, 2012, vol. 2 (2), pp. 121–136.

5. Andreev A.S., Tikhov S.F., Salanov A.N., Cherepanova S. V, Lapina O.B., Bolotov V.A., Tanashev Y.Y., d'Espinose de Lacaillerie J.-B., Sadykov V.A. "*Design of Al2O3/CoAlO/CoAl Porous Ceramometal for Multiple Applications as Catalytic Supports*." Adv. Mater. Res., 2013, vol. 702, pp. 79–87.

6. Landau L.D., Lifshitz E.M. "*Quantum mechanics. Non-relativistic theory*." Oxford Pergamon Press, 1977, 677 pp.

7. Abragam A. "*The principles of nuclear magnetism*." London, UK Oxford University Press, 1961, 599 pp.

8. Turov E.A., Petrov M.P. "*Nuclear Magnetic Resonance in Ferro- and Antiferromagnets*." Jerusalem : Israel Program for Scientific Tr. (Halsted Pr. N.Y.), 1972, 206 pp.

9. Portis A.M., Gossard A.C. "*Nuclear Resonace in Ferromagnet Cobalt*." J. Appl. Phys., 1960, vol. 31 (5), pp. S205–S213.

10. Guimarães A.P. "*Magnetism and Magnetic Resonance in Solids*." Chichester John Wiley & Sons, 1998, 298 pp.

11. Turov E.A. "*Nuclear Magnetic Resonance in Ferro- and Antiferromagnets*." Am. J. Phys., 1973, vol. 41 (7), pp. 935.

12. Vonsovskii S.V. "*Magnetism*." John Wiley & Sons, 1974, 1256 pp.

13. De Gennes P.G., Pincus P.A., Hartmann-Boutron F., Winter J.M. "*Nuclear Magnetic Resonance Modes in Magnetic Material. I. Theory*." Phys. Rev., 1963, vol. 129 (3), pp. 1105–1115.

14. Witt G., Portis A. "*Nuclear Magnetic Resonance Modes in Magnetic Materials. II. Experiment*." Phys. Rev., 1964, vol. 135 (6A), pp. A1616–A1618.

15. Borovik-Romanov A.S., Bun'kov Y.M., Dumesh B.S., Kurkin M.I., Petrov M.P., Chekmarev V.P. "*The spin echo in systems with a coupled electron-nuclear precession*." Sov. Phys. Uspekhi, 1984, vol. 27 (4), pp. 235–255.

16. Narath A. "*Nuclear Magnetic Resonance in Magnetic and Metallic Solids*." Hyperfine Interactions edited by A.J. Freeman, R.B. Frenkel. New York Academic Press Inc., 1967, . p. 287.

17. Tsifrinovitch V.I. "*Spin echo signal calculation*." Novosibirsk Nauka, SB RAS, 1986, 112 (In Rissian) pp.

18. Dzyuba S.A. "*Magnetic Resonance Basics*." Novosibirsk NSU, 1997, 138 (In Russian) pp.

19. Chizhik V.I. "*Quantum radiophysics*." Saint-Petersburg Saint-Petersurg State University publisher, 2004, 312 (In Russian) pp.

20. Turov E.A., Tankeev A.P., Kurkin M.I. "*To the theory of nuclear magnetic resonance susceptibility multidomain ferromagnets. I. The analysis of local frequencies.*" Fiz. Met. i Metalloved., 1969, vol. 28 (3), pp. 385–400 (In Russian).

21. Turov E.A., Tankeev A.P., Kurkin M.I. "*To the theory of nuclear magnetic resonance susceptibility multidomain ferromagnets. II. The local enhancement factor and integral susceptibility*." Fiz. Met. i Metalloved., 1970, vol. 29 (4), pp. 747–756 (In Rissian).

22. Kawakami M., Hihara T., Koi Y. "*The Co59 Nuclear Magnetic Resonance in Hexagonal Cobalt*." J. Phys. Soc. Jpn., 1972, vol. 33 (6), pp. 1591–1598.

23. Enokiya H. "*Nuclear Magnetic Resonance and Nuclear Relaxation in hcp Cobalt*." J. Phys. Soc. Jpn., 1977, vol. 42 (3), pp. 796–804.

24. Kawakami M., Enokiya H. "*Anomaly in Temperature Dependence of 59Co NMR Frequency in HCP Co*." J. Phys. Soc. Jpn., 1986, vol. 55 (11), pp. 4038–4043.

25. Bailey S.G., Creagh D.C., Wilson G.V.H. "*Domain wall and “domain” 59Co NMR in hexagonal cobalt*." Phys. Lett. A, 1973, vol. 44 (3), pp. 229–230.

26. Kunkel H.P., Searle C.W. "*Experimental identification of domain-wall-center and domain-wall-edge NMR resonances in magnetically ordered materials*." Phys. Rev. B, 1981, vol. 23 (1), pp. 65–68.

27. Gossard A.C., Portis A.M. "*Observation of nuclear resonanse in a ferromagnet*." Phys. Rev. Lett., 1959, vol. 3 (4), pp. 164–166.

28. Slichter C.P. "*Principles of Magnetic Resonance*." Berlin, Heidelberg Springer Berlin Heidelberg, 1990, .

29. Bloom A. "*Nuclear Induction in Inhomogeneous Fields*." Phys. Rev., 1955, vol. 98 (4), pp. 1105–1111.

30. Stearns M. "*Spin-Echo and Free-Induction-Decay Measurements in Pure Fe and Fe-Rich Ferromagnetic Alloys: Domain-Wall Dynamics*." Phys. Rev., 1967, vol. 162 (2), pp. 496–509.

31. Oliveira I.S., Guimarães A.P. "*A model for domain and domain wall NMR signals in magnetic materials*." J. Magn. Magn. Mater., 1997, vol. 170 (3), pp. 277–284.

32. Marshall W. "*Orientation of Nuclei in Ferromagnets*." Phys. Rev., 1958, vol. 110 (6), pp. 1280–1285.

33. Van Vleck J.H. "*On the Anisotropy of Cubic Ferromagnetic Crystals*." Phys. Rev., 1937, vol. 52, pp. 1178–1198.

34. Van Vleck J.H. "*Models of Exchange Coupling in Ferromagnetic Media*." Rev. Mod. Phys., 1953, vol. 25 (1), pp. 220–227.

35. Abragam A., Horowitz J., Pryce M.H.L., Morton K.W. "*On the Hyperfine Structure of Paramagnetic Resonance: The s-Electron Effect*." // Proc. R. Soc. A Math. Phys. Eng. Sci. 1955,. T. 230. № 1181. C. 169–187.

36. Winter J., Stepanov A.P. "*Magnetic resonance in metals*." edited by G.V. Skrotskiy. Moscow Mir, 1976, 288 (In Russian) pp.

37. Watson R.E., Freeman A.J. "*Origin of Effective Fields in Magnetic Materials*." Phys. Rev., 1961, vol. 123 (6), pp. 2027–2047.

38. Bibring H., Sebilleau F. "*The allotropic transformation of Cobalt*." Rev. Met., 1955, vol. 1642, pp. 209–217.

39. Stoner E.C. "*Collective Electron Ferromagnetism*." Proc. R. Soc. London. Ser. A. Math. Phys. Sci., 1938, vol. 165 (922), pp. 372–414.

40. Koi Y., Tsujimura A., Yukimoto Y. "*The Temperature and Pressure Dependence of the Nuclear Resonance of 59Co in Face-Centered-Cubic Cobalt Metal* ." J. Phys. Soc. Jpn., 1960, vol. 15, pp. 1342.

41. Patrick L. "*The Change of Ferromagnetic Curie Points with Hydrostatic Pressure*." Phys. Rev., 1954, vol. 93 (3), pp. 384–392.

42. Koi Y., Tsujimura A., Kushida T. "*NMR of Co59 in Ferromagnetic Hexagonal Cobalt Metal*." J. Phys. Soc. Jpn., 1960, vol. 15, pp. 2100.

43. Pogorelyi A.N., Kotov V.V. "*Temperature dependence of hcp Co NMR intensity*." JETP Lett., 1971, vol. 13 (10), pp. 561–562 (In Russian).

44. Sugibuchi K., Matsuura M., Hashi T. "*Spin Echoes of Co59 in fcc Cobalt Metal*." J. Phys. Soc. Jpn., 1961, vol. 16, pp. 1648.

45. Weger M., Hahn E.L., Portis A.M. "*Transient Excitation of Nuclei in Ferromagnetic Metals*." J. Appl. Phys., 1961, vol. 32 (3), pp. S124–S125.

46. Gossard A.C., Portis A.M., Rubinstein M., Lindquist R.H. "*Ferromagnetic Nuclear Resonance of Single-Domain Cobalt Particles*." Phys. Rev., 1965, vol. 138 (5A), pp. A1415–A1421.

47. Zhang Y.D., Budnick J.I., Hines W.A., Majetich S.A., Kirkpatrick E.M. "*Microstructure and magnetic behavior of carbon-coated Co nanoparticles studied by nuclear magnetic resonance*." Appl. Phys. Lett., 2000, vol. 76 (1), pp. 94–96.

48. Yasuoka H., Lewis R.T. "*Temperature Dependence of Co59 Nuclear Magnetic Resonance in Single-Domain Cobalt Particles*." Phys. Rev., 1969, vol. 183 (2), pp. 559–562.

49. Frenkel J., Doefman J. "*Spontaneous and Induced Magnetisation in Ferromagnetic Bodies.*" Nature, 1930, vol. 126 (3173), pp. 274–275.

50. Kondorskiy E.I. "*The nature of large coercive force in ferromagnetic particles, and the theory of single-domain structure*." Izv. AN SSSR, Phys., 1952, vol. 16 (4), pp. 398–411 (In Russian).

51. Kondorskiy E.I. "*Micromagnetism and remagnetization of quasi single-domain particles*." Izv. AN SSSR, Phys., 1978, vol. 42 (8), pp. 1638–1645 (In Russian).

52. Leslie-Pelecky D.L., Rieke R.D. "*Magnetic Properties of Nanostructured Materials*." Chem. Mater., 1996, vol. 8 (8), pp. 1770–1783.

53. Liu Y., Florea I., Ersen O., Pham-Huu C., Meny C. "*Silicon carbide coated with TiO2 with enhanced cobalt active phase dispersion for Fischer–Tropsch synthesis*." Chem. Commun., 2015, vol. 51 (1), pp. 145–148.

54. Chernavskii P.A., Dalmon J.-A., Perov N.S., Khodakov A.Y. "*Magnetic Characterization of Fischer-Tropsch Catalysts*." Oil Gas Sci. Technol. - Rev. l'IFP, 2009, vol. 64 (1), pp. 25–48.

55. Hardy W.A. "*Nuclear Resonances in Cubic, Hexagonal, and Mixed Phase Cobalt Powders and Thin Films*." J. Appl. Phys., 1961, vol. 32 (3), pp. S122–S123.

56. Sort J., Surinach S., Munoz J.S., Baro M.D., Wójcik M., Jedrica E., Nadolski S., Sheludko N., Nogues J. "*Role of stacking faults in the structural and magnetic properties of ball-milled cobalt*." Phys. Rev. B, 2003, vol. 68, pp. 14421–14427.

57. Speight R., Wong A., Ellis P., Hyde T., Bishop P.T., Smith M.E. "*A (59)Co NMR study to observe the effects of ball milling on small ferromagnetic cobalt particles*." Solid State Nucl. Magn. Reson., 2009, vol. 35 (2), pp. 67–73.

58. Speight R., Wong A., Ellis P., Bishop P.T., Hyde T.I., Bastow T.J., Smith M.E. "*(59)Co NMR study of the allotropic phase transformation in small ferromagnetic cobalt particles*." Phys. Rev. B, 2009, vol. 79 (5), pp. 054102–1 – 054102–8.

59. Toth L.E., Ravitz S.F. "*Ferromagnetic nuclear resonance in cobalt nuclei in stacking faults and twins*." J. Phys. Chem. Solids, 1963, vol. 24 (10), pp. 1203–1206.

60. Toth L.E., Cass T.R., Ravitz S.F., Washburn J. "*Determination of the predominant type of stacking fault in cobalt by nuclear magnetic resonance and electron microscopy*." Philos. Mag., 1964, vol. 9 (100), pp. 607–616.

61. Toth L.E., Day G.F., La Force R.C., Ravitz S.F. "*Identification of stacking faults in hexagonal cobalt by ferromagnetic nuclear resonance*." Acta Metall., 1964, vol. 12, pp. 311–313.

62. La Force R.C., Toth L.E., Ravitz S.F. "*The temperature dependence of the nuclear magnetic resonance of Co59*." J. Phys. Chem. Solids, 1963, vol. 24 (6), pp. 729–733.

63. Brömer H., Huber H.L. "*Nuclear magnetic resonance in ferromagnetic HCP and FCC 59cobalt* ." J. Magn. Magn. Mater., 1978, vol. 8 (1), pp. 61–64.

64. Creagh D.C., Bailey S.G., Wilson G.V.H. "*X-ray and NMR investigations of cobalt*." Philos. Mag., 1975, vol. 32 (2), pp. 405–415.

65. Street R., Rodbell D.S., Roth W.L. "*Nuclear Magnetic Resonance Spectrum of Co59 in Metallic Cobalt Powders*." Phys. Rev., 1961, vol. 121 (1), pp. 84–86.

66. Bubendorff J.L., Mény C., Beaurepaire E., Panissod P., Bucher J.P. "*Electrodeposited cobalt films: hcp versus fcc nanostructuring and magnetic properties*." Eur. Phys. J. B, 2000, vol. 17 (4), pp. 635–643.

67. Belesi M., Panagiotopoulos I., Pal S., Hariharan S., Tsitrouli D., Papavassiliou G., Niarchos D., Boukos N., Fardis M., Tzitzios V. "*Decoration of Carbon Nanotubes with CoO and Co Nanoparticles*." J. Nanomater., 2011, vol. 2011, pp. 1–9.

68. Mény C., Jędryka E., Panissod P. "*Satellite Structure of Co-59 Nmr-Spectra in Some Co Alloys*." J. Phys. Condens. Matter, 1993, vol. 5 (10), pp. 1547–1556.

69. De Tymowski B., Liu Y., Mény C., Lefèvre C., Begin D., Nguyen P., Pham C., Edouard D., Luck F., Pham-Huu C. "*Co–Ru/SiC impregnated with ethanol as an effective catalyst for the Fischer–Tropsch synthesis*." Appl. Catal. A Gen., 2012, vol. 419-420, pp. 31–40.

70. Murty A.N., Williams A.A., Obermyer R.T., Rao V.U.S. "*Zero-field NMR studies of physically admixed Co/Co-ThO2 ZSM-5 catalysts*." J. Appl. Phys., 1987, vol. 61 (8), pp. 4361–4363.

71. Murty A.N., Seamster M., Thorpe A.N., Obermyer R.T., Rao V.U.S. "*Nmr Evidence of Metal-Support Interaction in Syngas Conversion Catalyst Co-Tio2*." J. Appl. Phys., 1990, vol. 67 (9), pp. 5847–5849.

72. Van Alphen E., de Jonge W. "*Granular Co/Ag multilayers: Relation between nanostructure, and magnetic and transport properties*." Phys. Rev. B, 1995, vol. 51 (13), pp. 8182–8192.

73. Panissod P., Mény C. "*Nuclear magnetic resonance investigations of the structure and magnetic properties of metallic multilayers and nanocomposites*." Appl. Magn. Reson., 2000, vol. 19 (3-4), pp. 447–460.

74. Panissod P., Jay J.P., Mény C., Wójcik M., Jędryka E. "*NMR analysis of buried metallic interfaces*." Hyperfine Interact., 1996, vol. 97-98 (1), pp. 75–98.

75. Cerisier M., Attenborough K., Jędryka E., Wójcik M., Nadolski S., Haesendonck C. Van, Celis J.P. "*Structural study of nanometric electrodeposited Co films using 59Co NMR*." J. Appl. Phys., 2001, vol. 89 (11), pp. 7083–7085.

76. Jackson R.F., Scurlock R.G., Utton D.B., Wilmshurst T.H. "*[No title available]*." Proc. Intern. Conf. Magnetism. Nottingham , 1964, . p. 384.

77. Searle C., Kunkel H., Kupca S., Maartense I. "*NMR enhancement of a modulating field due to the anisotropic component of the hyperfine field in hcp Co and YCo5*." Phys. Rev. B, 1977, vol. 15 (7), pp. 3305–3308.

78. Robert C., Winter J.-M. "*Observation de la résonance nucléaire du fer 57 dans le fer métallique naturel en absence dans absence de champ extérieur*." Comptes rendus l'Académie des Sci., 1960, vol. 250 (5-6), pp. 3831–3833.

79. Benedek G.B., Armstrong J. "*Pressure and Temperature Dependence of the Fe57 Nuclear Magnetic Resonance Frequency in Ferromagnetic Iron*." J. Appl. Phys., 1961, vol. 32 (3), pp. S106.

80. Budnick J.I., Bruner L.J., Blume R.J., Boyd E.L. "*Nuclear Magnetic Resonance of Fe57 in Unenriched Fe*." J. Appl. Phys., 1961, vol. 32 (3), pp. S120.

81. Kushida T., Silver A.H., Koi Y., Tsujimura A. "*Nuclear Resonance in Ferromagnetic Alloys*." J. Appl. Phys., 1962, vol. 33 (3), pp. 1079.

82. Streever R.L., Bennett L.H., La Force R.C., Day G.F. "*Nuclear Resonance and the Hyperfine Field in Dilute Alloys of Nickel in Iron*." J. Appl. Phys., 1963, vol. 34 (4), pp. 1050.

83. Dho J., Kim M., Lee S., Lee W.-J. "*The enhancement effect in the domain and domain wall in Fe57 nuclear magnetic resonance*." J. Appl. Phys., 1997, vol. 81 (3), pp. 1362.

84. Gossard A.C., Portis A.M., Sandle W.J. "*Nuclear magnetic resonance in ferromagnetic Fe57*." J. Phys. Chem. Solids, 1961, vol. 17 (3-4), pp. 341–342.

85. Butler M., Wertheim G., Buchanan D. "*Domain and Wall Hyperfine Fields in Ferromagnetic Iron*." Phys. Rev. B, 1972, vol. 5 (3), pp. 990–996.

86. Dho J., Lee S. "*Nuclear magnetic relaxation in the domain and domain wall of pure iron*." Phys. Rev. B, 1997, vol. 56 (13), pp. 7835–7838.

87. Jaccarino V., Walker L., Wertheim G. "*Localized Moments of Manganese Impurities in Ferromagnetic Iron*." Phys. Rev. Lett., 1964, vol. 13 (25), pp. 752–754.

88. Budnick J., Burch T., Skalski S., Raj K. "*Spin-Echo Studies of Conduction-Electron Polarization about the Impurity Atom in Fe-Rich Alloys*." Phys. Rev. Lett., 1970, vol. 24 (10), pp. 511–514.

89. Matveev V. V., Bregan A.D., Volodin V.S., Lavrov S.A., Pleshakov I. V., Folmanis G.É. "*Nuclear magnetic resonance in nanocrystalline iron*." Tech. Phys. Lett., 2008, vol. 34 (10), pp. 832–834.

90. Abe H. "*Nuclear Magnetic Resonance of Ni 61 in Nickel-Ferrite*." J. Phys. Soc. Japan, 1965, vol. 20 (2), pp. 267–271.

91. Bruner L., Budnick J., Blume R. "*Nuclear Magnetic Resonance of Ni61 in Metallic Nickel*." Phys. Rev., 1961, vol. 121 (1), pp. 83–83.

92. Streever R., Bennett L. "*Line Shapes, Saturation Behavior, and Temperature Studies in the Nuclear Resonance of Nickel*." Phys. Rev., 1963, vol. 131 (5), pp. 2000–2009.

93. Cowan D., Anderson L. "*Nuclear Magnetic Resonance of Ni61 in Nickel Metal*." Phys. Rev., 1965, vol. 139 (2A), pp. A424–A428.

94. Riedi P. "*Temperature dependence of the magnetization of nickel using 61Ni NMR*." Phys. Rev. B, 1977, vol. 15 (11), pp. 5197–5203.

95. Streever R.L., Bennett L.H., La Force R.C., Day G.F. "*Nuclear Resonance and the Hyperfine Field in Dilute Alloys of Nickel in Iron*." J. Appl. Phys., 1963, vol. 34 (4), pp. 1050.

96. Hama T., Matsumura M., Yamagata H., Miyakawa M., Umetsu R., Fukamichi K. "*NMR/NQR study in β-MnOs alloys*." J. Magn. Magn. Mater., 2004, vol. 272-276, pp. 503–504.

97. Baumann C., Allodi G., Reutler P., Sidorenko A., Büchner B., De Renzi R., Revcolevschi A. "*Mixed valency of layered manganites from NMR*." J. Magn. Magn. Mater., 2004, vol. 272-276, pp. 452–453.

98. Jo E., Kim C., Lee S. "*55 Mn nuclear magnetic resonance for antiferromagnetic α-Mn2O3*." New J. Phys., 2011, vol. 13 (1), pp. 013018.

99. Kubo T., Goto T., Koshiba T., Takeda K., Awaga K. "*55Mn NMR in Mn12 acetate: Hyperfine interaction and magnetic relaxation of the cluster*." Phys. Rev. B, 2002, vol. 65 (22), pp. 224425.

100. Giri S., Nakamura H., Shiga M. "*55Mn NMR study of the hexagonal Laves phase compound ThMn2: Coexistence of magnetic and nonmagnetic sites of Mn*." Phys. Rev. B, 1999, vol. 59 (21), pp. 13943–13947.

101. Jackson R.F., Scurlock R.G., Utton D.B., Wilmshurst T.H. "*Distribution of Heff at Co in Co/Fe alloys from "NMR spin-echo spectra."*" Phys. Lett., 1964, vol. 11 (3), pp. 197–198.

102. Strauss G.H., Forester D.W. "*Short-Range Order Effects on 59Co NMR Spectra in Equiatomic FeCo*." J. Appl. Phys., 1971, vol. 42 (4), pp. 1304.

103. Pierron-Bohnes V., Cadeville M.C., Gautier F. "*Magnetism and local order in dilute FeCo alloys*." J. Phys. F Met. Phys., 1983, vol. 13 (8), pp. 1689–1713.

104. Muraoka Y., Shiga M., Yasuoka H., Nakamura Y. "*NMR Study of Ordered and Disordered Fe-Co Alloy*." J. Phys. Soc. Japan, 1976, vol. 40 (2), pp. 414–417.

105. Rubinstein M. "*Hyperfine Field Spectra of Binary Fe-Co Alloys: Nuclear Magnetic Resonance of Fe57 and Co59*." Phys. Rev., 1968, vol. 172 (2), pp. 277–283.

106. Stauss G. "*Hyperfine Fields in Dilute Alloys of Co in Fe*." Phys. Rev. B, 1971, vol. 4 (9), pp. 3106–3110.

107. Jay J.P., Wójcik M., Panissod P. "*Hyperfine field and ordering in bcc CoFe bulk alloys studied by 59Co NMR and Monte-Carlo simulation*." Zeitschrift für Phys. B Condens. Matter, 1994, vol. 101 (4), pp. 471–486.

108. Kôi Y., Tsujimura A., Hihara T., Kushida T. "*NMR of Co 59 in Ferromagnetic Cobalt Alloys*." J. Phys. Soc. Japan, 1961, vol. 16 (3), pp. 574–574.

109. Shavishvili T.M., Kiliptari I.G. "*Distribution of hyperfine fields and magnetic perturbation in cobalt alloys with 3d transition metals*." Phys. Status Solidi, 1979, vol. 92 (1), pp. 39–47.

110. Houdy P., Boher P., Giron F., Pierre F., Chappert C., Beauvillain P., Dang K. Le, Veillet P., Velu E. "*Magnetic and structural properties of rf-sputtered Co/Fe and Co/Cr multilayers*." J. Appl. Phys., 1991, vol. 69 (8), pp. 5667.

111. Silva H.G., Gomes H.L., Pogorelov Y.G., Pereira L.M.C., Kakazei G.N., Sousa J.B., Araújo J.P., Mariano J.F.L., Cardoso S., Freitas P.P. "*Magnetic and transport properties of diluted granular multilayers*." J. Appl. Phys., 2009, vol. 106 (11), pp. 113910.

112. Dekoster J., Jedryka E., Mény C., Langouche G. "*Epitaxial growth of bcc Co/Fe superlattices*." J. Magn. Magn. Mater., 1993, vol. 121 (1-3), pp. 69–72.

113. Lesnik N.A., Panissod P., Kakazei G.N., Pogorelov Y.G., Sousa J.B., Snoeck E., Cardoso S., Freitas P.P., Wigen P.E. "*Local structure in CoFe/Al2O3 multilayers determined by nuclear magnetic resonance*." J. Magn. Magn. Mater., 2002, vol. 242-245, pp. 943–945.

114. Wojcik M., Jay J.P., Panissod P., Jedryka E., Dekoster J., Langouche G. "*New phases and chemical short range order in co-deposited CoFe thin films with bcc structure: an NMR study*." Zeitschrift für Phys. B Condens. Matter, 1997, vol. 103 (1), pp. 5–12.

115. Reingardt A.E., Tsifrinovitch V.I., Novoselov O.V., Maltsev V.K. "*Multiple echo in cobalt containing ferromagnetic alloys*." Fiz. Tverd. Tela, 1983, vol. 25 (10), pp. 3163 –3164 (In Russian).

116. Malinowska M., Wójcik M., Nadolski S., Jędryka E., Mény C., Panissod P., Knobel M., Viegas A.D.C., Schmidt J.E. "*Identification of magnetic phases in granular Co10Cu90 alloy using 59Co NMR method*." J. Magn. Magn. Mater., 1999, vol. 198-199, pp. 599–601.

117. Panissod P., Malinowska M., Jedrica E., Wójcik M., Nadolski S., Knobel M., Schmidt J.E. "*Inhomogeneous structure and magnetic properties of granular Co10Cu90 alloys*." Phys. Rev. B, 2000, vol. 63 (1), pp. 014408(1)– 014408(10).

118. Thomson T., Riedi P.C., Morawe C., Zabel H. "*59Co NMR investigations of sputtered Co/Cu (100) and (111) multilayers*." J. Magn. Magn. Mater., 1996, vol. 156 (1-3), pp. 89–90.

119. Sinnecker E.H.C.., Oliveira I.., Tiberto P., Guimarães A.. "*Magnetic and structural properties of Cu–Co granular alloys measured with NMR*." J. Magn. Magn. Mater., 2000, vol. 218 (2-3), pp. 132–136.

120. Khalyapin D.L., Maltsev V.K., Kim P.D., Turpanov I.A., Betenkova A.Y. "*The Study of Co-Cu Heterogeneous Alloy Thin Films by NMR Method*." J. Sib. Fed. Univ. Math. Phys., 2010, vol. 3 (1), pp. 70–77.

121. De Gronckel H., Kopinga K., de Jonge W., Panissod P., Schillé J., den Broeder F. "*Nanostructure of Co/Cu multilayers*." Phys. Rev. B, 1991, vol. 44 (16), pp. 9100–9103.

122. Thomson T., Riedi P., Greig D. "*Interfacial quality and giant magnetoresistance in MBE-grown Co/Cu(111) superlattices*." Phys. Rev. B, 1994, vol. 50 (14), pp. 10319–10322.

123. Van Alphen E., te Velthuis S., de Gronckel H., Kopinga K., de Jonge W. "*NMR study of the strain in Co-based multilayers*." Phys. Rev. B, 1994, vol. 49 (24), pp. 17336–17341.

124. Iskhakov R.S., Kuzovnikova L.A., Komogortsev S. V., Denisova E.A., Mal'tsev V.K., Bondarenko G.N. "*Evolution of the Structure and Magnetic Properties of Composite Powder Co–Cu during Mechanical Alloying*." Khimiya v Interes. ustoichivogo Razvit., 2005, vol. 13 (2), pp. 209–216 (in Russian).

125. Frolov G.I., Zhigalov V.S., Mal'tsev V.K. "*Temperature effect on structural transformations in nanocrystalline cobalt films*." Phys. Solid State, 2000, vol. 42 (2), pp. 334–336.

126. Bennett L.H., Streever R.L. "*Internal Magnetic Fields in Nickel-Rich Nickel-Cobalt Alloys*." J. Appl. Phys., 1962, vol. 33 (3), pp. 1093–1094.

127. Riedi P.C. "*Satellite Lines in the 59Co Resonance in Cobalt-Nickel Alloys*." J. Appl. Phys., 1968, vol. 39 (2), pp. 1241–1242.

128. La Force R., Ravitz S., Day G. "*Effect of Dilute Solid Solutions of Iron and of Nickel on the Nuclear Resonance of Co59*." Phys. Rev. Lett., 1961, vol. 6 (5), pp. 226–228.

129. Van Alphen E., te Velthuis S., de Gronckel H., Kopinga K., de Jonge W. "*NMR study of the strain in Co-based multilayers*." Phys. Rev. B, 1994, vol. 49 (24), pp. 17336–17341.

130. Kohara T., Asayama K. "*NMR Study of Antiferromagnetic α-Mn Alloys*." J. Phys. Soc. Japan, 1974, vol. 37 (2), pp. 393–400.

131. Kohara T., Asayama K. "*NMR Study of Antiferromagnetic β-Mn Alloys*." J. Phys. Soc. Japan, 1974, vol. 37 (2), pp. 401–407.

132. Yasuoka H., Hoshinouchi S., Nakamura Y., Matsui M., Adachi K. "*Nuclear Magnetic Resonance of Co59 in Co-Mn Alloys*." Phys. Status Solidi B, 1971, vol. 46 (2), pp. K81–K84.

133. Thomson T., Riedi P.C., Wang Q., Zabe H. "*59Co and 55Mn NMR of CoMn alloys and multilayers*." J. Appl. Phys., 1996, vol. 79 (8), pp. 6300–6302.

134. Durand J., Lapierre M.F. "*NMR of Co 59 in amorphous CoP alloys*." J. Phys. F Met. Phys., 1976, vol. 6 (6), pp. 1185.

135. Riedi P.C., Scurlock R.G., Wilmshurst T.H. "*Nuclear magnetic resonance in ferromagnetic cobalt-vanadium alloys*." J. Phys. C Solid State Phys., 1969, vol. 2, pp. 259–263.

136. Kobayashi S., Asayama K., Itoh J. "*Nuclear Magnetic Resonance In Co Alloys*." J. Phys. Soc. Jpn., 1965, vol. 21 (1), pp. 65–74.

137. Thomson T., Riedi P.C., Krishnan R. "*59Co nuclear magnetic resonance study of molecular-beam epitaxy grown Co/V multilayers*." J. Appl. Phys., 2000, vol. 87 (9), pp. 6594.

138. Wurmehl S., Fecher G.H., Kroth K., Kronast F., Dürr H.A., Takeda Y., Saitoh Y., Kobayashi K., Lin H.-J., Schönhense G., Felser C. "*Electronic structure and spectroscopy of the quaternary Heusler alloy Co 2 Cr 1− x Fe x Al*." J. Phys. D. Appl. Phys., 2006, vol. 39 (5), pp. 803–815.

139. Wurmehl S., Kohlhepp J.T., Swagten H.J.M., Koopmans B. "*Hyperfine field distribution in the Heusler compound Co2FeAl probed by 59Co nuclear magnetic resonans*." J. Phys. D Appl. Phys., 2008, vol. 41, pp. 1–7.

140. Jędryka E., Wójcik M., Nadolski S., Kubinski D., Parsons M., Holloway H. "*Effect of deposition sequence on interface intermixing in Cu/Co/Ru and Ru/Co/Cu multilayers studied by NMR*." J. Appl. Phys., 2002, vol. 91 (10), pp. 7191–7193.

141. Velez M., Meny C., Valvidares S.M., Diaz J., Morales R., Alvarez-Prado L.M., Panissod P., Alameda J.M. "*Amorphous to polycrystalline transition in Co(x)Si(1-x) alloy thin films*." Eur. Phys. J. B, 2004, vol. 41 (4), pp. 517–524.

142. Yaacoub N., Meny C., Bengone O., Panissod P. "*Reduced interfacial mixing and exchange coupling in Co/Si multilayers*." J. Magn. Magn. Mater., 2007, vol. 316 (2), pp. e980–e983.

143. Yaacoub N., Meny C., Ulhaq-Bouillet C., Acosta M., Panissod P. "*Short period magnetic coupling oscillations in Co/Si multilayers: Role of crystallization and interface quality*." Phys. Rev. B, 2007, vol. 75 (17), pp. 174402.

144. Dubowik J. "*Ferromagnetic Resonance Studies of Ultrathin Co Layers in Co/Ag Multilayers*." J. Magn., 1999, vol. 4 (3), pp. 92–97.

145. Van Alphen E., de Jonge W. "*Granular Co/Ag multilayers: Relation between nanostructure, and magnetic and transport properties*." Phys. Rev. B, 1995, vol. 51 (13), pp. 8182–8192.

146. Wójcik M., Christides C., Jędryka E., Nadolski S., Panagiotopoulos I. "*Formation of a Co nanostructure revealed by Co-59 nuclear magnetic resonance measurements in Co/Au multilayers*." Phys. Rev. B, 2001, vol. 63 (1), pp. 012102–1 – 012102–4.

147. Hu M.-H., Guen K., André J.-M., Zhou S.K., Li H.C., Zhu J.T., Wang Z.S., Meny C., Mahne N., Giglia A., Nannarone S., Estève I., Walls M., Jonnard P. "*Investigation of the thermal stability of Mg/Co periodic multilayers for EUV applications*." Appl. Phys. A, 2011, vol. 106 (3), pp. 737–745.

148. Jonnard P., Wang Z.-S., Zhu J.-T., Meny C., Andre J.-M., Hu M.-H., Guen K. Le. "*Characterization of multilayers and their interlayers: applicationto Co-based systems*." Chin. Opt. Lett., 2013, vol. 11 (s1), pp. S10601.

149. Buschow K.H.J., Kropp H., Dormann E. "*Magnetic properties of MgCo2 studied by means of magnetic dilution and 59Co spin echo NMR*." J. Magn. Magn. Mater., 1981, vol. 23 (3), pp. 257–264.

150. Nakamura H., Nakahara A., Shiga M., Tsvyashchenko A.V., Fomicheva L.N. "*59Co Hyperfine Fields in CaCo2 and MgCo2*." Phys. status solidi, 2002, vol. 232 (2), pp. 352–355.

151. Patrin G.S., Turpanov I.A., Kobyakov A. V., Velikanov D.A., Patrin K.G., Li L.A., Mal'tsev V.K., Zharkov S.M., Yushkov V.I. "*Synthesis and magnetic states of cobalt in three-layer Co/Ge/Co films*." Phys. Solid State, 2014, vol. 56 (2), pp. 302–309.

152. Berzhanskii V.N., Kapel'nitskii S. V., Pokatilov V.S., Polulyakh S.N. "*Multiple structure of two-pulse nuclear spin echo in cobalt films*." Phys. Solid State, 2002, vol. 44 (1), pp. 88–91.

153. Kapel'nitskii S. V., Pokatilov V.S., Golikova V.V. "*Hyperfine fields on 59Co nuclei in fcc Co-Fe-Ni alloys. Phenomenological account of intraband correlation*." Fiz. Tverd. Tela, 1989, vol. 31 (4), pp. 261–263 (In Russian).

154. Pokatilov V.S., Kapel'nitskii S. V., Karazeev V.N. "*Thin ferromagnetic Co metal film study by nuclear magnetic resonance*." Fiz. Tverd. Tela, 1990, vol. 32 (7), pp. 1982–1991 (In Russian).

155. Pokatilov V.S., Kapel'nitskii S. V. "*59Co NMR nuclear relaxation in fcc Co-Fe-Ni alloys*." Fiz. Tverd. Tela, 1991, vol. 31 (7), pp. 2186–2193 (In Russian).

156. Yaacoub N., Meny C., Ulhaq-Bouillet C., Acosta M., Panissod P. "*Short period magnetic coupling oscillations in Co/Si multilayers: Role of crystallization and interface quality*." Phys. Rev. B, 2007, vol. 75 (17), pp. 174402.

157. Kushida T., Silver A.H., Koi Y., Tsujimura A. "*Nuclear Resonance in Ferromagnetic Alloys*." J. Appl. Phys., 1962, vol. 33 (3), pp. 1079.

158. Kubaschewski O. "*IRON - Binary Phase Diagrams*." Springer, 1982, 27 pp.

159. Wurmehl S., Kohlhepp J.T. "*Nuclear magnetic resonance studies of materials for spintronic applications*." J. Phys. D. Appl. Phys., 2008, vol. 41 (17), pp. 173002.

160. Matveev V. V, Baranov D.A., Yurkov G.Y., Akatiev N.G., Dotsenko I.P., Gubin S.P. "*Cobalt nanoparticles with preferential hcp structure: A confirmation by X-ray diffraction and NMR*." Chem. Phys. Lett., 2006, vol. 422 (4–6), pp. 402–405.

161. Mény C. "*PhD Thesis. Etude de multicouches magnétiques par RMN: méthodologie et application aux systèmes Co/Cu, Co/Cr, Co/Ru et Co/Fe. Université de Strasbourg 1, Strasbourg, FRANCE (Université de soutenance)*." 1994,.

162. Jay J.-P. "*PhD Thesis. Etude par resonance magnetique nucleaire de l'ordre a courte distance dans le systeme cobalt/fer : de l'alliage massif a la multicouche. Université Louis Pasteur - Strasbourg I.*" 1995,.

163. Fischer F., Tropsch H. "*Über die Herstellung synthetischer Ölgemische (Synthol) durch Aufbau aus Kohlenoxyd und Wasserstoff*." Brennst. Chem., 1923, vol. 4, pp. 276–285.

164. Fischer F., Tropsch H. "*Die Erodölsynthese bei ge wöhnlichem Druck aus den Vergangsprodukten der Kohlen*." Brennst. Chem., 1926, vol. 7, pp. 97–104.

165. Fischer F., Tropsch H. "*Über die direkte Synthese von Erdöl-Kohlenwasserstoffen bei gewöhnlichem Druck. (Erste Mitteilung)*." Berichte der Dtsch. Chem. Gesellschaft (A B Ser., 1926, vol. 59 (4), pp. 830–831.

166. Van Dyk J.C., Keyser M.J., Coertzen M. "*Syngas production from South African coal sources using Sasol–Lurgi gasifiers*." Int. J. Coal Geol., 2006, vol. 65 (3–4), pp. 243–253.

167. Steynberg A.P. "*Preface*." Studies in Surface Science and Catalysis edited by S. André, D. Mark. Elsevier, 2004, . p. vii–x.

168. Steynberg A.P. "*Chapter 1 Introduction to fischer-tropsch technology*." Studies in Surface Science and Catalysis edited by S. André, D. Mark. Elsevier, 2004, . p. 1–63.

169. Steynberg A.P., Dry M.E., Davis B.H., Breman B.B. "*Chapter 2 Fischer-Tropsch Reactors*." Studies in Surface Science and Catalysis edited by S. André, D. Mark. Elsevier, 2004, . p. 64–195.

170. Dry M.E. "*Chapter 3 Chemical concepts used for engineering purposes*." Studies in Surface Science and Catalysis edited by S. André, D. Mark. Elsevier, 2004, . p. 196–257.

171. Aasberg-Petersen K., Christensen T.S., Dybkjłr I., Sehested J., Østberg M., Coertzen R.M., Keyser M.J., Steynberg A.P. "*Chapter 4 Synthesis gas production for FT synthesis*." Studies in Surface Science and Catalysis edited by S. André, D. Mark. Elsevier, 2004, . p. 258–405.

172. Dry M.E., Steynberg A.P. "*Chapter 5 Commercial FT Process Applications*." Studies in Surface Science and Catalysis edited by S. André, D. Mark. Elsevier, 2004, . p. 406–481.

173. Dancuart L.P., de Haan R., de Klerk A. "*Chapter 6 Processing of primary Fischer-Tropsch products*." Studies in Surface Science and Catalysis edited by S. André, D. Mark. Elsevier, 2004, . p. 482–532.

174. Dry M.E. "*Chapter 7 FT catalysts*." Studies in Surface Science and Catalysis edited by S. André, D. Mark. Elsevier, 2004, . p. 533–600.

175. Claeys M., van Steen E. "*Chapter 8 Basic studies*." Studies in Surface Science and Catalysis edited by S. André, D. Mark. Elsevier, 2004, . p. 601–680.

176. Batholomew C.H. "*History of Co catalyst design for FTS*." AIChESpringMeeting. NewOrleans, LA, USA , 2003, .

177. Vannice M.A. "*The catalytic synthesis of hydrocarbons from H2CO mixtures over the group VIII metals: I. The specific activities and product distributions of supported metals*." J. Catal., 1975, vol. 37 (3), pp. 449–461.

178. Khodakov A.Y., Chu W., Fongarland P. "*Advances in the Development of Novel Cobalt Fischer−Tropsch Catalysts for Synthesis of Long-Chain Hydrocarbons and Clean Fuels*." Chem. Rev., 2007, vol. 107 (5), pp. 1692–1744.

179. Jager B. "*Developments in Fischer-Tropsch technology*." Studies in Surface Science and Catalysis edited by D.S.F.F.A.V. A. Parmaliana, A. F. Elsevier, 1998, . p. 25–34.

180. Espinoza R.L., Steynberg A.P., Jager B., Vosloo A.C. "*Low temperature Fischer–Tropsch synthesis from a Sasol perspective*." Appl. Catal. A Gen., 1999, vol. 186 (1–2), pp. 13–26.

181. Jager B., Espinoza R. "*Advances in low temperature Fischer-Tropsch synthesis*." Catal. Today, 1995, vol. 23 (1), pp. 17–28.

182. Dry M.E. "*The Fischer-Tropsch process: 1950-2000*." Catal. Today, 2002, vol. 71 (3-4), pp. 227–241.

183. Bromfield T.C., Vosloo A.C. "*Recent advances in the development of Fischer-Tropsch catalysts at Sasol*." Macromol. Symp., 2003, vol. 193, pp. 29–34.

184. Jager B., Van Berge P., Steynberg A.P. "*Developments in Fischer-Tropsch technology and its application*." Studies in Surface Science and Catalysis edited by J.J.S. E. Iglesia, T.H. Fleisch. Elsevier, 2001, . p. 63–68.

185. Steynberg A.P., Espinoza R.L., Jager B., Vosloo A.C. "*High temperature Fischer–Tropsch synthesis in commercial practice*." Appl. Catal. A Gen., 1999, vol. 186 (1–2), pp. 41–54.

186. Jacobs G., Chaney J.A., Patterson P.M., Das T.K., Davis B.H. "*Fischer–Tropsch synthesis: study of the promotion of Re on the reduction property of Co/Al2O3 catalysts by in situ EXAFS/XANES of Co K and Re LIII edges and XPS*." Appl. Catal. A Gen., 2004, vol. 264 (2), pp. 203–212.

187. Li J., Jacobs G., Zhang Y., Das T., Davis B.H., Force. "*Fischer-Tropsch synthesis: effect of small amounts of boron, ruthenium and rhenium on Co/TiO2 catalysts*." Appl. Catal. A Gen., 2002, vol. 223, pp. 195–203.

188. Voβ M., Borgmann D., Wedler G. "*Characterization of Alumina, Sililca, and Titania Supported Cobalt Catalysts*." J. Catal., 2002, vol. 212 (1), pp. 10–21.

189. Jongsomjit B., Panpranot J., Goodwin J.G.J. "*Co-Support Compound Formation in Alumina-Supported Cobalt Catalyst*." J. Catal., 2001, vol. 204 (1), pp. 98–109.

190. Lapidus A.L., Krylova A.Y. "*Catalytic synthesis of isoalkanes and aromatic hydrocarbons from CO and H2*." Russ. Chem. Rev., 1998, vol. 67 (11), pp. 941–950.

191. Jacobs G., Das T., Zhang Y., Li J., Racoillet G., Davis B.H. "*Fischer–Tropsch synthesis: support, loading, and promoter effects on the reducibility of cobalt catalysts*." Appl. Catal. A Gen., 2002, vol. 233 (1-2), pp. 263–281.

List of publications

ARTICLES

1. **M.N. Timofeeva, V.N. Panchenko, A.Gil, V.P. Doronin, A.V. Golovin, A.S. Andreev, V.A. Likholobov.** *Effect of the acid–base properties of Zr,Al-pillared clays on the catalytic performances in the reaction of propylene oxide with methanol*. Applied Catalysis B: Environmental 104 (2011) 54–63 (**DOI:** 10.1016/j.apcatb.2011.02.028).

2. **Andrey S. Andreev, Aleksey N. Salanov, Serguei F. Tikhov, Svetlana V. Cherepanova, Vladimir I. Zaikovskii, Vladimir V. Usoltsev, Vladislav A. Sadykov, and Olga B. Lapina.** *Formation of Micro, Nano and Atomic-Level Structure of CoAlO/Co-Al Cermets Prepared by Mechanical Alloying.* Journal of Materials Science and Engineering A 2 (2), 2012, pp. 121-136 (**DOI:** 10.17265/2161-6213/2012.02.001).

3. **Andrey S. Andreev, Serguey F. Tikhov, Aleksey N. Salanov, Svetlana V. Cherepanova, Olga B. Lapina, Vasiliy A. Bolotov, Yuriy Yu. Tanashev, Jean-Baptiste d'Espinose de Lacaillerie, and Vladislav A. Sadykov.** *Design of Al_2O_3/CoAlO/CoAl Porous Ceramometal for Multiple Applications as Catalytic Supports.* Advanced Materials Research Vol. 702 (2013) pp 79-87. (**DOI:** 10.4028/www.scientific.net/AMR.702.79)

4. **A.S. Andreev, O.B. Lapina, J.-B. d'Espinose de Lacaillerie, A.A. Khasin.** *Effect of alumina modification on the structure of cobalt-containing Fischer-Tropsch synthesis catalysts according to internal-field ^{59}Co NMR data.* Journal of Structural Chemistry. Vol 54 (2013), p. S103-S111 (**DOI:** 10.1134/S0022476613070093).

5. **M.N. Timofeeva, V.N., Panchenko, M.M. Matrosova, A. S. Andreev, S.V., Tsybulya, A., Gil, M.A. Vicente.** *Factors affecting the catalytic performance of Zr,Al-pillared clays in the synthesis of propylene glycol methyl ether.* Industrial & Engineering Chemistry Research (**DOI:** 10.1021/ie501048a), 2014, 53 (35), pp 13565–13574

6. **Natalia Bulina; Marina Chaikina; Andrey Andreev; Olga Lapina; Arcady Ishchenko; Igor Prosanov; Konstantin Gerasimov; Leonid Solovyov.** *Mechanochemical Synthesis of SiO44—Substituted Hydroxyapatite. Part II. Reaction*

Mechanism, Structure and Substitution Limit. European Journal of Inorganic Chemistry (**DOI:** 10.1002/ejic.201402246), 2014, vol 2014, pp 4810–4825

7. **Andrey S. Andreev, Olga B. Lapina, Svetlana V. Cherepanova.** *A new insight into cobalt metal powder internal field ^{59}Co NMR spectra.* Appl Magn Res (**DOI:** 10.1007/s00723-014-0580-0), 2014, vol. 45, pp 1009-1017

8. **Dina V Dudina, Oleg I Lomovsky, Konstantin R Valeev; Serguei F Tikhov, Natalya N Boldyreva, Aleksey N Salanov, Svetlana V Cherepanova, Vladimir I Zaikovskii, Andrey Andreev, Olga B Lapina, Vladislav A Sadykov.** *Phase formation during early stages of mechanical alloying of Cu-13wt.%Al powder mixtures in a high-energy ball mill.* Journal of Alloys and Compounds, Vol. 629, 2015, pp. 343-350 (**DOI:**10.1016/j.jallcom.2014.12.120).

9. **Evgeniy Papulovskiy, Dzhalil F. Khabibulin, Victor V. Terskikh, Eugene A. Paukshtis, Valentina M. Bondareva, Aleksandr A. Shubin, Andrey S. Andreev, and Olga Lapina.** *Effect of Impregnation on the Structure of Niobium Oxide/Alumina Catalysts Studied by Multinuclear Solid-State NMR, FTIR, and Quantum Chemical Calculations.* J Phys Chem C, Vol. 119, 2015, pp 10400−10411, (**DOI:** 10.1021/acs.jpcc.5b01616)

10. **A.S. Andreev, O.B. Lapina, J.-B. d'Espinose de Lacaillerie, A. Gerashenko.** *Supported on β-SiC Co metal FTS catalysts thermal stability and hcp-fcc allotropic transformation probed in situ by ferromagnetic NMR.* PCCP, 2015, vol. 17, is. 22, pp 14598-14604, (**DOI:** 10.1039/C4CP05327C).

11. **Anton Shalygin, Ivan Kozhevnikov, Evgeny Gerasimov, Andrey Andreev, Olga Lapina, Oleg Martyanov.** *Effect of the Si/Al ratio on properties of aluminosilicate aerogels synthesized using sol-gel method by NH_3 gelation.* Submitted to Microporous & Mesoporous Materials.

12. **Elizaveta Pustovgar, Rahul Sangodkar, Andrey Andreev, Marta Palacios, Robert Flatt, Bradley Chmelka, Jean-Baptiste d'Espinose de Lacaillerie.** *Transient hydration of silicate surfaces. The case of calcium silicate.* Submitted to Nature Communications.

13. **Andrey S. Andreev, Mariya A. Kazakova, Arcady V. Ishchenko, Alexander G. Selyutin, Olga B. Lapina, Vladimir L. Kuznetsov, Jean-Baptiste d'Espinose de Lacaillerie.** *Templating ferromagnetic Cobalt nanoparticles and wires within Carbon Nanotubes.* Submitted to *Journal of Materials Chemistry A*.

ORAL REPORTS

1. ***Andrey S. Andreev*****, Olga B. Lapina.** *Study of metallic Co-containing Fischer-Tropsch Synthesis catalysts by internal field ^{59}Co NMR technique*. International Symposium and summer school «Nuclear magnetic resonance in condensed matter. 9th meeting «NMR in Heterogeneous Systems», Saint Petersburg, Russia, July 9-13, 2012, p. 27.

2. ***Andrey S. Andreev*****, Olga B. Lapina.** *Structure of Co-containing Fischer-Tropsch catalysts by solid-state NMR techniques.* International satellite school for young scientists "Magnetic resonance and magnetic phenomena in chemical and biological physics". July 16-21, 2012, Novosibirsk, Russia, p.55.

3. ***Andrey S. ANDREEV*****, Olga B. LAPINA, and Jean-Baptiste d'ESPINOSE.** *Internal field ^{59}Co NMR for Fischer-Tropsch heterogeneous catalysts characterization.* EUROMAR 2013, 30th June – 5th July, Hersonissos, Crete, Greece, PS 197.

4. ***A.S. ANDREEV*****, J-B. d'Espinose de Lacaillerie, O.B. Lapina.** *Co metal based catalysts probed by ferromagnetic ^{59}Co NMR.* EUROMAR 2015, Prague, Czech Republic, on 5th – 10th July, 2015 (O 039)

Résumé :
Du fait de leur ferromagnétisme, les nanoparticules de Cobalt se prêtent à la réalisation d'expérience de Résonance Nucléaire Magnétique en Champ Interne du ^{59}Co (RMN-CI). Dans ce manuscrit, nous présentons tout d'abord une description générale de la RMN-CI dans le cadre du modèle de Bloch. Concernant plus précisément le Co(0), passant en revue la littérature, nous insistons sur les aspects controversés et les progrès récents en la matière. Une attention particulière est portée à la caractérisation du Co dans les catalyseurs Fischer-Tropsch (FT) qui représente aujourd'hui un champ majeur d'application de la technique ; l'histoire de la catalyse FT et une brève revue de la synthèse et de la structure de ces catalyseurs sont donc présentées.
Concernant le travail expérimental, celui-ci est structuré de la façon suivante. Tout d'abord, des échantillons modèles sont étudiés afin de mettre en place un modèle interprétatif basé sur les contributions structurales (fcc, hcp, sfs) et magnétiques (domaines, parois de domaines, mono-domaines) à la résonance. Nous passons ensuite à l'étude *in situ* par RMN-CI de la stabilité thermique de nanoparticules supportées sur du β-SiC. La transition hcp/fcc est observée dans la gamme de température 600-650 K. Ceci étant posé, des structures plus complexes ont été étudiées. Nous avons révélé la structure de la partie métallique de céramiques modifiées Co-Al-O.
Finalement, la structure et la stabilité de particules de Cobalt métallique déposées sur et dans des nanotubes de carbone ont été étudiées. Ces structures hybrides originales ont été examinées par RMN-CI, microscopie électronique en transmission et DRX synchrotron *in situ*.

Mots clés : cobalt, métal, RMN en champ interne, ferromagnétisme, catalyseurs, nanoparticules.

Internal field ^{59}Co Nuclear Magnetic Resonance, application to catalysts and related structures

Abstract :
This manuscript is devoted to the study of different catalysis-related materials by Internal Field ^{59}Co Nuclear Magnetic Resonance (IF-NMR). The principles of IF-NMR are stated, based on the Bloch model, which gives a good insight into the internal field NMR mechanism. Further, a short description of the possible range of materials than can be studied by IF-NMR is provided with a particular emphasis on Co Fischer-Tropsch synthesis catalysts.
The study of a model sample used to assess our understanding of IF-NMR spectra is included. This model is based on separating the structural (fcc, hcp, and sfs) and magnetic (domains, domain walls, and single-domain particles) contributions. Our experimental work uncovers the thermal stability of small Co nanoparticles probed *in situ* by IF-NMR. Co(0) supported on *β-SiC* is studied within the 300-850 K temperature range. The line position and width are mainly determined by magnetic properties, whereas the absolute and relative NMR intensities give crucial information regarding the Co particle stability. A study of Fischer-Tropsch catalysts synthesized by non-conventional co-precipitation routes on different modified aluminum oxides is presented. The IF-NMR application to Co-Al-O ceramic materials provided unique information on the metallic cermet part of the sample.
The structure and stabilization of different size Co(0) nanoparticles on multi-walled carbon nanotubes have been studied. These hybrid structures were examined by IF-NMR, HRTEM, and *in situ* synchrotron XRD, which provide crucial information on Co particles reduction, stability and structures.

Keywords : cobalt, metal, internal field NMR, ferromagnetism, catalysts, nanoparticles.